UNIVERSITY OF MILANO - BICOCCA
Department of Materials Science

PhD School in Nanostructures and Nanotechnologies
XXVIII cycle

Atomistic simulation of thermal transport and vibrational properties in phase change materials

A. A. 2014 – 2015

PhD dissertation of:
Davide Campi

Tutor:
Prof. Marco Bernasconi

Contents

Introduction **1**

1 Phase change materials and memories **5**
- 1.1 General features 5
- 1.2 Thermal transport in phase change materials 10
- 1.3 Novel architectures for phase change memories 13
  - 1.3.1 Multi-bit phase change memories and nanowires 13
  - 1.3.2 Interfacial phase change memories 16

2 Computational Methods **19**
- 2.1 Density functional theory 19
  - 2.1.1 Exchange-correlation functionals 21
  - 2.1.2 Plane waves and pseudo-potentials 22
  - 2.1.3 Brillouin zone sums 23
  - 2.1.4 Forces 24
  - 2.1.5 DFT-D semiempirical correction for long range dispersion forces . . . 25
- 2.2 Density Functional Perturbation Theory 26
  - 2.2.1 Linear response 26
  - 2.2.2 Phonons 27
- 2.3 Thermal conductivity from ab-initio calculations 29
- 2.4 Molecular Dynamics 35
- 2.5 Thermal conductivity from non-equilibrium molecular dynamics simulations . 37
- 2.6 Neural Network interatomic potential 38
  - 2.6.1 Neural Network potential energy surfaces for atomistic simulations . . 41
    - Symmetry functions 42
    - Forces and stress evaluation 44
    - Extrapolation 45
    - Neural Network potential for GeTe 45

3 Thermal conductivity in Phase Change Materials **47**
- 3.1 GeTe 48
  - 3.1.1 Ab initio structural and vibrational properties of crystalline GeTe . . . 49

3.1.2 Thermal conductivity of crystalline GeTe by ab initio DFPT calculations 52
3.1.3 Thermal conductivity of crystalline GeTe by neural network calculations 58
3.1.4 Thermal conductivity in amorphous GeTe 61
3.2 $Ge_2Sb_2Te_5$ 63
3.2.1 Ab initio structural and vibrational properties of crystalline GST 65
3.2.2 Thermal conductivity of GST 67
3.3 Sb_2Te_3 73
3.3.1 Ab initio structural and vibrational properties of crystalline Sb_2Te_3 . . 74
3.3.2 Thermal conductivity of Sb_2Te_3 75
3.4 InSbTe Alloys 76
3.4.1 Thermal conductivity of $In_3Sb_1Te_2$ 76
3.5 Conclusions 77

4 Thermal Boundary Resistance 79
4.1 Thermal boundary resistance at $Ge_2Sb_2Te_5$ interfaces 81
4.1.1 Electron-phonon contribution to the thermal boundary resistance at the interface of GST with metals and dielectrics 82
4.1.2 Lattice contribution to the thermal boundary resistance at the interface of GST with metals and dielectrics 85
4.2 Thermal boundary resistance at GeTe interfaces 90
4.2.1 Electron-phonon coupling and electronic contribution to the thermal boundary resistance 90
4.2.2 Lattice contribution to the thermal boundary resistance between GeTe and electrodes or dielectrics 94
4.2.3 Thermal boundary resistance at crystalline/amorphous GeTe interface. . 95
4.3 Conclusions 96

5 Surface phonons of Sb_2Te_3 and Bi_2Se_3 97
5.1 Sb_2Te_3 and Bi_2Se_3 (0001) Surfaces 98
5.2 Conclusion 106

6 Sb_2Te_3-GeTe superlattices 107
6.1 Structural properties and Raman spectra of $Ge_1Sb_2Te_4$ 109
6.2 Structural properties and Raman spectra of $(GeTe)_2$-Sb_2Te_3 superlattices 112
6.3 Conclusions 120

7 GeTe multilayers 121

8 Sb_2Te_3 Nanowires 129

9 Neural Network potential for GeTe Nanowires 137
9.1 Validation of the GeTe potential for nanowires 137
9.2 Thermal transport in GeTe Nanowires 142

Conclusions 147

Publications 149

Collaborations 151

Bibliography 153

Introduction

Phase change materials are a class of chalcogenide compounds employed for data storage applications. They are at the basis of commonly used optical memories (e.g. DVD-RW and Blue-Rays) and in the last few years they had been under scrutiny for the development of new electronic non volatile memories known as phase change memories (PCM) [1, 2]. Originally designed as a replacement for NOR Flash memories in recent years PCMs have widened their application range. It has been demonstrated that PCMs are promising candidates for the realization of the so called "storage class memories", non-volatile memories with an access speed comparable to that of the volatile DRAMs [3], and in applications for neuromorphic computing [4, 5]. Both optical disks and PCMs are based upon a fast and reversible transitions between the crystalline and an amorphous phases, that correspond to the two states of the memory, i.e. the 0 and 1 bits. The two states can be discriminated thanks to a large difference in their optical and electronic properties, the crystal being roughly speaking metallic and the amorphous phase being insulating. The phase transition is induced by heating, produced by a laser pulse in DVD's and by Joule effect in PCMs.

A PCM device consists of a resistor made of a thin film of a phase change material between a metallic contact and a resistive electrode that heats up the active layer. The programming operations are performed by applying a bias of few Volts, enough to have a sufficient current flow to induce either the melting of the crystal and subsequent amorphization or the recrystallization of the amorphous phase.

Thermal properties of phase change materials greatly influence almost every key figure of merit of PCMs such as the programming current, scalability and reliability [6–8]. For this reason quantities like thermal conductivity and thermal boundary resistance in PCMs have been largely studied from an experimental point of view. Most of these data, however, still need to be fully understood and explained into a theoretical picture. Just to mention one issue we remark that the hexagonal phase of $Ge_2Sb_2Te_5$ (GST), one of the most popular material for PCMs applications, presents an unusually low lattice thermal conductivity of just 0.5 W/m K [9] which is in the range of thermal conductivities of glass-like materials and not of crystals.

This thesis is devoted to the study of phonons and thermal transport of phase change materials of interest for applications in PCMs. To this aim we used atomistic simulations based on density functional theory (DFT) and molecular dynamics simulations suitably designed interatomic potentials. After a general introduction on the properties of phase change memories and materials given in chapter 1, we report a description of the computational detail in chapter 2.

In chapter 3 we report the results the thermal conductivity of three widely used phase change materials such as the aforementioned hexagonal $Ge_2Sb_2Te_5$, amorphous and crystalline GeTe and InSbTe alloys. The thermal conductivity of GST and crystalline GeTe has been computed solving the Boltzmann transport equation on the basis of harmonic and anharmonic force constants calculated with ab initio methods [10]. As a cross validation, and to directly evaluate the role of defects, thermal conductivity of crystalline GeTe has been computed also with a molecular dynamics(MD) approach [11] using a neural network interatomic potential developed in our group [12]. The same MD technique was also applied to studying amorphous GeTe, while a simplified model, known as minimum thermal conductivity model, was employed to estimate the thermal conductivity in InSbTe.

In chapter 4 we addressed the problem of estimating the thermal boundary resistance (TBR) between GST, GeTe and the materials commonly used as dielectrics or metallic contacts in memory devices. TBR can reach sizable values [9] in PCMs and their knowledge is essential for a complete electrothermal modeling of PCM cells. By mean of DFT calculations we have been able to identify the different contributions to the TBR of several interfaces of interest for PCMs

In the last few years the research on phase change materials expanded from the bulk materials to nanowires and superlattices.

Superlattices have recently attracted a considerable interest after the proposal of the so called “interface phase change memories” (iPCM) [13]. These memories rest on the transition among different crystalline phases in GeTe-Sb_2Te_3 superlattices without melting. This transition is expected to be produced by just a small movement in the Ge sublattice and requires thus far less energy than an amorphization-recrystallization process.

Although the effectiveness of superlattices in the realization of low power phase change memory has been demonstrated [13] the switching mechanism and even the actual crystal structure are still matter of debate. Among the different proposals, it has been suggested that the switching stems from a change in the topologically protected interface states that originates at the interface between the topological insulator Sb_2Te_3 and the normal insulator GeTe. The same states, appearing also at the surface of Sb_2Te_3, have been proposed to affect the dispersion relations of surface phonons. To address this issue, we computed surface phonons at the (0001) surface of Sb_2Te_3 and of the similar Bi_2Se_3 for sake of comparison as reported in chapter 5.

The vibrational properties of GeTe-Sb_2Te_3 superlattices are reported in chapter 6. Since the different structures proposed for these superlattices feature different bonding geometries in the GeTe blocks one would expect specific vibrational signatures of the different crystal structures. Would this be the case, one should also be able to identify the structures, monitor the switching process and perhaps also identify intermediate states by micro-Raman measurements. To this end we computed the Raman spectra for the most likely structures. Since no experimental data are available on these superlattices we first used $Ge_1Sb_2Te_4$ as a reference system to assess the reliability of our theoretical framework. The realization of precise and highly controlled iPCMs structures requires an accurate control of the growth process that can be achieved by molecular beam epitaxy (MBE). The MBE growth of GeTe multilayers is a first step towards this goal. Moreover GeTe multilayers are of great interest for they own properites like a giant Rashba splitting [14] and the possibility of a ferroelectric switching [15]. In chapter 7 we present the calculations of the Raman spectra of GeTe multilayers aimed at explaining the evolution of the peaks observed during their growth on Sb-passivated silicon surfaces.

Nanowires are otherwise promising systems to obtain defect-free crystal structures and overcome the size limitations imposed by lithographic processes pushing further the scaling limits of PCMs. Furthermore, nanowires in the form of core-shell systems are considered among the best candidates for the realization of multibit memories [16].

In chapter 8 we studied the energetic of the surfaces of Sb_2Te_3 nanowires, in order to explain the peculiar morphology and crystal structure observed. Finally, in chapter 9 we report about the fitting of an extend version of the neural network potential for bulk GeTe developed in Ref.[12] able to properly treat surfaces and nanowires and we present a first application of this potential in the calculation of the thermal conductivity of GeTe crystalline nanowires.

The theoretical activity of this thesis has been stimulated by collaborations with experimental groups mostly within the FP7-EU Project Synapse.

1 Phase change materials and memories

1.1 General features

Phase change materials are compounds of great technological relevance since they are nowadays commonly employed in the well established technology of optical memories (e.g. DVD-RW and Blue-Rays) and in a novel emerging class of electronic non volatile memories (NVM) known as Phase Change Memory (PCM) [1, 2]. Both applications rely on the fast and reversible transition between the crystalline and the amorphous phase, induced by heating produced either by a laser pulses (DVDs) or by Joule effect (PCMs) [17]. The crystalline and amorphous phases show large differences in both reflectivity and resistivity, exploited to store information in optical memories and PCMs.

The first material showing phase change properties was discovered back in the 60's by J.F. Dewald [18] and S. R. Ovshinsky [19], but the crystallization speed of this first alloy was too low for any practical application. Phase change materials were rediscovered in the '90, when the search for faster rewritable optical discs led to the discover of new and more performing phase change compounds based on chalcogenides alloys.

In particular, the family of the pseudobinary compounds $(GeTe)_x(Sb_2Te_3)_y$ whose phase diagram is shown in Fig.1.1, represents a prototypical system. The $Ge_8Sb_2Te_{11}$ is the composition actually used in Blue-Ray disks [2] while in PCM $Ge_2Sb_2Te_5$ (GST) has been the material of choice so far thanks to its high transformation speed and the high stability of the metastable amorphous phase [17]. Many other alloys, containing also In and Ga, have been studied for particular purposes such as application at high temperature in automotive electronics [20].

A 64 Mbits PCMs prototype was realized by Samsung back in 2004. In 2012 Micron reached the mass production scale and commercialized the first 45 nm PCM device for mobile applications [21, 22] as replacement for NOR Flash memories.

In past few years the technological interest for PCMs shifted towards their possible use in the realization of the so called storage class memories: non-volatile memories with an access speed comparable to that of the volatile DRAMs [3].

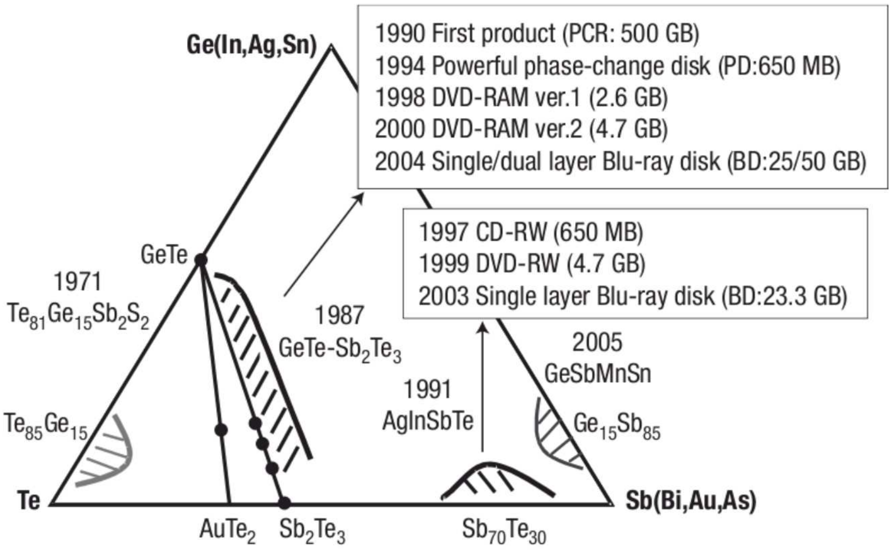

Figure 1.1: Sketch of the Ge Sb Te ternary phase diagram. Composition intervals of interest for applications in optical disks are highlighted (Ref. [17]).

In 2014 Western Digital announced a prototype of a PCM based storage disk with a reading speed 100 faster than state-of-the art solid state hard drives and a comparable writing speed. In July 2015 Intel and Micron have announced the release of a new “3D Xpoint” crossbar technology suitable to fabricate storage class memories [23]. Although no information has been released on the details of this new technology, it is common believe that PCMs are a leading contender for the realization of such storage class memories.

Although many different architectures have been developed over the years, the most common one is the so called “mushroom cell” shown in Fig.1.2. The single cell is composed by a transistor that acts as a selector that modulates the current pulse in the read and write operations, while the resistor is made by a thin film of phase change material sandwiched between a metallic contact and a resistive electrode, usually TiN, that operates as a heater.

There are two different operations in the programming process of the cell (Fig.1.3): SET and RESET. In the RESET the active material switches from the conductive crystalline phase to the amorphous insulating phase with a resistance of the order of few MΩ, while in the first process the chalcogenide switches back from the amorphous to the crystalline phase.

In the RESET operation, the temperature of the active layer is briefly raised over the melting temperature T_m using a short and intense current pulse after which a small dome of melted active material experiences a fast (30-50 ns) cooling in which the liquid freezes into the amorphous

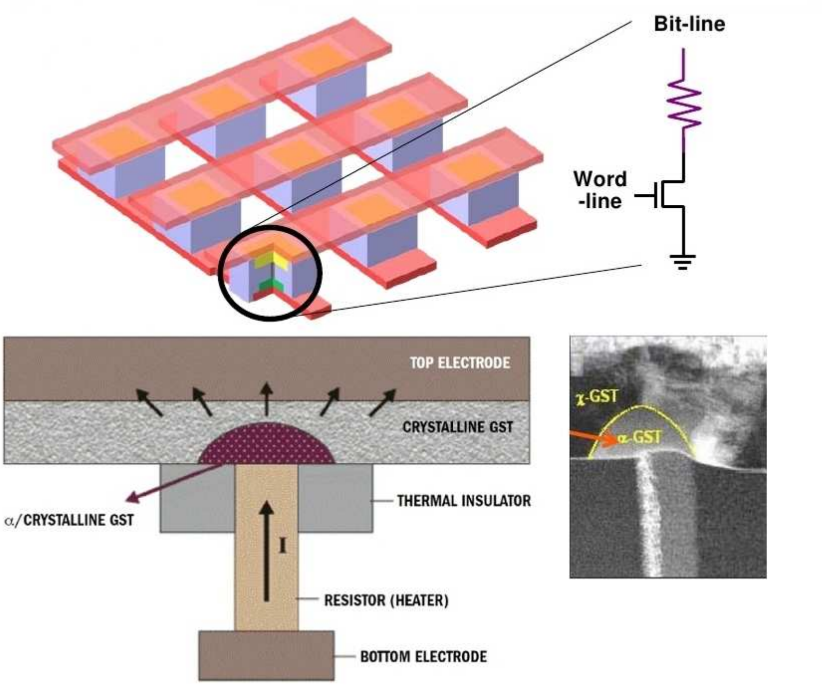

Figure 1.2: a-b) Architectures of a PCM cell in the so called "mushroom" configuration (Ref. [1]). c) SEM image of the programming region of the cell indicating the amorphous and the crystalline part.

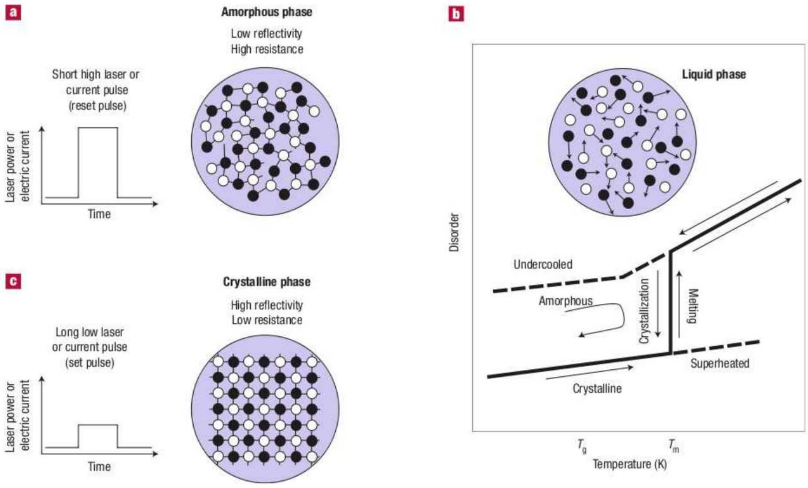

Figure 1.3: RESET a,b) and SET c) process typically used in PCM programming. The same concepts apply to the programming of optical memories based on phase change materials like e.g. DVD-RAM and Blu-Ray disks.

phase. To revert the transformation the material is heated up, with a longer and less intense pulse, to a temperature higher than the glass transition temperature T_g (or crystallization temperature) at which the atomic mobility is high enough to allow the recrystallization on the time scale of approximately 100 ns.

The Joule heating of the amorphous phase in the SET process is enabled by a peculiar electronic behavior of the amorphous phase, which shows a high electrical resistivity at low voltages (mV), by increasing the applied bias above a threshold voltage (V_{th}) of the order of few Volts, it undergoes a purely electronic transition to a less resistive state (a process known as threshold switching) which allows for a sufficient current flow.

The current-voltage characteristic of the amorphous phase displaying the threshold switching is shown in Fig. 1.4. The crystal has instead a simple Ohmic behavior as also shown in Fig. 1.4. The reading of the memory is performed applying a voltage lower than V_{th}.

A key factor for the application of phase change materials in memory devices is their very high crystallization speed and in particular their very high nucleation rate. Over the years many proposals have been raised to explain this peculiar property.

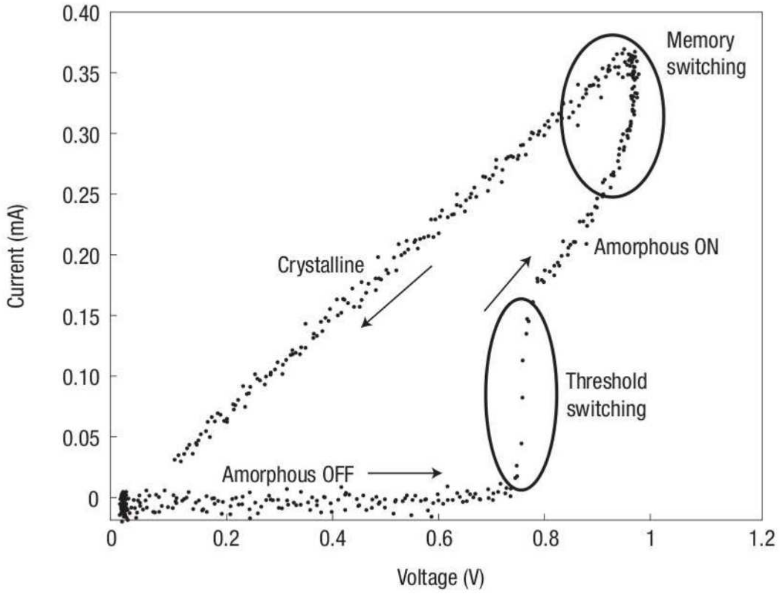

Figure 1.4: Typical current-voltage characteristic of a phase change device. When the applied voltage is low, a very low current flows through the amorphous material, while, by applying a bias above a threshold voltage of about 0.7 V, the resistance drops and the current intensity increases (threshold switching) allowing Joule heating and recrystallization. The crystalline phase is metallic with a low ohmic resistance [17].

On the basis of Extended X-Ray absorption fine structure (EXAFS) spectra [24–26], Kolobov et al.[27, 28] proposed that the crystallization consists of a small movement of Ge atoms that change their coordination from a tetrahedral geometry in the amorphous to the octahedral geometry of the crystal, which has been thus called “umbrella flipping” model.

Ab-initio molecular dynamic (MD) simulations have later proposed a different model for the amorphous phase in which only 1/3 of Ge atoms are in tetrahedral configuration while the majority is in a defective octahedral bonding geometry with bonding angles typical of the octahedral environment of the crystal but a coordination number lower than six [29, 30, 33].

Hegedus and Elliott [31] further recognized that the network topology in the amorphous phase consists of mostly four-membered rings which are also the building block of the crystalline rocksalt phase. They suggested that the phase transition occurs thanks to a fast realignment of four-membered rings [32–34] present in both the amorphous and crystalline phases.

More recently, however, it has been realized that the crystallization during the SET operation actually occurs at temperatures well above the glass transition which implies that high speed of crystallization actually depends on the properties of the supercooled liquid. Recent ultra-fast differential scanning calorimetry (DSC) measurements on GST [35] and MD simulations [36] actually ascribed the fast crystallization of these materials to the fragility of the liquid phase.

The fragility of a liquid is defined on the basis of the temperature dependence of the viscosity η. Strong liquids show an Arrhenius behavior of η as a function of temperature T in the range between the melting temperature T_m and the glass transition temperature T_g. Fragile liquids, instead, are characterized by a super-Arrhenius behavior of η as shown in Fig.1.5.

For fragile liquids, η can be very low down to temperatures close to T_g resulting in a high atomic diffusivity which can boost the crystallization speed as predicted classical nucleation theory. Moreover it has been proved both experimentally [35] and theoretically [37] that another factor that boost the crystallization speed in phase change materials is the breakdown of the Stokes-Einstein relation (SER). The SER, that relates the viscosity η with the diffusivity D as:

$$D = \frac{k_B T}{6\pi\eta r_p} \tag{1.1}$$

where k_B is the Boltzmann constant and r_p the dimension of the particles, is strictly valid in the hydrodynamic regime, but it is often not satisfied in fragile liquids where both a high diffusivity and a large viscosity can be present.

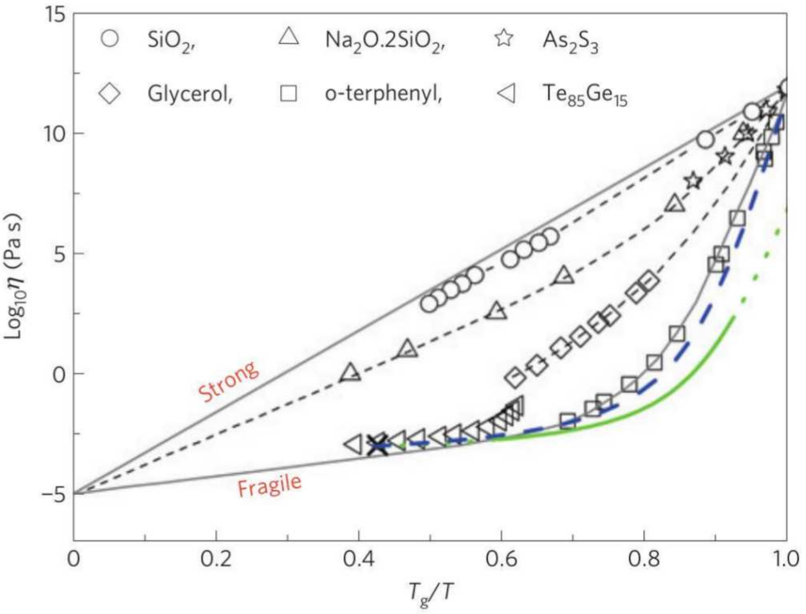

Figure 1.5: Behavior of the viscosity as a function of the reduced temperature for different supercooled liquids. In strong liquids the viscosity follows an Arrhenius behavior, while a super-Arrhenius behavior is observed for fragile liquids. The blue (green) curve represent the viscosity η values estimated in Ref. [35] for $Ge_2Sb_2Te_5$ from ultra-fast DSC assuming (or not) the Stoks-Einstein relation to hold.

In phase change materials a very high diffusivity, that allows for a fast structural reorganization, has been indeed observed even at temperature very close to the glass transition where the viscosity becomes high. This effect further contributes to speed up the crystallization. The breakdown of the Stokes-Einstein relation has been studied in details in GeTe [37] where it has been ascribed to the presence of a dynamical heterogeneity, i.e. localized regions where atoms move with a higher speed and regions where atoms move slower.

1.2 Thermal transport in phase change materials

Thermal properties of phase change materials recently attracted a considerable interest. Thermal design and engineering in fact play an important role in optimizing the performance of both optical and PCM devices. In PCMs in particular, thermal properties influence almost every relevant parameter for technological applications such as the programming current, scalability, reliability, and cross talk among neighboring cells.[6–8] Several device studies indicated that increasing interfacial [38, 39] and volumetric[40, 41] thermal resistances can reduce programming current and improve reliability [38, 42]. Furthermore, beside their application as phase change materials, chalcogenide have also attracted much attention as candidates for thermoelectric power conversion applications [43, 44].

Experimental measurements of lattice and electronic thermal conductivity and of the resistance at the interface between two materials due to the partial heat carrier transmission (thermal boundary resistance or TBR), have been performed mainly on thin chalcogenide films using different techniques such as the 3ω method, optical transient thermoreflectance (TTR) and optical time domain thermoreflectance (TDTR). Commonly, for samples below 100 nm, 3ω and TTR can only access effective thermal properties, spatial averages which include both the effect of bulk and interfacial resistance, while only TDTR has in principle the temporal resolution to potentially resolve the TBR and intrinsic thermal properties uniquely in a single measure.

In the 3ω method a microfabricated metal line is used as both a heater and thermometer to measure the thermal response of the underlying thin films and/or substrate. A current, I_{ω} , at frequency ω is used to induce heat generation at frequency 2ω in the metal line. The linear thermal transfer function of the thin films and substrate relates the 2ω heating to the 2ω temperature rise in the metal line. The metal line resistance varies linearly with temperature, causing resistance oscillations, $R_{2\omega}$, at 2ω, and voltage oscillations at 3_{ω} (due to the product of I_{ω} and $R_{2\omega}$) which is measured and used to determine the thermal transfer function [45]. Since phase change materials are electrically conductive they need to be isolated from the metal line with a passivation layer. The measured thermal impedance include thus also the contribution of the interface resistance and multiple measurements with different film thickness are necessary to decouple the TBR from the intrinsic material properties.

Several authors report the thermal conductivity of PCM materials using the thin film 3ω method [46–49]. Fallica et al.[9] reported measurements of the total thermal conductivity for two crystalline phases of GST (hexagonal κ=1.13 W/m K and rocksalt κ=0.55 W/m K) and amorphous GST (κ=0.21 W/m K) and an estimate of the thermal boundary resistance between these three phases and silica (94, 72 and 159 m^2 K GW^{-1} respectively). In another work [51] a total thermal conductivity of κ=3.08 W/m K was reported for crystalline GeTe and κ=0.23 W/m K for its amorphous phase.

Optical thermometry techniques (TTR and TDTR) measure the transient change in reflectance to probe the thermal response of a thin film stack. In contrast to the 3ω technique, optical techniques are noncontact and do not require electrical passivation layers. In thermoreflectance measurements, a high-intensity laser pulse causes a temperature excursion in the sample. A probe beam samples the temperature of a metal transducer via its relative reflectance change. In time domain thermoreflectance the reflectivity is measured with respect to time, with a resolution down to 10 ps, and the data received can be matched to a model which contain coefficients that correspond to thermal properties [53].

Recent TDTR measurements [54] provided further data on the thermal conductivity of GST (κ=1.32 W/m K of which 0.73 W/m K due to electronic contribution for the crystalline hexagonal phase, κ=0.45 W/m K for the rocksalt phase and κ=0.23 W/m K for the amorphous). GST has thus a glass-like thermal conductivity also in the crystalline phase due to different types of disorder. Moreover the thermal boundary resistance between GST and TiN was measured leading to a much lower value (12 m^2 K GW^{-1} for the hexagonal-GST/TiN interface and 24 m^2 K GW^{-1} for cubic-GST/TiN interface) than the previous measurements for the GST/silica interface.

From a theoretical point of view thermal conductivity in phase change materials has been addressed so far only with simplified models. The lattice thermal conductivity has been estimated with good results [47, 55] in amorphous and rocksalt GST (which is characterized by a strong disorder on Ge/Sb sublattice) using the minimum thermal conductivity model. This model attributes all the thermal conductivity to the acoustic modes and assumes a mean free path of the phonons of the same order of magnitude of the interatomic distances, an approximation that can hold in highly anharmonic systems or systems characterized by a large scattering contribution from disorder or vacancies.

In the case of electrically conducting phase change materials, electron contribution to the thermal conductivity has been commonly estimated on the basis of electrical conductivity measurements and the application of the Wiedemann-Franz-Lorenz rule that links the electron contribution to the thermal conductivity κ_e to the electrical conductivity σ as $\kappa_e/\sigma = LT$ where L is the Lorenz number (2.45×10^{-8} W Ω K^{-2}) and T is the temperature.

Thermal boundary resistance in phase change materials can have different contributions. At the interface between any two materials is present a TBR term which originates from the imperfect transmission of phonons through the interface. This term has been estimated in literature for PCMs with varying degrees of success [9, 54] using acoustic mismatch model (AMM) [56] and diffuse mismatch model (DMM) [57, 58] that in their simplest form predict interfacial phonon transmission and reflection rates on the basis of the mismatch between the sound velocities in the two media.

A second contribution to the TBR may rise when electrons contribute significantly to the thermal conductivity of one or both contacting materials, since they also affect interfacial transport. Electron-electron contribution to the TBR has been estimated for phase change materials using the so called interfacial Wiedemann-Franz-Lorenz (which states that electron-electron term of thermal boundary resistance is equal to the electric interface resistance divided by the LT factor) but is usually considered to have a negligible effect at the interfaces relevant for PCMs.

Finally an interesting case might be represented by the interface among a conductor and an insulator where electrons and phonons must interact to transport heat across the boundary. A general theory that describe such an interface has been developed Majumdar and Reddy [59] but the problem has never been addressed in literature for PCMs.

As briefly summarized in the introduction we have addressed some of these issues on thermal properties by means of atomistic simulations. In chapter 3 we report on the atomistic calculations of thermal conductivity in bulk GeTe, GST and Sb_2Te_3 to address the role of different type of disorder while in chapter 4 we studied the different contributions to the TBR of GST and GeTe with metals and dielectrics.

1.3 Novel architectures for phase change memories

In recent years several new possibility of development for phase change materials emerged in the form of new applications, new materials and new scaling perspectives. In the next paragraphs we will briefly present two of them, addressed to some extent in the present thesis. We will discuss first the possible realization of multi-bit memories cells in bulk and especially in nanowires and then a new class of PCMs, called “Interfacial phase change memories” realized in $(GeTe)_2Sb_2Te_3$ superlattices and particularly promising for low power applications.

1.3.1 Multi-bit phase change memories and nanowires

The realization of a multi-bit memory represent an effective way to significantly increase the storage density of a memory device. The realization of multi-bit memory based on phase change materials was already proposed in 1995 by Ovshinsky and co-workers [60] exploiting the possibility to create intermediate-resistance states by controlling the dimensions of the amorphized region within the active layer and exploiting the large span of resistivity (up to three order of magnitude) between the amorphous and crystalline phases.

Multi-bit memories have been realized using the classical “mushroom” configuration using nitrogen doped GST [61]. Moreover it has been demonstrated that up to 16 intermediate resistance levels can be realized in this architecture by using a read-verify-write algorithm [62, 63]. In this method several writing pulses are applied on a cell to reach a target resistance level. The shapes of the pulses are adjusted at each iteration on the basis of the distance of the actual resistance from the target value.

Multi-bit memories have also been fabricated or with stack of three layers of a phase change material with three heaters of different sizes as shown in Fig.1.6 that induce a layer-by-layer transformation [64–66].

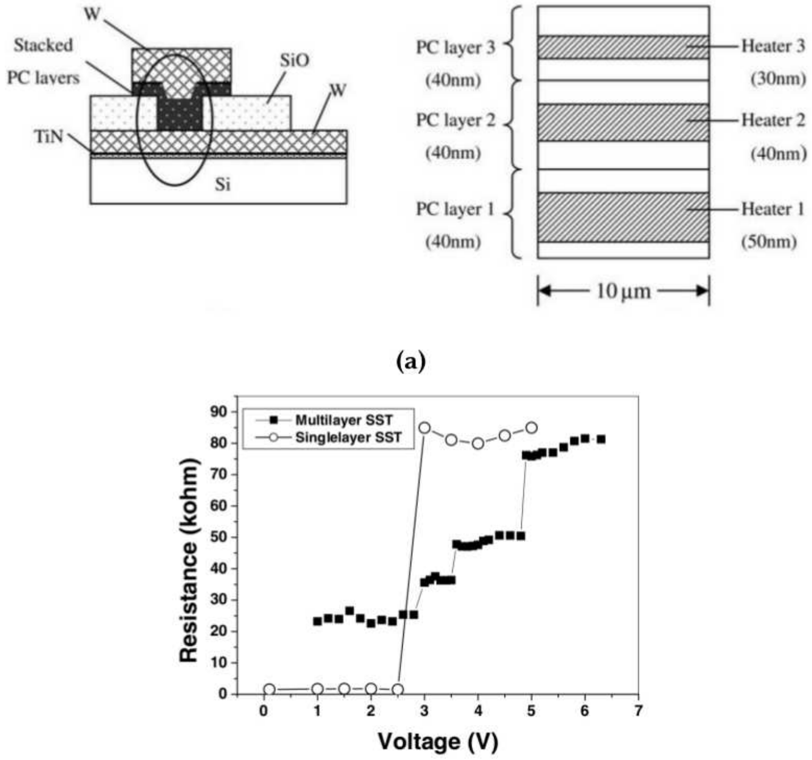

(a)

(b)

Figure 1.6: Scheme of a stacked 2-bits (00, 01, 10, 11) phase change memory cell and the relative R-V characteristic.

However, the realization of complex multi-stack devices using a standard top-down approach based on the deposition of thin films and subsequent lithographic steps is an extremely delicate process and could easily bring to uncontrollable structural defects and ultimately limit the scalability. For this reason an alternative promising technique technology is represented by the multi-bit memories realized with core-shell nanowires (CS-NW). Nanowires present the advantage of a defect-free crystal structure and sublithographic dimensions (ideally down to 10 nm) which can result in a lower power consumption compared to conventional PCMs as already demonstrated for single-level memories based on GeTe or In_2Se_3 [67]. Multi-level devices can be realized by using CS-NW where the two phase change alloys of the core and shell have a different melting or crystallization temperatures. Programming can be carried out by applying current pulses of different intensity in order to induce a sequential melting of the shell and the core and reach intermediate values of resistance.

Multi-level memories with CS-NW made of $Ge_2Sb_2Te_5$ (core) and GeTe (shell) have recently been realized [16] managing to obtain three well separated resistance levels (cf. Fig. 1.7). The cell has the lowest resistance when both the GST and GeTe are in the crystalline phase. By applying a current pulse of 1.2 mA, the GST core melts and amorphize, while GeTe remains crystalline obtaining an intermediate value for the resistance. The higher resistive state is reached when both GST and GeTe are in the amorphous phase.

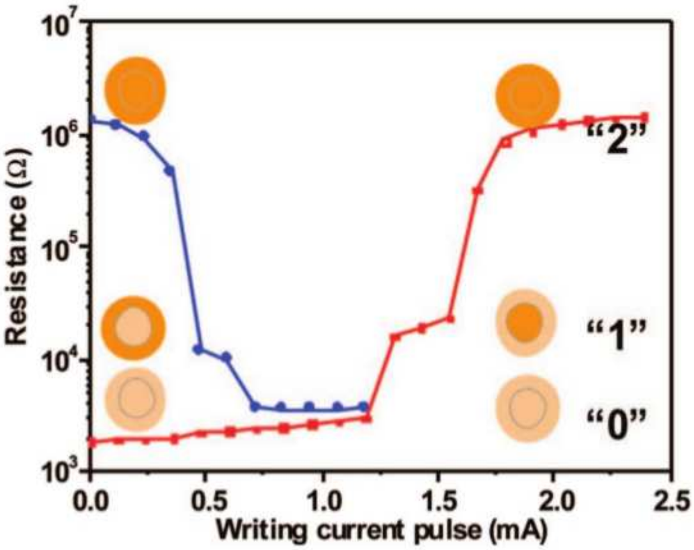

Figure 1.7: Variation of resistance of a core/shell GST/GeTe nanowire device as a function of current pulses with varying amplitudes. The three different resistive states (low, intermediate, and high) achieved with application of current pulses are clearly distinct. The schematic represents the cross section of the core/shell nanowire at each stage of transition, where color change corresponds to the phase transition: light orange represents crystalline phase, and dark orange is amorphous. Blue line refers to an initially amorphous nanowire, while red line to a nanowire initially in the crystalline phase [16]

In this thesis we addressed the various issues on the properties of nanowires that arised within a collaboration with an experimental team in the joint FP7-EU project Synapse. In particular we studied the morphology of Sb_2Te_3 nanowires and the thermal conductivity of GeTe nanowires.

Finally it is worth noticing that the continuous transition between resistance levels in a PCM used in an analog manner, can mimic the behavior of a biological synapse. A phenomenon called spike-timing-dependent plasticity (a biological process where the strength of connections between neurons are adjusted during learning) has also been demonstrated in PCM devices using specific programming schemes [68]. PCMs are thus under scrutiny as active elements for the design of neuromorphic computers with electronic hardware that resembles the functions of brain elements. Image recognition using a neural network of PCM devices was also demonstrated [4, 5].

1.3.2 Interfacial phase change memories

Recently, a new type of phase change memory device called 'interfacial phase change memory' (iPCM) has been proposed and is attracting considerable interest since the SET-RESET phase switching energy was demonstrated to be far smaller than that in conventional GST alloys and could thus play an important role in low power devices.

The iPCMs consist of hexagonal $(GeTe)_n$-$(Sb_2Te_3)_m$ superlattices deposited by sputtering along a growth direction corresponding to the c axis of rhombohedral Sb_2Te_3. The precise structure of the crystalline phases involved is, nowadays still matter of debate.

Although the effectiveness of iPCM based cells has been proven, the mechanism of phase transition, that can be induced by a nanosecond electrical pulse, is still unclear. It is believed that the transformation involves small displacements of a subset of atoms without melting and subsequent amorphization. Thus in the case of iPCMs, rather than a transformation between an amorphous and a crystalline phase the transition is between two different crystalline structures with distinct conductive properties.

An example of two possible crystal structures representing a SET and a RESET state and their relative band structure is reported in Fig.1.8.

On the basis of high resolution transmission electron microscope (TEM) images of $(GeTe)_2$-Sb_2Te_3 superlattices, it was proposed [13] that the SET state corresponds to a ferroelectric arrangement of the $(GeTe)_2$ blocks and that the RESET state could be obtained by a displacement along the superlattice axis (c) of a layer of Ge atoms in order to form Ge-Ge bonds. (Switched Inverted Petrov)

The RESET state has been later proposed [69] to correspond to the so-called inverted Petrov structure ideally obtained by switching Ge and neighboring Te atoms in the crystalline structure of $Ge_2Sb_2Te_5$ proposed by Petrov et al. [70]. The Inverted-Petrov structure is lower in energy than the Switched-Ferro configurations. A switch between the Petrov (SET) and the Inverted-Petrov (RESET) configurations has also been proposed [71]. In a recent paper, calculations

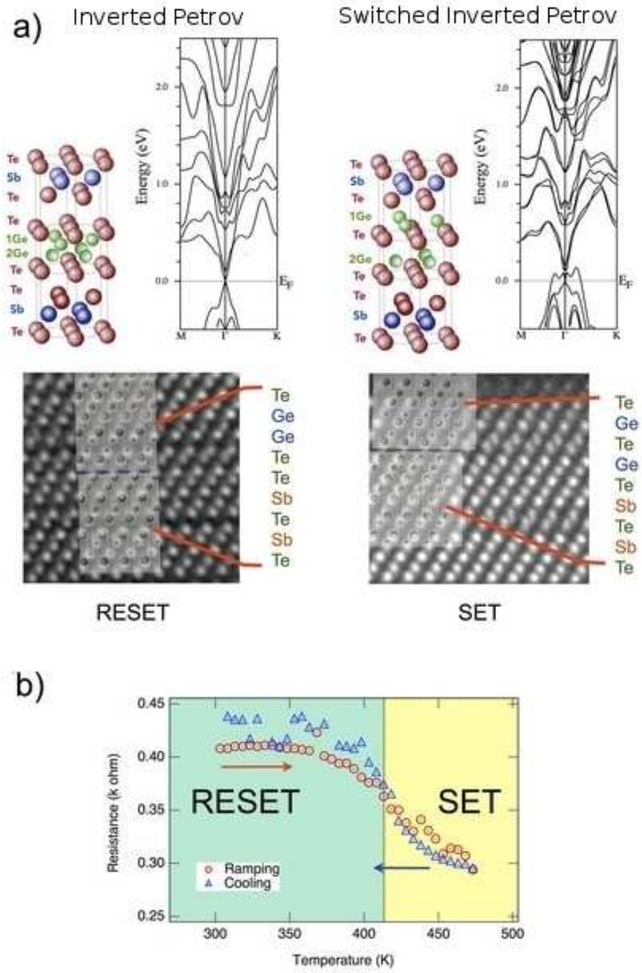

Figure 1.8: In panel a) are sketched the crystalline structures of two possible superlattices named Inverted Petrov and Switched Inverted Petrov together with the theoretical band structures calculated in Ref.[69] and the TEM images for the stuctures. In panel b) is reported the evolution of the resistivity during the switching process.

based on Density Functional Theory have shown that the Ferro → Inverted-Petrov transformation involves both a vertical displacement of one Ge plane and a lateral displacement and a lateral displacement of GeTe layer [72].

More controlled methods to grow chalcogenide superlattices such as Molecular Beam Epitaxy (MBE) are under scrutiny to gain insights on the behavior of iPCMs. As a first step multilayers of GeTe have been grown. In this thesis we contributed to the understanding of the behavior of GeTe multilayers by means of DFT calculations as discussed in chapter 7.

2 Computational Methods

In this thesis, phonons and thermal conductivity have been computed for several systems by different means. For crystalline systems with a relatively small unit cell we used fully ab-initio methods based on density functional theory (DFT see Sec.2.1) and density functional perturbation theory (DFPT, Sec.2.2). The full solution of the Boltzmann transport equation from DFT anharmonic force constants has then been obtained (Sec.2.3).

For large or disordered systems such as nanowires and amorphous materials we performed molecular dynamics (MD) simulations (Sec.2.4) by using a non-equilibrium scheme (Sec.2.5) and an interatomic potential generated with a Neural Network method (Sec. 2.6).

The DFT calculations have been performed with the Quantum-Espresso suite of programs [73] while the Neural Network molecular dynamics simulations have been performed with the proprietary code RuNNer [74] and the DLPOLY code as a MD driver [75].

2.1 Density functional theory

The quantum mechanical behavior of electrons in solids is described by the many-particle Schroedinger equation. This equation contains all the available physical information but except few very special and simple cases is far too complex to be solved exactly. Several models to simplify the complexity of the many-particle problem has been studied, such as the Free Electron, nearly Free Electrons and Tight-Bindings model [76]. None of these models treat the elecron-electron interaction explicitly. An early approach where the electrostatic interaction between electrons is taken into account is the Hartree equation. A further step in increasing accuracy is represented by the Hartree-Fock method that extends the Hartree approximation including also the effects of exchange interaction. The Hartree-Fock method gives good results in systems where the effects of exchange are much more important than the correlation effects. The attempts to include also correlation effects, that for a realistic material are impossible to treat exactly, lead to Density Function Theory (DFT) that, includes both exchange and correlation interactions.

Density functional theory is based on the Hohenberg and Kohn theorem [77]. This theorem states that two different potentials acting on electrons can not give rise to the same ground state electronic charge density $n(r)$. Using this property and the Rayleight-Ritz variational principle. It can be shown that a universal functional of the electron charge density $F[n(\mathbf{r})]$ exists such that the energy E

$$E[n] = F[n] + \int n(\mathbf{r})V(\mathbf{r})d\mathbf{r} \tag{2.1}$$

is minimized by the electron charge density of the ground state corresponding to the external potential $V(\mathbf{r})$, under the constrain

$$\int n(\mathbf{r})d\mathbf{r} = N \tag{2.2}$$

where N is the number of the electrons in the system. Furthermore, the value of the minimum coincides with the ground-state energy. The conceptual simplification introduced by this theorem is enormous: the problem of determining the ground state energy and charge density is now reduced to the minimization of a functional of n(**r**),which depends only on three variables, while the wave functions depend on 3N variables. The major problem of this formulation is that the form of the functional F[n] is unknown. Kohn and Sham [78] had the idea to recast this functional separating out of it a term, $T_0[n]$, defined as the kinetic energy of a non interacting system with the same ground states density n(**r**) of the interacting one, and a Hartree term that represents the classical electrostatic interaction between electrons:

$$F[n] = T_0[n] + \frac{1}{2}\int \frac{n(\mathbf{r})n(\mathbf{r}')}{|\mathbf{r}-\mathbf{r}'|}d\mathbf{r}d\mathbf{r}' + E_{xc}[n] \tag{2.3}$$

We use here atomic units. Now all our ignorance is confined to the exchange-correlation energy $E_{xc}[n]$. The variation of the total energy functional with respect to n(**r**) with the constraint of a fixed number of electrons, leads formally to the same equation of a system of noninteracting electrons subject to an effective potential, called the self-consistent field (SCF) potential, given by

$$V_{SCF}(\mathbf{r}) = V(\mathbf{r}) + \int \frac{n(\mathbf{r}')}{\mid \mathbf{r}-\mathbf{r}' \mid}d\mathbf{r}' + v_{xc}(\mathbf{r}) \tag{2.4}$$

where

$$v_{xc}(\mathbf{r}) = \frac{\delta E_{xc}}{\delta n(\mathbf{r})} \tag{2.5}$$

is the functional derivative of the exchange-correlation energy, called exchange-correlation potential. The advantage of this formulation is that if one knew v_{xc}, the problem for noninteracting electrons could be easily solved. To this end, one should solve the one-electron Schroedinger equation

$$\left[-\frac{\nabla^2}{2} + V_{SCF}(\mathbf{r})\right]\Psi_i(\mathbf{r}) = \varepsilon_i\Psi_i(\mathbf{r}) \tag{2.6}$$

The ground state charge density distribution would then be given by

$$n(\mathbf{r}) = 2\sum_{i} \mid \Psi_i(\mathbf{r}) \mid^2 \theta(\varepsilon_i - \varepsilon_F) \tag{2.7}$$

where the Fermi energy ε_F is defined by the condition on the number of electrons Eq 2.2 and the single-particle orbitals satisfy the orthonormality constrain $\int \Psi_i^*(\mathbf{r})\Psi_j(\mathbf{r})d\mathbf{r} = \delta_{i,j}$. The ground state energy can now be equivalently expressed in terms of the Kohn-Sham eigenvalues:

$$E[n] = 2\sum_{i=1}^{N/2} \varepsilon_i - \frac{1}{2}\int \frac{n(\mathbf{r})n(\mathbf{r}')}{\mid \mathbf{r}-\mathbf{r}' \mid} d\mathbf{r}d\mathbf{r}' + E_{xc}[n] - \int n(\mathbf{r})v_{xc}(\mathbf{r})d\mathbf{r} \tag{2.8}$$

Is worth noting that for electrons in a crystal the external potential $V(\mathbf{r})$ is generated by ionic cores:

$$V(\mathbf{r}) = V_{ion}(\mathbf{r}) = -Z\sum_{\mathbf{R}} \frac{1}{\mid \mathbf{r}-\mathbf{R} \mid} \tag{2.9}$$

where **R** indicates ions coordinates. Moreover to the energy functional E[n] one had to add the ion-ion interaction energy

$$E_N = \frac{1}{2}\sum_{I\neq J} \frac{Z_I Z_J}{\mid \mathbf{R}_I - \mathbf{R}_J \mid} \tag{2.10}$$

2.1.1 Exchange-correlation functionals

The Kohn-Sham scheme constitutes a useful way to implement density-functional theory, provided an accurate and reasonably easy-to-use approximation is available for the exchange-correlation energy $E_{xc}[n]$ whose exact form is unknown. Two of the most used approximations for the exchange-correlation energy are the local density approximation (LDA) [79] and the generalized gradient approximation (GGA) [80]. Within LDA the exchange-correlation energy of the electronic system is constructed by assuming that the exchange-correlation energy per electron at a point **r** is equal to exchange-correlation energy per electron in a homogeneus electron gas with an electron density as at the point **r**

$$E_{xc}^{LDA}[n(\mathbf{r})] = \int n(\mathbf{r})\varepsilon_{xc}(n(\mathbf{r}))d\mathbf{r} \tag{2.11}$$

The LDA is exact in the limit of high density or of a slowly varying charge-density distribution. Appreciably good results using LDA approximation were obtained for semiconductors and simple metals. On the other hand LDA is well-known to considerably overstimate crystal cohesive and molecular binding energies. A generalization of the LDA approximation is the GGA that includes also the gradient of the electron density. The GGA exchange-correlation functional depends on both the electron density and its gradient as:

$$E_{xc}^{GGA}[n(\mathbf{r})] = \int n(\mathbf{r})\varepsilon_{xc}(n(\mathbf{r}), \nabla n(\mathbf{r}))d\mathbf{r} \tag{2.12}$$

In general GGA gives better results than LDA. In this thesis we mostly used the GGA functional developed by Perdew, Burke and Ernzerhof (PBE) [81], for few systems the LDA functional was also used.

2.1.2 Plane waves and pseudo-potentials

In order to accurately describe the Kohn-Sham single-particle wave functions of a system, it is necessary to choose a suitable set of basis functions over which the electron wave functions can be expanded. Several approaches exist. One is to consider the most natural basis functions from real space viewpoint, that is atomic-like basis functions. Alternatively, one could employ a basis set more suitable for a momentum space description of the material, that is the plane waves basis set particularly suitable for periodic systems. This is the basis employed in the Quantum-Espresso program that we used for our simulations. According to Bloch's theorem, in a periodic system, each single particle electronic wave function can be written as a product of a cell-periodic part and a wave like part,

$$\Psi_{n,\mathbf{k}} = u_{n,\mathbf{k}}(\mathbf{r})e^{i\mathbf{k}\cdot\mathbf{r}} \tag{2.13}$$

Using a basis set consisting of a set of plane waves, we can expand the cell-periodic part of the wave function in terms of reciprocal lattice vectors,

$$u_{n,\mathbf{k}}(\mathbf{r}) = \sum_{\mathbf{G}} c_{n,\mathbf{k}+\mathbf{G}} e^{i\mathbf{G}\cdot\mathbf{r}} \tag{2.14}$$

Thus we have

$$\Psi_{n,\mathbf{k}}(\mathbf{r}) = \sum_{\mathbf{G}} c_{n,\mathbf{k}+\mathbf{G}} e^{i(\mathbf{k}+\mathbf{G})\cdot\mathbf{r}} \tag{2.15}$$

For pratical reasons the plane wave basis set has to be truncated by choosing a kinetic energy cutoff through the condition;

$$\frac{1}{2} \mid \mathbf{k}+\mathbf{G} \mid \leq E_{cut} \tag{2.16}$$

Plane waves offer important advantages: they are simpler to use because calculations can be simply checked for convergence by increasing the size of the basis set, they are orthonormal by construction and they are not biased by atomic positions. On the other hand, they present also some drawback like the dependence of the basis set from volume shape and size and a uniform spatial resolution particularly unsuited to describe both the strongly localized core states and the delocalized valence states. Plane waves are used in conjunction with pseudopotentials. The electrons in a solid can be divided into two categories, core and valence electrons. The core electrons organize them self into closed shells which screen the positively charged nucleus, while the valence electrons take part in the bonding between atoms. The wave functions that describe the core electrons and the valence electrons oscillate rapidly close to the nuclei. Using plane-waves as a basis set one would need a large number of expansion coefficients to describe this region with a good accuracy. Fortunately, the core electrons on different atoms are almost inert and only the valence electrons participate in the interactions between atoms. Hence, the core electrons may be assumed to be fixed and a pseudo potential may be constructed which takes into account the effects of the nucleus and the core electrons on valence electrons. A pseudopotential is a fictitious electron-ion interaction potential, acting on valence electrons only, that mimics the interaction with the inner electrons, which are supposed to be frozen in the core, as well as the effective repulsion exerted by the latter on the former due to their mutual orthogonality. The constructed pseudo potential should coincide with the true potential at and beyond some given cut-off radius r_c . At the cut-off radius and beyond, the pseudo wave functions must match the corresponding true wave function, while within the core region the pseudo wave functions are constructed to be smoother than the true wave functions. Actual normconserving pseudopotentials are determined uniquely by the properties of the isolated atom, while the requirement of norm conservation ensures transferability, i.e. the ability of a pseudopotential to provide results whose quality is to a large extent independent on the local chemical environment. A second property, in order to have optimum transferability, is that the logarithmic derivatives of the true and pseudo wave functions agree at the cut-off radius. The smoothness of a pseudopotential is essential in plane wave calculations because it allows to reduce the number of expansion coefficients. To improve this feature in 1990 Vanderbilt introduced ultrasoft pseudopotentials [82]. In this scheme, the orbitals are allowed to be as soft as possible in the core region; this comes at the price of giving up both the norm conservation and the standard orthonormality condition. Orthonormality is recovered by introducing a generalized overlap operator which depends on the ionic positions. The full electron density in obtained by adding to the square modulus of the orbitals an augmentation charge localized in the core regions.

2.1.3 Brillouin zone sums

Many quantities like the charge density or the total energy involves integrals over $\mathbf{k}$ in the Brillouin Zone.

$$\langle P\rangle = \frac{\Omega_{BZ}}{(2\pi)^3} \sum_{n\,occ} \int_{BZ} P_n(\mathbf{k}) d^3k \tag{2.17}$$

where n the band index and Ω_{BZ} is the volume of the Brillouin Zone. In practice one does not perform an integral but a sum over a finite number $N_{\mathbf{k}}$ of $\mathbf{k}$-points,

$$\langle P\rangle = \frac{1}{N_{\mathbf{k}}}\sum_{n\,occ}\sum_{\mathbf{k}\in BZ} P_n(\mathbf{k}) \tag{2.18}$$

Only points in the irreducible brillouin zone (IBZ) with appropriate weights f can be considered in the sum as:

$$\langle P\rangle = \frac{1}{N_{\mathbf{k}}}\sum_{n\,occ}\sum_{\mathbf{k}\in IBZ} P_n(\mathbf{k})f(\mathbf{k}) \tag{2.19}$$

For metals at T=0, Eq.2.17 corresponds to an integral over all wave-vectors contained within the Fermi surface. For the highest band there is a sharp discontinuity in k-space between occupied and unoccupied states and many k-point are needed to reproduce it accurately. To avoid such a problem usually in metals the sharp step function at the Fermi level is replaced with a smoother function. For example one can use a gaussian smearing: the step function is thought as the integral of a δ function and the δ function is replaced with a smooth gaussian with a variance σ gives rise to an occupation function

$$f(E) = \frac{1}{2}\left[1 - erf\left(\frac{E-E_F}{\sigma}\right)\right] \tag{2.20}$$

2.1.4 Forces

The calculation of the forces is the basis of geometry optimization and is also the starting point for phonon calculation as we will see in the next chapter. Forces can be calculated thanks to Hellman-Feynman theorem:

$$F_I = -\frac{\partial E}{\partial \mathbf{R}_I} = -\frac{\partial\langle\Psi \mid H \mid \Psi\rangle}{\partial \mathbf{R}_I} = -\langle\Psi \mid \frac{\partial H}{\partial \mathbf{R}_I} \mid \Psi\rangle \tag{2.21}$$

Where $\mathbf{R}_I$ represent the position of the I^{th}-ion and Ψ represents the ground state function. An important consequence of the variational character of DFT is that the Hellmann-Feynman form for forces, Eq.2.21 is still valid in a DFT framework. In fact, the DFT expression for forces contains a term coming from the explicit derivation of the energy functional E[n] with respect to atomic positions, plus a term coming from its implicit dependence via the derivative of the charge density:

$$F_I^{DFT} = -\int n(\mathbf{r})\frac{\partial V(\mathbf{r})}{\partial \mathbf{R}_I}d\mathbf{r} - \frac{\partial E_N}{\partial \mathbf{R}_I} - \int \frac{\delta E[n]}{\delta n(\mathbf{r})}\frac{\partial n(\mathbf{r})}{\partial \mathbf{R}_I}d\mathbf{r} \tag{2.22}$$

For the ground state charge density the last term in Eq.2.22 vanish and thus $F_I^{DFT} = F_I$. The geometry optimization allows to obtain the atomic positions that minimize the total energy. At each optimization step the Schroedinger equation for the electronic system is solved and the forces acting on each atom are calculated. Different algorithms are available to move atoms according to the forces such as the BFGS [83, 84] and damped dynamic [85] methods which allow a fast convergence toward the local energy minimum.

2.1.5 DFT-D semiempirical correction for long range dispersion forces

One of the drawback of DFT with current GGA exchange and correlation functionals is that it can not describe long-range electron correlations that are responsible for van der Waals forces. S.Grimme [86] proposed a method, the DFT-D, that provides a semiempirical correction to compensate for such deficiency. In DFT-D the total energy is written as

$$E_{DFT-D} = E_{DFT} + E_{disp} \tag{2.23}$$

where E_{DFT} is the self consistent energy as obtained from the usual DFT method and E_{disp} is

$$E_{disp} = -\sum_{i=1}^{N_{at}-1} \sum_{j=i+1}^{N_{at}} \frac{C_6^{ij}}{R_{ij}^6} f_{damp}(R_{ij}) \tag{2.24}$$

Here, N_{at} is the number of atoms in the system, C_6 denotes the dispersion coefficient for atom pair ij, and R_{ij} is the interatomic distance. The function f_{damp} is given by

$$f_{damp}(R_{ij}) = \frac{s_6}{1 + e^{-d(R_{ij}/R_r - 1)}} \tag{2.25}$$

where R_r is the sum of the VdW radii of the two atoms obtained from ab initio results and s_6 is a global scaling factor that only depends on the functional used. C_6^{ij} is given by

$$C_6^{ij} = \sqrt{C_6^i C_6^j} \tag{2.26}$$

and

$$C_6^a = 0.05 N I_p^a \alpha^a \tag{2.27}$$

where N has the value 2,10,18,36,54 for atoms from rows 1-5 of the periodic table, I_p^a is the ionization potential and α is the static dipole polarizability. Recently an improvement of this method, called DFT-D3, has been proposed [87]. In this new approach the C_6 parameters are calculated as

$$C_6^{ij} = \frac{3}{\pi} \int_0^\infty \alpha^i(i\omega) \alpha^j(i\omega) d\omega \tag{2.28}$$

where $\alpha^i(\omega)$ is the frequency-dependent polarizability of the atom i calculated using time dependent density functional theory (TDDFT) and the damping function is given by

$$f_{damp} = \frac{1}{1+6(R_{ij}/(sR_r))^{-\gamma}} \tag{2.29}$$

where s is a constant that depends on the functional and γ=14

2.2 Density Functional Perturbation Theory

As described in the previous chapter, DFT can provide information such as the ground state electron structure of a material or Hellmann-Feynman forces between atoms. However, many interesting features are related to higher order derivatives of the ground state energy. For example vibrational modes in a crystal are determined by the second derivative of the total energy with respect to ionic displacements. Many approaches have been developed to study the lattice dynamics from first principle calculations such as frozen-phonon, molecular-dynamics and density functional perturbation theory. Within the frozen-phonon method a suitable choice of atomic displacement is made in order to determine force constants from differences of Hellmann-Feynman forces calculated as a function of atomic displacement, small but finite, from equilibrium positions. A frozen-phonon calculation for a lattice vibration at a generic vector **q** requires a super-cell having **q** as a reciprocal lattice vector. This obviously turns out to be a significant limitation for calculations at small **q** because they would require large super-cells. In molecular-dynamics (MD) simulations [88], the finite-temperature dynamics of atoms which vibrate about their equilibrium position are studied. The harmonic approximation can be applied, for low enough temperatures, to describe the atomic trajectories from the classical equations of motions. The Hellmann-Feynman forces have to be essentially the exact derivatives of the total energy in order to obtain accurate trajectories and correct phonon density of states from the Fourier transform of the velocity-velocity autocorrelation function. As in the frozen-phonon method MD requires large super-cells in order to describe large wavelength phonons (small **q**). The approach of DFPT [89–93] is based on the response of the atoms to arbitrary infinitesimal displacements and the corresponding changes of the ionic effective one-electron potential as calculated within linear response theory as we will see in the next sections. DFPT can provide phonon dispersion relations over the whole BZ.

2.2.1 Linear response

Within the Born-Oppenheimer adiabatic approximation it has been shown that an explicit expression for interatomic force constants (FC) can be obtained by differentiating the Hellman-

Feynman force constants with respect to ionic coordinates

$$\frac{\partial^2 E[n]}{\partial \mathbf{R}_I \partial \mathbf{R}_J} = \int \frac{\partial n(\mathbf{r})}{\partial \mathbf{R}_J} \frac{\partial V(\mathbf{r})}{\partial \mathbf{R}_J} d\mathbf{r} + \delta_{IJ} \int n(\mathbf{r}) \frac{\partial^2 V(\mathbf{r})}{\partial \mathbf{R}_I \partial \mathbf{R}_J} d\mathbf{r} + \frac{\partial^2 E_N}{\partial \mathbf{R}_I \partial \mathbf{R}_J.} \tag{2.30}$$

The FC can thus be calculated from the charge density and the linear response to a distortion of the nuclear geometry $\partial n(\mathbf{r})/\partial \mathbf{R}_I$. The charge-density linear response can be evaluated by linearizing Eqs.2.33-2.31 that leads to

$$\frac{\partial n(\mathbf{r})}{\partial \mathbf{R}_I} = 4Re \sum_{i=1}^{N/2} \Psi_i^*(\mathbf{r}) \frac{\partial \Psi_i(\mathbf{r})}{\partial \mathbf{R}_I} \tag{2.31}$$

The derivatives of Kohn-Sham orbitals are obtained from linearization of equation 2.6 and 2.31

$$(H_{SCF} - \varepsilon_i) \frac{\partial \Psi_i(\mathbf{r})}{\partial \mathbf{R}_I} = -\left(\frac{\partial V_{SCF}(\mathbf{r})}{\partial \mathbf{R}_I} - \frac{\partial \varepsilon_i}{\partial \mathbf{R}_I} \right) \Psi_i(\mathbf{r}) \tag{2.32}$$

where

$$\frac{\partial V_{SCF}(\mathbf{r})}{\partial \mathbf{R}_I} = \frac{\partial V(\mathbf{r})}{\partial \mathbf{R}_I} + \int \frac{1}{\mid \mathbf{r} - \mathbf{r}' \mid} \frac{\partial n(\mathbf{r}')}{\partial \mathbf{R}_I} d\mathbf{r}' + \int \frac{\delta v_{xc}(\mathbf{r})}{\delta n(\mathbf{r}')} \frac{\delta n(\mathbf{r}')}{\partial \mathbf{R}_I} d\mathbf{r}' \tag{2.33}$$

and

$$\frac{\partial \varepsilon_i}{\partial \mathbf{R}_I} = \langle \Psi_i \mid \frac{\partial V_{SCF}}{\partial \mathbf{R}_I} \mid \Psi_i \rangle \tag{2.34}$$

The equations eq.2.31-2.33 form a set of self-consistent equations for the perturbed system completely analogous to the Kohn-Sham equations in the unperturbed case. Efficient iterative algorithms such as conjugate gradient methods can be used for the solution of the linear system.

2.2.2 Phonons

Phonons are normal mode of the harmonic lattice. Within the adiabatic approximation, the lattice dynamics can be studied as if the ions were classical charges moving in an effective potential determined by the ground-state electronic energy. In the previous sections we indicated atomic positions with a single generalized index I that we make explicit as $I = l, s$ where l is the index of unit cell and s the index of the atom inside the unit cell. The position of the Ith atom is thus

$$\mathbf{R}_I = \mathbf{R}_l + \tau_s + \mathbf{u}_s(l) \tag{2.35}$$

Here $\mathbf{R}_l$ is the position of the lth unit cell in the Bravais lattice, τ_s is the equilibrium position of the s atom in the unit cell, and $\mathbf{u}_s(l)$ indicates the deviation from equilibrium of the nuclear position. For small displacements of atoms around their equilibrium positions the total energy of the crystal can be expanded up to the second order as:

$$E^{tot}(\mathbf{u}_s(l)) = E_0^{tot} + \frac{1}{2} \sum_{(l,s)(m,t)} \frac{\partial^2 E^{tot}}{\partial \mathbf{u}_s(l) \partial \mathbf{u}_t(m)} \mathbf{u}_s(l) \mathbf{u}_t(m) \tag{2.36}$$

The harmonic oscillations around equilibrium positions are governed by the equation of motion:

$$M_s \ddot{u}_s^{\alpha}(l) = -\frac{\partial E^{tot}}{\partial u_{\alpha s}(l)} = -\sum_{m,t,\beta} C_{st}^{\alpha\beta}(l,m) u_m^{\beta}(m) \tag{2.37}$$

where the greek superscripts indicates Cartesian components.

$$C_{st}^{\alpha\beta}(l,m) = \frac{\partial^2 E}{\partial u_s^{\alpha}(l) \partial u_t^{\beta}(m)} = C_{st}^{\alpha\beta}(\mathbf{R}_l - \mathbf{R}_m) \tag{2.38}$$

The Fourier transform of $C_{st}^{\alpha\beta}(\mathbf{R})$ with respect of $\mathbf{R}$, $C_{st}^{\alpha\beta}(\mathbf{q})$ si defined by:

$$C_{st}^{\alpha\beta}(\mathbf{q}) = \sum_{\mathbf{R}} e^{-i\mathbf{q}\cdot\mathbf{R}} C_{st}^{\alpha\beta}(\mathbf{R}) = \frac{1}{N_c} \frac{\partial^2 E}{\partial u_s^{\alpha}(\mathbf{q}) \partial u_t^{\beta}(\mathbf{q})} \tag{2.39}$$

where N_c is the number of unit cells in the crystal, and the vector $\mathbf{u}_s(\mathbf{q})$ is defined by the distortion pattern

$$\mathbf{R}_I[\mathbf{u}_s(\mathbf{q})] = \mathbf{R}_l + \tau_s + \mathbf{u}_s(\mathbf{q}) e^{i\mathbf{q}\cdot\mathbf{R}_l} \tag{2.40}$$

Phonon frequencies $\omega(\mathbf{q})$ are the solution of the secular equation

$$det \left[\frac{1}{\sqrt{M_s M_t}} C_{st}^{\alpha\beta}(\mathbf{q}) - \omega^2(\mathbf{q}) \right] = 0 \tag{2.41}$$

The quantity

$$\frac{1}{\sqrt{M_s M_t}} C_{st}^{\alpha\beta}(\mathbf{q}) = D_{st}^{\alpha\beta}(\mathbf{q}) \tag{2.42}$$

is called dynamical matrix. Translational invariance imply that a lattice distortion of wave vector $\mathbf{q}$ does not induce a force response in the crystal at wave vector $\mathbf{q}' \neq \mathbf{q}$. Because of this property, interatomic force constants are more easily calculated in reciprocal space and, where needed in direct space, can be obtained by a Fourier transform. The reciprocal-space expression for the matrix of interatomic force constants is the sum of an electronic and ionic contribution:

$$C_{st}^{\alpha\beta}(\mathbf{q}) =^{el} C_{st}^{\alpha\beta}(\mathbf{q}) +^{ion} C_{st}^{\alpha\beta}(\mathbf{q}) \tag{2.43}$$

where

$$ {}^{el}C_{st}^{\alpha\beta}(\mathbf{q}) = \frac{1}{N_c}\left[\int \left(\frac{\partial n(\mathbf{r})}{\partial u_s^{\alpha}(\mathbf{q})}\right)\frac{\partial V_{ion}(\mathbf{r})}{\partial u_s^{\beta}(\mathbf{q})}d\mathbf{r} + \int n(\mathbf{r})\frac{\partial^2 V_{ion}(\mathbf{r})}{\partial u_s^{\alpha}(\mathbf{q})\partial u_t^{\beta}(\mathbf{q})}d\mathbf{r}\right] \tag{2.44} $$

and

$$ V_{ion}(\mathbf{r}) = \sum_{ls} v_s[\mathbf{r} - \mathbf{R}_l - \tau_s - \mathbf{u}_s(l)] \tag{2.45} $$

where v_s is the ionic pseudopotential. All derivatives are calculated for $\mathbf{u}_s(\mathbf{q}) = 0$. The ionic contribution comes from the ion-ion interaction and it does not depend on the electronic structure. An explicit expression of this term can be found in Ref.[93] Since phonon frequencies are usually rather smooth functions of the wave vector a complete phonon dispersion can be obtained using interpolation techniques. Fourier analysis show that the smoother the phonon dispersion, the shorter is the range of real-space interatomic constants:

$$ C_{st}^{\alpha\beta}(\mathbf{R}) = \frac{1}{N_c}\sum_{\mathbf{q}} e^{i\mathbf{q}\cdot\mathbf{R}} C_{st}^{\alpha\beta}(\mathbf{q}) \tag{2.46} $$

Real-space interatomic force constants can thus be obtained by Fourier analyzing a set of force-constant matrices calculated over a uniform grid of points in reciprocal space.

For some materials in this thesis the vdW corrections discussed in Sec.2.1.5 turned out to be necessary to reproduce the experimental phonon spectra. Therefore the dynamical matrix in Eq.2.43 had to include the contributions from the interatomic vdW potential of Eq.2.28. To this end we developed a post-processing tool interfaced with the Quantum-Espresso program. As a benchmark calculation we studied the phonon dispersion relations in the bulk and at the surface of crystalline Xe which is a typical vdW solid. We do not discuss here the details for which we refer to Ref.[94].

2.3 Thermal conductivity from ab-initio calculations

The determination of the intrinsic lattice thermal conduction in a crystal requires the knowledge of the harmonic phonon energies and anharmonic phonon-phonon scattering coefficients. As we have seen in the previous section phonons can be efficiently calculated by using DFPT. The anharmonic scattering coefficients can be determined by the third-order derivative of the energy with respect to three phonon perturbations, corresponding to wave vectors **q**,**q**’ and **q**”. For the thermal transport problem, it is necessary to know these derivatives with respect to three arbitrary wave vectors satisfying the condition **q**+**q**’+**q**”=**G** where **G** is a reciprocal lattice vector. In principle, these coefficients can be obtained within DFPT [95] by using the so-called “2n + 1” theorem as formulated in Ref.[96]. This theorem allows to access the third derivative of the total energy by using only the first derivative of ground-state density and wave functions; without the need to perform expensive supercell calculations. The knowledge of phonons and phonon-phonon scattering coefficients, however, represents only the starting point for the calculation of thermal conductivity.

A microscopic description of the thermal conductivity has been formulated in 1929 by Peierls and it is known as Boltzmann transport equation (BTE). This equation involves the unknown perturbed phonon population and it describes how the perturbation due to a gradient of temperature is balanced by the change in the phonon population due to scattering processes. The calculation of the thermal conductivity requires the solution of this equation and thus the determination of the perturbed phonon populations. The exact solution of the BTE equation is a difficult task due to the complexity and the mutual interconnection of the scattering terms. The BTE equation is commonly solved within the so called single mode relaxation time approximation (SMA) in which is assumed that the phonon scattering processes can be described by frequency-dependent relaxation times. However, a method to solve exactly the BTE equation within DFPT has recently been developed. In what follows we give a brief overview of this method following this recent work [10].

The fundamental heat equation $\mathbf{Q} = -\kappa\nabla T$, where $\mathbf{Q}$ is the heat flux, κ the thermal conductivity tensor and T the temperature, can be written for a crystal as

$$\frac{1}{N_0\Omega}\sum_{\mathbf{q},j}\hbar\omega_{\mathbf{q},j}c_{\mathbf{q},j}n_{\mathbf{q},j} = -k\frac{\partial T}{\partial x} \tag{2.47}$$

where $\omega_{\mathbf{q},j}$ is the angular frequency of the phonon mode with wavevector $\mathbf{q}$ and branch index j, $c_{\mathbf{q},j}$ is the group velocity, $n_{\mathbf{q},j}$ the perturbed phonon population and Ω is the volume of the unit cell and k is the κ_{xx} component of the thermal conductivity tensor κ. The sum runs over a uniform mesh of N_0 $\mathbf{q}$-points and we assumed without loss of generality that the temperature gradient and the heat flux are both along the x direction. The knowledge of the perturbed phonon population allows heat flux and subsequently thermal conductivity to be evaluated. The Boltzmann transport equation represents a balance equation for the unknown perturbed phonon population and can be written as

$$-c_{\mathbf{q},j}\frac{\partial T}{\partial x}\left(\frac{\partial n_{\mathbf{q},j}}{\partial T}\right) + \frac{\partial n_{\mathbf{q},j}}{\partial t}\,|_{scatt} = 0 \tag{2.48}$$

where the first term indicating the phonon diffusion due to the temperature gradient and the second term the scattering rate due to all the scattering processes.

For small perturbations from equilibrium, the temperature gradient of the perturbed phonon population is replaced with the temperature gradient of the equilibrium phonon population $\partial n_{\mathbf{q},j}/\partial T = \partial \overline{n}_{\mathbf{q},j}/\partial T$ where $\overline{n}_{\mathbf{q},j} = (\exp^{\hbar\omega_{\mathbf{q},j}/k_BT} - 1)^{-1}$; while the scattering terms are expanded about its equilibrium value in terms of a first-order perturbation f^{EX} that can be written as

$$n_{\mathbf{q},j} \approx \bar{n}_{\mathbf{q},j} + \bar{n}_{\mathbf{q},j}(\bar{n}_{\mathbf{q},j}+1)\frac{\partial T}{\partial x} f^{EX}_{\mathbf{q},j}\,. \tag{2.49}$$

The linearized BTE can thus be written in the form:

$$\begin{aligned} -c_{\mathbf{q},j}\left(\frac{\partial \bar{n}_{\mathbf{q},j}}{\partial T}\right) = & \sum_{\mathbf{q}'j',\mathbf{q}''j''} [P^{\mathbf{q}''j''}_{\mathbf{q}'j',\mathbf{q}j}\left(f^{EX}_{\mathbf{q}j} + f^{EX}_{\mathbf{q}'j'} - f^{EX}_{\mathbf{q}''j''}\right) \\ & + \frac{1}{2}P^{\mathbf{q}'j',\mathbf{q}''j''}_{\mathbf{q}j}\left(f^{EX}_{\mathbf{q}j} - f^{EX}_{\mathbf{q}'j'} - f^{EX}_{\mathbf{q}''j''}\right)] \\ & + \sum_{\mathbf{q}'j'} P^{isot}_{\mathbf{q}j,\mathbf{q}'j'}\left(f^{EX}_{\mathbf{q}j} - f^{EX}_{\mathbf{q}'j'}\right) + P^{be}_{\mathbf{q}j} f^{EX}_{\mathbf{q}j} \end{aligned} \tag{2.50}$$

where the sum over $\mathbf{q}'$ and $\mathbf{q}''$ is performed over a uniform grid over the whole BZ and where the EX superscript denotes the exact solution of the linearized BTE.

The four components at the right side of Eq.2.50 represent the four different scattering processes shown in Fig.2.1

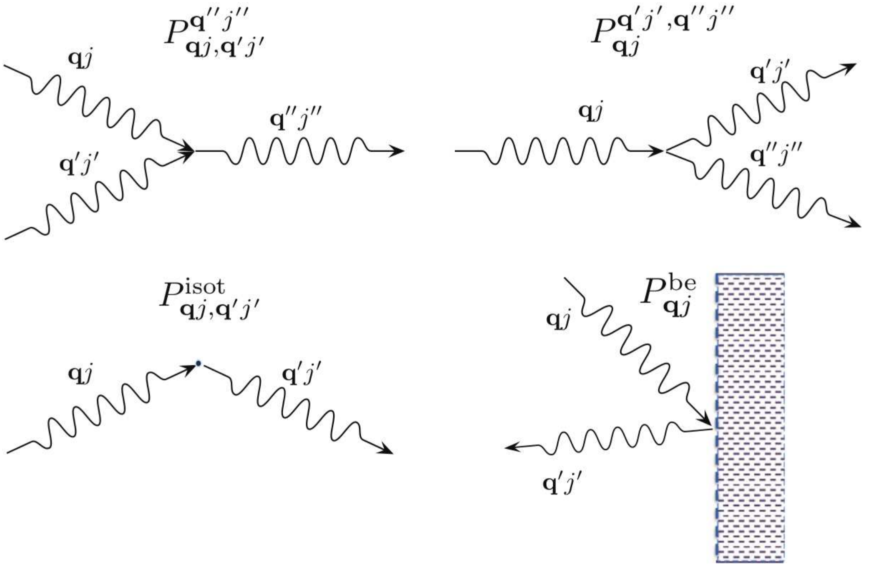

Figure 2.1: Phonon scattering processes in an anharmonic crystal in presence of isotopic impurities P^{isot} and boundary scattering P^{be}.

In particular the first term $P^{\mathbf{q}''j''}_{\mathbf{q}'j',\mathbf{q}j}$ is the scattering rate at equilibrium of a process in which a phonon mode $\mathbf{q}j$ scatters by adsorbing another phonon $\mathbf{q}'j'$ to give rise to a third phonon $\mathbf{q}''j''$.

The second term $P_{\mathbf{q}j}^{\mathbf{q}'j',\mathbf{q}''j''}$ represents the opposite process where a phonon $\mathbf{q}'j'$ decays into two phonon $\mathbf{q}''j''$ and $\mathbf{q}j$. The third term $P^{isot}_{\mathbf{q}j,\mathbf{q}'j'}$ represents the scattering on an isotopic impurity while the last therm $P^{be}_{\mathbf{q}j}$ is the scattering from the boundaries in a finite system.

The first two scattering rates have the form:

$$\begin{aligned} P^{\mathbf{q}''j''}_{\mathbf{q}'j',\mathbf{q}j} = \frac{2\pi}{N_0\hbar^2}\sum_{\mathbf{G}} \mid V^3(\mathbf{q}j,\mathbf{q}'j',-\mathbf{q}''j'') \mid^2 \\ \times\bar{n}_{\mathbf{q}j}\bar{n}_{\mathbf{q}'j'}(\bar{n}_{\mathbf{q}''j''}+1)\delta_{\mathbf{q}+\mathbf{q}'-\mathbf{q}'',\mathbf{G}} \\ \times\delta(\hbar\omega_{\mathbf{q}j}+\hbar\omega_{\mathbf{q}'j'}-\hbar\omega_{\mathbf{q}''j''}) \end{aligned} \tag{2.51}$$

and

$$\begin{aligned} P^{\mathbf{q}''j''}_{\mathbf{q}'j',\mathbf{q}j} = \frac{2\pi}{N_0\hbar^2}\sum_{\mathbf{G}} \mid V^3(\mathbf{q}j,-\mathbf{q}'j',-\mathbf{q}''j'') \mid^2 \\ \times\bar{n}_{\mathbf{q}j}(\bar{n}_{\mathbf{q}'j'}+1)(\bar{n}_{\mathbf{q}''j''}+1)\delta_{\mathbf{q}-\mathbf{q}'-\mathbf{q}'',\mathbf{G}} \\ \times\delta(\hbar\omega_{\mathbf{q}j}-\hbar\omega_{\mathbf{q}'j'}-\hbar\omega_{\mathbf{q}''j''}) \end{aligned} \tag{2.52}$$

where $V^{(3)}$ are the third derivatives of the total energy of the crystal E^{tot}, with respect to the atomic displacements $X_{\mathbf{q}}$

$$V^3(\mathbf{q}j,\mathbf{q}'j',\mathbf{q}''j'') = \frac{\partial^3 E^{cell}}{\partial X_{\mathbf{q}j}\partial X_{\mathbf{q}'j'}\partial X_{\mathbf{q}''j''}} \tag{2.53}$$

where E^{cell} is the energy per cell and the quantities $X_{\mathbf{q}j}$ are defined as:

$$X_{\mathbf{q}j} = \frac{1}{N_0}\sum_{l,s,\alpha}\sqrt{\frac{2M_s\omega_{\mathbf{q}j}}{\hbar}}z^{s\alpha^*}_{\mathbf{q}j}\,u^{\alpha}_s(\mathbf{R}_l)\exp^{-i\mathbf{q}\cdot\mathbf{R}_l} \tag{2.54}$$

According to Ref.[97] the rate of the elastic scattering with isotopic impurities can be written in the form

$$\begin{aligned} P^{isot}_{\mathbf{q}j,\mathbf{q}'j'} = \frac{\pi}{2N_0}\omega_{\mathbf{q}j}\omega_{\mathbf{q}'j'}\left[\bar{n}_{\mathbf{q}j}\bar{n}_{\mathbf{q}'j'}+\frac{\bar{n}_{\mathbf{q}j}+\bar{n}_{\mathbf{q}'j'}}{2}\right] \\ \times\sum_s g^s_2 \mid \sum_\alpha z^{s\alpha^*}_{\mathbf{q}j}\cdot z^{s\alpha}_{\mathbf{q}'j'} \mid^2 \delta(\omega_{\mathbf{q}j}-\omega_{\mathbf{q}'j'}) \end{aligned} \tag{2.55}$$

with

$$g_2^s = \varepsilon(1-\varepsilon)\frac{\mid \Delta M_s \mid}{\langle M_s \rangle} \tag{2.56}$$

where ε is the concentration of the minority isotope, ΔM_s the mass difference of the two isotopes and $\langle M_s \rangle = M_s + \varepsilon \Delta M_s$.

The last term, according to literature [98, 99] can be written as

$$P_{\mathbf{q}j}^{be} = \frac{c_{\mathbf{q}j}}{LF}\overline{n}_{\mathbf{q}j}(\overline{n}_{\mathbf{q}j}+1) \tag{2.57}$$

where L is the Casimir length and F a correction factor which depends on the width-to-length ratio of the boundary.

After linearization, the BTE can be written as a linear system in matrix form

$$\mathbf{A}\mathbf{f}^{EX} = \mathbf{b} \tag{2.58}$$

with $b_{\nu'} = -c_{\nu'}\hbar\omega_{nu'}\overline{n}_{\nu'}(\overline{n}_{\nu'}+1)$ and

$$\begin{aligned} A_{\nu,\nu'} = {} & \left[\sum_{\nu'',\nu'''}\left(P_{\nu,\nu'''}^{\nu''} + \frac{P_{\nu''',\nu''}^{\nu}}{2}\right) + \sum_{\nu''} P_{\nu,\nu''}^{isot} + P_{\nu}^{be}\right]\delta_{\nu,\nu'} \\ & - \sum_{\nu''}\left(P_{\nu,\nu''}^{\nu'} - P_{\nu,\nu'}^{\nu''} + P_{\nu',\nu''}^{\nu}\right) + P_{\nu,\nu'}^{isot} \end{aligned} \tag{2.59}$$

where we used the contracted index ν instead of $\mathbf{q}j$. In this form the matrix $\mathbf{A}$ can be decomposed as $\mathbf{A} = \mathbf{A}^{out} + \mathbf{A}^{in}$ where

$$A_{\nu,\nu'}^{in} = -\sum_{\nu''}\left(P_{\nu,\nu''}^{\nu'} - P_{\nu,\nu'}^{\nu''} + P_{\nu',\nu''}^{\nu}\right) + P_{\nu,\nu'}^{isot} \tag{2.60}$$

and

$$A_{\nu,\nu'}^{out} = \frac{\overline{n}_{\nu}(\overline{n}_{\nu'}+1)}{\tau_{\nu}^{T}}\delta_{\nu,\nu'} \tag{2.61}$$

and where τ_{ν}^{T} is the phonon-phonon relaxation time defined as

$$(\tau_\nu^T)^{-1} = (\tau_\nu)^{-1} + (\tau_\nu^{be})^{-1} + (\tau_\nu^{isot})^{-1} \tag{2.62}$$

where

$$\begin{aligned}(\tau_{\mathbf{q}j})^{-1} = 2\Gamma_{\mathbf{q}j} = \frac{\pi}{\hbar^2 N_0} \sum_{\mathbf{q}'j',j''} &\mid V^3(\mathbf{q}j,\mathbf{q}'j',\mathbf{q}''j'') \mid^2 \\ \times[2(\bar{n}_{\mathbf{q}'j'} - \bar{n}_{\mathbf{q}''j''})&\delta(\hbar\omega_{\mathbf{q}s} + \hbar\omega_{\mathbf{q}'j'} - \hbar\omega_{\mathbf{q}''j''}) \\ +(1+\bar{n}_{\mathbf{q}'j'} + \bar{n}_{\mathbf{q}''j''})&\delta(\hbar\omega_{\mathbf{q}s} - \hbar\omega_{\mathbf{q}'j'} - \hbar\omega_{\mathbf{q}''j''})]\end{aligned} \tag{2.63}$$

while the boundary and isotopic relaxation times τ_ν^{be} and τ_ν^{isot} are

$$(\tau_{\mathbf{q}j}^{be})^{-1} = \frac{c_{\mathbf{q}j}}{LF} \tag{2.64}$$

$$\begin{aligned}(\tau_{\mathbf{q}j}^{isot})^{-1} = \frac{\pi}{2N_0}\omega_{\mathbf{q}j}^2 \sum_{\mathbf{q}'j'} &\delta(\omega_{\mathbf{q}j} - \omega_{\mathbf{q}'j'}) \\ \times \sum_s g_2^s \mid \sum_\alpha &z_{\mathbf{q}j}^{s\alpha^*} z_{\mathbf{q}'j'}^{s\alpha} \mid^2\end{aligned} \tag{2.65}$$

The A^{out} diagonal matrix describes the depopulation of phonon states due to the scattering mechanisms while the A^{in} matrix describes their repopulation due to the incoming scattered phonons.

All the complexity of the solution of the BTE lies in the process of inverting the large $\mathbf{A}$ matrix as

$$\mathbf{f}^{EX} = \frac{1}{\mathbf{A}}\mathbf{b} \tag{2.66}$$

for which the thermal conductivity can be evaluated as

$$k = \frac{1}{N_0\Omega k_B T^2}\mathbf{b}\cdot\mathbf{f}^{EX} = -\frac{\hbar}{N_0\Omega k_B T^2}\sum_\nu c_\nu \omega_\nu \bar{n}_\nu(\bar{n}_\nu + 1) f_\nu^{EX} \tag{2.67}$$

It is worth noticing that if the A^{in} term is neglected, the inversion of the A^{out} term is rather trivial and the solution correspond to the single mode approximation

$$\mathbf{f}^{SMA} = \frac{1}{\mathbf{A}^{out}}\mathbf{b} \tag{2.68}$$

$$k^{SMA} = \lambda\mathbf{b}\cdot\mathbf{f}^{SMA} = \frac{\hbar^2}{N_0\Omega k_B T^2}\sum_\nu c_\nu^2\omega_\nu^2\bar{n}_\nu(\bar{n}_\nu+1)\tau_\nu^T \tag{2.69}$$

The solution of the exact equation 2.66 including A^{in} can be addressed with a variational approach as in Ref.[10]. In particular, it can be shown [100, 101] that the solution of the BTE is the vector $\mathbf{f}^{EX}$ which makes stationary the quadratic form

$$F(\mathbf{f}) = \frac{1}{2}\mathbf{f}\cdot\mathbf{A}\mathbf{f} - \mathbf{b}\cdot\mathbf{f} \tag{2.70}$$

It can be shown [10] that the convergence can be speeded up if instead of directly minimize Eq.2.70, the minimization is carried out with respect to the rescaled variable

$$\widetilde{\mathbf{f}} = \sqrt{\mathbf{A}^{out}}\mathbf{f} \tag{2.71}$$

which defines the functional

$$\widetilde{F}(\widetilde{\mathbf{f}}) = \frac{1}{2}\widetilde{\mathbf{f}}\cdot\widetilde{\mathbf{A}}\widetilde{\mathbf{f}} - \widetilde{\mathbf{b}}\cdot\widetilde{\mathbf{f}} \tag{2.72}$$

where

$$\widetilde{\mathbf{A}} = \frac{1}{\sqrt{\mathbf{A}^{out}}}\mathbf{A}\frac{1}{\sqrt{\mathbf{A}^{out}}} \tag{2.73}$$

and

$$\widetilde{\mathbf{b}} = \frac{1}{\sqrt{\mathbf{A}^{out}}}\mathbf{b} = \widetilde{\mathbf{f}}^{SMA} \tag{2.74}$$

The minimization of the $\widetilde{F}(\widetilde{\mathbf{f}})$ functional is carried out with a conjugate-gradient method. For the details on the variational solution we refer to the original paper Ref.[10].

2.4 Molecular Dynamics

Molecular dynamics is a technique that allows calculating the time evolution of a system of atoms, considered as classical particles, once the initial conditions of positions, velocities and the interaction potential between particles at time t_0 are known. Position and velocity of all the particles at any time subsequent t_0 are calculated by integrating the Newton's equations of motion. The accuracy and the computational cost of the calculation depends on the nature of the interaction potential.

In classical molecular dynamics, the interatomic potential is generally described by analytical expressions that contains empirical parameters obtained from the fitting of experimental data or ab-initio results. This approach has a low computational cost which scales linearly with the number of atoms for short range potentials and allows the simulation of very large systems (up to 10^7 atoms) for a long time (several ns). Accurate results, however, are likely to be obtained only in conditions similar to those at which the parameters of the potential were fitted.

In ab-initio molecular dynamics, ions are still treated as classical particles but electrons are treated at a quantum level. The forces acting on the ions can be obtained from the solution of the electronic problem, commonly using DFT, within the adiabatic approximation as described in Sec.2.1.4. This method ensures a better accuracy and a great flexibility with respect to classical MD, but it is computationally expensive, scales as the square of the number of atoms and thus can allow only the simulation of small systems (at most several hundred atoms) for few hundreds of ps.

Once the forces acting on the ions have been computed, the time evolution is given by the classical Newton's equation:

$$M_I \ddot{\mathbf{R}}_I = \mathbf{F}_I \tag{2.75}$$

where $\mathbf{F}_I$ is the force on the I-th nucleus and M_I and $\ddot{\mathbf{R}}_I$ are the nuclear mass and acceleration, respectively. The numerical integration of the equation of motion (2.75) is performed by finite difference methods discretizing the time in steps Δt according to different algorithms [102–105].

One of the most simple and stable algorithm is the Velocity Verlet algorithm [104, 105]. In this method, positions $\mathbf{R}_I$ and velocities $\mathbf{v}_I$ at time $t+\Delta t$ can be obtained from the values at time t from

$$\begin{aligned} \mathbf{R}_I(t+\Delta t) &= \mathbf{R}_I(t)+\mathbf{v}_I(t)\Delta t+\frac{\mathbf{F}(\{\mathbf{R}_I(t)\})}{2M_I}(\Delta t)^2 \\ \mathbf{v}_I(t+\Delta t) &= \mathbf{v}_I(t)+\frac{\mathbf{F}_I(\{\mathbf{R}_I(t)\})+\mathbf{F}_I(\{\mathbf{R}_I(t+\Delta t)\})}{2M_I}\Delta t. \end{aligned} \tag{2.76}$$

The knowledge of atomic trajectories allows computing equilibrium observables A which can be expressed as a function of ions positions and velocities. Under the assumption of ergodicity, A is obtained as a time average over the trajectories

$$\langle A \rangle_{ens} = \langle A \rangle_{exp} = \lim_{\tau\to\infty} \frac{1}{\tau}\int_0^\tau A(\{\mathbf{R}_I(t)\},\{\mathbf{v}_I(t)\})dt. \tag{2.77}$$

2.5 Thermal conductivity from non-equilibrium molecular dynamics simulations

We computed the thermal conductivity from molecular dynamics simulations using the Reverse Non-Equilibrium Molecular Dynamics scheme (RNEMD) developed by Muller-Plathe in Ref.[11]. Among the different methods to evaluate the thermal conductivity from MD calculations, such as the Green-Kubo method based on the autocorrelation function of the heat flux $\mathbf{Q}(t)$ [106] or the direct gradient method, the RNEMD offers a faster convergence with a comparable accuracy. By assuming the heat flux and the temperature gradient both along the x direction, the thermal conductivity component $k = \kappa_{xx}$ can be simply obtained from a MD calculation in terms of temporal averages

$$\kappa = \lim_{\partial T/\partial x \to 0} \lim_{t \to \infty} -\frac{\langle Q_x(t) \rangle}{\langle \partial T/\partial x \rangle} \tag{2.78}$$

The most natural way to obtain the thermal conductivity, in analogy to what is done experimentally, would be to impose a temperature gradient using two thermostats at the extremes of the sample and to calculate the heat flux $Q_x(t)$ parallel to the gradient. This method, however, is rather inefficient because the quantity $Q_x(t)$ is subject to large oscillations and consequently its average converges very slowly.

The RNEMD scheme proceeds in the opposite direction, instead of imposing a temperature gradient and waiting for the average of $Q_x(t)$ to converge, the heat flux is imposed on the system while the temperature gradient is measured from the simulation. Since the temperature is averaged over time as well as over a considerable number of particle is less subject to large fluctuation with respect to $Q_x(t)$ and its gradient converge much faster.

In order to impose a heat flux and to calculate a temperature profile, the simulation box is divided into N slabs perpendicular to the x direction (cf. Fig.2.2).

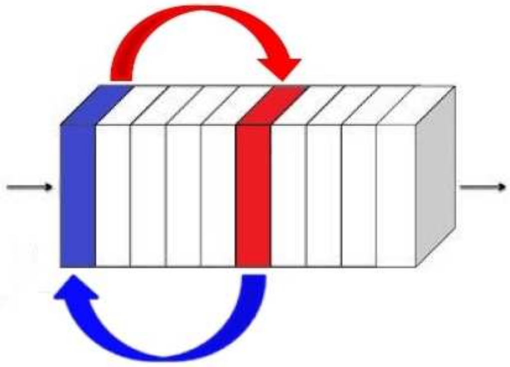

Figure 2.2: Simulation box for a RNEMD calculation.

A slab at one edge of the box is defined as the cold source while another slab, positioned at the center of the simulation box acts as the hot source. Alternatively the two sources can be placed at the opposite edges of the simulation box and the periodic images can be decoupled by interposing a slab of fixed atoms.

The heat flux is generated by exchanging the velocity vectors of an atom in the cold slab and one in the hot slab in such a way that the temperature increases in the hot slab and decreases and the cold slab. This procedure leaves the total linear momentum, the total kinetic energy, and the total energy unchanged. Since the kinetic energy exchange is known, the heat flux can be calculated exactly at each step. Within this scheme the thermal conductivity can be simply computed as

$$\kappa = -\frac{\sum_{transfers} \frac{m}{2}(v_h^2 - v_c^2)}{2tL_yL_z\langle \partial T/\partial x\rangle} \tag{2.79}$$

where the sum is taken over all transfer events during the simulation time t, v_h and v_c are the velocities in the hot and cool source exchanged at each iteration, L_y and L_z are the dimension of the simulation box perpendicular to the heat flux and $\langle \partial T/\partial x\rangle$ is the thermal gradient computed in the simulation.

2.6 Neural Network interatomic potential

In order to obtain a reliable potential with an accuracy close to the ab initio calculations but with a computational cost and scalability comparable to classical potential, an interatomic potential for GeTe has been developed in our group by fitting a database of DFT energies [12] with the Neural Network (NN) method proposed by Behler and Parrinello [107].

Neural networks are a class of algorithms, inspired by the structure and mechanism of the brain, widely used in machine learning, classification problems such as speech [108] and pattern recognition. Moreover, they proved to be an efficient fitting algorithm, in particular for real-valued non-linear functions in many variables [109, 110] where usual fitting methods fails.

This latter application makes neural nterworks particularly useful in material simulations. An interatomic potential is essentially an approximation of the potential energy surface (PES) of the system which in turn is a continuous real-valued function, usually of high dimensionality.

A non-linear multivariable function (in our case a potential energy surface) can be seen as a combination of single-variable non-linear functions (called activation function in the contest of NN) generated by a feed-forward neural network, a type of NN schematically represented in Fig.2.3, formed by different layers where the information can move in one direction, from the input layer to the output layer and never goes backwards.

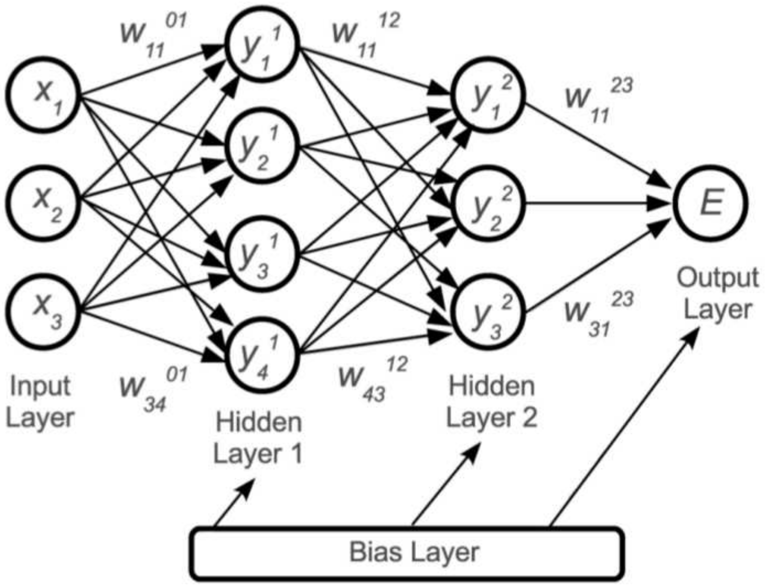

Figure 2.3: Schematic representation of a simple feed-forward NN topology with two hidden layers.

A feed-forward NN is a mathematical object characterized by different layers and different nodes on each layer. The numbers of input nodes, hidden layers and nodes of each hidden layer fix the topology of the network. Each node of the network acts like a neuron in a biological system. The flexibility of the NN can be increased by increasing the number of hidden layers or the number of nodes in the hidden layers and hence the number of fitting parameter on which the function depends.

These fitting parameters can be considered as "weights" that connect the nodes in a layer with the nodes in the next one. In Fig. 2.3 the parameter that weighs the i node in the k layer connecting it with the j node in the l layer is indicated by w_{ij}^{kl}. Moreover, the hidden layers can be linked with a bias layer with weights b_i^j which allows a rigid shift of the activation functions.

In order to calculate the output of the neural network, each point x_i of the fitting dataset is assigned to a different node in the input layer and the output values y_j^1 of the first hidden layer are calculated through two steps. In the first step the input values are linearly combined with the weights w_{ij}^{01} and a bias value b_j^1 is added

$$\chi_j^1 = b_j^1 + \sum_i^4 w_{ij}^{01} \cdot x_i. \tag{2.80}$$

Then, a highly non-linear function f_j^1 is applied to the χ_j^1 values

$$y_j^1 = f_j^1(\chi_j^1). \tag{2.81}$$

In a similar way, the values of the nodes of the next layers and of the output can be obtained from the values calculated in the previous layers. The output of the NN may be an array of values or a single number calculated by summing up the results of the hidden layers as exemplified by the equation

$$E = f_1^3\left(b_1^3 + \sum_{i=1}^{3} w_{i1}^{23} + f_i^2\left(b_i^2 + \sum_{j=1}^{4} w_{ji}^{12} f_j^1 - \left(b_j^1 + \sum_{k=1}^{3} w_{kj}^{01} x_k\right)\right)\right) \tag{2.82}$$

that describe the procedure sketched in Fig. 2.3.
Within the Neural Network, an activation function f is applied to the nodes in each hidden layer. The f function is generally a non-linear function that asymptotically converges to a finite value for very large and very small arguments, while in between it displays a non-linear behavior to emulate the threshold-like behavior of biological neurons. Different types of activation functions can be used, a common choices are the sigmoid function

$$f(x) = \frac{1}{1+e^{-x}}, \tag{2.83}$$

the hyperbolic tangent or Gaussian functions.

Generally, from the last hidden layer to the output layer, the activation functions are linear in order to avoid any constraint in the range of output values.

In order to determine the values of the fitting parameters, an error function Γ, that describes how far is the i-th output value of the NN E$_{i,NN}$ from a reference value E$_{i,ref}$ of the dataset, must be defined:

$$\Gamma = \frac{1}{2N}\sum_{i=1}^{N}\left(E_{i,NN} - E_{i,ref}\right)^2 \tag{2.84}$$

where N is the number of points in the dataset.

If the activation functions in the neural network are differentiable, also the output of the NN will be differentiable with respect to both input variables and weights and hence the error function Γ is a differentiable function of the weights. The error functions can thus be minimized by finding the roots of the partial derivatives of the error function with respect to the weights through a minimization procedure. The algorithm for evaluating the derivatives of the error function is known as "back propagation", since it corresponds to a propagation of errors backwards through the NN. The process by which the weights are iteratively improved until they provide a reasonable approximation of the underlying function is called ”training” or ”learning”, and each iteration of this process is known as ”epoch” in the NN context.

2.6.1 Neural Network potential energy surfaces for atomistic simulations

Neural networks have been successfully used in the past to build the potential energy surface of small molecules (5-10 atoms) [111] or isolated gas molecules interacting with a surface [112].

In this systems the input parameter are typically the atomic internal coordinates of the molecular system. The use of a single NN for all the atoms is easy to implement, the training of the network does not pose particular problems since the number of weights is small.

However, this approach suffers important limitations the most crucial being that the resulting potential have a very little transferability since it cannot be applied to systems with a different number of atoms. In fact, the number of input nodes, and hence the values of the weights, is fixed and assigned by the number of degrees of freedom of the system. Moreover the number of degrees of freedom of the system must be necessarily small since when the NN tool is applied to systems of thousands of atoms, the fitting procedure gets longer and it would not be feasible to generate a different NN potential for each system size. Therefore a straightforward extension of this approach to larger systems is not possible.

A first NN scheme designed to deal with a large number of degrees of freedom and independent on the system size was proposed by Hobday *et al.* [113] for carbon and C-H systems. In this scheme, the atomic positions are not directly used as input parameter for the NN but the chemical environment of each bond in the model was decomposed into a variable number of input vectors characterizing three-atom chains, which all have the same dimensionality.

In a conceptually new approach to NNs, the total energy of the system has been written as sum of the atomic energies, each obtained from a single atomic NN [114]. Each of these individual NNs has an input vector with a fixed number of elements that describe the local environment of the atom and returns as output an atomic energy.

A further improvement to this approach was developed in 2007 by Behler and Parrinello [107]. In this work the total energy is still considered as sum of the atomic energies

$$E_{tot} = \sum_{i=1}^{N} E_i(\{\mathbf{r}\}). \tag{2.85}$$

but the architecture of the NN is fixed for a given chemical element allowing to use a standard NN for each atom (cf. Fig. 2.4). Only one input vector of fixed dimensionality is needed per atom to describe its local chemical environment, which is considered up to a certain cutoff radius.

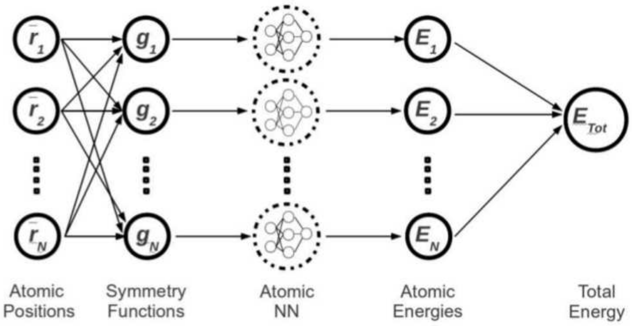

Figure 2.4: Sketch of a neural network according to the scheme proposed by Behler and Parrinello [107].

In order to decouple the number of input nodes from the number of neighbours of each atom, the environment is described not in terms of Cartesian functions, but through special types of many-body descriptors called “symmetry functions”. The symmetry functions provide information on the radial and angular arrangement of neighbours for each atom in the system.

The symmetry functions must be chosen in order to ensure the invariance of the energy with respect to symmetry operations such as translations and rotations of the whole system and the exchange of two atoms of the same species.

A vector of the symmetry function values $\{G_i\}$, each of them depending on the coordinates of all the atoms of the environment within the cut-off, is used as input values of a single-atom NN. For a given atomic species, the architecture and the fitting parameters of the NN are fixed, ensuring the invariance of the total energy with respect to the exchange of two atoms of the same type. The weights of the neural network can be determined by training the network on a database of DFT total energies of different configurations.

Symmetry functions

In the generation of the NN potential for GeTe [12], two types of symmetry functions have been used: radial symmetry functions and angular symmetry functions. The formers are written as sums of two-body terms, while the latter contain also three-body terms. The radial environment of atom i is described using two different radial functions with the form

$$\begin{aligned} G_i^1 &= \sum_j f_c(R_{ij}) \\ G_i^2 &= \sum_j e^{-\eta(R_{ij}-R_s)^2} \cdot f_c(R_{ij}). \end{aligned} \tag{2.86}$$

The cut-off function f_c is defined by

$$f_c(r_{ij}) = \begin{cases} 0.5\left[cos\left(\frac{\pi r_{ij}}{r_c}\right)+1\right] & \text{for } r_{ij} < r_c, \\ 0 & \text{for } r_{ij} > r_c. \end{cases} \tag{2.87}$$

Function G_i^1 is the sum of the cutoff functions with respect to all neighboring atoms j, while G_i^2 is a sum of Gaussian functions centered at a certain radial distance R_s and multiplied by the cut-off function.

These "shifted" G_i^2 functions are suitable to describe a spherical coordination shell around the reference atom. The radial distribution of neighbours can be described by using a set of radial functions with different spatial extensions, for example G_i^1 functions with different cut-off radii, or G_i^2 functions with different cut-offs and/or η and R_S parameters.

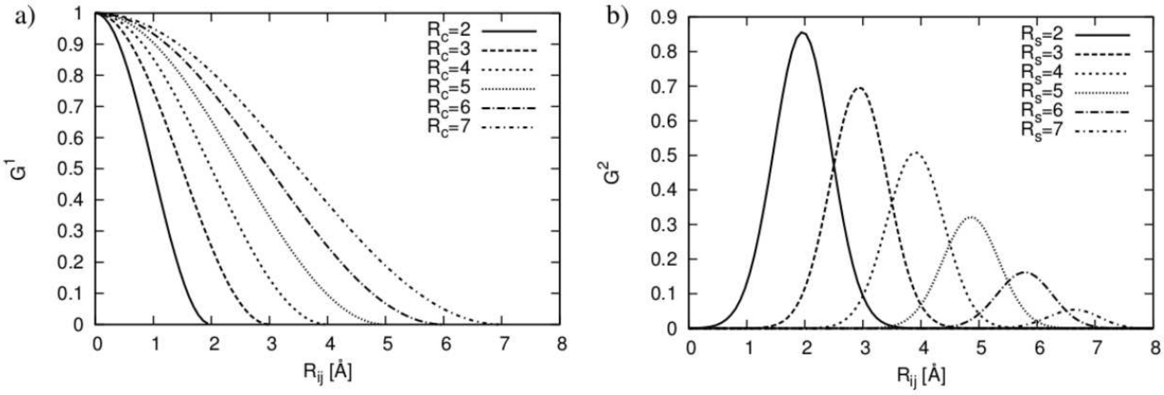

Figure 2.5: Radial symmetry functions. a) G_i^1-type symmetry functions for different cut-off radii. b) G_i^2-type symmetry functions for different radial distances R_s with η=2 and R_c=8 Å respectively.

Typical forms of the radial symmetry functions are plotted in Fig. 2.5 for several parameter values. Angular symmetry functions are defined as functions of the bond angle θ_{jik} that the *i*-th atom forms with its two neighbours j and k and have the form

$$G_i^3 = 2^{1-\xi} \sum_{j,k\neq i}^{all} (1+\lambda cos\theta_{ijk})^{\xi} \cdot e^{-\eta(R_{ij}^2+R_{ik}^2+R_{jk}^2)^2} \cdot f_c(R_{ij}) \cdot f_c(R_{ik}) \cdot f_c(R_{jk}). \tag{2.88}$$

The parameter λ can assume values ±1 shifting the maxima from 0° and 180° to 90°. The angular resolution is controlled by the parameter ξ. High ξ values yield a narrower range of non-zero symmetry function values (Fig. 2.6). A set of angular functions with different ξ-values can thus be used to obtain a measure of the bond angle distribution function of each reference atom. The angular distribution is sampled at various distances from the central atom by a suitable

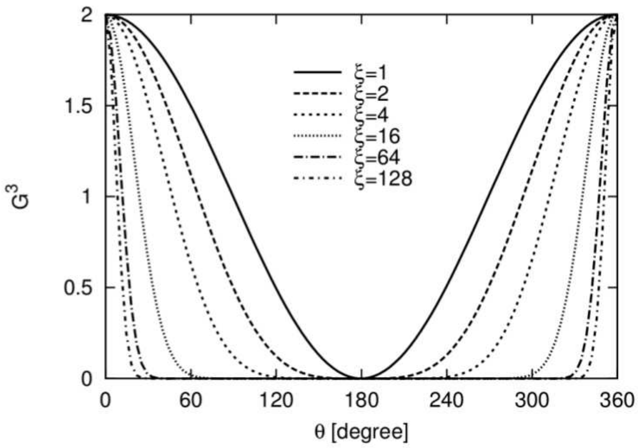

Figure 2.6: Angular symmetry functions G_i^3 for several values of ξ with $\lambda = 1$.

choice of η and R_c, which control the radial part. The parameters that define the symmetry functions are fixed in the training process of the NN. The total number of values of symmetry functions describing a given structure is much larger than the number of degrees of freedom of the system. This ensures that the full dimensionality of the system is captured and the resulting redundancy of the information is not usually a problem for a NN algorithm.

Forces and stress evaluation

Since the NN energy is an analytical function of the symmetry functions, which in turn depend on the atomic coordinates, the energy is an analytical function of the ionic coordinates. The atomic forces and the stress tensor can thus be computed analytically. The force $\mathbf{F}_k$ acting on the k-th atom is

$$\begin{aligned} \mathbf{F}_k &= -\frac{\partial E}{\partial \mathbf{R}_k} \\ &= -\sum_{i=1}^{N} \frac{\partial E_i}{\partial \mathbf{R}_k} \\ &= -\sum_{i=1}^{N} \sum_{j=1}^{M_i} \frac{\partial E_i}{\partial G_{i,j}} \frac{\partial G_{i,j}}{\partial \mathbf{R}_k} \qquad (2.89) \end{aligned}$$

where i runs on atoms and j on the symmetry functions. Since the energy is a function of interatomic distances $\mathbf{R}_{kj} = \mathbf{R}_k - \mathbf{R}_j$, the stress tensor can be obtained from the virial theorem [103] as

$$\sigma_{\alpha\beta} = \sum_{i=1}^{N} \sum_{k=1}^{N} R_{ik,\alpha} \cdot \frac{\partial E}{\partial R_{ik,\beta}} \qquad (2.90)$$

where α and β are Cartesian coordinates.

Extrapolation

The NN method allows interpolation of the points in the dataset of a multi-variate function with any arbitrary functional form. However, the NN algorithm fails in predicting the value of the fitted function outside the configurational space spanned by the training dataset. This condition can be simply checked by keeping memory of the minimum and maximum values assumed by each symmetry function for the whole input dataset. In this way, the values assumed by the symmetry functions depending on the atomic positions during the simulation can be compared with the values of the G functions of the dataset. If a certain atom configuration cause one or more symmetry functions to assume values outside the range defined by the training set, a so called extrapolation occurs and the resulting NN energy could be not reliable. To fix this issue, the atomic environment that causes the extrapolation can be added to the initial dataset fitting again the potential to extend its transferability.

Neural Network potential for GeTe

The NN potential for bulk GeTe was generated by fitting the total energy of about 30000 configurations of 64-, 96- and 216-atom supercells computed within DFT in Ref.[12]. Crystalline, liquid and amorphous configurations and mixed crystalline/amorphous models were generated with the PBE functional. Configurations at different pressure, temperature and stoichiometry were also included in the dataset. The structure of the neural network employed to fit the ab-initio data includes three hidden layers with 20 nodes each. The local environment of each atom is described by the value of 159 radial and angular symmetry functions defined in terms of the positions of all neighbors within a distance cut-off of 6.88 Å.

The generated NN potential reproduces well the structural features of amorphous, liquid and crystalline GeTe [12] and it has been validated in several works addressing the study of the crystallization kinetics of GeTe [36, 37], the properties of the supercooled liquid [115], the aging and the thermal transport of the bulk amorphous phase [116, 117].

3 Thermal conductivity in Phase Change Materials

Thermal conductivity (κ) is one of the fundamental property for the PCMs operation, since the phase changes corresponding to the memory writing/erasing processes are induced by Joule heating. Heat dissipation and transport greatly affect the power consumption and the switching speed of the memory cell. These quantities also influence the thermal cross-talks among the different bits in a memory array which can rise serious reliability issues. In ultrascaled devices, where the cells are few nanometers apart, it is crucial to ensure that the programming of a cell never influences the state of the neighboring ones.

Although data on thermal conductivity are available from several experimental works for the bulk thermal conductivity of the prototypical GeSbTe phase change alloys [7, 54, 118–120] and the related binary compounds GeTe [51, 121–125] and Sb_2Te_3 [121], these data are not always univocal. Moreover it is unclear whether or not the values measured in the bulk could also describe the behavior of the material in nanoscaled devices (10-20 nm) which might be smaller than the phonon mean free path or under extreme temperature gradient conditions as those present in the real devices. Finally, there is a broader and general interest in understanding the mechanisms that are responsible for the low thermal conductivity of these materials due to their close relations with thermoelectric materials.

Atomistic simulations can provide crucial insights into the thermal transport properties of phase change materials suitable to aid a reliable modeling of the device operation, engineering of the device and the selection of new more performing compounds. To this end, we performed simulations based on density functional theory (DFT) and classical molecular dynamics calculations based on neural network potential [12] of different phase change compounds such as GeTe, $Ge_2Sb_2Te_5$, InSbTe alloys and the closely related Sb_2Te_3 compound.

The results are reported in the following in separate section for each compound.

3.1 GeTe

The first material that we examined is the binary GeTe compound. Even if is not employed in nowadays PCM cells, GeTe is widely studied as a prototypical phase change material as it shares most of the properties with the more efficient and commonly used but more complex ternary GST. Moreover, recent works put GeTe under scrutiny for memristive and spintronic applications [15] because of a giant bulk Rashba effect [14]. GeTe is now also being reconsidered for memory applications at high temperatures due to its higher crystallization temperature [126].

GeTe presents two crystalline phases at normal pressure [127]. The stable phase at low temperature is the trigonal α-phase with space group $R3m$, lattice parameter $a = 4.2398$ Å and angle $\alpha = 57.9°$ [128].

The α-phase of GeTe, with two atoms per unit cell, can be viewed as a distorted rocksalt geometry with an elongation of the cube diagonal along the [111] direction and an off-center displacement of the inner Te atom along the [111] direction giving rise to a 3+3 coordination of Ge with three short and stronger bonds (2.84 Å) and three long and weaker (3.17 Å) bonds. In the conventional hexagonal unit cell of the trigonal phase, the structure can be also seen as an arrangement of GeTe bilayers along the *c* direction with shorter intrabilayer bonds and weaker interbilayers bonds (cf. Fig. 3.1).

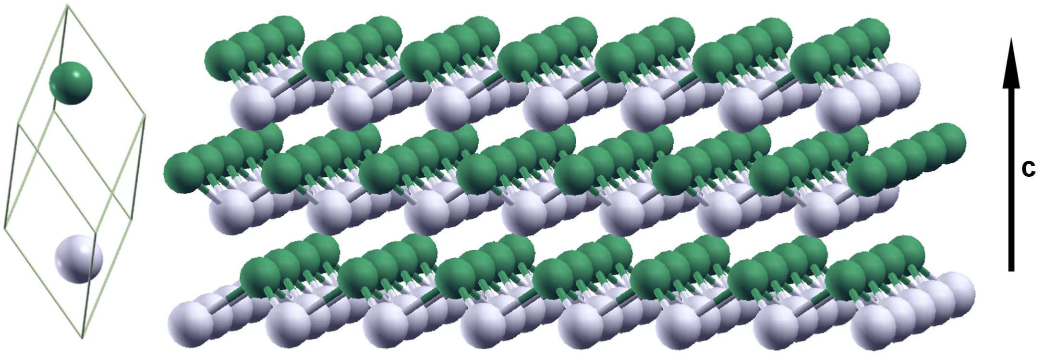

Figure 3.1: Geometry of the α-GeTe crystal seen as a stacking of bilayers along the *c* axis of the conventional hexagonal unit cell with the three short intrabilayers bonds and three long interbilayers bonds.

The ideal GeTe crystal is a narrow gap semiconductor with an experimental band gap of 0.6 eV. It turns into a *p*-type degenerate semiconductor because of defects in stoichiometry, in the form of Ge vacancies, which induce the formation of holes in the valence band [129]. Hole concentrations in native p-type doped GeTe are typically between $5 \cdot 10^{19}$ holes/cm^3 reported in Ref.[130] and $1.6 \cdot 10^{21}$ holes/cm^3 This last concentration, considering two electrons per vacancy, correspond to a vacancy content of about 4.3 $atom\%$ in the Ge sublattice reported [131].

The trigonal ferroelectric phase transforms into the cubic paraelectric (β) phase (space group $Fm\overline{3}m$) with lattice parameter $a = 5.996$ Å above the Curie temperature of 705 K [132]. The structure the β-GeTe and the nature of the α-β transition is still subject of investigation but recent EXAFS measurements [133] suggest that the $3+3$ coordination with shorter and longer bonds locally survives also in the cubic phase and the overall cubic symmetry observed in X-rays and neutron scattering experiments [134] is an effect of the spatial average.

Concerning the lattice thermal conductivity, the experimental data for crystalline GeTe at 300 K are scattered over a wide range of values 0.1-4.1 W/m K [51, 121–125] possibly because of different defects concentration (the presence of Ge vacancies which can be hardly controlled in the growth process) or because of difficulties in separating the overall thermal conductivity into the lattice and electronic contributions.

In order to understand these data, explore the role of high anharmonicity and defect scattering, we calculated the lattice contribution to the thermal conductivity in crystalline α-GeTe. To obtain a cross-validation between independent methods we computed this quantity both with non equilibrium molecular dynamics (See Sec.2.5) with the neural network potential (See Sec.2.6) and by solving the Boltzmann transport equation based on DFPT second and third order force constants (See Sec.2.3).

3.1.1 Ab initio structural and vibrational properties of crystalline GeTe

As a preliminary step we studied the structural properties and the phonon dispersions using three different approximations LDA, PBE and PBE with semiempirical van der Waals corrections according to the DFT-D scheme (Sec.2.1.5). The calculations has been performed using the Quantum Espresso package. The Brillouin Zone (BZ) integration for the self-consistent electron density was performed over a 12x12x12 MP mesh [135] and the Kohn-Sham states were expanded in plane waves up to 30 Ry cutoff. Norm-conserving pseudopotentials with only the outermost s and p electron in valence were used. Atomic positions where relaxed until the forces were smaller than $1 \cdot 10^{-4}$ Ry/a.u.. The theoretical structural parameters optimized at zero temperature for the ideal semiconducting structure using the LDA and the PBE functional with or without vdW corrections are compared in Table 3.1 with experimental data.

All the functionals yield a good agreement with the experimental data. In particular the PBE functional gives the best results, with a slight overestimation of the lattice parameter by 0.46% and of the equilibrium volume by 2%, while both PBE+VdW correction and LDA functional produces an underestimation of 1.8% and 3.4% in the lattice parameter and in the volume respectively. α-GeTe has an electronic band gap of about 0.45 eV in DFT-PBE as usual slightly underestimated with respect to the experimental value (0.6 eV).

Structural parameters	LDA	PBE	PBE+vdW	Exp.
a (Å)	4.23	4.33	4.22	4.31
α	58.79°	58.14°	58.84°	57.9°
Unit Cell Volume (Å^3)	52.00	54.98	51.75	53.88
x	0.2384	0.2358	0.2380	0.2366
Short, long bonds (Å)	2.83, 3.11	2.85, 3.21	2.82, 3.11	2.84, 3.17

Table 3.1: Structural parameters of the trigonal phase of crystalline α-GeTe computed within DFT with the PBE or LDA functionals and with the addition of van der Waals interactions according to Grimme [87] and from experimental data [128]. The lengths of the short and long bonds are also given.

Phonon dispersion relations have been obtained by Fourier transforming the dynamical matrix computed on a 6x6x6 MP grid in the BZ. The phonon dispersions along the high symmetry directions of the Brillouin Zone (sketched in 3.2b) for the undoped case and the two limiting cases of low (n_{h1}=8 $\cdot$ 10^{19} holes/cm^3) and high (n_{h2}=2.1 $\cdot$ 10^{21} holes/cm^3) concentration of holes are reported in in Fig.3.2a calculated with the PBE functional at the theoretical equilibrium lattice parameters. A denser grid of 18x18x18 k-points was used in the undoped case to converge the effective charge tensor. The p-doping is introduced by removing electrons and by neutralizing the system with a uniform positive background [131]. We relaxed the atom positions at the two doping levels by keeping the lattice parameters fixed at the values of the ideal crystal: the x internal coordinate becomes 0.2359 for both n_{h1} and n_{h2}. The Ge vacancies, present in the real crystal but lacking in our models of the *p*-type compound, are in fact expected to affect the lattice parameters, as much as the holes in the valence bands do [131].

It can be observed that the metallic character of the hole-doped systems removes the discontinuities in the phonon dispersion at the Γ point (TO-LO splitting) present in the stoichiometric compound. The highest frequency phonon of A$_1$ symmetry (at Γ) softens continuously with increasing *p*-doping as already shown in Ref. [131]. The A$_1$ mode, measured experimentally by Raman spectroscopy [136], shows a strong temperature dependence as it corresponds to the soft mode of the ferroelectric transition. The experimental frequency extrapolated to zero temperature is 140.2 cm^{-1} in the sample measured in Ref. [136], for which the doping level is unknown. The theoretical frequency, within this approximation, is 149.9 cm^{-1} in the stoichiometric compound and 120.1 cm^{-1} in the system with n$_{h2}$=2.1 $\cdot$ 10^{21} holes/cm^3, which means that we could match the experimental frequency by a suitable choice of doping. On the other hand the acoustic modes are rather unaffected by the presence of holes.

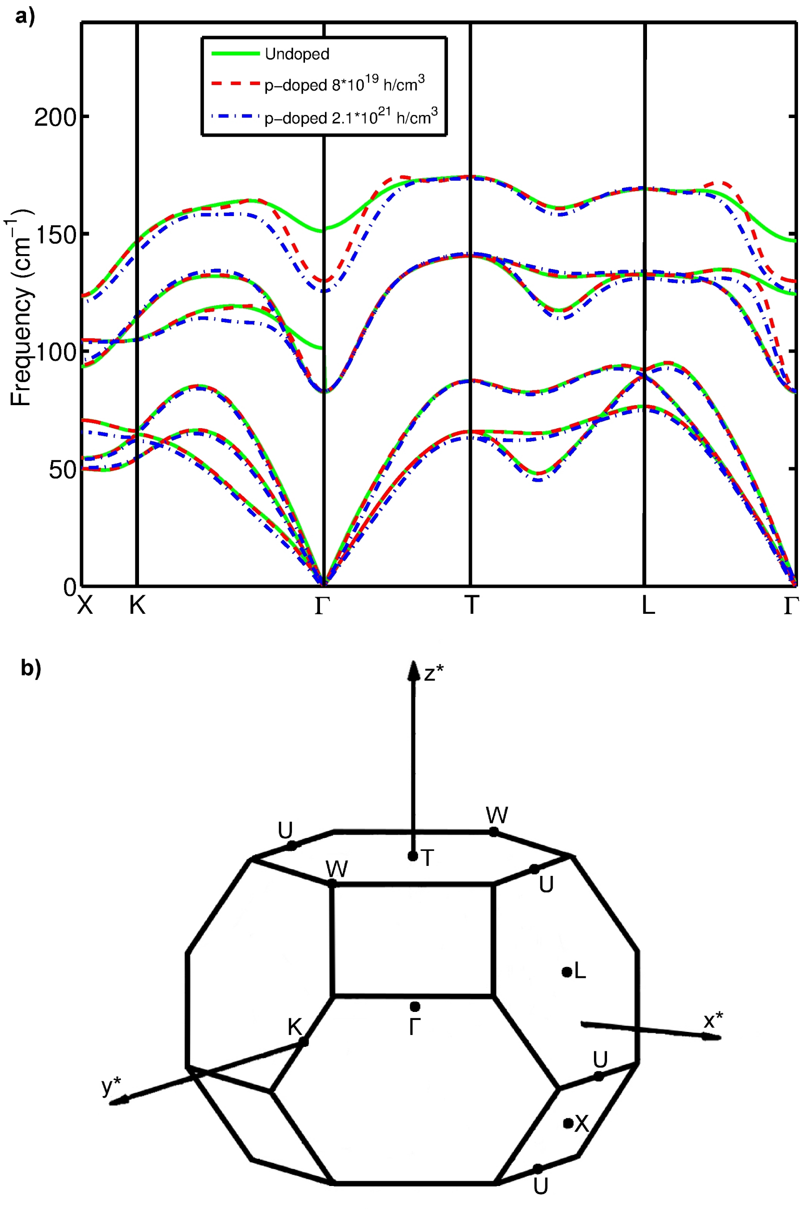

Figure 3.2: a) Phonon dispersion relations along high symmetry direction calculated with PBE at equilibrium volume for the ideal undoped crystal (green solid line), low hole concentration (red dashed line) and high hole concentration (blue dot-dashed line). b) The Brillouin zone of α-GeTe.

A comparison between the phonon dispersions along the high symmetry directions obtained with different functionals in the low doping conditions is reported in Fig.3.3. It can be observed that the slope of the acoustic modes is quite sensible to the equilibrium volume while it seems to be less affected by the choice of the functional once the volume is set.

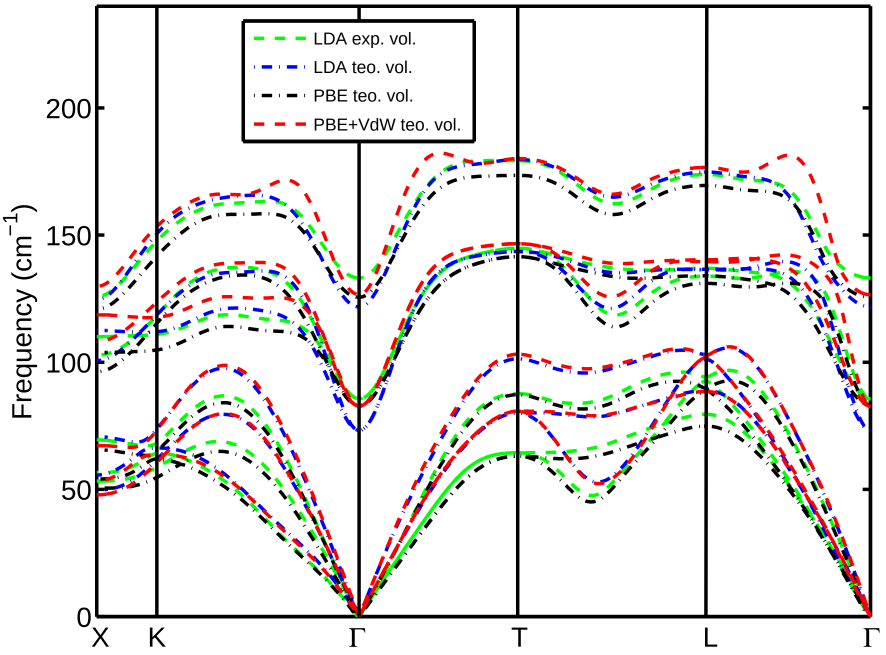

Figure 3.3: Phonon dispersion relations of trigonal GeTe along high symmetry direction calculated with LDA, PBE and PBE+VDW at the respective equilibrium volume and with LDA at the experimental volume.

3.1.2 Thermal conductivity of crystalline GeTe by ab initio DFPT calculations

To gain direct access to the microscopic quantities that characterize the thermal conductivity of an ideal material, such as phonon linewidth and mean free path, we performed the calculation of the thermal conductivity of α-GeTe with method based on the variational solution of the Boltzmann transport equation Eq.2.50. Harmonic and anharmonic force constant have been computed exploiting the 2*n*+1 theorem within DFPT as described in Sec.2.3

We first computed the lattice thermal conductivity for the ideal crystal without vacancies. Anharmonic force constants have been computed on a 4x4x4 q-point phonon grid on the BZ, Fourier interpolated with a finer 15x15x15 mesh for the calculations of phonon scattering rates in the Boltzmann equation. Phonon energies have been broadened with a Gaussian function with smearing of 2 cm^{-1} for energy conservation in three-phonon scattering processes. The convergence was checked with grid up to 25x25x25. Due to the actual limitations of the code, the anharmonic force constants were computed only with the LDA functional. We performed the calculations at experimental, theoretical PBE and theoretical PBE+vdW lattice parameters with both the internal geometry unoptimized and optimized with the LDA functional. Anharmonic force constants showed a very small dependence upon internal coordinate optimization. All the phonon calculation and the anharmonic force constants have been performed with the lower hole concentration n_{h1}.

The resulting lattice thermal conductivity at 300 K computed with PBE phonons along the z direction, parallel to the c axis in the hexagonal notation (cf. Fig. 3.1), is κ_z=2.00 W/m K while the lattice thermal conductivity in the xy plane parallel to the GeTe bilayers (cf. Fig. 3.1) is κ_x=2.90 W/m K. For a polycrystalline sample the calculated average thermal conductivity is $\kappa_{av}=\frac{2}{3}\kappa_x+\frac{1}{3}\kappa_z$= 2.6 W/m K, which is an upper limit, as it neglects the effects of defects (vacancies in particular) and grain boundary scattering. κ_{av} is comparable, although slightly larger, than the experimental value of 2.35 $\pm$ 0.53 W/m K of Ref. [51]. By using the LDA functional for both the harmonic and anharmonic force constants at the experimental lattice parameters one obtains an even larger lattice thermal conductivities of κ_z=2.37 W/m K, κ_x=3.62 W/m K and κ_{av}=3.20 W/m K.

Using the equilibrium Boltzmann distribution of phonons instead of the quantum Bose-Einstein distribution has no effect on the lattice thermal conductivity at 300 K (within the figures given here) due to the low Debye temperature of GeTe(180 K).

For the same reason, the lattice thermal conductivities computed within the SMA (cf. Sec.2.3) are κ_z=2.00 W/m K, κ_x=3.10 W/m K and κ_{av}=2.7 W/m K, i.e. only slightly lower than the values obtained from the full solution of the BTE given above with LDA phonons (κ_{av}=3.20 W/m K).

The cumulative lattice thermal conductivity within the SMA of ideal α-GeTe as a function of phonon frequency is shown in Fig. 3.4 computed using LDA phonons and anharmonic constants. Group velocities, phonon lifetimes and mean free paths calculated on a 25x25x25 grid are reported as function of the phonon frequency in Fig. 3.5 a,b and c respectively while the averages of the same quantities in small energy windows are reported in Fig. 3.6.

The anharmonic broadening of the phonon branches computed as the inverse lifetime (Sec.2.3) within the SMA are also reported in Fig. 3.7, while the spectral function $\sigma(\mathbf{q},\omega)$ as defined in Ref. [10] is reported in Fig. 3.8.

Comparison of Fig. 3.4 and Figs. 3.6-3.8 shows that acoustic phonons mostly contribute to the thermal conductivity at 300 K (up to 80%) because optical phonons have both low group velocities and lifetimes.

We then included the effects of vacancies in the Ge sublattice by adding a rate of elastic scattering due to isotopic defects in the BTE (See Sec.2.3). We considered two limiting vacancy contents of 0.073 *atom*% on the Ge sublattice corresponding to the hole concentration of $8 \cdot 10^{19}$ holes/cm^3, and of 3 *atom*% that corresponds to a hole concentration of $1.1 \cdot 10^{21}$ holes/cm^3 close to that studied experimentally in Ref. [131].

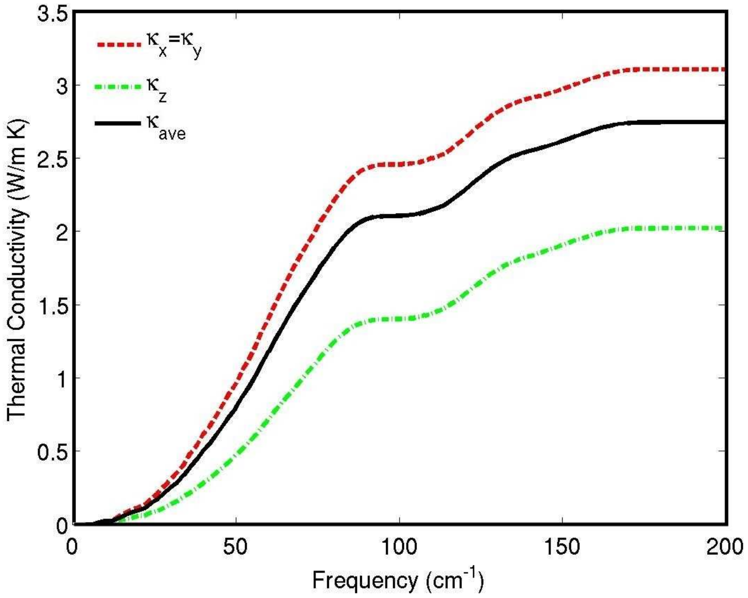

Figure 3.4: Cumulative lattice thermal conductivities within the SMA at 300 K of trigonal GeTe along the *c* axis in the hexagonal notation (κ_z) in the perpendicular plane (κ_x) and their average for a polycrystalline sample (κ_{av}).

The lattice thermal conductivities (LDA phonons) turn into κ_z=2.0 W/m K, κ_x=3.0 W/m K and κ_{av}=2.7 W/m K for the low vacancy content or κ_z=0.9 W/m K, κ_x=1.4 W/m K and κ_{av}=1.2 W/m K for the higher vacancy concentration to be compared with the values for ideal GeTe of κ_z=2.3 W/m K, κ_x=3.6 W/m K and κ_{av}=3.2 W/m K as given above. Even a small amount of Ge vacancies has thus a dramatic effect on the lattice thermal conductivity of GeTe which can be more than halved for a 3 $atom$% in agreement with the experimental data in Ref. [125].

In the presence of holes in the valence bands, the phonon lifetimes can be reduced also by electron-phonon scattering processes. These effects are, however, negligible in GeTe at the doping levels discussed above. To estimate the reduction of thermal conductivity due to electron-phonon scattering we removed from the calculation of κ the contribution of all phonons with wavevector q smaller than twice the larger wavevector on the Fermi surface. These phonons are the only one that can be affected by electron-phonon coupling. This would corresponds to a large overestimation of the effects of the electron-phonon coupling that, nevertheless, leads to a slight reduction of the thermal conductivities to κ_z=2.2 W/m K and κ_x=3.1 W/m K.

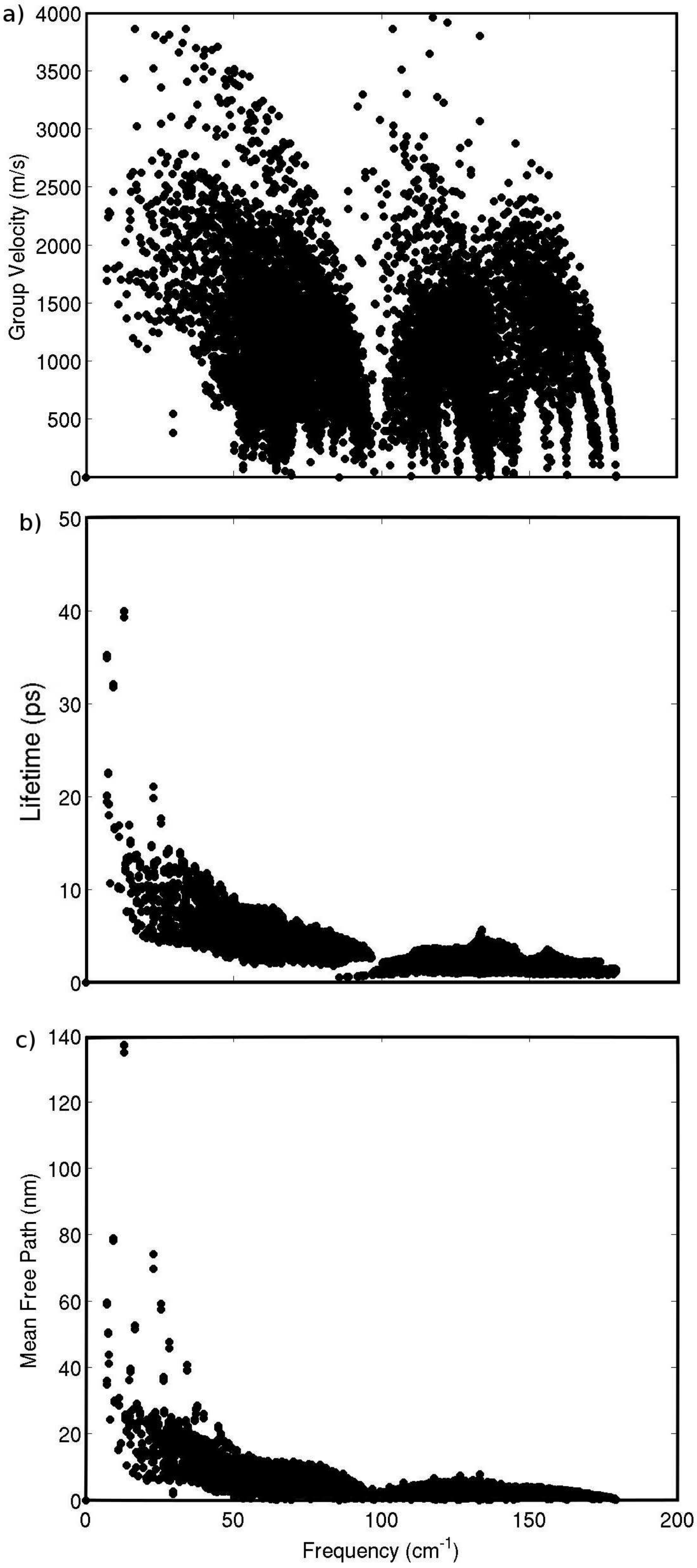

Figure 3.5: a) Group velocities, b) phonon lifetimes and c) mean free paths of trigonal GeTe calculated on a 25x25x25 grid. Each point correspond to a phonon of an individual branch in a **q**-point of the mesh.

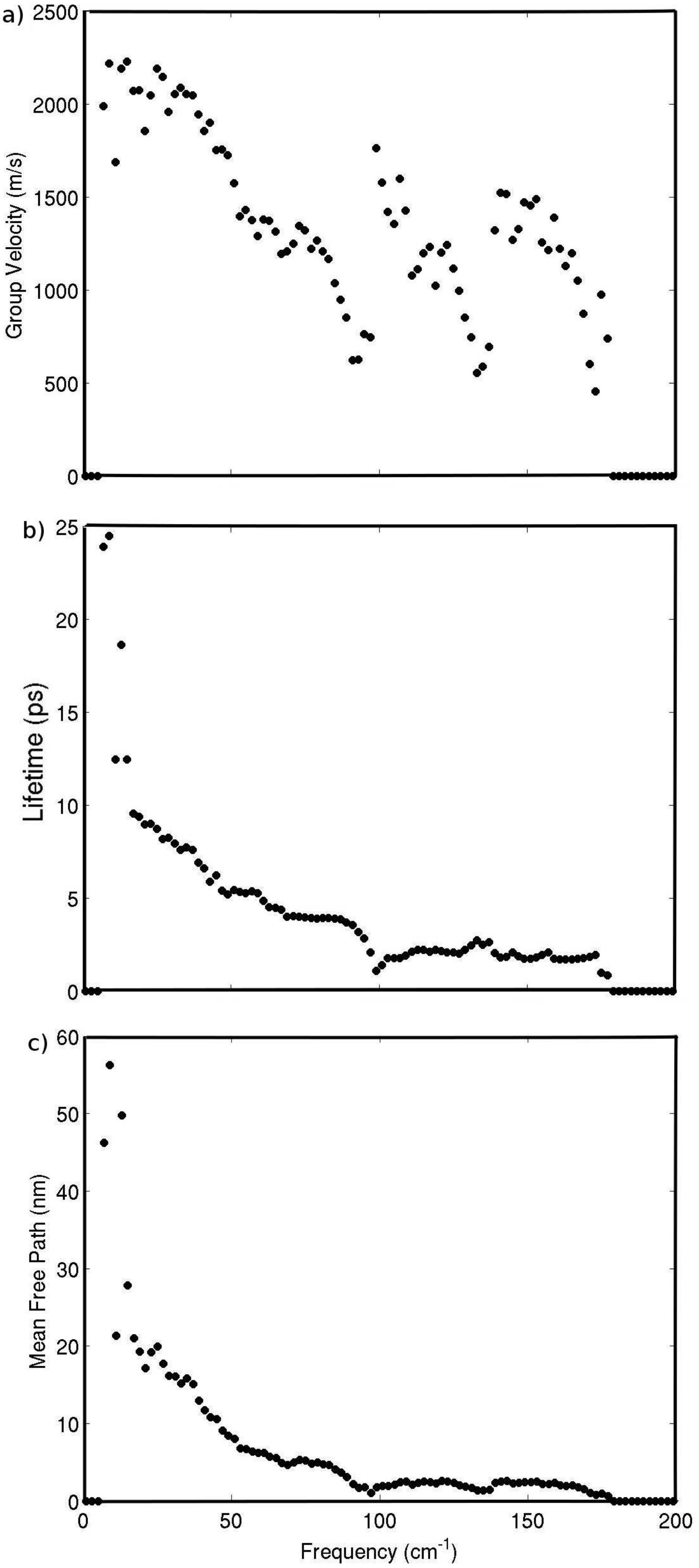

Figure 3.6: a) Group velocities, b) phonon lifetimes and c) mean free paths of trigonal GeTe averaged over all phonons within a small energy window of 2 cm^{-1}.

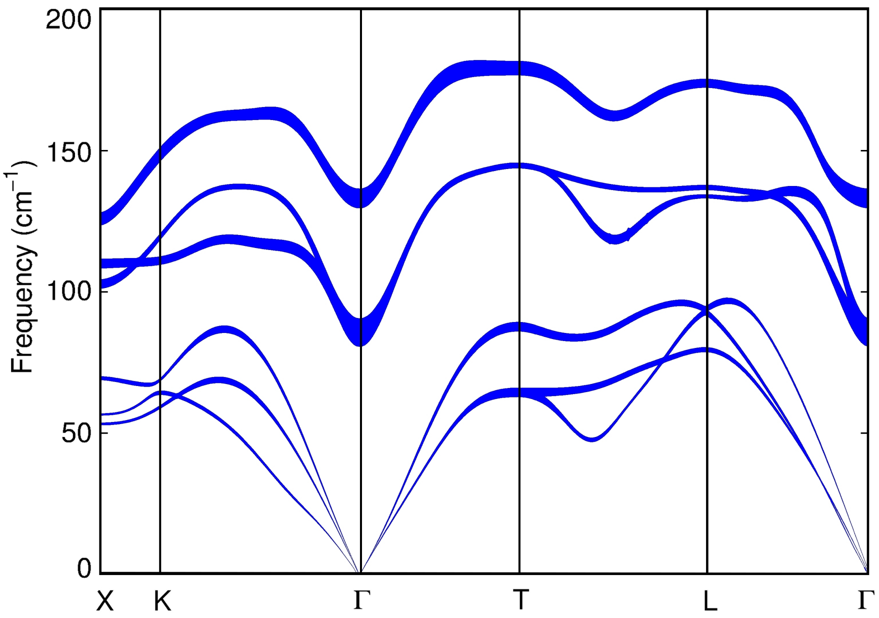

Figure 3.7: Anharmonc broadening (FWHM in cm^{-1}) at 300K calculated within LDA at the experimental volume.

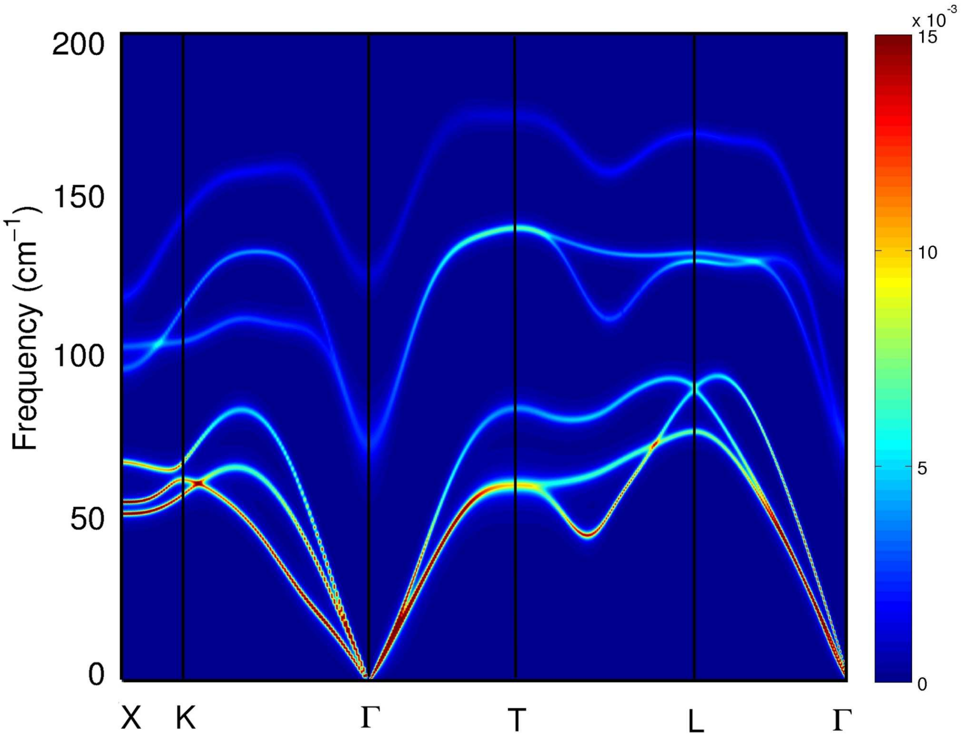

Figure 3.8: Spectral function as a function of **q** and frequency.

Finally, we calculated the temperature dependence of the thermal conductivity in GeTe with a 3% vacancies as reported in Fig.3.9. As discussed in Sec.2.3 in the single relaxation time approximation the thermal conductivity is given by $\kappa_{SMA} = \sum_\nu 1/3 C_\nu v_\nu^2 \tau$. Where C_ν is the specific heat per phonon mode, v and τ_ν are the group velocity and the lifetime. The steep rise of the thermal conductivity at low T is due to the increase in the specific heat per mode C_ν.
The relaxation time τ_ν first decreases exponentially when Umklapp processes are thermally activated and then decreases as 1/T above the Debye temperature, leading to a maximum in κ and a steady linear decrease at high temperatures.

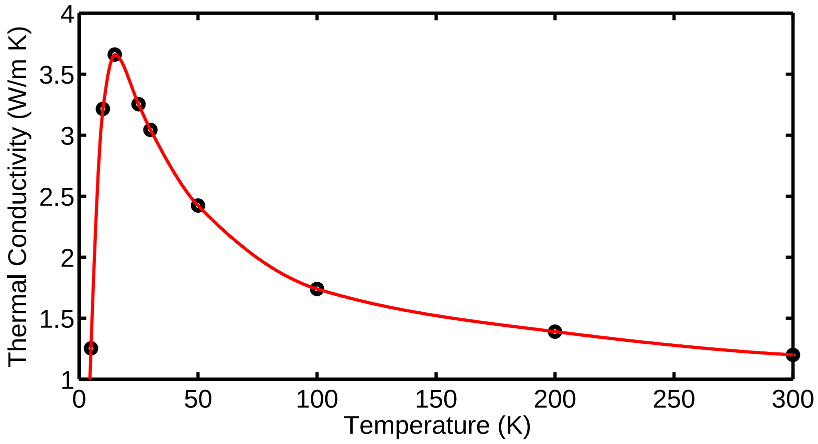

Figure 3.9: Temperature dependence of thermal conductivity in GeTe with 3% vacancies.

It is worth to stress that the effect of vacancies on the thermal conductivity has been actually introduced perturbatively as isotopic defects according to Ref. [52]. Because of the important approximations involved, the applicability of such method can not be taken as granted. To assess the reliability of this approximation we have performed non-equilibrium molecular dynamics (NEMD) simulations by using a Neural Network interatomic potential for GeTe (See Sec.2.6 and [12]) in which vacancies can be treated explicitly. The reliability of the classical approximation for phonons population at 300 K in GeTe, and thus the possibility to directly compare NEMD results and DFPT results has been demonstrated above.

3.1.3 Thermal conductivity of crystalline GeTe by neural network calculations

As a preliminary step to the calculation of thermal transport with the NN potential, we determined the theoretical equilibrium cell for the neural network potential. The structural parameters optimized at zero temperature with the NN potential reported in Table 3.2 are in reasonably good agreement with both experimental and DFT results.

Structural parameters	DFT (PBE)	NN	Exp.
a (Å)	4.33	4.47	4.31
α	58.14°	55.07°	57.9°
Volume (Å^3)	54.98	55.95	53.88
x	0.2358	0.2324	0.2366
Short, long bonds (Å)	2.85, 3.21	2.81, 3.31	2.84, 3.17

Table 3.2: Structural parameters of the trigonal phase of crystalline GeTe computed with the NN potential, within DFT using the PBE approximation and from the experimental data [128]. The lengths of the short and long bonds are also given.

The values of κ_z and κ_x were computed within reverse-NEMD (See Sec.2.5) by constructing supercells and setting the planes of the sink and sources either parallel or perpendicular to the z direction of the trigonal phase at the theoretical lattice parameters optimized at zero temperature.

Since the neural network calculation costs sensibly more than a classical force field molecular dynamics calculation, we decided to adopt a non-symmetric configuration instead of the more commonly used symmetric Muller-Plathe [11] configuration. In order to halve the computational cost, the heat source and sink are placed at the edges of the cell and consist of a slice of mobile atoms 5 Å thick and a 10 Å region of fixed atoms. Which decouple the source and the sink in the presence of periodic boundary conditions. The temperature profile and heat flux reach a converged steady condition after a time ranging from 0.7 to 2 ns depending on the model. A plot of the temperature profile and heat-flux in a typical simulation cell is shown in Fig. 3.10.

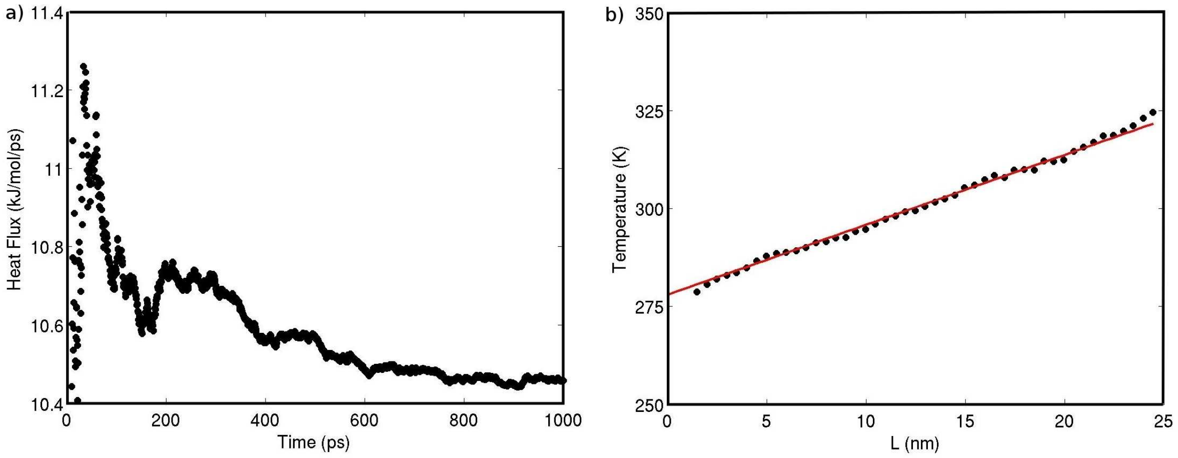

Figure 3.10: a) Heat flux as a function of time and b) temperature profile of a typical simulation cell of the trigonal GeTe. The heat flux is along the c direction.

In order to ensure the correct convergence of the results, we calculated the thermal conductivity in supercells of different size. In particular κ_z is obtained with supercells with sizes from 28.6 Å x 24.8 Å x 56.71 Å to 28.6 Å x 24.8 Å x 748.61 Å where the longer edges are along the *c* direction of the conventional hexagonal cell, while $\kappa_x = \kappa_y$ is obtained with sizes from 21.5 Å x 22.7 Å x 62.0 Å up to 21.5 Å x 22.7 Å x 744.1 Å. The dependence of κ on L is reported in Fig. 3.11. The convergence with respect to lateral dimensions of the cell, perpendicular to the heat flux direction was checked by doubling the lateral surface area in 49.9 nm long supercells.

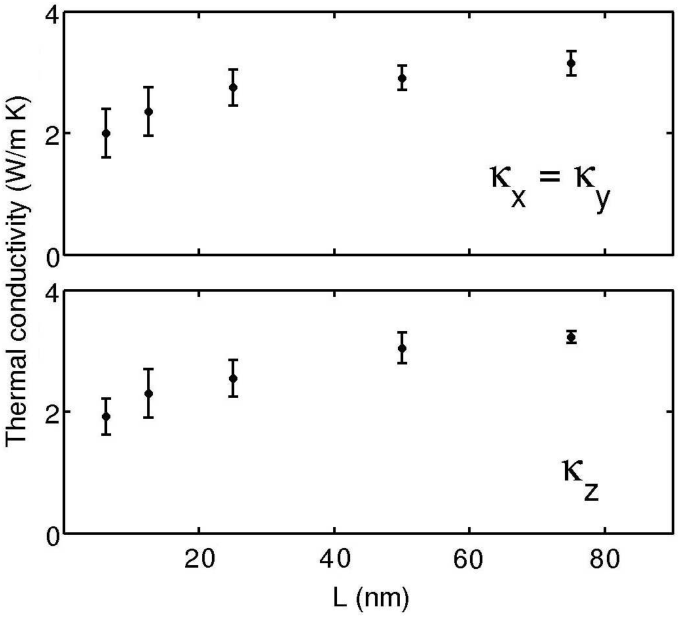

Figure 3.11: The dependence of the thermal conductivity κ as a function of the length of the simulation cell L for the trigonal crystalline phase. The thermal conductivity perpendicular (parallel) to the c-axis is reported in the upper (lower) panel.

We obtained a converged value κ_z = 3.23 ± 0.1 W/m K and $\kappa_x = \kappa_y$=3.15 ± 0.2 W/m K. For a polycrystalline sample the calculated average thermal conductivity is $\kappa_{av}=\frac{2}{3}\kappa_x + \frac{1}{3}\kappa_z$=3.20 W/m K. κ_{av} is very close to the result obtained within the DFPT calculations for the ideal crystal (κ_{av}=2.7 W/m K with PBE and κ_{av}=3.18 W/m K with LDA). However, the Neural Network potential does not manage to reproduce accurately the anisotropy of the thermal conductivity. This can be mainly due to the lower anisotropy of the NN phonon dispersions reported in Fig. 3.12. The overall agreement between DFT and NN phonon dispersion relations is satisfactory but for a lower anisotropy of the sound velocities in the NN which is responsible for a lower anisotropy of the thermal conductivity.

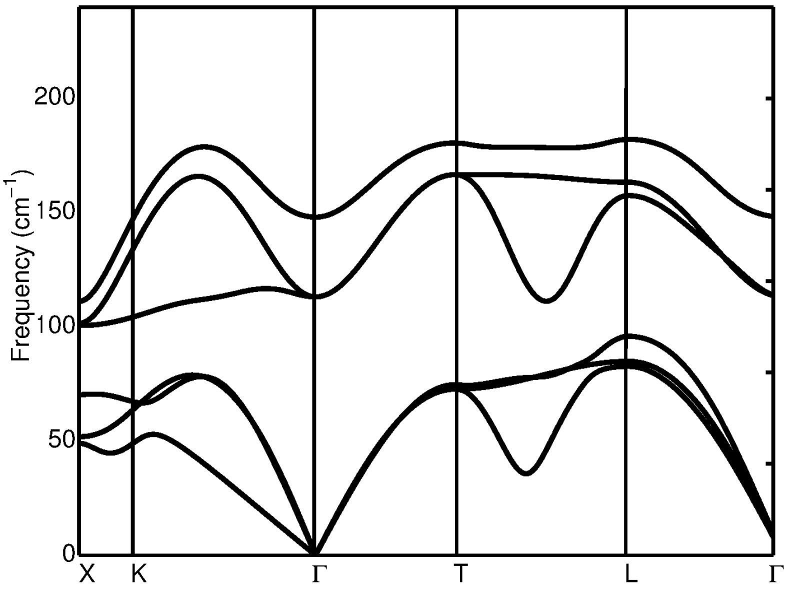

Figure 3.12: Phonon dispersion relations of trigonal GeTe within NN potential using finite difference methods.

We introduced vacancies in a random manner on the Ge sublattice with concentration of 3 % corresponding to the hole concentration of $1.1{\cdot}10^{21}$ holes/cm^3. We then repeated the simulations with vacancies and a 28.6 Å x 24.8 Å x 499.0 Å supercell obtaining κ_z=1.55 ± 0.1 W/m K which is 49% lower than the value obtained with the same supercell at the same average temperature of 300 K for the stoichiometric compound. Similarly we obtained $\kappa_x = \kappa_y$=1.3 ± 0.2 W/m K with the supercell of size 21.5 Å x 22.7 Å x 496.0 Å which is 56% lower than the value for the stoichiometric compound at the same conditions. The reduction of κ, in percentage, agrees perfectly with that obtained using ab initio anharmonic force constants and the approximate treatment of the vacancies as a kind of isotopic defect, which demonstrates the applicability of this approach.

In conclusion, the DFPT calculations have shown that the large spread in the experimental values of thermal conductivity of trigonal GeTe can be ascribed to different vacancy concentrations.

3.1.4 Thermal conductivity in amorphous GeTe

To complete the picture of thermal conductivity in GeTe and gain some general hints about the thermal conductivity in the amorphous states of change materials, we further studied the thermal conductivity in amorphous GeTe by means of non-equilibrium molecular dynamics simulations.

The calculation of the thermal conductivity in an amorphous system requires very long simulations (on the ns scale) of large models (thousands of atoms) that are presently beyond the reach of fully DFT simulations and thus it has been performed only with the NN potential.

NN equilibrium molecular dynamics (MD) calculation of the thermal conductivity of bulk amorphous GeTe performed in our group yielded $\kappa = 0.27 \pm 0.05$ W/m K [12, 116] at 300 K, which is very close to experimental results of 0.24-0.25 W/m K [51].

However, in equilibrium molecular dynamic simulations, thermal conductivity is computed within linear response theory which is valid only for small temperature gradients. In the actual device, temperature gradients can be as large as 30 K/nm. Under these conditions it is unclear whether or not the linear response approximation still holds. To address this issue we computed the thermal conductivity by means of RNEMD method introduced in Sec.2.5 which allows studying possible non-linear effects.

The amorphous models were generated by quenching from the melt (1000 K) to 300 K in 100 ps, according to the protocol used in our previous works [12, 116]. We considered several supercells with different size, up to 24.8 Å x 24.8 Å x 397.3 Å (8192 atoms). As in the previous case the heat source and sink are placed at the edges of the cell along the z-direction.

A plot of the temperature profile in a typical simulation run is shown in Fig. 3.13. The temperature profile reaches a converged steady condition after 800 ps.

The temperature of the sink and source are 220 K and 390 K and the imposed flux is q=3.02 $\cdot 10^{-8}$W. From the Fourier law and the slope of the temperature profile we obtain κ=0.26 W/m K which is very close to our previous result of 0.27 ± 0.05 W/m K at 300 K obtained from equilibrium MD and the use of the Green-Kubo formula [116]. We checked the convergence of κ by using supercells with different cross section areas perpendicular to the heat flux (24.8 x 24.8 Å^2 and 49.7 x 49.7 Å^2), and with different length along z.

Since the phonon mean free path in a-GeTe is always below few Å [116], κ is already converged in a smaller 24.8 Å x 24.8 Å x 99.3 Å (2048 atoms) cell.

As shown in a previous work [116] the thermal conductivity of a-GeTe is mostly due to diffusions, i.e. delocalized quasi-stationary modes. Their contribution can be evaluated by using the theory developed by Allen and Feldman [137] which assigns $\kappa_{AF} = \sum_j C_j \frac{1}{3} \sum_{\alpha=1}^{3} D_{\alpha j}$ where C_j is the contribution of the j-th phonon to the specific heat and $D_{\alpha j}$ is the “diffusivity” given by

$$D_{\alpha j} = \frac{\Omega^2}{8\pi^2 \hbar^2 \nu_i^2} \sum_{n \neq j} \mid \langle \mathbf{e}_j \mid \mathbf{J}_\alpha \mid \mathbf{e}_n \rangle \mid^2 \delta(\nu_j - \nu_n). \tag{3.1}$$

Here $\langle \mathbf{e}_j \mid \mathbf{J}_\alpha \mid \mathbf{e}_n \rangle$ are the matrix elements of the α Cartesian component of the energy flux operator between two harmonic normal modes $\mathbf{e}_n$ and $\mathbf{e}_j$ with frequencies ν_n and ν_j. Since the phononic specific heat has already reached its classical value at 300 K and the diffusivity in Eq. 3.1 is temperature independent, we expect a weak dependence of κ on the temperature above 300 K in a-GeTe.

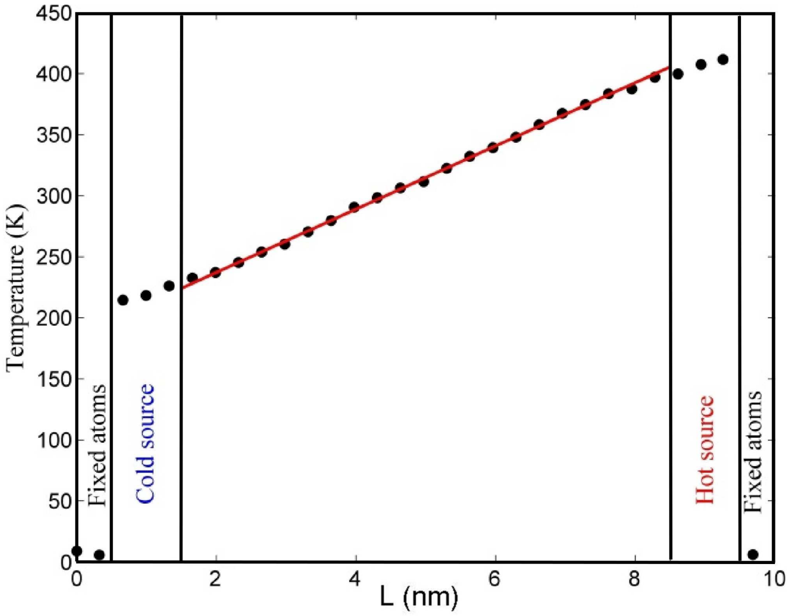

Figure 3.13: Temperature profile in the NEMD simulation of bulk amorphous GeTe.

We investigated possible non-linear effects by tuning the initial temperature and the heat flux in order to have large temperature gradients from 1 K/nm up to a value of 30 K/nm. We actually did not observe changes of κ within the error bar of 0.03 W/m K for $\frac{dT}{dz}$ in the range given above and for an average temperature in the range 200-400 K at which the amorphous phase is stable against crystallization on the time scale of our simulations. We can conclude that at the conditions of PCM operation we can still use the bulk value of the thermal conductivity of a-GeTe measured/computed for small temperature gradients.

3.2 $Ge_2Sb_2Te_5$

$Ge_2Sb_2Te_5$ (GST) is the material of choice for commercial PCM devices thanks to the stability of the amorphous phase and the very fast phase transition. GST presents two crystalline phases at normal pressure [70, 138]. The stable structure has a hexagonal symmetry with space group $P\bar{3}m1$, the unit cell contains nine atoms in an octahedral coordination arranged in nine layers stacked along the *c* axes.

The internal arrangement of Ge and Sb atoms in the stacks is still debated and three sequences have been experimentally proposed:

A Te–Ge–Te–Sb–Te–Te–Sb–Te–Ge–Te (Kooi)
from high resolution transmission electron microscope [138];

B Te–Sb–Te–Ge–Te–Te–Ge–Te–Sb–Te (Petrov)
from XRD measurements [70];

C Te–(Sb/Ge)–Te–(Sb/Ge)–Te–Te–(Sb/Ge)–Te–(Sb/Ge)–Te (Matsunaga)
from XRD measurements with a random distribution of Ge and Sb [139].

The Te-Te bonds are actually weak as the structure can be seen as a stacking of $Ge_2Sb_2Te_5$ 9-layers bound by vdW interaction across the Te-Te vdW gap. The structure of the two order phases is shown in Fig.3.14.

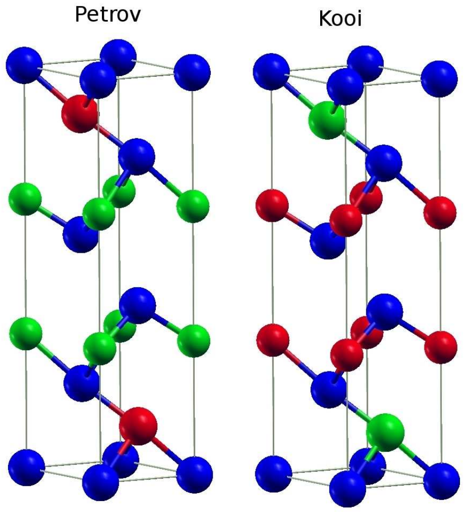

Figure 3.14: Structure of $Ge_2Sb_2Te_5$ in the hexagonal cell . Two formula units along the c axis, and period replica of atoms at the edges of the hexagonal cell in the ab plane are shown. The positions of Ge and Sb atoms are interchanged. The weak Te-Te bonds (3.7 long) connecting adjacent slabs are not shown to emphasize the presence of $Ge_2Sb_2Te_5$ stacks. The Petrov (B) and Kooi (A) stackings are shown.

In PCM, a metastable cubic crystal is obtained upon crystallization of the amorphous phase. The cubic phase (c-GST) has a rocksalt geometry with Te occupying one sublattice and Ge, Sb and 20% of vacancies occupying randomly the other sublattice [139]. The metastable cubic phase turns into the stable hexagonal phase at higher temperatures.

From the point of view of thermal conductivity several experimental works reported on the measurements of the bulk thermal conductivity of different GeSbTe alloys [7, 54, 119, 120].

In the case of cubic $Ge_2Sb_2Te_5$, disorder is present in the form of a random distribution of Ge, Sb atoms and 20 % of vacancies in one sublattice of the rocksalt structure, the other being full occupied by Te atoms. Disorder leads to a lattice thermal conductivity κ=0.40 W/m K close to the value of 0.27 W/m K measured for the amorphous phase [54]. Vacancies in the Ge sublattice of crystalline trigonal GeTe are also responsible for scattering of the measured thermal conductivity over a wide range of values 0.1-4.1 W/m K [51, 121–125] as previously shown for GeTe.

The lattice thermal conductivity is interestingly very low (0.45 W/m K) [54] also in the hexagonal phase, in which the vacancy concentration is expected to be relatively low. In this latter case, disorder may arise by a partial random distribution of Sb/Ge atoms corresponding to the stacking (C) proposed by Matsunaga et al. [139]. The thermal conductivity can thus be a good probe to determine the real structure of this material.

3.2.1 Ab initio structural and vibrational properties of crystalline GST

The geometry of $Ge_2Sb_2Te_5$ in the two ordered stackings within DFT-PBE was optimized in a previous work [140], the results are reported in parenthesis in Tab. 3.3, compared with the results obtained by adding the Grimme semiempirical van der Waals correction [87] and with the experimental parameters. The calculations have been performed by using the Quantum Espresso package [73]. The Brillouin Zone (BZ) integration for the self-consistent electron density was performed over a 8x8x2 MP mesh and the Kohn-Sham states were expanded in plane waves up to 20 Ry cutoff. Norm-conserving pseudopotentials with only the outermost s and p electron in valence were used. Atomic positions where relaxed until the forces were smaller than $1\cdot10^{-4}$ Ry/a.u..

	Stacking		
	A	B	Exp.[a]
Energy (meV/atom)	0 (0)	16.3 (19)	
	Cell Parameters (Å)		
a	4.191 (4.28)	4.178(4.25)	4.225
c	17.062 (17.31)	17.41 (17.74)	17.239

Table 3.3: Relative energies (meV/atom) and theoretical equilibrium lattice parameters (Å) for stacking A (Kooi) and B (Petrov) optimized with the PBE+vdW functional. Data without vdW corrections are reported in parenthesis.

In the hexagonal crystalline phase, GST is a degenerate p-type semiconductor due to Ge/Sb deficiency. As for GeTe the degenerate p-type character of GST was reproduced by removing electrons and by neutralizing the system with a uniform positive background. We considered a hole concentration of 0.084 holes/cell, i.e. $3.0 \cdot 10^{20}$ holes cm^{-3} close to the typical experimental value of $2.73 \cdot 10^{20}$ holes cm^{-3} at 3K of Ref. [141].

The Kooi phase (A) resulted to be energetically more favorable with both PBE and PBE+vdW. Previous calculations [140] showed that the disordered Matsunaga stacking is only marginally higher in energy than stacking A, actually within the free energy contribution expected for configurational disorder, and it is even marginally lower in energy than stacking A if the hybrid B3PW functional [142] is used.

However, the calculation of phonon dispersion relations, (Fig.3.15 and 3.16) obtained by Fourier transforming the dynamical matrix computed on a 4x4x4 MP grid in the BZ revealed that the Kooi phase is dynamically unstable in the PBE approximation, but it is stabilized by including vdW interactions. The comparison between the phonons calculated with and without vdW correction show that, as opposed to GeTe, the vdW correction does not significantly affect the slope of the acoustic modes while it has remarkable effects (a shift of nearly 8 cm^{-1}) only on the optical modes.

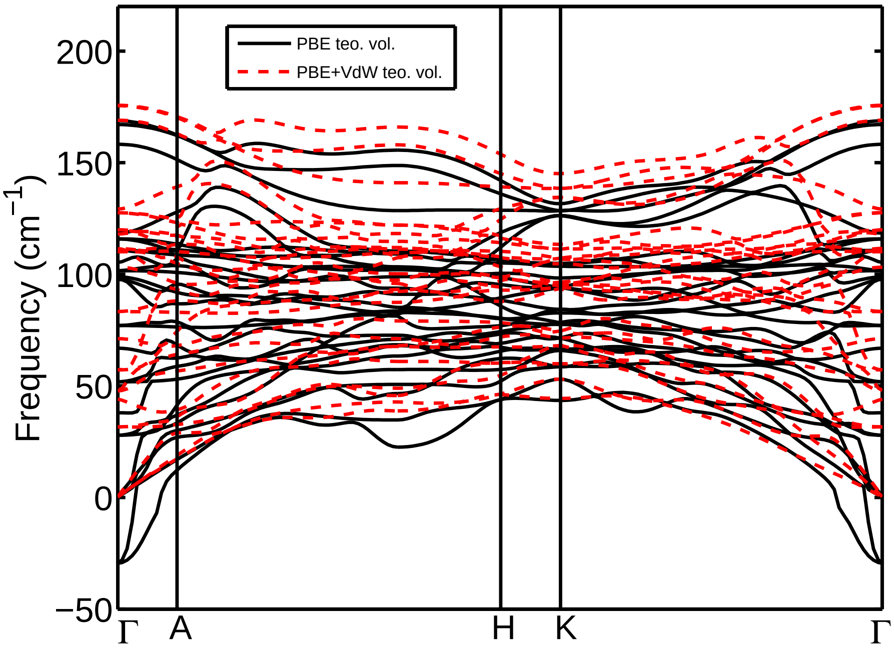

Figure 3.15: Phonon dispersion of $Ge_2Sb_2Te_5$ in the Kooi stacking with PBE and PBE+vdW at the respective equilibrium lattice parameters.

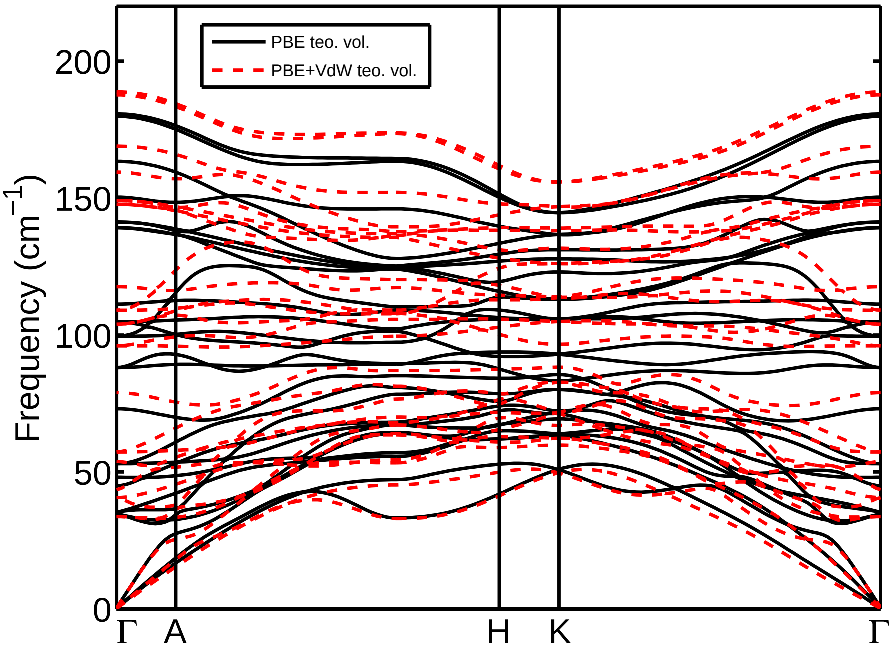

Figure 3.16: Phonon dispersion of Ge$_2$Sb$_2$Te$_5$ in the Petrov stacking with PBE and PBE+vdW at the respective equilibrium lattice parameters.

3.2.2 Thermal conductivity of GST

The thermal conductivity has been computed using phonons calculated with the PBE functional both with and without vdW corrections for the Petrov phase. In the Kooi phase the calculations were carried out exclusively with PBE including the vdW correction because this phase is otherwise unstable. Anharmonic force constants have been computed only with the LDA functional on a 4x4x1 q-point phonon grid on the BZ, for the cells at the PBE+vdW equilibrium parameters (and also at the equilibrium parameters of PBE without vdW corrections for the Petrov phase) with both the internal coordinates optimized and unoptimized within the LDA approximation. Also in this case only a marginal difference has been observed as a consequence of the two different internal geometry. The third order coefficients have been then Fourier interpolated with a finer 20x20x7 mesh for the solution of the Boltzmann equation. Phonon energies have been broadened with a Gaussian function with smearing of 2 cm^{-1} for energy conservation in three-phonon scattering processes.

The thermal conductivities at 300 K for the ordered Ge$_2$Sb$_2$Te$_5$ crystal in stacking A and B obtained from the full solution of the BTE with the PBE+vdW functional are reported in Table 3.4. The average thermal conductivity of about 1.6-1.2 W/m K is sizably larger than the experimental value of 0.45 W/m K [54].

We then introduced in the BTE the scattering due to vacancies in either the Sb or Ge sublattice with a concentration assigned by the holes density measured by the Hall effect which yields $3 \cdot 10^{20}$ holes/cm^3 [141]. This holes density corresponds to either 1.8 atom% vacancies in the Ge sublattice (two holes per vacancy involving only the *p* electrons) or to 1.25 atom% vacancies in the Sb sublattice (three electrons per vacancy). The average thermal conductivity is reduced to about 1.1 W/m K (Table 3.4) which is still much higher than the experimental value. By increasing the vacancy concentration up to 3 atom% in the Ge sublattice the average thermal conductivity is further reduced to 0.64-0.86 W/m K. To bring the thermal conductivity to a value closer to experiments we have then introduced the disorder in the Ge/Sb sublattice by adding an isotopic phonon scattering rate in the BTE. By considering a full Ge/Sb mass mixing and neglecting Ge/Sb vacancies the average thermal conductivity is sizably reduced to 0.61-0.76 W/m K (cf. Table 3.4). By further adding on top of Ge/Sb disorder the scattering due to 1.8 atom% Ge vacancies or 1.25 atom% Sb vacancies, the average thermal conductivity is further reduced to 0.43-0.58 W/m K or 0.28-0.42 W/m K (cf. Table 3.4).

	A (Kooi)			B (Petrov)		
	κ_z	κ_x	κ_{av}	κ_z	κ_x	κ_{av}
Ideal	0.34	1.59	1.20	0.59	2.10	1.60
1.8 % Ge vac	0.28	1.19	0.83	0.42	1.49	1.13
1.25 % Sb vac	0.25	1.10	0.82	0.47	1.50	1.16
Ge/Sb disorder	0.20	0.77	0.61	0.30	0.99	0.76
Ge/Sb + Ge vac	0.16	0.56	0.43	0.25	0.75	0.58
Ge/Sb + Sb vac	0.11	0.37	0.28	0.23	0.51	0.42

Table 3.4: Lattice thermal conductivity of hexagonal $Ge_2Sb_2Te_5$ at 300 K along the *c* axis in the hexagonal notation (κ_z, cf. Fig. 3.14) in the perpendicular plane (κ_x) and their average for a polycrystalline sample (κ_{av}). The first row report the values for the ideal crystal in which only the anharmonic effect are taken into account. In second and third row are reported the values of thermal conductivity including the isotopic scattering due to the two possible vacancy type in a percentage compatible with experiments. In the fourth row is stated the values of thermal conductivity taking into account the isotopic scattering produce by a complete disorder in the Ge/Sb sublattice while in the fifth and sixth row the combined effect of disorder and vacancies is taken into account.

For the Petrov stacking the use of PBE instead of PBE+vdW leads to a slightly lower conductivity. For the ideal Petrov phase the average thermal conductivity is 1.47 W/m K, and drops to 0.69 W/m K and 0.47 W/m K with the inclusion of vacancies and vacancies plus complete lattice disorder on the Ge/Sb sublattice.

In GST the thermal conductivity calculated within the SMA is lower by less than 5 % with respect to the full solution of the BTE.

The spectral function $\sigma(\mathbf{q},\omega)$ calculated at 300K with PBE+vdW for the Kooi and Petrov ideal phases are reported in Fig.3.17. The cumulative lattice thermal conductivity, average group velocities, phonon lifetimes and mean free paths calculated within the SMA of $Ge_2Sb_2Te_5$ calculated with PBE+vdW as a function of phonons frequency is shown in Fig. 3.18 for the ideal stacking Kooi and Petrov stackings and for the disordered Matsunaga structure including vacancies.

From Figs. 3.18 and 3.17 it is clear that, as in GeTe, the acoustic phonons mostly contribute to the thermal conductivity at 300 K, with a small contribution of the lower energy optical modes and a negligible contribution of the high energy optical modes. In the disordered Matsunaga phase in particular, the whole lattice thermal conductivity originates from the acoustic modes with energy below 30 cm^{-1}.

It is clear that both vacancies and disorder are needed to achieve a good agreement between theoretical and experimental data and this result strongly suggests that the low thermal conductivity in the hexagonal phase is actually an indicator of the (Ge/Sb) sublattice disorder as also suggested by recent experimental data from Z-resolved TEM in GST nanowires [143].

The temperature dependence of thermal conductivity for the disordered phase, including sublattice disorder and vacancies treated perturbatively, is reported in Fig.3.19.

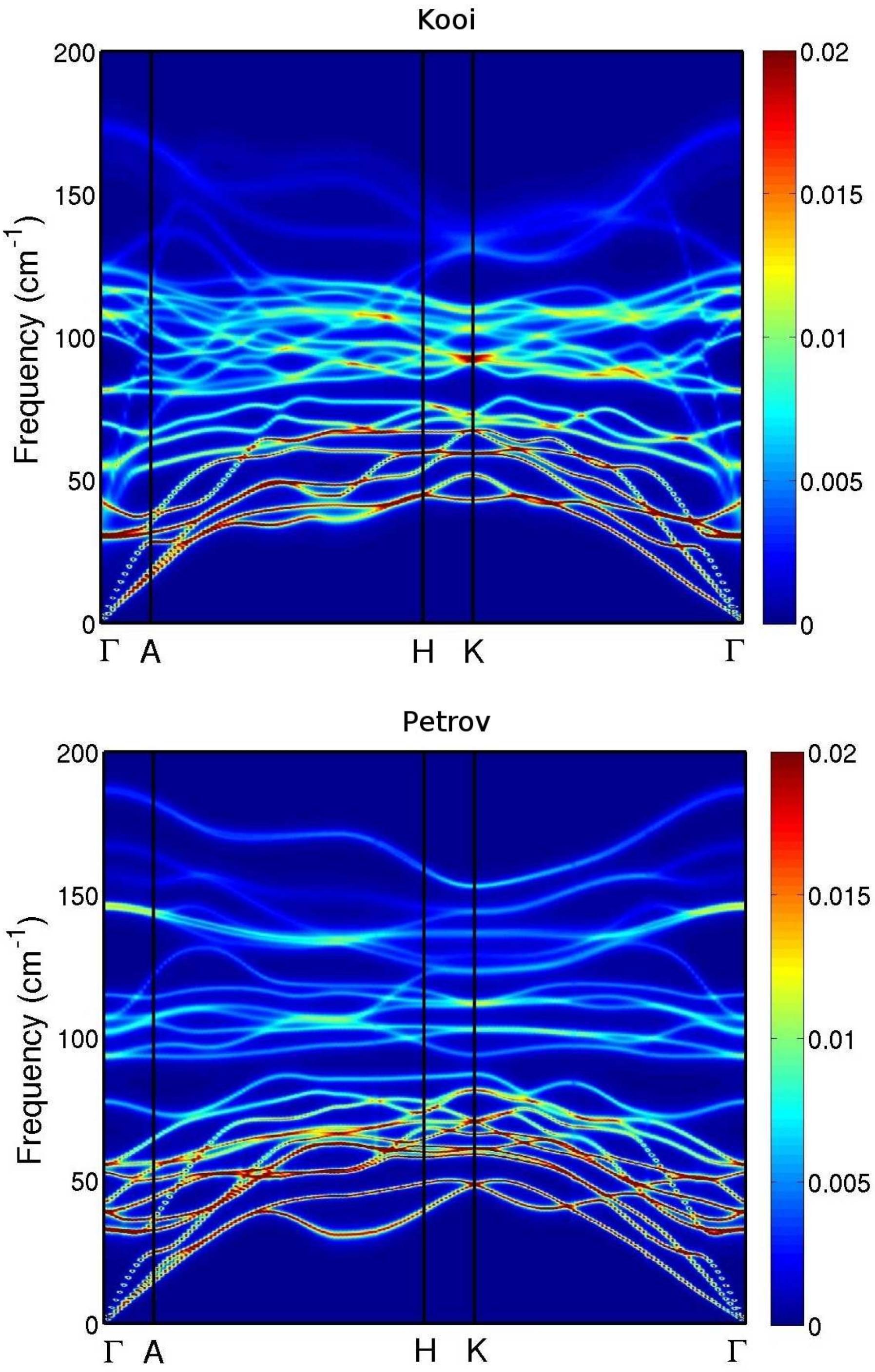

Figure 3.17: Spectral function at 300K for $Ge_2Sb_2Te_5$ in the Kooi and Petrov stackings with PBE+vdW at the respective equilibrium lattice parameters.

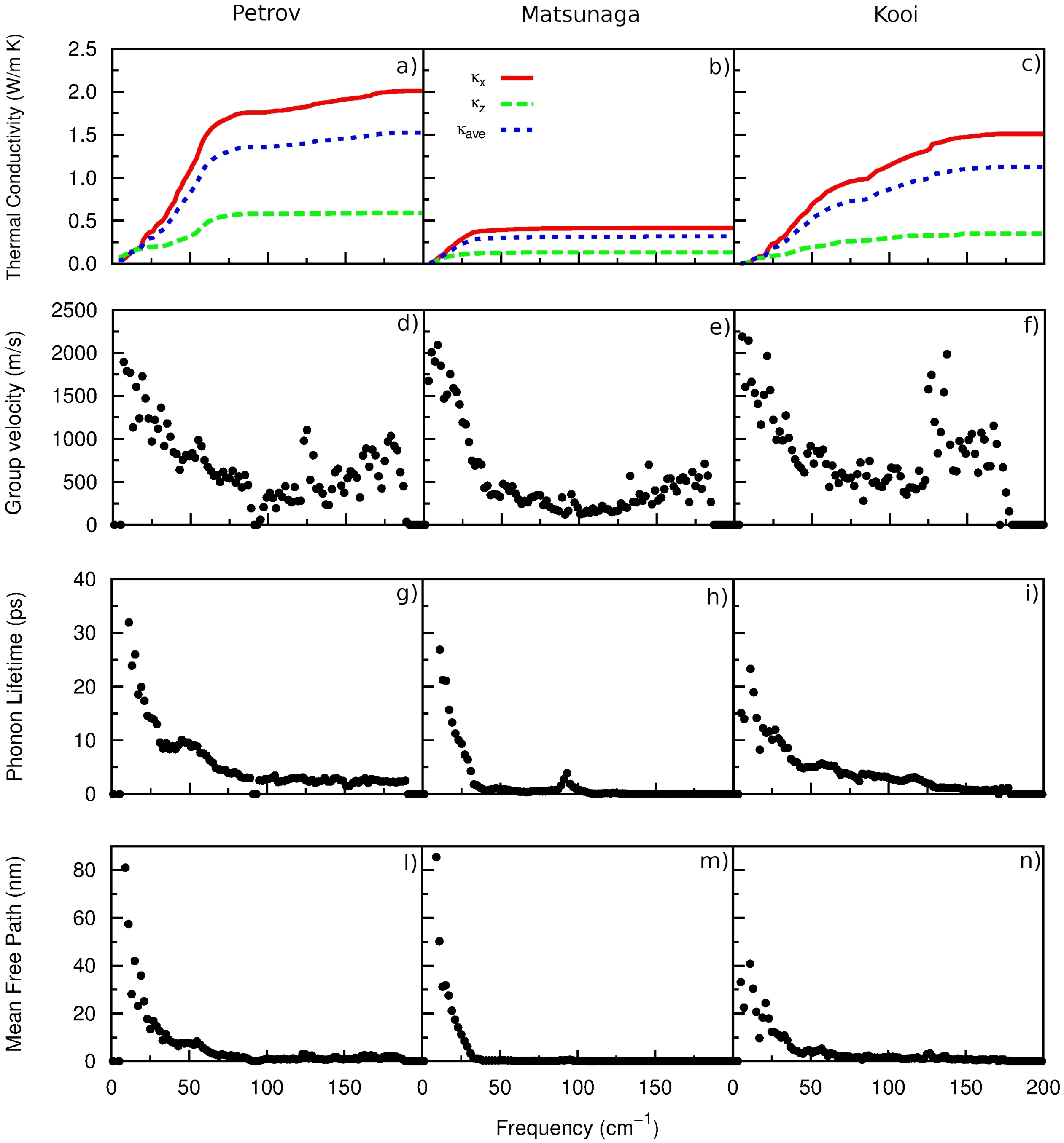

Figure 3.18: Cumulative lattice thermal conductivities within the SMA at 300K along the *c* axis in the hexagonal notation (κ_z) in the perpendicular plane (κ_x) and their average for a polycrystalline sample κ_{av}) for the Petrov a), Matsunaga b) and Kooi c) stackings. Averaged velocities d),e),f) lifetimes g),h),i) and mean free path l),m),n) for the three different arrangements respectively.

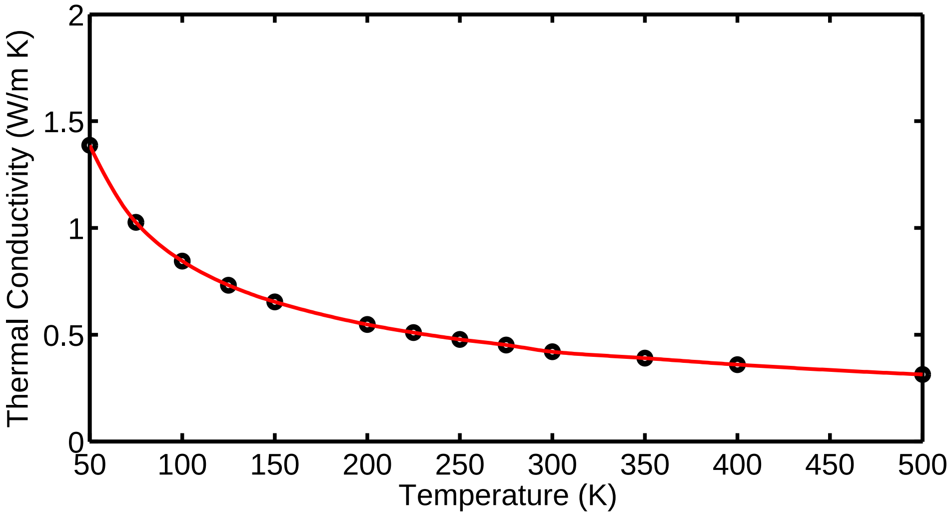

Figure 3.19: Temperature dependence of thermal conductivity for the Matsunaga stacking of $Ge_2Sb_2Te_5$, including vacancies, calculated using PBE+vdW and starting from the unperturbed Petrov harmonic and anharmonic force constants with sublattice disorder and vacancies treated perturbatively as a mass disorder.

Finally, we verified that the thermal conductivity in the disordered hexagonal phase can be well described within the minimal thermal conductivity model, according to Cahill which yields for acoustic bands only:

$$\kappa_{min} = \left(\frac{\pi}{6}\right)^{1/3} k_B n^{3/2} \sum_s v_{g,s} \left(\frac{T}{\Theta_{D,s}}\right)^2 \int_0^{\Theta_{D,s}/T} \frac{x^3 e^x}{(e^x-1)^2} dx \tag{3.2}$$

where $x = \hbar\omega/k_B T$, n the atomic number density. The sum runs over two transverse and one longitudinal phonon branches, each with individual sound velocities $v_{g,s}$ and cut-off Debye temperatures $\Theta_{D,s} = (6\pi^2 n)^{1/3} v_{g,s}\hbar/k_B$. For temperatures much above θ_D as is in the case of GST at 300 K Eq.3.2 reduces to

$$\kappa_{min} = \frac{3}{2}\left(\frac{\pi}{6} n^2)^{1/3} v_g k_B\right). \tag{3.3}$$

By plugging in the Cahill formula 3.3 the sound velocities ($v_{gL} = 3120$ m/s and $v_{gT} = 1950$ m/s) and the atomic density computed within DFT, we obtained a value of κ_{min}=0.43 W/m K, very close to the experimental value and the rigorous first-principle result. This result suggest that the minimal thermal conductivity can be used to estimate κ in other similarly disordered phase change materials.

3.3 Sb_2Te_3

Sb_2Te_3 is not a material commonly used in PCM cells because of the insufficient stability of the amorphous phase. However, it is a semiconductor of interest for several technological applications, ranging from thermoelectrical devices to spintronic applications thanks to its topological insulating properties. Only recently, slightly Ge-doped SbTe has also been reported [144] as an interesting alloy for applications in PCM.

Crystalline Sb_2Te_3 is a small band gap (0.28 eV) semiconductor with a rhombohedral geometry ($R\bar{3}m$ space group (D^5_{3d})) with five atoms in the elemental unit cell [145]. The crystal structure can be better visualized in the conventional hexagonal supercell with three formula units (Fig. 3.20). In the hexagonal cell we recognize three slabs, each formed by five hexagonal layers stacked along c in the sequence Te-Sb-Te-Sb-Te, each layer containing a single atom in the unit cell. The weak Te-Te bonds, 3.736 Å long [145], connecting adjacent slabs are not shown in Fig. 3.20 to emphasize the presence of Sb_2Te_3 structural units. The three atoms independent by symmetry are at crystallographic positions Te1 = (0, 0, 0), Te2 = (0, 0, x) and Sb = (0, 0, y) (Fig. 3.20).

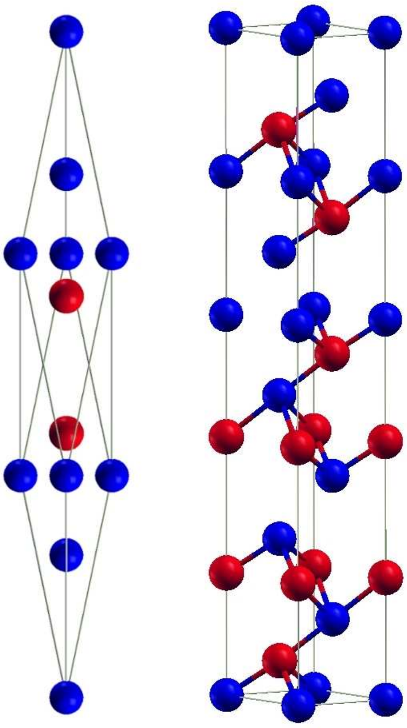

Figure 3.20: Structure of Sb_2Te_3 in the elemental and conventional hexagonal supercell

3.3.1 Ab initio structural and vibrational properties of crystalline Sb_2Te_3

The calculations were performed by integrating self-consistent electron density over a 6x6x6 MP mesh in the Brillouin Zone (BZ). Kohn-Sham states were expanded in plane waves up to 30 Ry cutoff. Norm-conserving pseudopotentials with only the outermost s and p electron in valence were used. Atomic positions were relaxed until the forces were smaller than $1{\cdot}10^{-4}$ Ry/a.u.. The PBE functional was employed both with and without the semiempirical vdW corrections. Phonon dispersion relations have been obtained by Fourier transforming the dynamical matrix computed on a 6x6x6 MP grid in the BZ. The phonon dispersion relations along the high symmetry directions of the conventional hexagonal cell are reported in Fig.3.21. As for GST the vdW corrections do not significantly affect the acoustic modes and low energy optical modes while causes a blue shift of nearly 10 cm^{-1} in the highest frequency optical modes.

Structural parameters	PBE	PBE+vdW	Exp.
a (Å)	4.316	4.219	4.264
c (Å)	31.037	30.692	30.458
x	0.785	0.786	0.787
y	0.397	0.397	0.399

Table 3.5: Structural parameters of crystalline Sb_2Te_3 computed using the PBE approximation with and without vdW correction compared with experimental data.

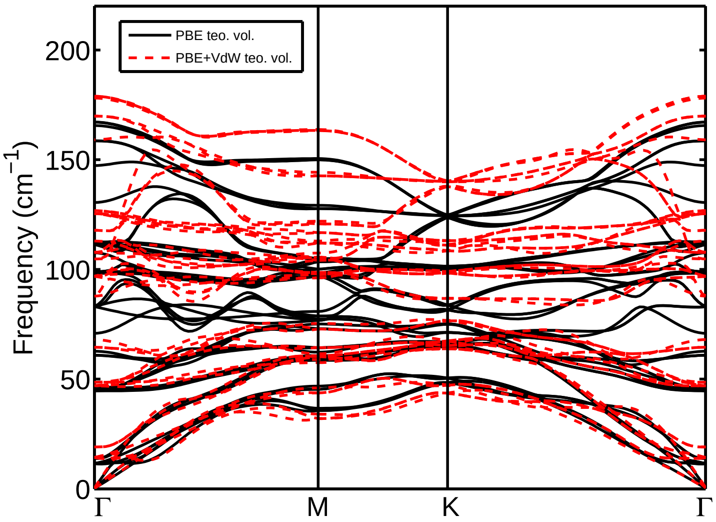

Figure 3.21: Phonon dispersions of crystalline Sb_2Te_3 along high symmetry directions of the hexagonal cell calculated with PBE with and without vdW correction.

3.3.2 Thermal conductivity of Sb_2Te_3

The lattice thermal conductivity at 300 K has been computed with PBE+vdW phonons. Anharmonic force constants have been computed with the LDA functional on a 4x4x4 q-point phonon grid on the BZ, for the elementary cell at the PBE+vdW equilibrium parameters. A Fourier interpolation over 15x15x15 mesh and a smearing of 2 cm^{-1} has been used for the variational Boltzmann optimization.

The cumulative lattice thermal conductivity within the SMA of Sb_2Te_3 as a function of phonons frequency as well as average group velocity, phonon lifetimes and mean free paths are shown in Fig. 3.22.

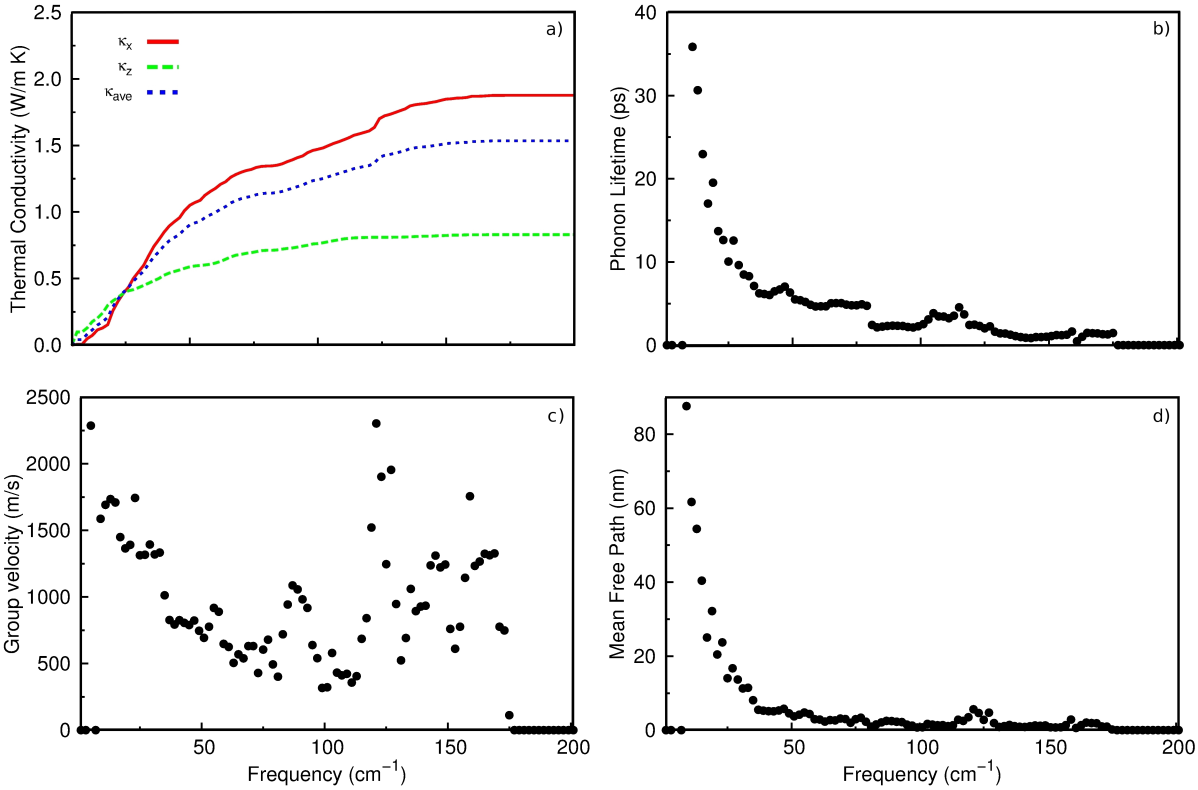

Figure 3.22: a) Cumulative lattice conductivity of Sb_2Te_3 at 300 K within SMA, b) averaged group velocity c) lifetime and d) mean free path.

The results are κ_z=0.7 W/m K, κ_x=2.0 W/m K, and κ_{av}= 1.6 W/m K. These results are in good agreement with the experimental values, κ_{av}= 1.3 W/m K reported in Ref. [121] and 1.8 W/m K of Ref. [146], obtained by subtracting the electronic thermal conductivity estimated from the Wiedemann-Franz law from the measured total thermal conductivity. As for GeTe and GST, thermal conductivity of Sb_2Te_3 presents a strong anisotropy in directions parallel and perpendicular to the c axis as a consequence of the presence of weak bonds across the vdW gap. In Sb_2Te_3 the contribution of optical modes to the thermal conductivity is marginally more important than in the previous cases and contributes up to 35%.

3.4 InSbTe Alloys

The In-Sb-Te (IST) alloys have recently attracted a considerable interest for phase change memory applications as an alternative to the most widely used $Ge_2Sb_2Te_5$ compound because of its higher crystallization temperature. Moreover, they have been suggested as promising candidates for multi-level PRAM because IST alloys demonstrate a stable multi-phase change mechanism from the amorphous to a cubic phase, leading to multiple resistance levels.

$In_3Sb_1Te_2$ is particularly interesting because of its high melting temperature of about 650 °C [147], close to that of GST and an amorphous phase that shows a very high stability with a crystallization temperature T_x of about 292 °C [148] compared to the value of 120 °C of GST.

Moreover, $In_3Sb_1Te_2$ has recently been grown in form of nanowires within the Synapse project, opening the possibility of new developments in ultrascaled devices and core-shell multilevel memories.

3.4.1 Thermal conductivity of $In_3Sb_1Te_2$

$In_3Sb_1Te_2$ crystallizes in a rocksalt geometry with In fully occupying one sublattice and an expected disordered distribution of Sb and Te on the other sublattice. Such a high level of disorder can bring the lattice thermal conductivity to a value close to the minimal thermal conductivity as occurs in cubic and hexagonal $Ge_2Sb_2Te_5$ that also show a mostly random mass distribution in the Sb/Ge sublattice. Therefore, we computed phonon dispersion relations of crystalline $In_3Sb_1Te_2$ and we estimated k_{min} as given by Eq.3.3.

To this end we did not included explicitly the disorder but we modeled the disordered cubic phase by an ordered hexagonal 6-atom supercell mimicking the ABC stacking of atomic planes along the [111] direction of the cubic phase. The In-Sb-In-Te-In-Te- stacking was chosen. Calculations have been performed by means of DFPT and norm conserving pseudopotentials. Plane waves expansion of Kohn-Sham orbitals up to 35 Ry and the PBE [81] functional were used. The geometry of the unit cell was optimized by fixing the c/a ratio of the hexagonal cell in order to mimic the cubic-like geometry of the real disordered system. A 8x8x4 grid was used for the integration of the BZ and the semiempirical vdW [87] was used. The resulting equilibrium lattice parameter turns out to be 6.05 Å which is close to the experimental value of 6.126 Å [149]. The phonon dispersion relations for the model of crystalline $In_3Sb_1Te_2$, calculated starting from a 6x6x4 q-points mesh, are shown in Fig.3.23.

The transverse and longitudinal sound velocities averaged over the different directions of the Brilluoin Zone are v_T= 1900 m/s and v_L=3100 m/s respectively. By plugging in the Cahill

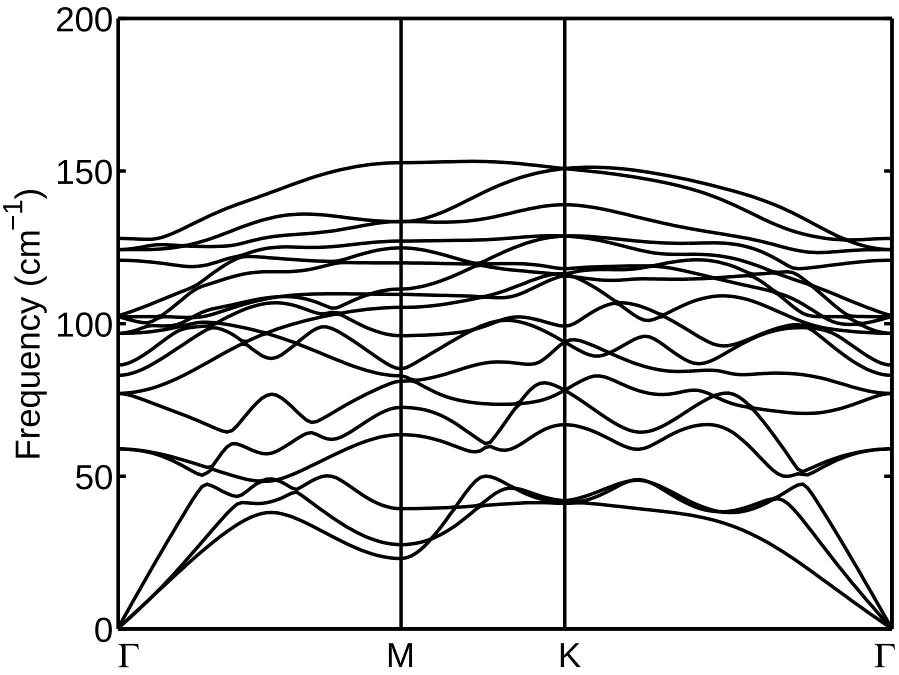

Figure 3.23: Phonon dispersions of $In_3Sb_1Te_2$ along high symmetry directions of the hexagonal cell calculated with PBE including vdW correction.

formula the resulting sound velocities and the atomic density, a minimum thermal conductivity of 0.42 W/m K at 300 K was obtained, which is much smaller than the electronic contribution of about 23 W/m K estimated from the measured electrical conductivity [150] of 3.2 10^4 S/cm at 25 °C and the application of the Wiedemann-Franz law. The lattice contribution to the thermal conductivity of crystalline $In_3Sb_1Te_2$ is therefore negligible.

3.5 Conclusions

In summary, the bulk thermal conductivity has been computed on the basis DFT calculations for crystalline GeTe, Sb_2Te_3 and GST. These calculations allowed us to identify the origin of the great variability in the experimental data for GeTe and the origin of the glass-like thermal conductivity in GST providing an indirect proof of the disordered structure of hexagonal $Ge_2Sb_2Te_5$. Thermal conductivity of GeTe has been computed also with a complementary method, using a Neural Network potential and non-equilibrium molecular dynamics simulations. These calculations proved on one hand the reliability of the NN potential in predicting thermal properties of crystalline GeTe and on the other hand supported the approximations used in the treatment of vacancies and disorder in the DFT calculations. Moreover, the MD simulations have also shown that non-linear effects in the thermal conductivity are negligible up to very high thermal gradients of about 30 K/nm such as those present in PCM devices. Finally, an estimate of thermal conductivity of $In_3Sb_1Te_2$ was also given based on the minimal thermal conductivity model and ab-initio phonons.

4 Thermal Boundary Resistance

The thermal boundary resistance (TBR) between the crystalline and the amorphous phase of the active medium and between the active medium in PCM and the surrounding dielectrics or metallic electrodes are crucial parameters for the control of thermal cross-talks with adjacent cells which may arise during memory programming. A large TBR can also lead to a reduction in the programming current thanks to heat confinement effects [118]. The complete electrothermal modeling of PCM operation requires the knowledge of the TBR at different interfaces which are often difficult to measure accurately at the operation conditions of the device.

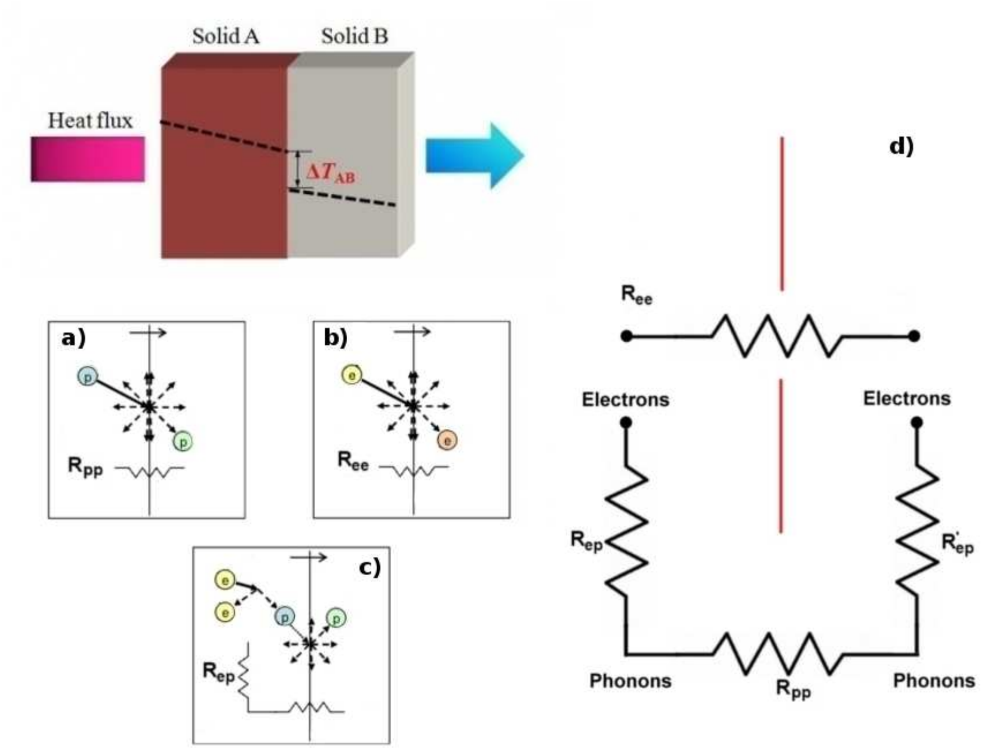

Figure 4.1: Thermal boundary resistance, defined as the temperature jump at the interface for a fixed heat flux, and the three mechanisms responsible for it: a) phonon-phonon contribution, b) electron-electron contribution and c) electron-phonon contribution. The sum of all the contributions are given as parallel and series resistances in panel d).

The TBR also named Kapitza resistance R between two media at the interface sketched in Fig. 4.1 is defined by $R = \frac{T_2 - T_1}{q}$ where T_1 and T_2 are the temperatures in the two media in proximity of the interface. In the most general case we would expect the presence of both electronic and lattice contributions to the TBR. In particular we would expect three processes to contribute to the thermal boundary resistance as shown in Fig.4.1a-c.

The first contribution comes inevitably at every interface due to mismatch in the vibrational modes of the two materials and the resulting phonon-phonon scattering (R_{pp}). The second contributions, important in the case of an interface between two good conductors is due to the direct transfer of heat from electrons crossing the interface and acts as a parallel channel of resistance (R_{ee}). The third contribution (R_{ep}), that can be seen as a resistance in series with the phonon-phonon channel, is particularly relevant at the interface between an insulator and a conductor. It originates from the fact that at the metallic side of the interface an energy transfer from electrons to ions has to take place to allow for the phonons to transfer heat across the junction.This is possible because a non-equilibrium steady state is established, in which the temperature of the electrons (T_e) is higher than the temperature of the ions (T_p) as sketched in Fig. 4.2.

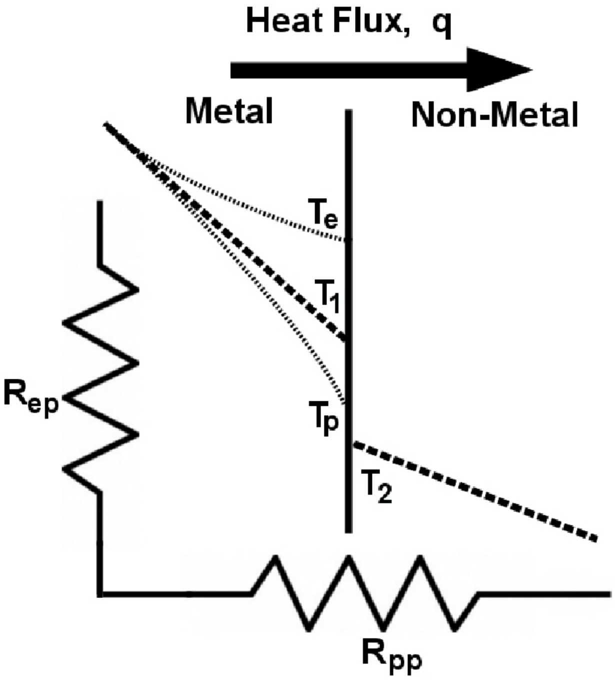

Figure 4.2: Temperature profile of the electrons (T_e) and ions (T_p) at the metal/non-metal interface crossed by a heat flux density q according to the theory of Majumdar and Reddy [59]. $R_{pp} = \Delta T_p/q = (T_p - T_2)/q$ is the phonon contribution to the total thermal boundary resistance $R = (T_1 - T_2)/q$. The electronic contribution due to electron-phonon coupling is $R_{ep} = (T_1 - T_p)/q$.

Majumdar and Reddy [59] developed a theory to cope with this effect that provides an expression for the thermal boundary resistance R given by the sum of a phononic (R_{pp}) and electron-phonon (R_{ep}) contribution:

$$R = R_{pp} + R_{ep} = R_{pp} + (\frac{\kappa_e}{\kappa})^{\frac{3}{2}} \sqrt{\frac{1}{G\kappa_{ph}}} \tag{4.1}$$

where $\kappa = \kappa_e + \kappa_{ph}$ is the total thermal conductivity, κ_e and κ_{ph} are the electronic and phononic contribution to the thermal conductivity, and R_{pp}= $\Delta T_p/q$ (Fig. 4.2).

R_{ep} is controlled by the parameter G, defined by $\frac{dE}{dt} = -G(T_e - T_p)$, where E is the electronic energy density and t is the time. The parameter G controls the electron to phonon energy transfer rate per unit volume, which depends on the electron-phonon coupling constant λ and on the electronic density of states (DoS) at the Fermi level $N(E_F)$ as [103]

$$G = \pi k_B \lambda \hbar < \omega^2 > N(E_F) \tag{4.2}$$

where $< \omega^2 >$ is the second moment phonon spectrum according to McMillan. At the contact between two metals an electron-phonon contribution to the TBR is present at both sides of the interface (R_{ep} and R_{ep}’) in Fig. 4.1

A microscopic insight into the different contributions to the TBR is of great relevance to aid the search for better performing materials for PCM and to engineer their properties. Unfortunately, this information can hardly be accessed experimentally. We estimated these different contributions for some of the most typical interfaces in PCM cells.To this end, we used DFPT calculations to estimate phonons and electron-phonon coupling to compute R_{ep}. The phonon-phonon contribution R_{pp} has been computed either with a phenomenological model, the diffuse mismatch model (DMM), briefly outlined in Sec.4.1.2 or by means of non-equilibrium molecular dynamics for the particular case of the amorphous/crystalline interface of GeTe for which a reliable interatomic potential is available (See Sec.2.6.1).

4.1 Thermal boundary resistance at $Ge_2Sb_2Te_5$ interfaces

$Ge_2Sb_2Te_5$ is the compound most widely used in PCM applications, the thermal boundary resistance at the interface between GST and other materials commonly present in the device is thus of great practical importance for the electrothermal modeling and for the performance improvement of the memory cells.

The hexagonal crystalline GST is a degenerate p-type semiconductor [141] in which heat is carried by both electrons and phonons. Therefore at the contact between hexagonal GST (hex-GST) and a dielectric, thermal resistance consists of the sum of the phononic (R_{pp}) and electron-phonon (R_{ep}) contributions which act as series resistances [59]. At the interface with a metal the direct electronic contribution R_{ee} is also in principle present.

Experimental data are actually available for the TBR at the interface of GST with silica [9] and with several metals including TiN and Al [54, 151] but no information is available on the relative contribution of phonons and electron-phonon coupling to the total thermal boundary resistance R.

The contribution to the TBR from electrons crossing the interface R_{ee} can be estimated from the measured electronic contact resistance and the interfacial Wiedemann-Franz law as $R_{ee} = \rho_c/(L_o T)$ where L_o is the Lorenz number (2.44 W Ω K^2) and T is the temperature and ρ_c the contact electric resistance (See Sec.1.2).

At the interface between hex-GST and the metals used in the devices (TiN or TiW) ρ_c is typically rather high (about 10^{-7} cm^2) as measured in Ref.[54, 152]. Thus the resulting values of R_{ee} are typically very large (10^3 m^2 K GW^{-1}) compared to R_{pp} and R_{ep} . The parallel channel for heat transfer given by R_{ee} can thus be safely neglected.

To gain microscopic insight into the different contributions to the TBR, we computed by DFPT the electron-phonon interaction in hexagonal GST which allows us to estimate the electron-phonon contribution to the TBR as described in Sec.4.1.1. The phononic contribution to the TBR at the interface with Al, TiN and amorphous silica is computed within the Diffuse Mismatch Model (DMM) [56] from the full phonon dispersion relations according to the theory developed of Chen [153] as briefly outlined in Sec.4.1.2.

4.1.1 Electron-phonon contribution to the thermal boundary resistance at the interface of GST with metals and dielectrics

In order to estimate the electron-phonon contribution to the TBR is essential to determine the electron cooling rate G given by Eq.4.2 which requires the knowledge of the density of states at the Fermi level and the electron-phonon coupling constant.

The electron-phonon coupling constant λ can be computed by means of DFPT as

$$\lambda = 2\int_0^\infty \frac{\alpha^2 F(\omega)}{\omega} d\omega \tag{4.3}$$

where $\alpha^2 F(\omega)$ is the Eliashberg spectral function which measures the contribution of phonons with frequency ω to the electron-phonon coupling:

$$\alpha^2F(\omega) = \frac{2}{\hbar N(E_F)}\sum_{\vec{q},\nu}\delta(\omega-\omega_{\vec{q},\nu})\times$$
$$\sum_{\vec{k},n,m}\delta(\varepsilon_{\vec{k},n}-E_F)\mid g^{n,m}(\vec{k}\vec{q}\nu)\mid^2\delta(\varepsilon_{\vec{k}+\vec{q},m}-E_F) \tag{4.4}$$

where the first sum runs over phonon bands at frequency $\omega_{\vec{q},\nu}$ while in the second sum the index n,m runs over electronic states at energies $\varepsilon_{\vec{k},n}$ and $\varepsilon_{\vec{k}+\vec{q},m}$. $N(E_F)$ is the electronic density of states of both spins per cell at the Fermi energy E_F and $g^{n,m}(\vec{k}\vec{q}\nu)$ is the electron-phonon matrix element. This is given in turn by

$$g^{n,m}(\vec{k}\vec{q}\nu) = \sqrt{\frac{\hbar}{2\omega_{\mathbf{q},\nu}}}\langle u_{\mathbf{k}+\mathbf{q},m}\mid M^{-\frac{1}{2}}\nabla V^{\mathbf{q}}_{\text{eff}}\varepsilon_{\nu\mathbf{q}}\mid u_{\mathbf{k},n}\rangle \tag{4.5}$$

where M is the atomic mass matrix, $u_{\mathbf{k},n}$ is the periodic part of the KS state, $\varepsilon_{\nu\mathbf{q}}$ is the normalized eigenstate of the dynamical matrix, and $\nabla V^{\mathbf{q}}_{\text{eff}}$ is the derivative of the Kohn-Sham effective potential with respect to the atomic displacement caused by a phonon with wavevector **q**. The Eliashberg function provides also the average phonon frequency according to McMillan entering Eq.4.2 as

$$<\omega^2>=\frac{\int \omega\alpha^2F(\omega)d\omega}{\int\frac{\alpha^2F(\omega)d\omega}{\omega}} \tag{4.6}$$

For the hex-GST, the electron-phonon matrix elements are computed by means of DFPT on a dense 64x64x32 **k**-points grid and a 64x64x32 **q**-point grid. The two δ functions containing the electronic energies were replaced by order one Hermite-Gauss smearing function with different value of variance ranging from 0.002 to 0.05 Ry [154].

We first considered the stacking proposed by Petrov with a p-doping of $3\cdot 10^{20}$ holes/cm^3 close to the experimental value (cf. Sec. 3.2.1). The electronic band structure and the electronic DOS close to the Fermi level are shown in Fig. 4.3 with $N(E_F)$=0.9257 states/(eV · cell).

The calculation of the electron-phonon coupling yields λ=0.11, and $(<\omega^2>)^{1/2}$=97.5 cm^{-1} from which we can estimate from Eq. 4.2 a value of G=$3.75\cdot 10^{15}$ W/(m^3 K). To obtain a fairly converged value, eliminating the dependence from $N(E_F)$, the value of λ is obtained by multiplying $\lambda/N(E_F)$ by a more accurate value of $N(E_F)$ computed using the tetrahedron method over a uniform 96x96x48 **k**-point mesh. We estimated a total error in λ below 11%. Note that a value of λ=0.1 for the similar hexagonal $GeSb_2Te_4$ was also estimated from experimental data on magnetoresistance [155].

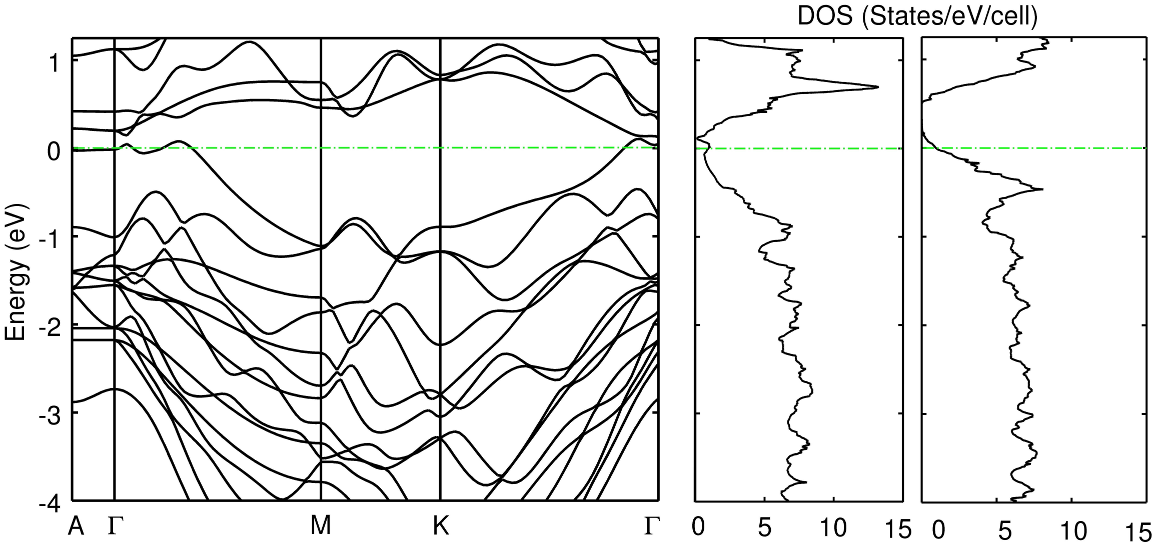

Figure 4.3: Electronic bands along the high symmetry directions of the Brillouin Zone of hexagonal $Ge_2Sb_2Te_5$ in the stacking of Ref. [70] with p-doping of $3 \cdot 10^{20}$ holes/cm^3. The Electronic density of states close to the Fermi level (zero of energy) of the optimized cell are reported in the central and right panel for the stackings of Refs. [70] (Petrov) and [138] (Kooi) respectively with the same p-doping used in the band calculation. The density of states at the Fermi level is $3.34 \cdot 10^{21}$ states/(eV cm^3) or $3.62 \cdot 10^{21}$ states/(eV cm^3) for the stackings of Ref. [70] (Petrov) or Ref. [138] (Kooi).

We also computed the value of $N(E_F)$ for the Kooi stacking (see Sec.3.2.1 and Ref. [138]). To this end the cell parameters have been optimized by including a van der Waals (vdW) correction according to Grimme [87] which ensures a stable structure as described in Sec.3.2.1. We got a value of $N(E_F)$=0.9404 states/(eV · cell). Thus, we obtained $N(E_F)$=$3.34{\cdot}10^{21}$ states/(eV cm^3) or $3.62{\cdot}10^{21}$ states/(eV cm^3) for the Petrov and Kooi stacking respectively, which assigns an uncertainty in $N(E_F)$ below 10 %.

By plugging in Eq. 4.1 the calculated value of G for the stacking of Ref. [70] and the experimental values for the electronic and phononic contributions to the thermal conductivity κ_e=0.87 W/m K and κ_p=0.42 W/m K from Ref. [54], we finally obtained an electronic contribution to the thermal boundary resistance of R_{ep}= 14.0 m^{2}K/GW. Actually κ_e is obtained in Ref. [54] from the electronic conductivity and the application of the Wiedemann-Franz law and κ_p is then obtained from the measured total thermal conductivity κ=κ_e+κ_p. The hole concentration in the hexagonal GST samples measured in Ref. [54] ranges from $8.2 \cdot 10^{19}$ cm^{-3} to $1.5 \cdot 10^{20}$ cm^{-3}. Note that, by assuming $\lambda/N(E_F)$ only slightly dependent on $N(E_F)$, the factor $(G\kappa_p)^{\frac{-1}{2}}$ in the expression for R_{ep} (cf. Eq. 4.1) scales as $N(E_F)^{-1}$ and thus only mildly on the hole concentration as $n_h^{-1/3}$. The value of R_{ep}= 14.0 m^{2}K/GW is in the same range of the experimental values for the TBR at the interface between hex-GST and TiN (12 ± 10 ^{2}K/GW) [54]. The electron-phonon contribution to the TBR is thus not negligible for GST.

As discussed in Sec.4.1 the electron-phonon contribution to the TBR inside good metals (R'_{ep}, cf. Fig. 4.2) like Al and TiN is negligible. The contribution to the TBR due to direct electron-electron coupling is also negligible as already stated in Sec.1.2 and thus the total thermal boundary resistance for all the interfaces that we considered reduces to the sum R=R_{ep}+ R_{pp}. In the next section, we report the calculation of the phonon contribution R$_{pp}$ which will provide the total TBR to be compared with experiments.

4.1.2 Lattice contribution to the thermal boundary resistance at the interface of GST with metals and dielectrics

The phonon-phonon contribution to the TBR, R$_{pp}$, has been computed with the phenomenological Diffuse Mismatch Model (DMM) by taking into account the full phonon dispersion according to the scheme proposed by Chen [153] to which we refer for all the details. This approximation yields $R_{pp} = 4/(T_{A\to B}\overline{Cv_{g_A}})$ where A and B refer to two media and $\overline{Cv_g}$ is group velocity v_g weighted by the phonon heat capacity averaged over all phonon bands as $\overline{Cv_g} = \sum_\nu \int_{BZ} \frac{d^3\mathbf{q}}{8\pi^3} \hbar\omega_\nu(\mathbf{q}) v_g(\nu,\mathbf{q}) \frac{\partial f_B(\omega_\nu(\mathbf{q}))}{\partial T}$ where f_B is the Bose function. The transmissivity $T_{A\to B}$ at the interface for phonons incident from medium A to medium B is written in turn [153] as $T_{A\to B} = \overline{Cv_{g_B}}/(\overline{Cv_{g_A}} + \overline{Cv_{g_B}})$.

To compute R_{pp} at 300 K, we used the DFPT phonon dispersion relations for GeTe, Al and TiN. Phonon dispersion relation were computed in the framework of DFPT as implemented in the Quantum-Espresso suite of programs [73] with the Perdew-Becke-Ernzerhof [81] functional for all the materials.

The lattice parameters, the hole concentration (0.084 holes/cell) and the details of the self-consistent and linear response calculations are the same as those reported in Sec.3.2.1.

We used a norm conserving pseudopotential for Al and Vanderbilt Ultrasoft [82] pseudopotentials for Ti and N. Kohn-Sham orbitals were expanded in a plane waves basis up to a kinetic cutoff of 20 Ry for Al and 30 Ry for TiN with a charge density cutoff of 450 Ry. The BZ integration for the self-consistent electron density was performed over a 12×12×12 Monkhorst-Pack (MP) mesh [135]. A Gausssian smearing of 0.05 Ry was used for Al and 0.02 for TiN.

Both Al and TiN crystallize in a fcc structure, the theoretical equilibrium lattice parameter resulted to be a=4.059 Å for Al and a=4.29 Å for TiN to be compared with an experimental lattice parameter of a=4.049 Å [156] and a=4.24 [157] Å.

The dynamical matrix was computed within DFPT on a 4x4x4 uniform q-points mesh in the BZ for Al, a 6x6x6 mesh for TiN.

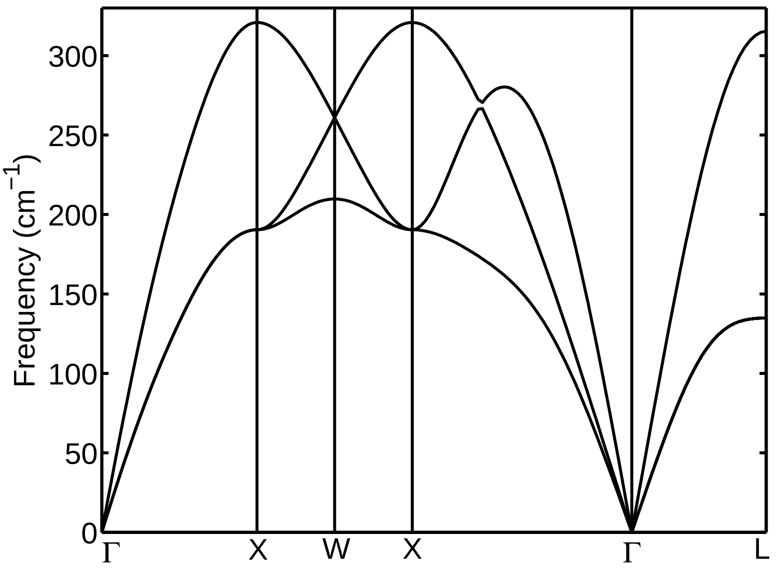

Figure 4.4: Phonon dispersion relaxation of Al along high symmetry directions.

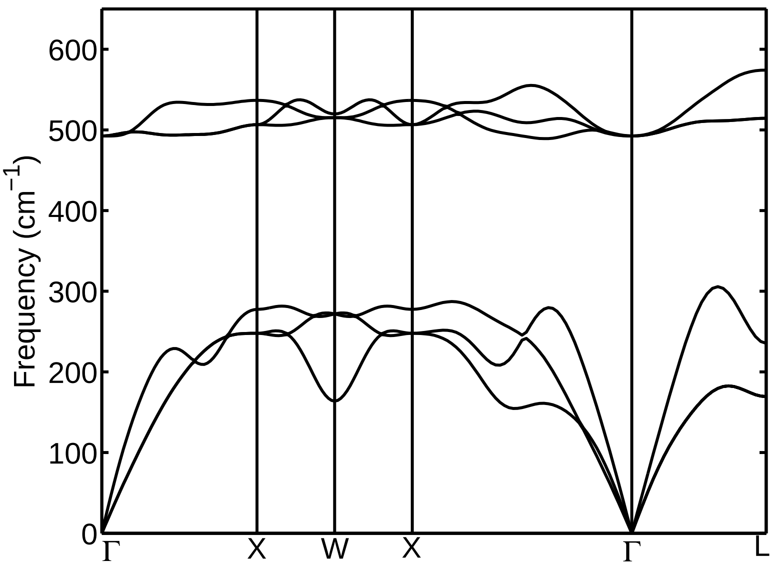

Figure 4.5: Phonon dispersion relaxation of TiN along high symmetry directions.

The resulting dispersion curves are reported in Fig. 4.4 and 4.5 for Al and TiN. For amorphous silica, which has a Debye temperature of θ_D=500 K [158] much higher than that of GST (136 K), we adopted the Debye approximation for the phonon density of states with the experimental transverse and longitudinal sound velocities of v_T=3.7 km/s and v_L=5.8 km/s [159] which yields $\overline{Cv}(T) \sim C(T)\bar{v_g} = 3(v_L + 2v_T)nk_Bx_D^{-3}\int_0^{x_D}\frac{x^4e^x}{(e^x-1)^2}dx$ where n is the atomic density, $x_D = \theta_D/T$ and T is the temperature.

To check the reliability of the Debye approximation for amorphous silica we compared the results of the Debye approximation with that of fully ab-initio calculation in the similar but more easily accessible system α-quartz.

For α-quartz we used the Local Density Approximation (LDA) to the exchange and correlation functional. Norm conserving and Vanderbilt Ultrasoft [82] pseudopotentials were used for Si and O. Kohn-Sham orbitals were expanded up to a kinetic cutoff 35 Ry with a charge density cutoff of 450 Ry. The BZ integration for the self-consistent electron density was performed over a $6 \times 6 \times 6$ mesh. The dynamical matrix was computed within DFPT on a 4x4x4 uniform q-points mesh in the BZ. The theoretical lattice parameters of quartz in the hexagonal (space group P 32 2 1) phase are a=4.89 Å c=5.41 Å to be compared with the experimental values of a=4.91 Å c=5.40 Å (exp. ref. [160]).

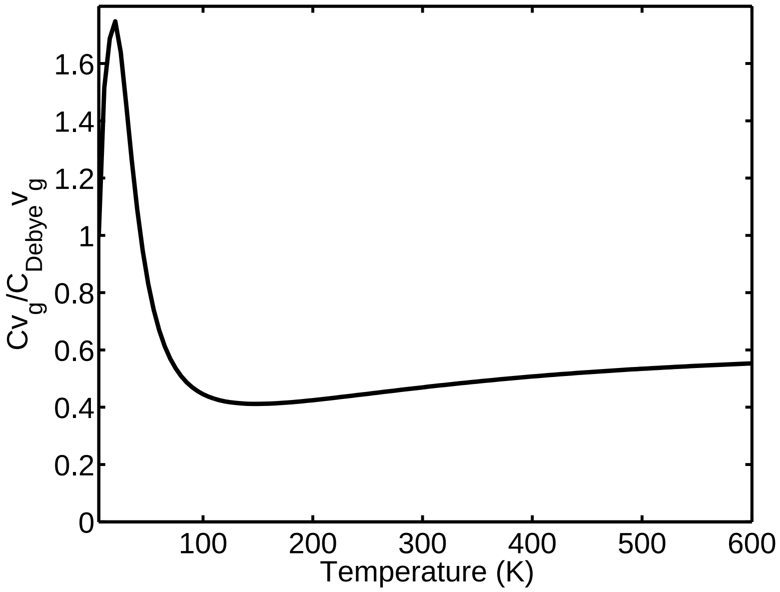

Figure 4.6: Ratio between $\overline{Cv_g}$ from full phonon calculation and Debye approximation for α-quartz.

In Fig. 4.6 we report the ratio between $\overline{Cv_g}$ values as a function of temperature for quartz computed from the full phonon dispersion relation and from the Debye approximation with the Debye temperature of 590 K and an average velocity of sound of 4890 m/s.

Even if, similarly, the use of the Debye approximation could introduce an error up to a factor 2 in the $\overline{Cv_g}$ of amorphous silica, it implies an error of at most 12% in the TBR between silica and GST.

The $\overline{Cv_g}$ values as a function of temperature for hex-GST, amorphous silica, Al and TiN are shown in Fig. 4.7.

The temperature dependence of the DMM contribution to the TBR for GST/Al, GST/TiN and GST/silica are reported in Fig. 4.8.

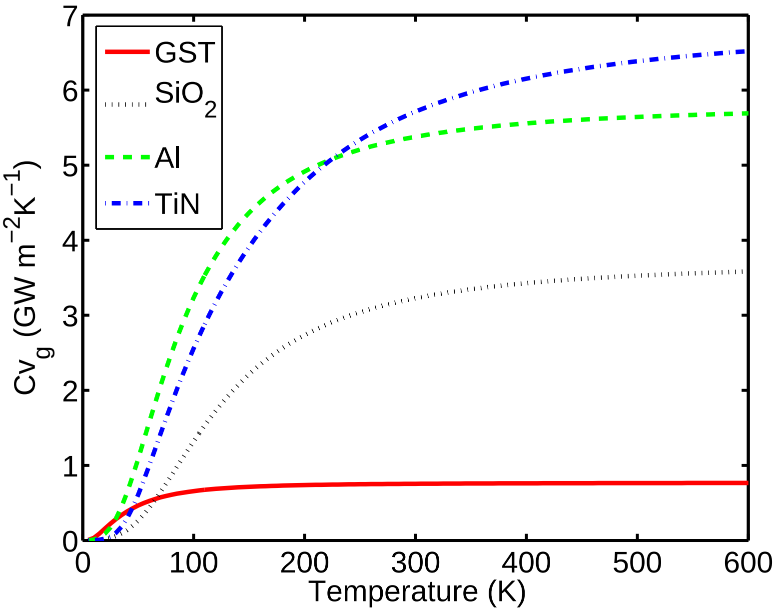

Figure 4.7: The $\overline{Cv_g}$ values as a function of temperature for quartz computed from the full phonon dispersion relation or within the Debye approximation

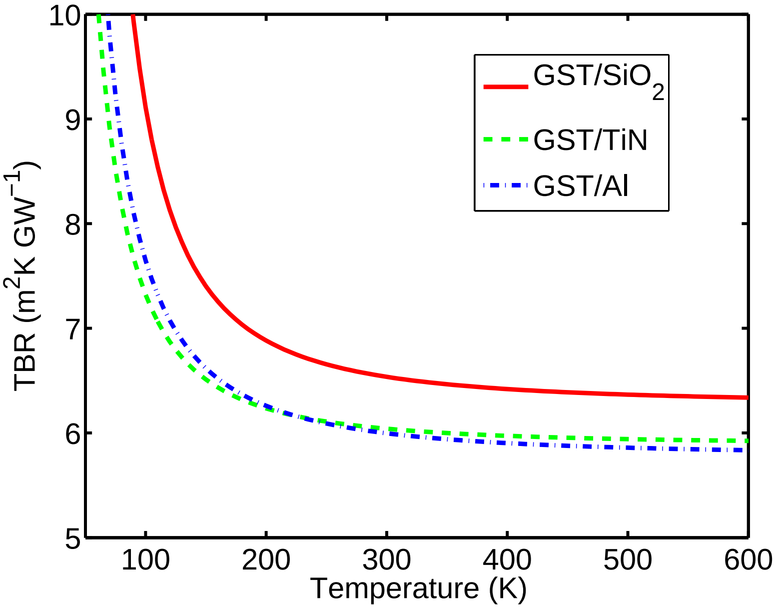

Figure 4.8: Temperature dependence of the phononic contribution to the thermal boundary resistance (TBR) at the GST/SiO_2, GST/Al and GST/TiN interfaces computed with the DMM model. The total TBR is obtained by summing the electron-phonon contribution of 14 m^2K/GW to all the curves.

Taking into account the values obtained above and the R_{ep} contribution calculated in the previous section the total TBR at 300 K is 20.1 m^2K/GW for hex-GST/silica, 19.8 m^2K/GW for hex-GST/Al, and 19.7 m^2K/GW for hex-GST/TiN. In the case of hex-GST/TiN the calculated TBR (19.7 m^2K/GW) is in very good agreement with the experimental value of 12 ± 10 m^2K/GW of Ref. [54]. In the case of the other two interfaces the theoretical TBR is largely lower than the experimental value of 80 ± 2 m^2K/GW for hex-GST/Al [151] and 116 m^2K/GW for hex-GST/SiO_2 [161].

It is worth noticing, however, that in the same experimental works a value of 6 ± 2 m^2K/GW for c-GST/Al [151] and of about 5 m^2K/GW for c-GST/SiO_2 [161] are reported. These values are very close to the R_{pp} contribution of about 5-6 m^2K/GW computed here from the DMM for the interfaces with hex-GST (cf. Fig. 4.8). Because of the similarities between the phonon spectra of the cubic and hexagonal phases, we might assume that the calculated values of R_{pp} might also apply to the interfaces with c-GST.

On the other hand a precise estimate of the R_{ep} contribution for c-GST is difficult because of the disorder in the cubic structure. However, we might take as a reasonable estimate for λ in c-GST the value of 0.1 obtained from magnetotransport measurement in cubic $GeSb_2Te_4$ in Ref. [155]. An electron density $N(E_F)$ of about $3.6 \cdot 10^{20}$/(eV cm^3) can be obtained in turn from the experimental hole concentration of $8 \cdot 10^{11}/cm^3$ [141] and the hole effective mass of 2.06 m_e obtained in Ref.[162] from DFT calculation of 270-atom supercell . By plugging in Eq. 4.2, these latter numbers for λ and $N(E_F)$ and from the experimental values of κ_e= 0.04 W/m K and κ_p=0.45 W/m K for c-GST [54] one obtain $R_{ep} \sim 2.3$ m^2K/GW for c-GST. The theoretical total TBR of about 8 m^2K/GW for c-GST/Al and c-GST/SiO_2 is thus in good agreement with the experimental vales [151, 161].

This means that the large underestimation of the TBR for the hex-GST/Al and hex-GST/SiO_2 interfaces must be actually traced back to a strong non-ideality of the real interfaces. As a matter of fact, the interfaces of Al and silica with hex-GST are obtained by heating the stacks initially formed with as-deposited amorphous GST. The amorphous phase first crystallizes at about 400 K into c-GST and then turns into hex-GST only above 580 K where sizable mass interdiffusion is expected to occur at the interface. Indeed, it was shown in Ref. [151] by using the DMM and a 2 nm thick interface the value of R_{pp} raised by an order of magnitude to about 100 m^2K/GW. A similar effect might occur at the hex-GST/SiO_2 interface.

4.2 Thermal boundary resistance at GeTe interfaces

We studied the interfaces between GeTe and the most common materials used for electrical contacts in the devices, such as TiN and Al, and surrounding dielectrics such as SiO_2.

Since crystalline GeTe is a degenerate p-type semiconductor, at the interface with a insulator like silica we have to consider two contribution to thermal boundary resistance, one coming form the phonon-phonon processes and the other due the electronic contribution which rise from electron-phonon coupling.

The same electron-phonon contribution is expected at the interface between amorphous and crystalline GeTe since the crystal is metallic while the amorphous is insulating. This interface can be considered as a prototypical example of the interfaces between the two states of the active media in PCM devices in which the TBR, especially due to the presence of the R_{ep} term, may not be negligible and might play and important role in the heat confinement during the formation of the amorphous dome.

At the interface between GeTe and a metal, another electron-phonon coupling term R'_{ep} arises in series with R_{ep} and R_{pp} (cf.4.1). In the case of a good metal, however, the electronic density of states $N(E_F)$ is large making R'_{ep} negligible with respect to R_{ep} and R_{pp} in GeTe as we have discussed in the previous section for GST. Finally the contribution of the parallel channel constituted by the direct electron-electron contribution R_{ee}, present only at the interface with a metal, could be estimated from the application of interfacial Wiedemann-Franz law once a measure of the electronic contact resistance is available. From the high value of electrical contact resistance given in Ref.[51] between GeTe nanowires and gold and the measurements of electrical contact resistance in similar materials such as GST [54] we assumed that the contribution from the electron-electron channel can be considered negligible also for the interfaces with bulk GeTe.

4.2.1 Electron-phonon coupling and electronic contribution to the thermal boundary resistance

To compute the electron phonon-coupling and hence the electron-phonon contribution to the TBR we used the PBE functional at theoretical equilibrium lattice parameters. The details of the calculation and the parameters used in the structural and phonon calculation are reported in Sec.3.1.1. We performed the calculations for the two extremes of holes concentration reported in literature n_{h1}=$8 \cdot 10^{19}$ holes/cm^3 and n_{h2}=$2.1 \cdot 10^{21}$ holes/cm^3. As previously described, the p-doping is introduced by removing electrons and by neutralizing the system with a uniform positive background. The electronic band structures and density of states corresponding to the two doping cases are reported in Fig4.9.

The electron-phonon matrix elements are computed by means of DFPT on a 6×6×6 **q**-point grid for the phonons and on a dense 132×132×132 **k**-points grid for n_{h1} and 96×96×96 **k**-point

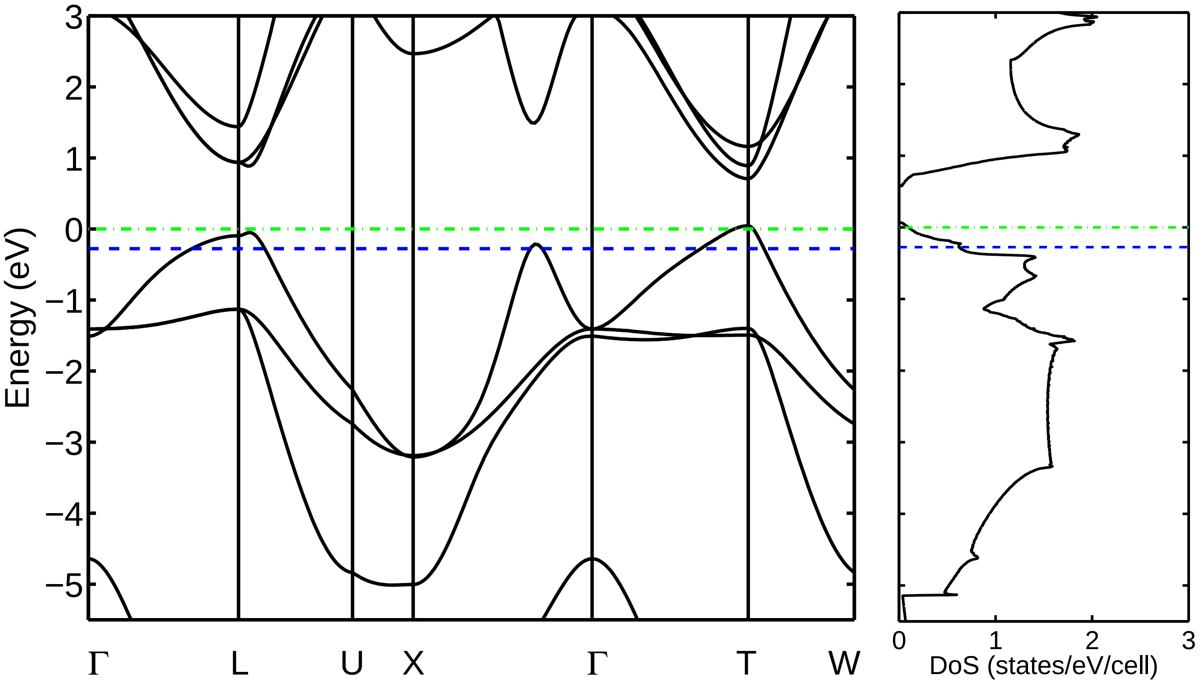

Figure 4.9: Electronic bands along high symmetry directions and electronic density of states (DoS) of trigonal GeTe. The DoS does not change by hole doping on the scale of the figure. The position of the Fermi level is indicated by a dot-dashed (dashed) line for hole concentration n_{h1}=8 $\cdot$ 10^{19} holes/cm^3 (n_{h2}=2.1 $\cdot$ 10^{21} holes/cm^3). The DoS has been computed with the tetrahedron method on a 160x160x160 mesh.

grid for n$_{h2}$ for the electrons. The two δ functions containing the electron band energies were replaced by order-one Hermite-Gauss smearing function with different value of variance ranging from 0.1 to 50 mRy [154]. Most of the variation of the value of λ with the size of **k** and **q**-point meshes can be ascribed to fluctuations in the density of states at the Fermi level. The quantity $\alpha^2 F(\omega)/N(E_F)$ thus converges faster with the size of the **k** and **q**-point meshes [163]. Then the value of λ is obtained by multiplying $\lambda/N(E_F)$ by a more accurate value of $N(E_F)$ computed using the tetrahedron method over a uniform $160\times160\times160$ **k**-point mesh. We estimated a total error in λ below 10% coming from the uncertainties in $\lambda/N(E_F)$ quantified by the convergence with respect to the smearing and the **k**-point meshes shown in Fig. 4.10.

The Eliashberg function and the phonon density of states are reported in Fig. 4.11 for the two doping levels. The electronic density of states (DoS) does not depend on the hole concentration in the range considered here as shown in Fig. 4.9. The average phonon frequency according to Eq. 4.6 is $(<\omega^2>)^{\frac{1}{2}} = 105.25$ cm^{-1} for n$_{h1}$=8 $\cdot$ 10^{19} holes/cm^3 and $(<\omega^2>)^{\frac{1}{2}} = 87.02$ cm^{-1} for n$_{h2}$. As shown in Fig. 4.9, an increase in n$_h$ simply shifts the Fermi level deeper in the valence band with no significant changes in the DoS. Integration of $\alpha^2 F(\omega)$ leads to very similar values of $\lambda/N(E_F)$ for the two doping levels, namely 0.816 (states/eV/cell)$^{-1}$ for both

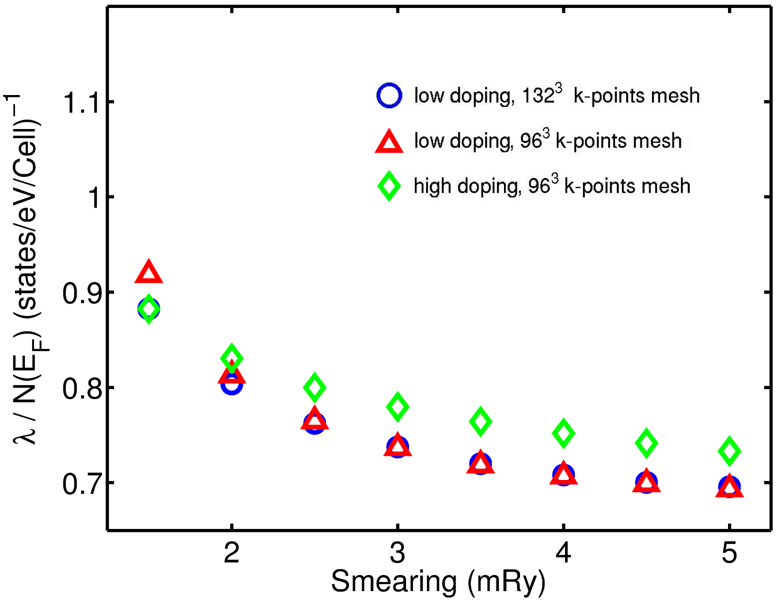

Figure 4.10: Dependence of the electron-phonon coupling constant $\lambda/N(E_F)$ on the smearing parameter (mRy) of the Dirac δ-functions in Eq. 4.4 for the low and high doping systems.

n_{h1} and n_{h2}. The DoS at the Fermi level is in turn 0.094 states/eV/cell and 0.632 states/eV/cell, which yields λ=0.077 for n_{h1} and λ=0.51 for n_{h2}. Since $\lambda/N(E_F)$ is poorly dependent of the hole concentration, it is possible to estimate the value of λ at different doping levels by multiplying our result for $\lambda/N(E_F)$ with the actual density of state at the Fermi level.

The parameter G (Eq. 4.2) has been computed for the two representative hole concentrations $n_{h1}=8 \cdot 10^{19}$ holes/cm^3 and $n_{h2}= 2.1 \cdot 10^{21}$ holes/cm^3 (cf. [130, 131]) from the value of λ and $\langle\omega^2\rangle$ discussed above. The values of G is $1.43 \cdot 10^6$ GW/(m^3 K) for n_{h1} and $4.5 \cdot 10^7$ GW/(m^3 K) for n_{h2} . By using the phononic thermal conductivity $\kappa_{ph} \sim 3.2$ W/m K as calculated in Sec.3.2.2, the ratio κ_e/κ can be chosen such that the prefactor $(\kappa_e/\kappa)^{\frac{3}{2}}$ in R$_{ep}$ (cf. Eq. 4.1) is in the range $0.080 < (\kappa_e/\kappa)^{\frac{3}{2}} < 1$ where the lower extreme corresponds to the low value of κ_e=0.73 W/m K for the sample measured in Ref. [51]. By plugging these numbers into formula 4.1, R_{ep} falls in the range 1.2-14.8 m^{2}K/GW for n_{h1} and 0.21-2.6 m^{2}K/GW for n_{h2}.

Note that the sample with hole concentration $n_{h1}= 8 \cdot 10^{19}$ holes/cm^3 measured in Ref. [130] displays an electrical resistivity of $\rho=1.4 \cdot 10^{-4}$ Ω cm while in another work [164] Hall measurements on samples with the same resistivity of about $\rho=1.4 \cdot 10^{-4}$ Ω cm yielded a much higher hole concentration of $8 \cdot 10^{20}$ holes/cm^3 due to a different hole mobility. In fact, it was shown (see Figs. 1 and 2 in Ref. [165]) that the resistivity is not a monotonic function of the Hall carrier density [165]. Note that different holes pockets with different effective masses are progressively filled by increasing the hole content (cf. Fig. 4.9) which also opens new channels for intervalley scattering.

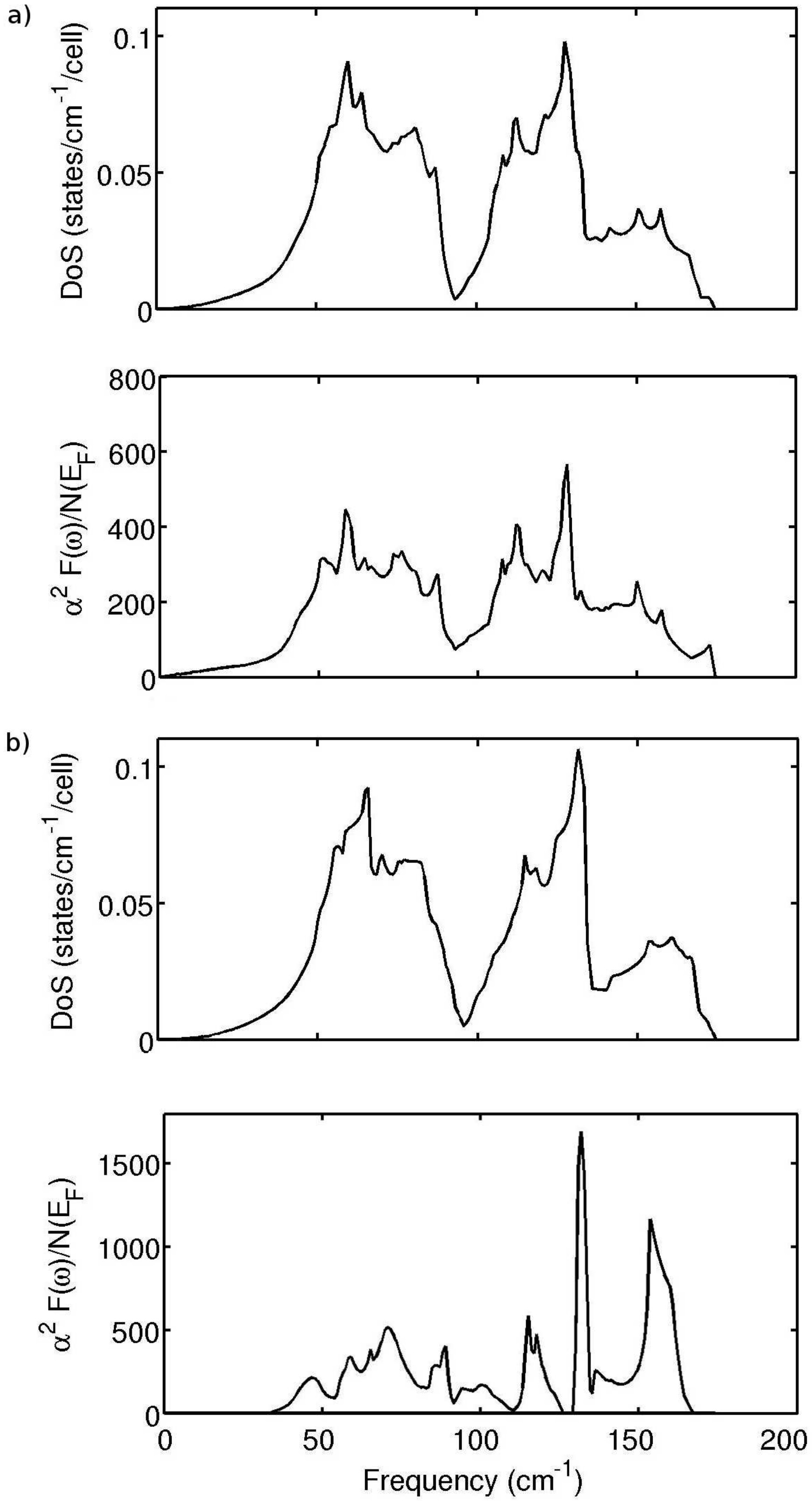

Figure 4.11: Phonon density of states (DoS) and Eliashberg function $\alpha^2 F(\omega)/N(E_F)$ (states/cm^{-1}/cell)$^{-1}$ for GeTe with hole concentrations of a) n_{h1}=$8\cdot10^{19}$ holes/cm^3 and b) n_{h2}=$2.1\cdot10^{21}$ holes/cm^3.

The estimate of R_{ep} for a specific sample thus requires the measurements of both n_h (or $N(E_F)$ by whatever means) and κ_e eventually from ρ and the application of the Wiedemann-Franz law. For the specific sample of Ref. [130] for which both n_h ($8 \cdot 10^{19}$ holes/cm^3) and ρ ($1.4 \cdot 10^{-4}$ Ωcm) are known we can estimate κ_e=5.22 W/m K from the Lorenz number L_o= $2.44 \cdot 10^{-8}$ WΩ/K and κ_e=L_oT/ρ for T=300 K, which finally yields R_{ep}= 7 m^{2}K/GW. This value is of the same order of magnitude of the TBRs measured at the interface between phase change materials like GST and metals and thus it is not a negligible quantity. Just to give a term of comparison a TBR of 10 m^{2}K/GW is equivalent in thermal resistance to 14 nm of silica or 190 nm of TiN.

4.2.2 Lattice contribution to the thermal boundary resistance between GeTe and electrodes or dielectrics

To give a complete picture of the TBRs in a device we computed the phononic contribution R$_{pp}$ for the three interfaces GeTe/Al, GeTe/TiN and GeTe/silica. The first two are common materials for the electric contacts and the heater while the last one is the material in which the active medium is commonly embedded. As for GST we used the diffuse mismatch model outlined in Sec.4.1.2 to estimate R$_{pp}$. The computational details for GeTe are the same reported in Sec.3.1.1 while the details for Al, TiN and silica are reported in Sec.4.1.2.

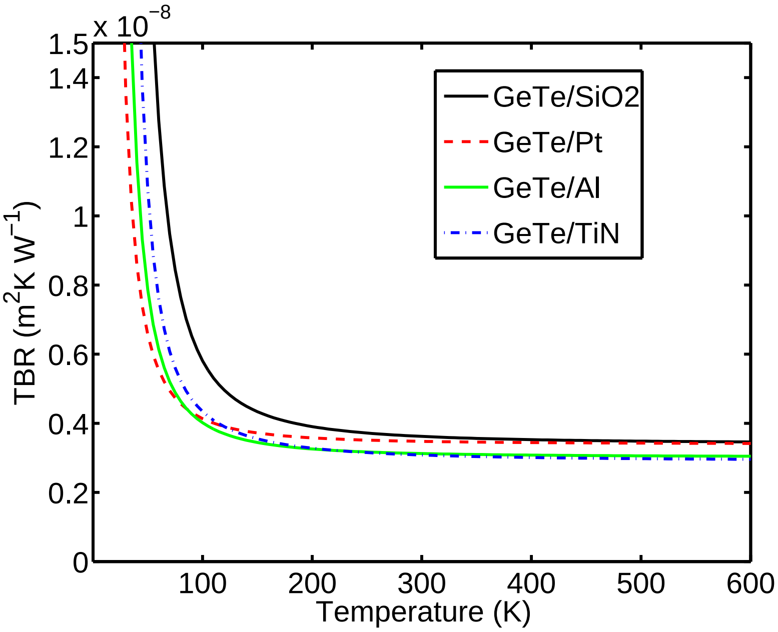

Figure 4.12: Temperature dependence of the phononic contribution to the thermal boundary resistance (TBR) at the GeTe/SiO$_2$, GeTe/Al and GeTe/TiN interfaces computed with the DMM model.

The results for the phonon-phonon contribution to the TBR for GeTe/Al, GeTe/TiN, and GeTe/silica, calculated within DMM contribution are reported as a function of temperature in Fig. 4.12. Summing up the electron-phonon contribution calculated in the previous section we can thus estimate a total thermal boundary resistance between 6 and 12 m^2/GW. The only experimental data available are the measurement of a total TBR of 80 m^2/GW relative to the GeTe/SiO_2 interface reported in Ref.[51]. The large value observed experimentally might be ascribed to a bad quality of the interface as discussed in Sec.4.1 for the interfaces of GST.

4.2.3 Thermal boundary resistance at crystalline/amorphous GeTe interface.

In Sec.4.2.1 we have estimated a non-negligible contribution to the TBR in GeTe and GST from the electron-phonon term. Since this term is also present at the interface between crystalline and amorphous phases the total TBR among these two phases of the same material cannot be neglected. Moreover a lattice contribution could stem from the mismatch in the vibrational modes of the two phases. In the case of GeTe, the phonons of the amorphous phase display a softening in the acoustic branches, with respect to the crystal, due to a lower density and a stiffening in the highest frequency region due to the appearance of phonons at about 200 cm^{-1}, localized on the $GeTe_4$ tetrahedra [12, 30, 166]. Furthermore, while in crystalline GeTe the thermal conductivity is due to propagating phonons that can be described within the Boltzmann transport equation, in the amorphous phase the heat carriers are mostly non-propagating delocalized vibrations (diffusions) [116, 137].

Since for GeTe we had a reliable potential [12] able to accurately describe the interactions in every GeTe phase and the interplay different phases, we opted for a direct simulation of the GeTe crystalline/amorphous interface.

To study the lattice contribution to the TBR we used the RNEMD scheme proposed by Müller-Plathe [11] described in Sec2.5. The simulations were performed with the NN code RuNNer [74] by using the DL_POLY v2.19 [75] code as MD driver. The time step was set to 2 fs.

We considered two interfaces, one lying on the (0001) crystalline plane and a second in the $(2\bar{1}\bar{1}0)$ crystalline plane in the hexagonal notation for the GeTe crystal. For the (0001) interface we used a supercell with dimensions of 50.1 Å x 49.6 Å x 348.5 Å made by a junction between a 28.6 Å x 24.8 Å x 249.5 Å cell of the bulk crystal and a 28.6 Å x 24.8 Å x 99.3 Å cell of the bulk amorphous phase. The length along the *z* direction of the amorphous and crystalline regions is comparable to the typical size of an ultra-scaled PCM device. In order to allow the interface to adjust, the supercell was then annealed at 500 K for 20 ps and then quenched again at 300 K in 20 ps. We considered the ideal stoichiometric compound, without defects.

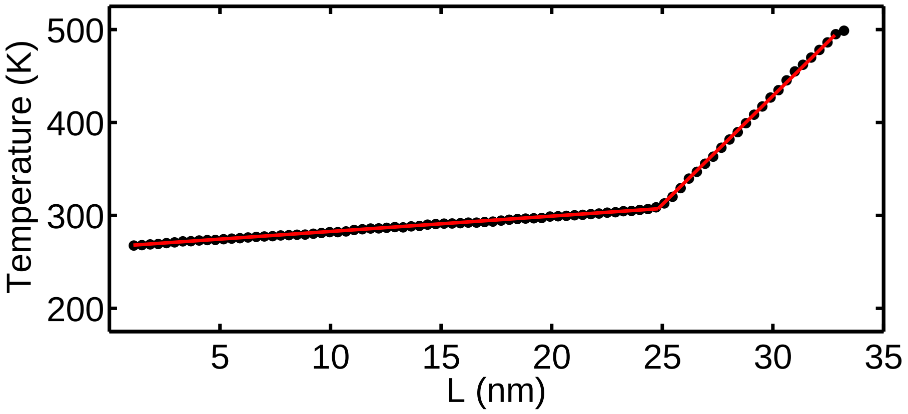

Figure 4.13: Temperature profile in the NEMD simulation of the junction between the amorphous and crystalline phases of GeTe. The heat sink and source are separated by 33 nm. The interface lies on the (0001) crystalline plane in the hexagonal notation. The heat flux is $1.62 \cdot 10^{-8}$ W.

The steady temperature profile reached in about 2.2 ns of simulation is shown in Fig. 4.13. A temperature jump at the interface can not be clearly identified in Fig. 4.13. If any, it is smaller than the temperature fluctuations still present in the model due to its finite size. We repeated the simulations for the $(2\,\bar{1}\,\bar{1}0)$ plane with similar results. We can thus set an upper limit to R_{pp} for both interfaces of about only 2 m^{2}K/GW. The dominant contribution to the TBR of the amorphous/crystalline interface of GeTe is thus due to electron-phonon interactions yielding a value of 7 m^{2}K/GW.

4.3 Conclusions

Atomic simulations allowed to identify the different contributions to the TBR at the interface between GST and GeTe with metals and dielectrics in PCM devices. Due to the low but not negligible metallicity of GST and GeTe, a large contribution to the TBR arises from the electron-phonon coupling (R_{ep}). The sum of the R_{ep} term with the phononic contribution (R_{pp}) computed from DFPT phonons within the diffuse mismatch model provides a good agreement with experiments for the TBR at the interfaces of hex-GST with Al and TiN of c-GST with Al and silica. A bad agreement between theory and experiments for other interfaces can be ascribed to non-idealities (such as interdiffusivity or roughness) of the interface. The theoretical value of R_{ep}+R_{pp} computed here thus represent a lower bound for the actual interfaces.

5 Surface phonons of Sb_2Te_3 and Bi_2Se_3

Besides being a fundamental building block of chalcogenide alloys exploited as phase change materials and a well known thermoelectric, Sb_2Te_3 has recently attracted a huge interest since it is, together with Bi_2Se_3 and Bi_2Te_3, one of the first materials theoretically predicted and experimentally confirmed [167] to be 3D topological insulators (TI). Topological insulators are a new class of material that exhibits unique properties: they present a complete band gap in the bulk but develops topologically protected metallic states at surface whose presence and properties can be inferred exclusively from the bulk band structure in which the strong spin-orbit coupling gives rise to a non-trivial order of the bands [168, 169].

These surface states, that appears like a Dirac cone around the Γ-point, have a particular spin texture (cf. Fig.5.1) responsible for peculiar properties such as relative insensibility to surface details and protection against backscattering by non-magnetic impurities [168, 169].

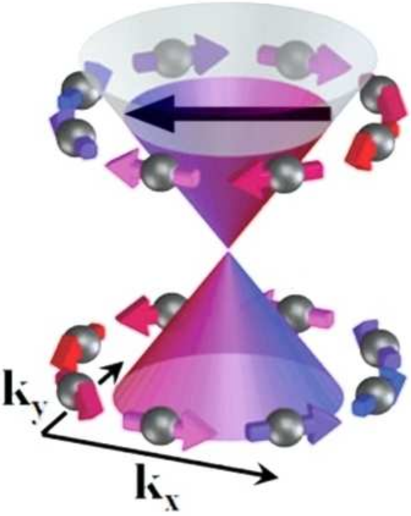

Figure 5.1: Spin texture of the surface Dirac cone of a 3D topological insulator. The black arrow indicate one of the equivalent nesting vectors that connects two sides of the Fermi surface (line).

Electron-phonon interaction mediated by spin-orbit coupling is supposed to be the most relevant scattering process for these states of interest for spintronic applications. The interest in the determination of the interaction of topologically protected states with phonons motivated an increasing number of experimental and theoretical works. However, the conclusions drawn in these works are not unique: Angle Resolved Photoemission Spectroscopy (ARPES) data [170–172] and some theoretical works [173, 174] suggested a very small electron-phonon coupling but surface phonons at the Bi_2Se_3 (0001) surface measured with helium atom scattering (HAS) and reported in Fig.5.2 revealed a feature in the dispersion relations interpreted as a Kohn anomaly which would suggest the presence of a strong electron-phonon coupling [175, 176].

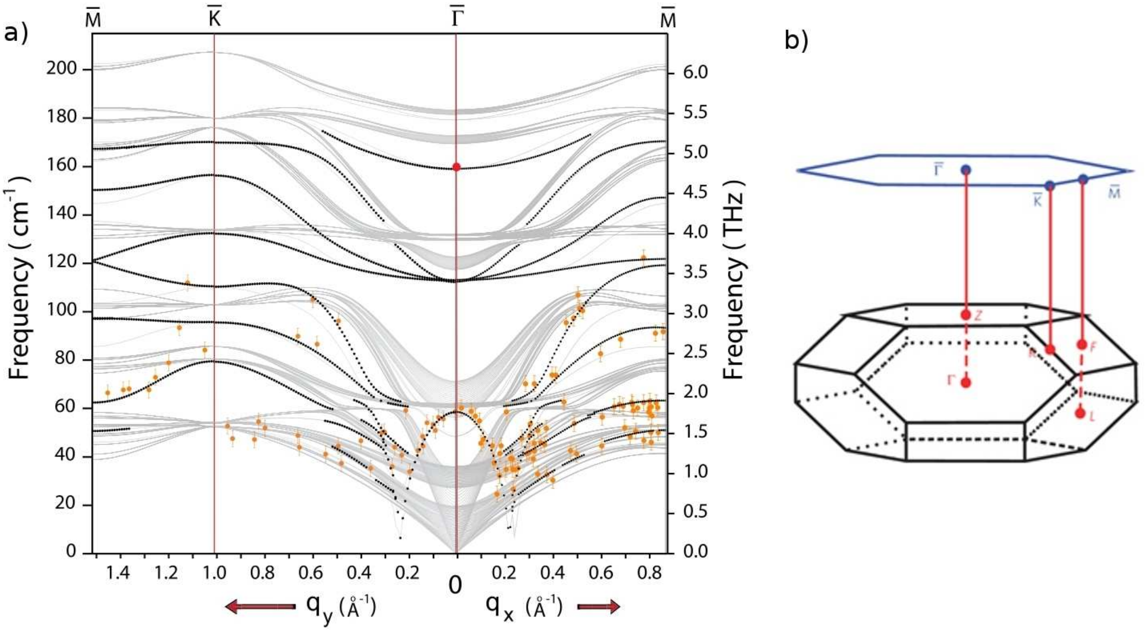

Figure 5.2: a) Experimental HAS data (points) measured in Ref. [175]. for Bi_2Se_3 (0001) surface. The lines are the results of an empirical bond-charge model. A scheme of the bulk and surface projected Brillouin zone is reported in panel b).

To asses the presence and the origin of the proposed anomaly we calculated the phonon dispersion relation of Bi_2Se_3 (0001) surfaces by means of density functional perturbation theory. For the sake of comparison we computed surface phonons of the Sb_2Te_3 (0001) surface as well for which experimental data are not available.

5.1 Sb_2Te_3 and Bi_2Se_3 (0001) Surfaces

Sb_2Te_3 and Bi_2Se_3 share the same rhombohedral crystal structure described in Sec.3.3.1 that can be seen as blocks of five hexagonal layers stacked in the sequence Te(Se)-Sb(Bi)-Te(Se)-Sb(Bi)-Te(Se) linked to the other blocks by weak vdW interactions.

We studied the dynamical properties of Sb_2Te_3 and Bi_2Se_3 (0001) surfaces in hexagonal notation by means of density functional perturbation theory. Norm conserving pseudopotentials were used for all the elements, the local density approximation (LDA) [79] for the exchange-correlation energy functional was used for Bi_2Se_3 while the PBE approximation [81] was found to produce better results for Sb_2Te_3. The theoretical equilibrium lattice parameters were used. The lattice parameters of Sb_2Te_3 have already been reported in Sec.3.3.1 while for Bi_2Se_3 we obtained a=4.10 Å and c=28.33 Å to be compared with the experimental values of a=4.14 Å and c=28.64 Å [156].

Spin-orbit effect are treated self-consistently with fully relativistic pseudopotentials and the formalism for non-collinear spin magnetization. The Khon-Sham orbitals were expanded in plane waves up to an energy cutoff of 35 Ry. The surface was modelled by a slab geometry with 15 layers i.e. 3 quintuple layers (QL) and a vacuum region 20 Å wide. The surface Brilloin zone (SBZ), if not specified differently, was sampled over a 8x8x1 Monkhorst-Pack grid and the dynamical matrix was calculated on a 6x6x1 mesh of q-points. The surface atomic positions were relaxed until forces became lower than 0.1 mRy/a.u..

The electronic band structure of the slabs calculated with and without spin-orbit coupling (SOC) is shown in Figs.5.3a and 5.3b for Sb_2Te_3 and Bi_2Se_3 respectively.

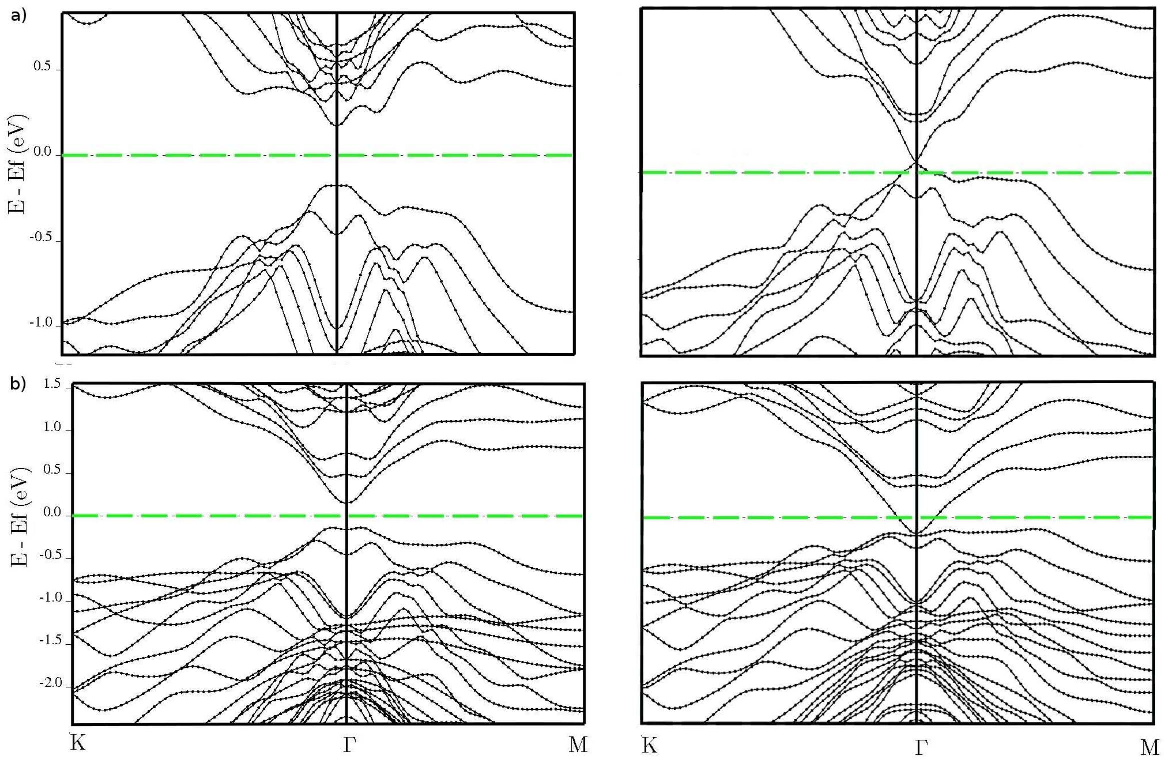

Figure 5.3: Surface electronic bands of (a) Sb_2Te_3 and (b) Bi_2Se_3 omitting (left) and including (right) spin-orbit coupling.

A small amount of additional charge of -0.03 electron/cell and 0.02 electron/cell was added in order to reproduce the typical position of the Fermi level reported in [177] and [171] measured by ARPES. Without SOC the Sb_2Te_3 and Bi_2Se_3 are insulators even at the surface with a band gap respectively 0.25 eV and 0.35 eV wide. By including SOC both materials present the gapless, spin-polarized and Dirac cone shaped surface bands around the Γ-point, typical of 3D topological insulators [168, 169].

We first computed the phonon dispersion relations without the SOC. These are shown in Fig.5.4 for Sb_2Te_3 and in Fig.5.6 for Bi_2Se_3, with phonon densities projected on the first, second and third layer.

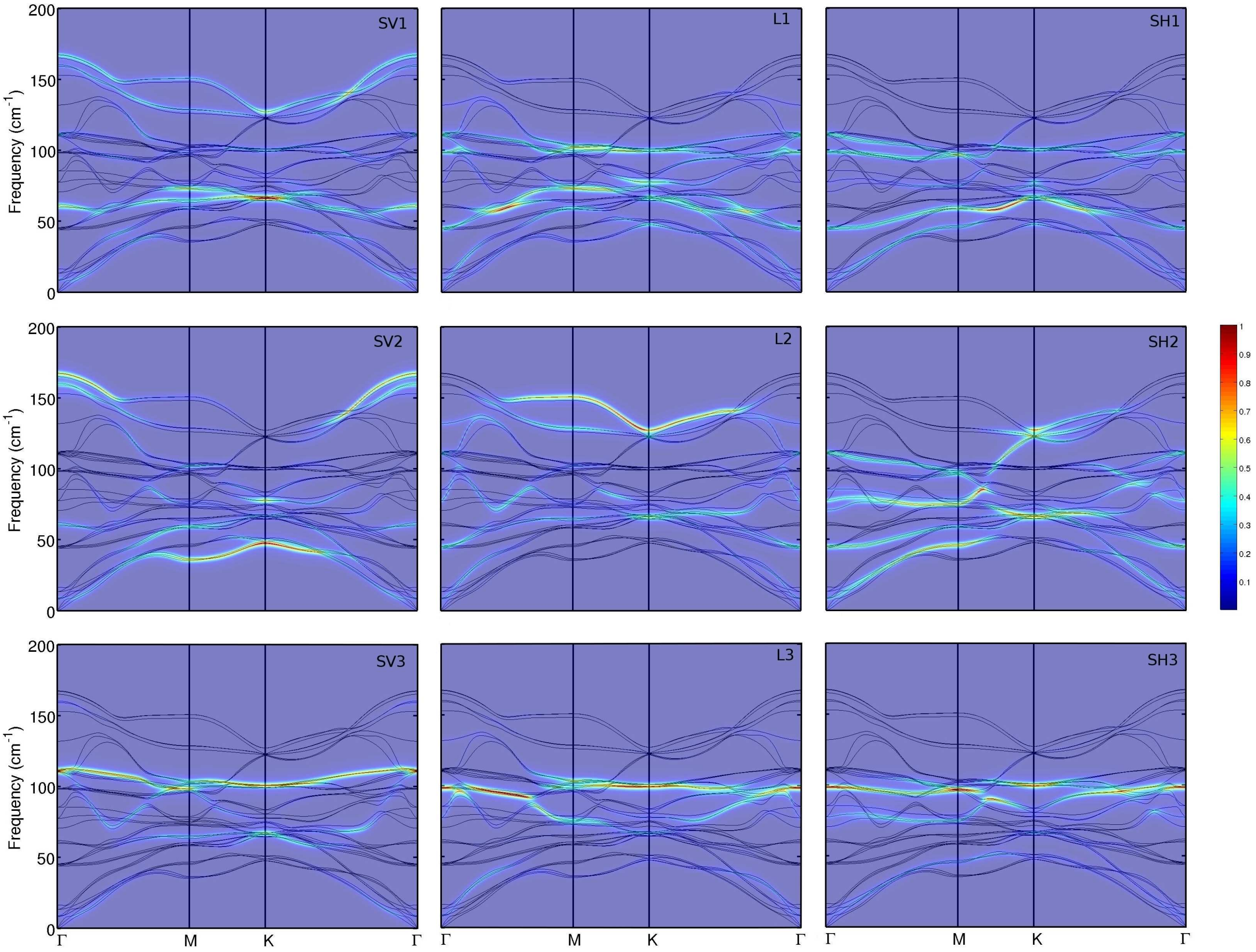

Figure 5.4: Surface phonons of Sb_2Te_3 omitting spin-orbit coupling. The colors represent the projections on the first, second and third layers according to the different polarizations: shear vertical (SV), longitudinal (L) and shear horizontal (SH).

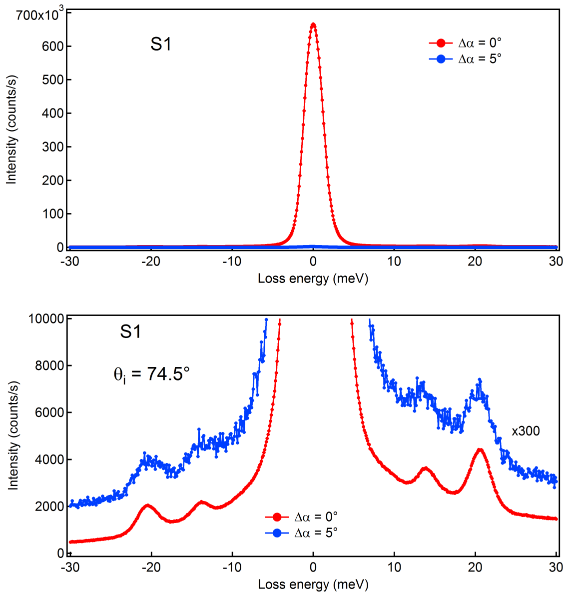

Figure 5.5: Experimental data for Sb_2Te_3 (0001) surface obtained by HREELS. Courtesy of A.Politano and V.de Renzi. The two curves in the bottom panel correspond to two different momentum transfers corresponding to the Γ-point and a neighboring point along the ΓM direction.

The surface spectra of Sb_2Te_3 is rather complex, at the topmost part of the spectra at Γ we can find a mode that is mostly shear vertical polarized and localized on the first and the second layer with a frequency of 170 cm^{-1}; at approximately 1/2 of the ΓM direction and at 1/3 of the ΓK it changes character becoming longitudinally polarized and completely localized on the second layer. Two strong resonances are present in the middle part of the spectrum: the first one starting at 113 cm^{-1} at the Γ-point and almost dispersionless and completely localized in the third layer and has a purely shear vertical polarization near the Γ-point that turns into a mixed shear-vertical and longitudinal polarization at the zone boundary. The second one, also mainly localized on the third layer, starts at 101 cm^{-1} with a mixed longitudinal and shear horizontal character that gradually gives way to a prevalently longitudinal polarization after an avoided crossing with the upper resonance. At low energies the main features are a nearly flat, shear-vertical mode at 60.5 cm^{-1} involving mainly the first layer and, at the lowermost end of the spectrum, a shear-vertical mode localized in the second layer that exhibits the typical behavior of the Rayleigh wave but for the unusual localization on the second layer. At the best of our knowledge there are not experimental measurements for Sb_2Te_3 surface phonons in literature to compare with. Recent unpublished high resolution electron energy loss spectroscopy (HREELS) measurements, performed by the group of V. DeRenzi with the collaboration of A. Politano, at and close to the Γ point are reported in Fig.5.5. The frequencies of the two features clearly visible in the spectra fairly agree with those of the theoretical highest, shear vertical mode at 170 cm^{-1} and of the strong resonance at 113 cm^{-1}.

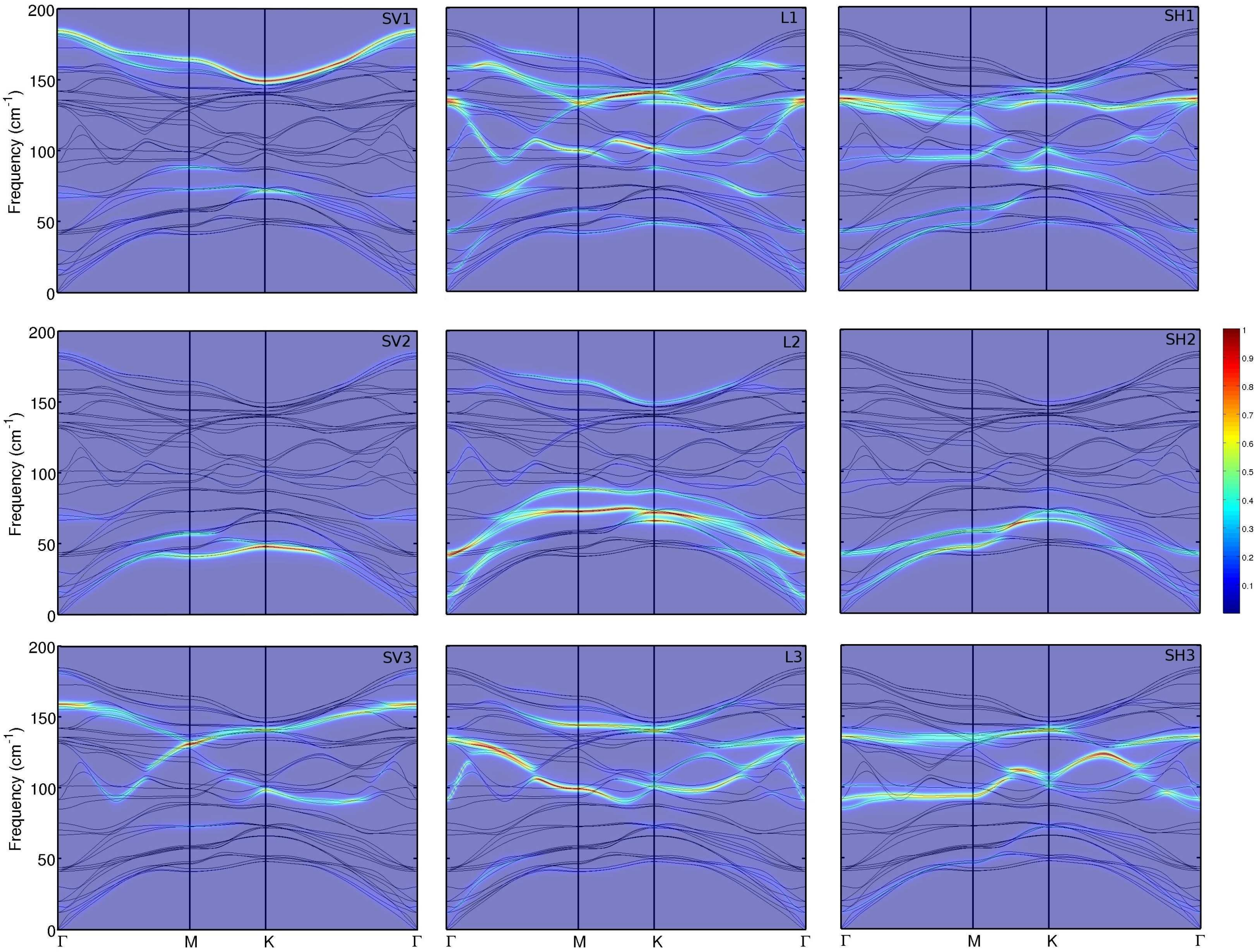

Figure 5.6: Surface phonons of Bi_2Se_3 omitting spin-orbit coupling. The colors represent the projections on the first, second and third layers according to the different polarizations: shear vertical (SV), longitudinal (L) and shear horizontal (SH).

The results for the surface phonon spectra of 3QL of Bi_2Se_3 are very similar to those obtained using one and two QL in Ref. [178]. The upper part of the spectrum is dominated by the modes involving the lighter Se atoms. Purely shear vertical vibrations of the outermost Se layer give rise to the highest energy mode (185 cm^{-1} at Γ), clearly visible also in the experimental HREELS data reported in Fig.5.7 with an energy of 23 meV ($\approx$ 185.5 cm^{-1}). The shear vertical vibrations of Se atoms which compose the third layer, partially hybridized with longitudinal modes of the first give rise to a sharp resonance around 153 cm^{-1}. Longitudinal modes localized in the third layer give rise to two bands that cross almost all the SBZ. One moves from 137 cm^{-1} at Γ down to 88 cm^{-1} along the MK direction, while the other, evident only at the zone border, is almost flat with an energy around 145 cm^{-1} . Finally shear-horizontal modes

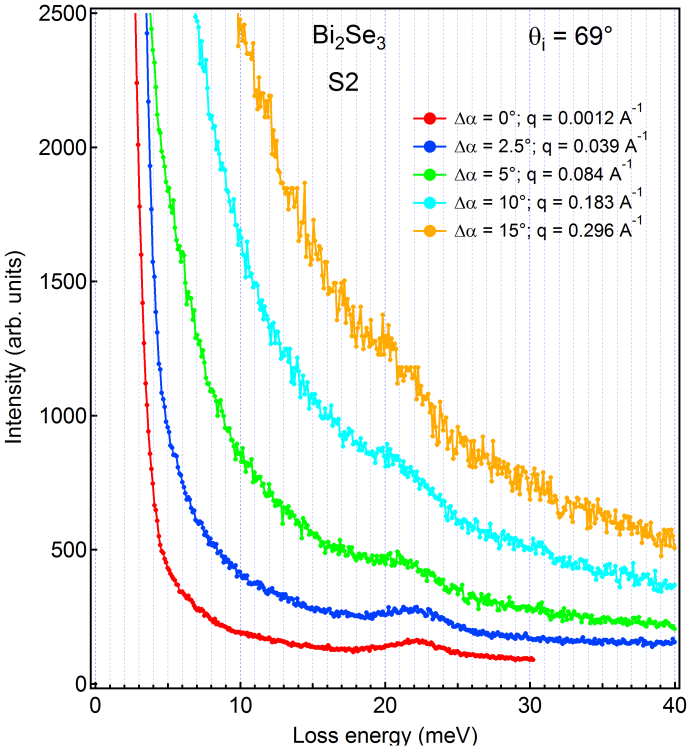

Figure 5.7: Experimental data for Bi_2Se_3 (0001) surface obtained by HREELS. Courtesy of A. Politano and V. De Renzi. The curves correspond to different momentum transfers corresponding to the Γ-point and neighboring points along the ΓM direction reported in the legend.

of the Se atoms in the first and third layer give rise to a broad resonance at 129 cm^{-1} and two narrow bands around 133 cm^{-1} and 97 cm^{-1} that are nearly dispersionless along the ΓM direction while they exhibit an avoided crossing along the ΓK. Modes related to the Bi atom are clustered at low energy. In particular a shear vertical mode can be highlighted at the lower end of the spectrum with a strong projection on the second layer for large q vectors that, as in the case of Sb_2Te_3 can be ascribed to the Rayleigh wave. These low energy modes could account for almost all the experimental data obtained by means of HAS in Ref.[175] (cf. Figs. 5.8, 5.9). The lowest energy data, in particular along the ΓM direction can be ascribed to a mostly shear vertical vibration of the second layer while most of the points with slightly higher energy can be assigned to two broad longitudinal resonances localized on the bismuth atoms. The feature ascribed to the strong Kohn anomaly in Ref.[175] seems to fell in a region where there is no evidence of surface modes but for a shallow shear vertical resonance on the first and second layer with a slightly higher frequency.

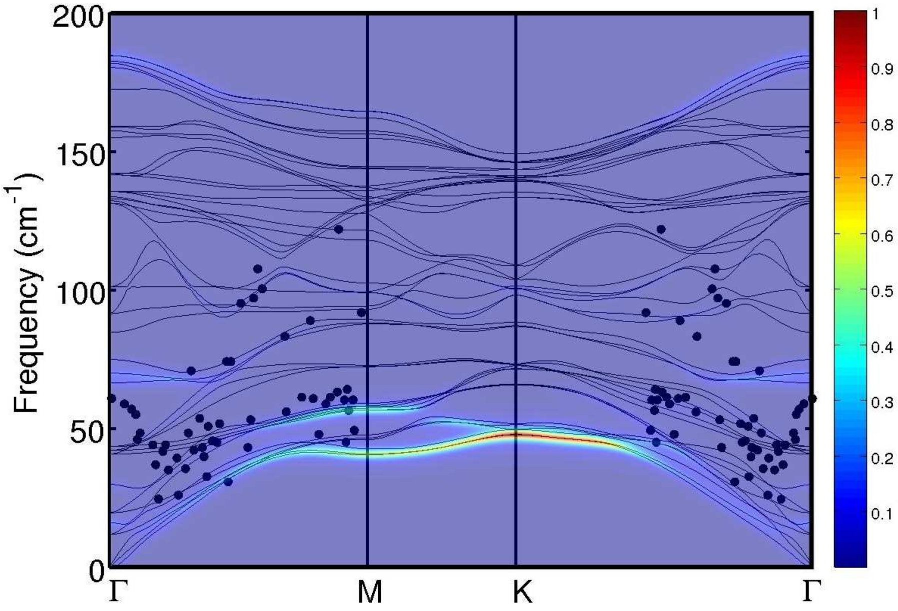

Figure 5.8: Surface phonons of Bi_2Se_3 (0001) surface projected on the second layer and on shear vertical polarization compared with experimental HAS data. [175]

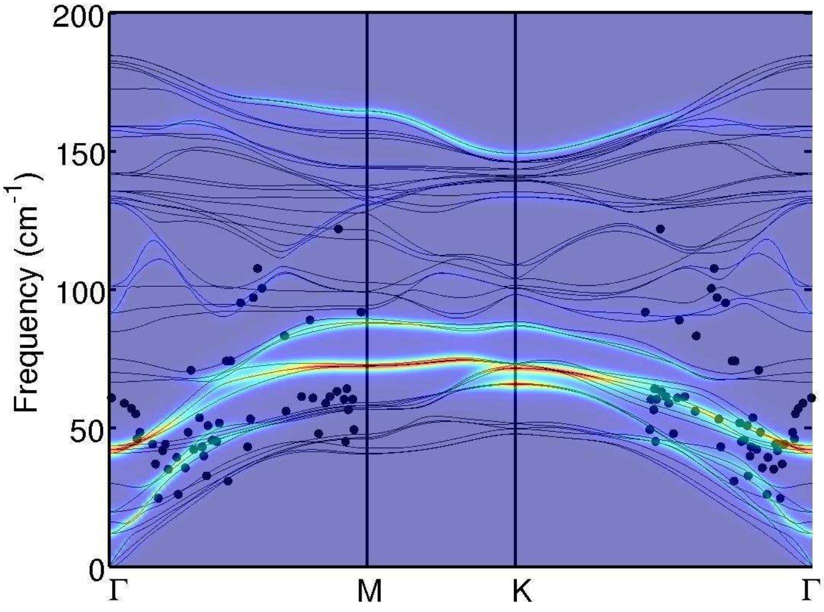

Figure 5.9: Surface phonons of Bi_2Se_3 (0001) surfaceprojected on the second layer and on longitudinal polarization compared with experimental HAS data. [175]

When SOC is taken into account a topological insulator exhibits metallic surface states. It has been suggested that the presence of such states crossing the Fermi level could give rise to a Kohn anomaly in the surface phonon spectra in correspondence of the nesting vector of the Fermi surface (line) on the Dirac cone (see Fig.5.1). In the calculation reported in Figs.5.4 and 5.6 we omitted the SOC and therefore there are no surface metallic states.

In order to verify the effect of such states on surface phonons we repeated the phonon calculations at the q-point corresponding to the nesting vector ($2k_F$) by including SOC. We compared this result with that obtained by discarding the SOC.

To perform these calculations we had to improve the sampling of the Brillouin zone close to the Fermi surface which is particularly important to resolve an eventual anomaly. Given the peculiar shape of the Fermi surface in Sb_2Te_3 and Bi_2Se_3 slabs consisting of a ring around the Γ-point, we used a graded k-point mesh (equivalent to a 50x50x1 uniform mesh) near the Γ-point and a coarser one (equivalent to a 8x8x1 mesh) near the zone boundary. The results are reported in Figs.5.10 and 5.11. A one to one comparison between phonon modes calculated with and without SOC shows that there is no evidence of a Kohn anomaly induced by the presence of the surface metallic states, involving any of the surface phonon modes. The spin-orbit coupling results only in a overall softening of the phonon modes of at most 3% in Sb_2Te_3 and 6% in Bi_2Se_3.

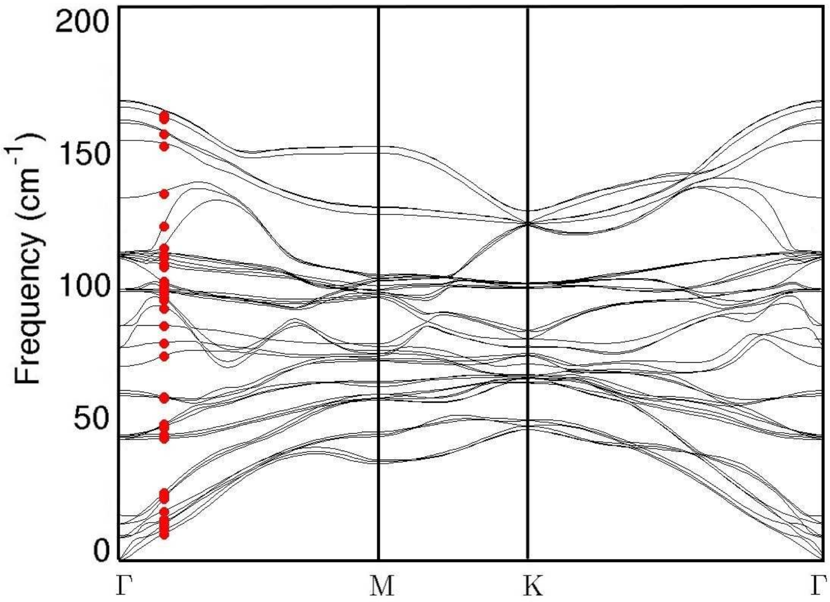

Figure 5.10: Surface phonons of Sb_2Te_3 omitting spin-orbit coupling (black continuous line) and including (red dots) at a q vector corresponding to the nesting vector $2k_F$.

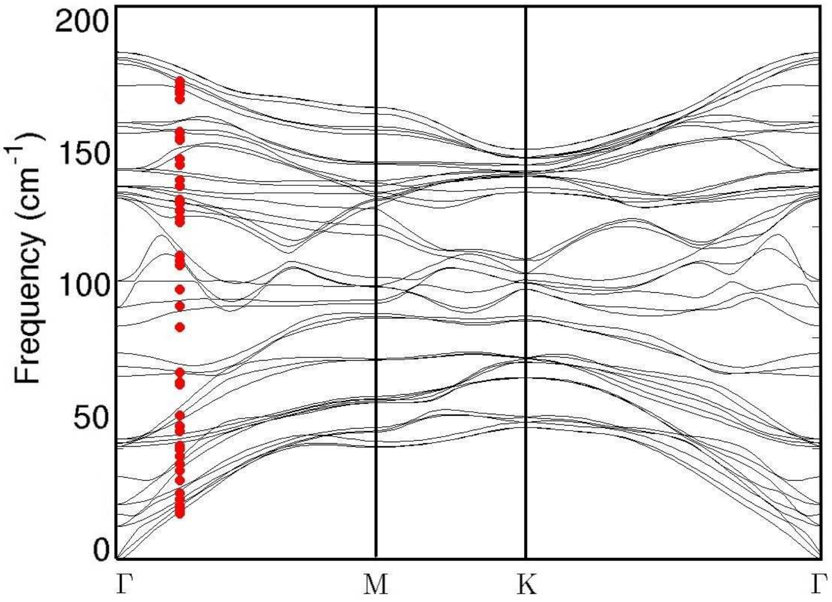

Figure 5.11: Surface phonons of Bi_2Se_3 omitting spin-orbit coupling (black continuous line) and including (red dots) at a q vector corresponding to the nesting vector $2k_F$.

5.2 Conclusion

The DFPT calculations of the surface phonons of Sb_2Te_3 and Bi_2Se_3 (0001) surfaces do not seem to confirm the presence of a Kohn anomaly observed experimentally for Bi_2Se_3(0001). One might speculate that the experimental feature assigned to the Kohn anomaly, if confirmed, could arise from non-adiabatic effects which are missing in the adiabatic DFPT framework we used. Another possibility recently proposed in a theoretical paper is that the anomaly arises from the coupling of phonons with plasmon (collective) excitation which are also missing in the DFPT framework.

6 Sb_2Te_3-GeTe superlattices

Recently, it has been shown that GeTe-Sb_2Te_3 superlattices could allow the realization of PCM devices requiring a considerably lower switching power in SET/RESET operations than conventional PCM alloys (cf. Sec.1.3.2 and Ref.[13]).

In these devices, referred to as interfacial phase change memories (iPCM) [13], it is believed that the transformation involves small displacements of a subset of atoms without melting and subsequent amorphization [13] as described in Sec.1.3.2.

On the basis of high resolution transmission electron microscope (TEM) images of $(GeTe)_2$-Sb_2Te_3 superlattices, it was proposed [13] that the SET(low resistivity) state corresponds to a ferroelectric arrangement of the $(GeTe)_2$ blocks (Ferro cf. Fig. 6.1) and that the RESET (high resistivity) state could be obtained by a displacement of a Ge atom along the superlattice axis (*c*), in a sort of umbrella-flipping process, in order to form Ge-Ge bonds ending up in the Swithced-Ferro configuration (cf. Fig 6.1).

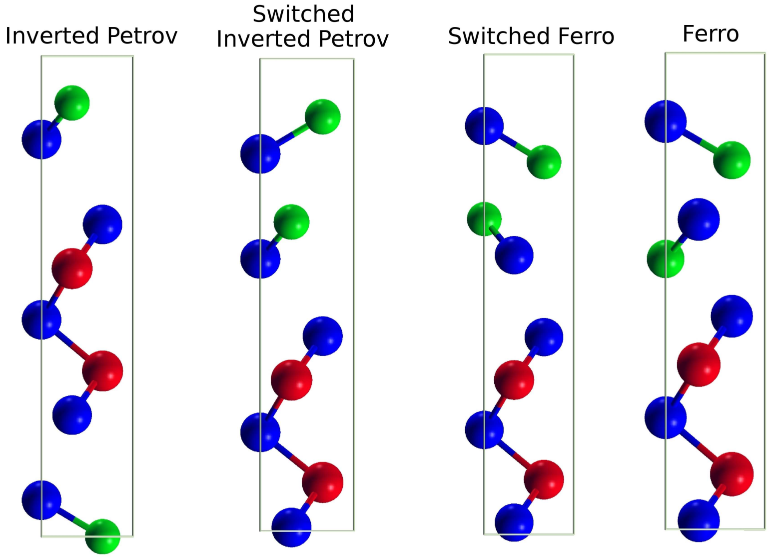

Figure 6.1: Structure of $(GeTe)_2Sb_2Te_3$ superlattice in different configurations. a) Inverted Petrov, b) Switched Inverted Petrov, c) Ferro and d) Switched Ferro.

The RESET state has been later proposed [69] to correspond to the so-called inverted Petrov structure ideally obtained by switching Ge and neighboring Te atoms in the crystalline structure of $Ge_2Sb_2Te_5$ proposed by Petrov [70] (cf. Fig.3.14). A switch between the Petrov (SET) and the Inverted-Petrov (RESET) configurations has also been proposed [71].

DFT calculations of electronic band structure revealed that the Inverted-Petrov structure shows a Dirac cone at the Γ point with the Fermi level at the cone vertex which should correspond to the interfacial topologically protected states present at the interface between the topological insulator Sb_2Te_3 and the normal insulator (semiconductor) GeTe. The switched Inverted-Petrov has instead a large density of states at the Fermi level consistent with a SET state.

A more recent calculation has shown that among the four configurations Ferro, Switched-Ferro, Inverted-Petrov and Switched-Inverted-Petrov, the Ferro and Inverted-Petrov are the lowest in energy with an electronic band structure compatible with the SET/RESET character. The Switched-Ferro and Switched-Inverted-Petrov have been further proposed as intermediate states along a Ferro $\longleftrightarrow$ Inverted-Petrov transition.

All these structures have been proposed on the basis TEM data and symmetry arguments. However, since the TEM measurements are usually not Z-resolved the identification of the different species is often uncertain.

Since the different phases discussed above feature different bonding geometries in the GeTe blocks one would expect specific vibrational signatures of the different crystal structures. Would this be the case, one should also be able to identify the structures, monitor the switching process and perhaps also identify intermediate states by micro-Raman measurements.

In this section, we report on first principles calculation of the Raman spectrum of the four different geometries Ferro, Inverted-Petrov, Switched-Ferro, Switched-Inverted-Petrov discussed above.

Furthermore recent TEM and Raman experimental data suggest a more complicated picture [179], in which the structures involved are not limited to the simple superlattices described above but are organized in more complex structures which are likely to contain $GeSb_2Te_4$ blocks.

So far no experimental Raman spectra of $(GeTe)_2$-Sb_2Te_3 superlattices are available. To asses the reliability of the theoretical framework we have thus first computed the Raman spectra of the hexagonal phase of crystalline $GeSb_2Te_4$ for which experimental Raman spectra to compare with are available. In the next section we report the results on $GeSb_2Te_4$ while the calculations on the superlattices are reported in Sec.6.2.

6.1 Structural properties and Raman spectra of $Ge_1Sb_2Te_4$

Structural parameters of $Ge_1Sb_2Te_4$ have been optimized with PBE exchange and correlation energy functional both including and neglecting van der Waals (See Sec.2.1.5). The crystal structure belongs to the $R\overline{3}m$ space group and it consists of seven layers ($Ge_1Sb_2Te_4$) forming lamellae separated by vdW gaps similarly to the structure of $Ge_2Sb_2Te_5$. A partial disorder in the Ge/Sb sublattice has been inferred form X-ray diffraction data [139]. In the calculations we neglected the disorder in the Ge/Sb sublattice and we used the equivalent hexagonal cell with three $Ge_1Sb_2Te_4$ lamellae, stacked along the c axis (cf. Fig.6.4). Kohn-Sham (KS) orbitals were expanded in a plane waves basis up to a kinetic cutoff of 35 Ry. Brillouin Zone (BZ) integration was performed over a $12\times12\times2$ shifted by 1x1x1 Monkhorst-Pack mesh [135]. The resulting equilibrium lattice parameters turned out to be a=4.29 Å and c=41.48 Å neglecting vdW correction and a=4.21 Å c=40.89 Å including it.

We computed the Raman spectrum from phonons at the Γ point within density functional perturbation theory [93] for the theoretical equilibrium geometries. The differential cross section for Raman scattering (Stokes) in non-resonant conditions is given by (for a unit volume of scattering sample)

$$\frac{d^2\sigma}{d\Omega d\omega} = \sum_j \frac{\omega_S^4}{c^4} \left|\mathbf{e}_S \cdot R^j \cdot \mathbf{e}_L\right|^2 (n_B(\omega/k_bT)+1)\delta(\omega-\omega_j), \tag{6.1}$$

where $n_B(\omega/k_bT)$ is the Bose factor, ω_S is the frequency of the scattered light, $\mathbf{e}_S$ and $\mathbf{e}_L$ are the polarization vectors of the scattered and incident light, respectively. The Raman tensor R^j associated with the j-th phonon is given by

$$R^j_{\alpha\beta} = \sqrt{\frac{V_o\hbar}{2\omega_j}} \sum_{\kappa=1}^{N} \frac{\partial\chi^\infty_{\alpha\beta}}{\partial\mathbf{r}(\kappa)} \cdot \frac{\mathbf{e}(j,\kappa)}{\sqrt{M_\kappa}}, \tag{6.2}$$

where V_o is the unit cell volume, $\mathbf{r}(\kappa)$ is the position of the κ-th atom and $\chi^\infty = (\varepsilon^\infty - \mathbf{1})/4\pi$ is the electronic susceptibility. The tensors R^j were computed from χ^∞ by finite differences, by moving the atoms independent by symmetry with maximum displacement of 0.01 Å .

The Raman cross section is computed for a single crystal and unpolarized light in backscattering geometry along the (c) axis.

The resulting spectra calculated including and neglecting the vdW correction at the respective equilibrium lattice parameter is reported in Fig.6.2 calculated with a 5 cm^{-1} linewidth. A comparison between the theoretical spectrum and experimental data recently obtained by Battaglia et al.[180] on thin $Ge_1Sb_2Te_4$ films is reported in Fig.6.3. The theoretical spectra reproduce very well the position of the experimental peaks once the vdW corrections are included. The relative intensity of the peaks, strongly influenced by the measurement conditions, shows only a qualitative agreement.

A sketch of the displacement patterns of most important Raman-active modes is reported in Fig.6.4 calculated including vdW corrections. Both the E_g-type modes at 115 cm^{-1} and 125 cm^{-1} contribute to the main peak but with a strong predominance of the first one. The comparison with experiments suggests that vdW corrections are mandatory to accurately reproduce the phonon spectra.

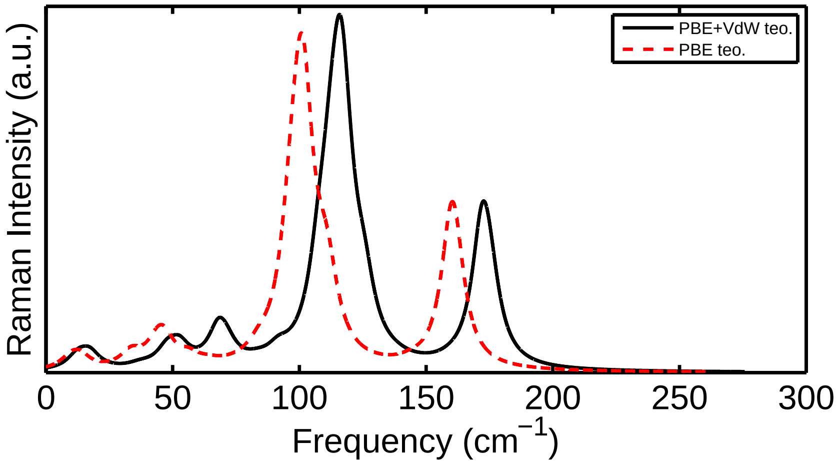

Figure 6.2: Raman spectra of $Ge_1Sb_2Te_4$ calculated including and neglecting vdW correction.

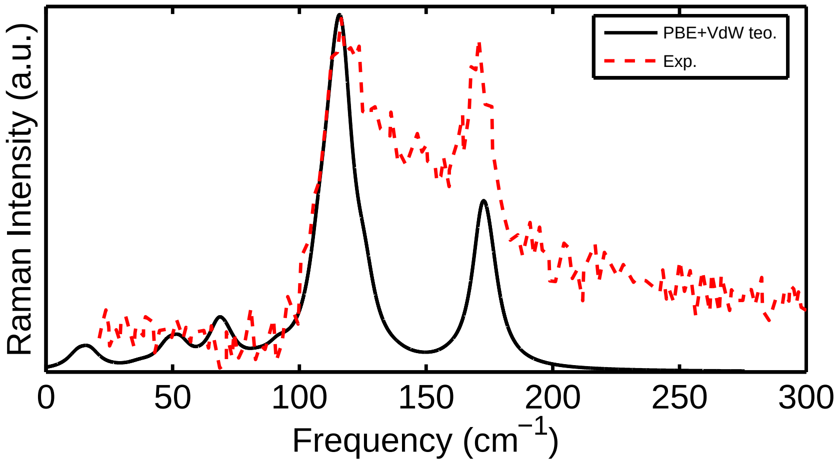

Figure 6.3: Raman spectra of $Ge_1Sb_2Te_4$ calculated including vdW correction compared with experimental data.[180]

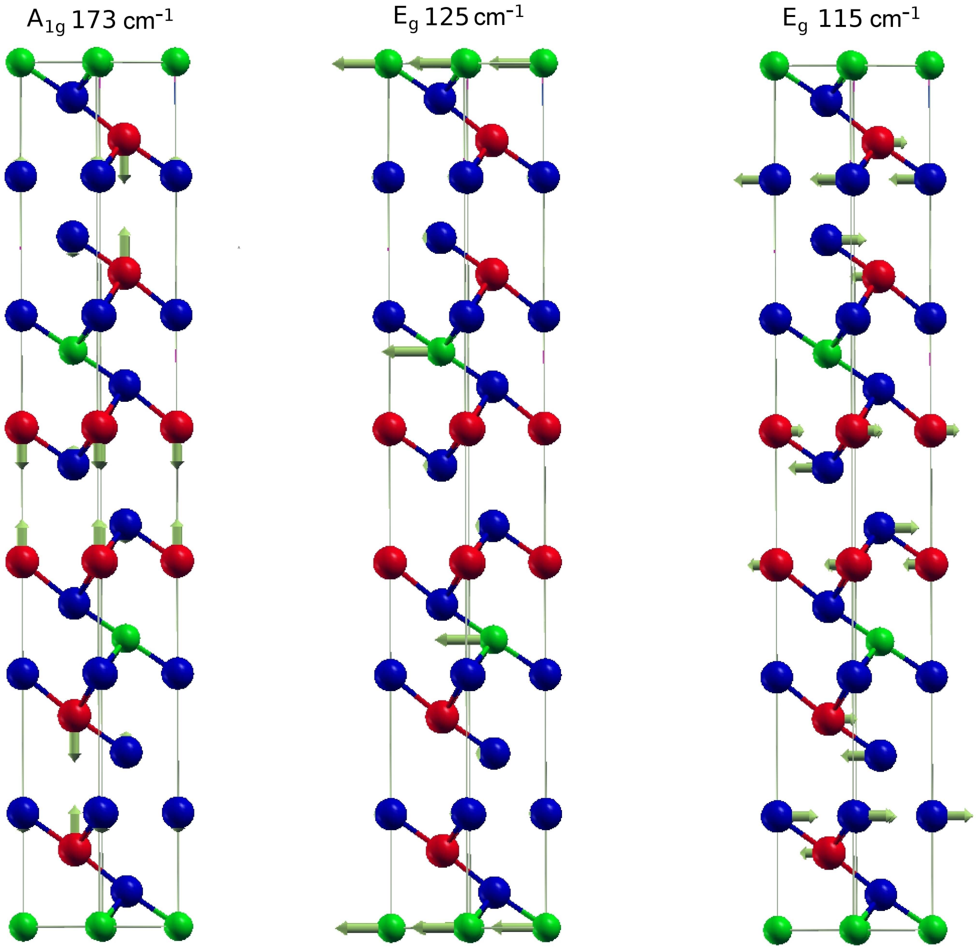

A_{1g} 173 cm^{-1} E_g 125 cm^{-1} E_g 115 cm^{-1}

Figure 6.4: Sketch of the most active Raman modes of $Ge_1Sb_2Te_4$ calculated including vdW correction.

6.2 Structural properties and Raman spectra of $(GeTe)_2$-Sb_2Te_3 superlattices

Raman spectra of superlattices were computed from DFPT phonons as described in the previous section. We used PBE exchange and correlation energy functional and norm conserving pseudopotentials. The calculations were performed both including and neglecting van der Waals corrections [87].

Kohn-Sham (KS) orbitals were expanded in a plane waves basis up to a kinetic cutoff of 35 Ry. Brillouin Zone (BZ) integration was performed over a 12×12×4 shifted by 1x1x1 Monkhorst-Pack (MP) mesh [135].

As a preliminary step, we have optimized the internal structure of the four different geometries: Inverted-Petrov, Switched-Inverted-Petrov, Ferro and Switched-Ferro. The lattice parameters *a* and *c* are given in Table 6.1. In both SET states (Inverted-Petrov and Switched-Ferro) Ge-Ge contacts are present in the GeTe blocks. The total energy (eV/atom) of the optimized structures given in Table 6.1 show that the most stable SET and RESET structures are the Ferro and the Inverted Petrov geometries. One might thus conceive that the switching process would involve these two lowest energy structures and it would thus consist of both a displacement of the Ge layer along the *c* direction and a sliding of Ge and Te layers in the *ab* plane.

Structure	a (Å)	c (Å)	Energy (meV/atom)
(SET) Inverted-Petrov	4.12 (4.19)	18.14 (19.03)	0.13 (0.50)
(RESET) Switched-Inverted-Petrov	4.21 (4.13)	18.65 (18.47)	1.99 (1.64)
(RESET) Ferro	4.18 (4.265)	17.22 (17.45)	0.0 (0.0)
(SET) Switched-Ferro	4.10 (4.17)	18.95 (19.64)	2.53 (2.31)

Table 6.1: Theoretical *a* and *c* equilibrium lattice parameters and total energy (eV/atom) of the Ferro , Switched-Ferro , Inverted-Petrov and Switched-Inverted-Petrov structures calculate with PBE including and, in parenthesis, discarding vdW correction.

The Raman spectra have been computed as described for $Ge_1Sb_2Te_4$ in non resonant conditions. This is possible in a rigorous way only for insulating phases. However, these materials have a very low density of states at the Fermi level originating from states near the Γ-point in the BZ (cf Fig.1.8). By performing the BZ integration over the shifted 12x12x4 mesh, the k-points are sufficiently far from the Γ-point so that all the configurations behave as insulators which allows computing the Raman tensors for these phases. However, we must consider that in these latter cases larger errors in the Raman cross section are possible, because of possible resonance effects with the laser probe (in a zero gap system) neglected in Eq. 6.1.

Inverted-Petrov (SET)	
E_g	49 , 122, 132 (39, 116, 127)
A_{1g}	75, 184 (64, 177)
Switched-Inverted-Petrov (RESET)	
E	51, 98, 103, 119, 149 (46, 88, 96, 113, 139, 146)
A_1	167, 180, 189 (157, 171, 180)
Ferro (RESET)	
E	101, 116, 135 (94, 110, 124)
A_1	155, 174 (145, 164)
Switched-Ferro (SET)	
E	49, 121, 150 (46, 116, 142)
A_1	54, 69, 186, 194, 199 (48, 64, 178, 187, 194)

Table 6.2: Frequency (cm^{-1}) of phonons at the Γ-point of the two SET and the two RESET geometries. For the Inverted-Petrov structure the Raman active modes have E_g or A_{1g} symmetry while for all the other structures the Raman active modes have E or A_1 symmetry. The frequencies refer to calculation including the vdW correction. Data without vdW correction are reported in parenthesis.

The phonon modes and Raman spectrum have been calculated as in the previous section. The frequency of phonons at the Γ-point is reported in Table 6.2 for the four structures. The Raman active modes have E_g or A_{1g} symmetry in the Inverted-Petrov structure, while for all the other structures the Raman active modes have E or A_1 symmetry.

The Raman spectra for the four structures are reported in Fig. 6.5 calculated with PBE with vdW correction and using a phonon gaussian linewidth of 5 cm^{-1} which seems adequate to reproduce the experimental Raman spectra of $Ge_1Sb_2Te_4$ computed in the previous section. To resolve the different modes contributing to the Raman features we also computed the spectrum with a smaller linewidth of 0.5 cm^{-1} reported in Fig. 6.6. The spectra calculated including the vdW correction are reported in Fig. 6.7 with a linewidth of 5 cm^{-1}.

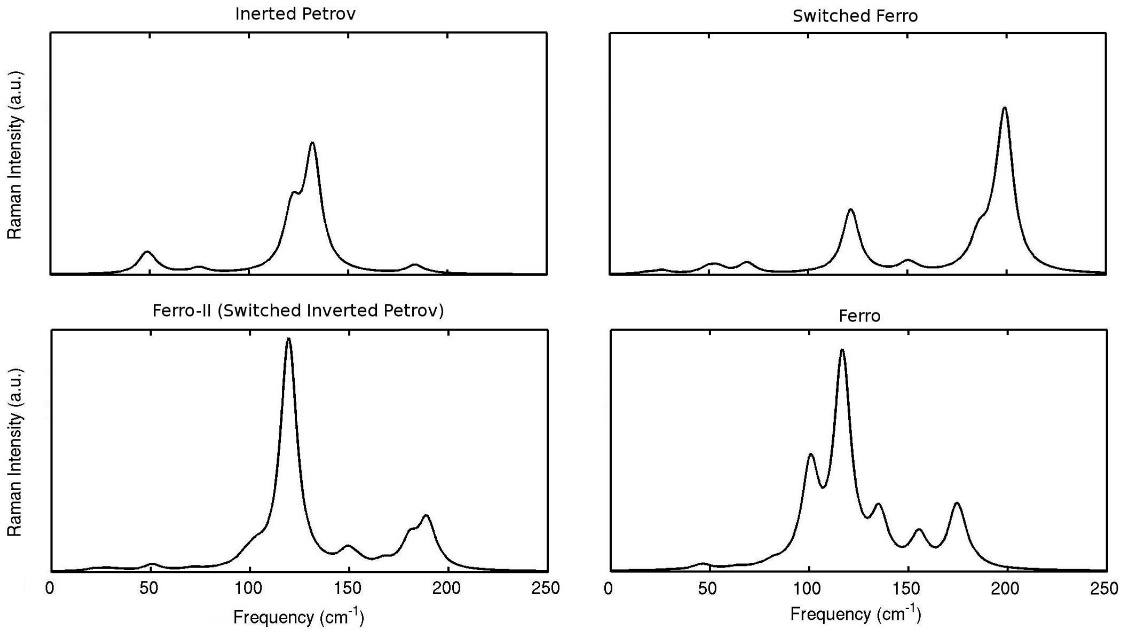

Figure 6.5: Raman spectra for the four GeTe-Sb_2Te_3 superlattice structures calculated with PBE+vdW, phonon gaussian linewidth of 5 cm^{-1}

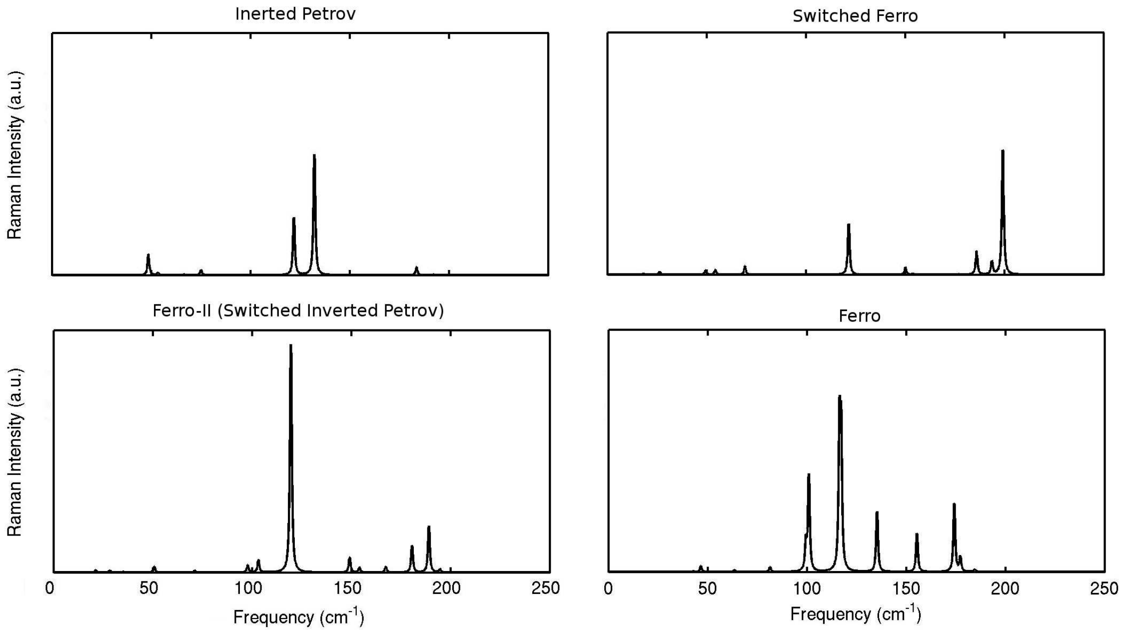

Figure 6.6: Raman spectra for the four GeTe-Sb_2Te_3 superlattice structures calculated with PBE+vdW, phonon gaussian linewidth of 0.5 cm^{-1}

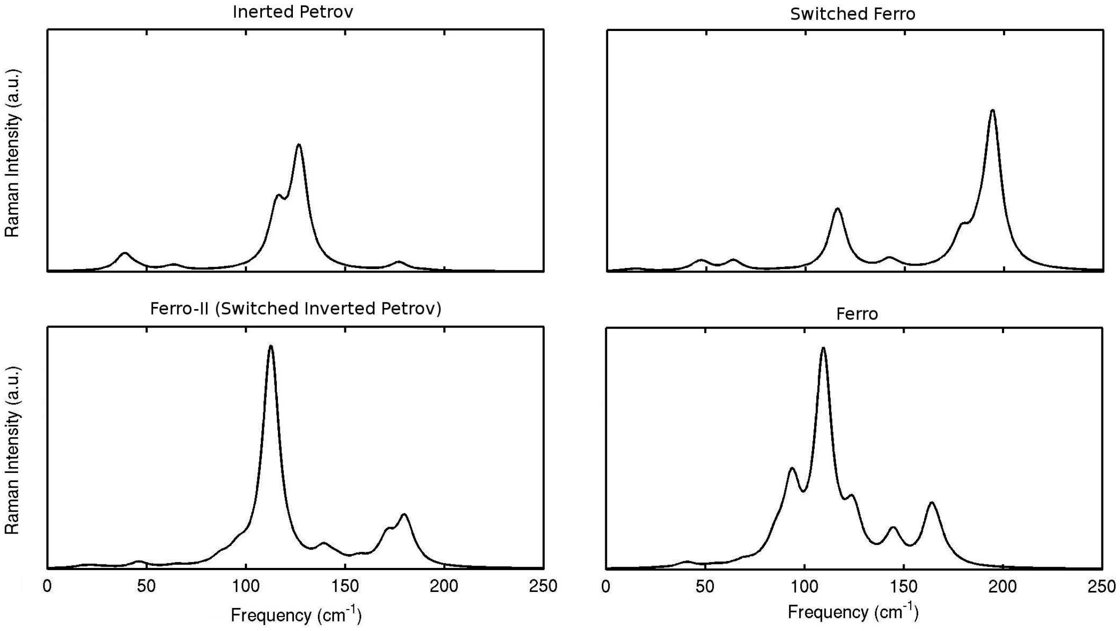

Figure 6.7: Raman spectra for the four GeTe-Sb$_2$Te$_3$ superlattice structures calculated without vdW correction, phonon gaussian linewidth of 5 cm^{-1}

Phonons with E-type symmetry correspond to displacement pattern in the *ab* plane while A-type phonons correspond to displacements along the *c* axis. The displacement pattern of the main Raman active modes for the four structures are reported in Figs. 6.8-6.11.

To our knowledge no experimental data are available on the Raman spectra of these structure. At this stage our results are theoretical predictions to be confirmed by experimental measurements. Overall the differences in the spectra of all the four phases are large enough to allow for an easy discrimination among the different structures and for the identification of the switching process by Raman spectroscopy.

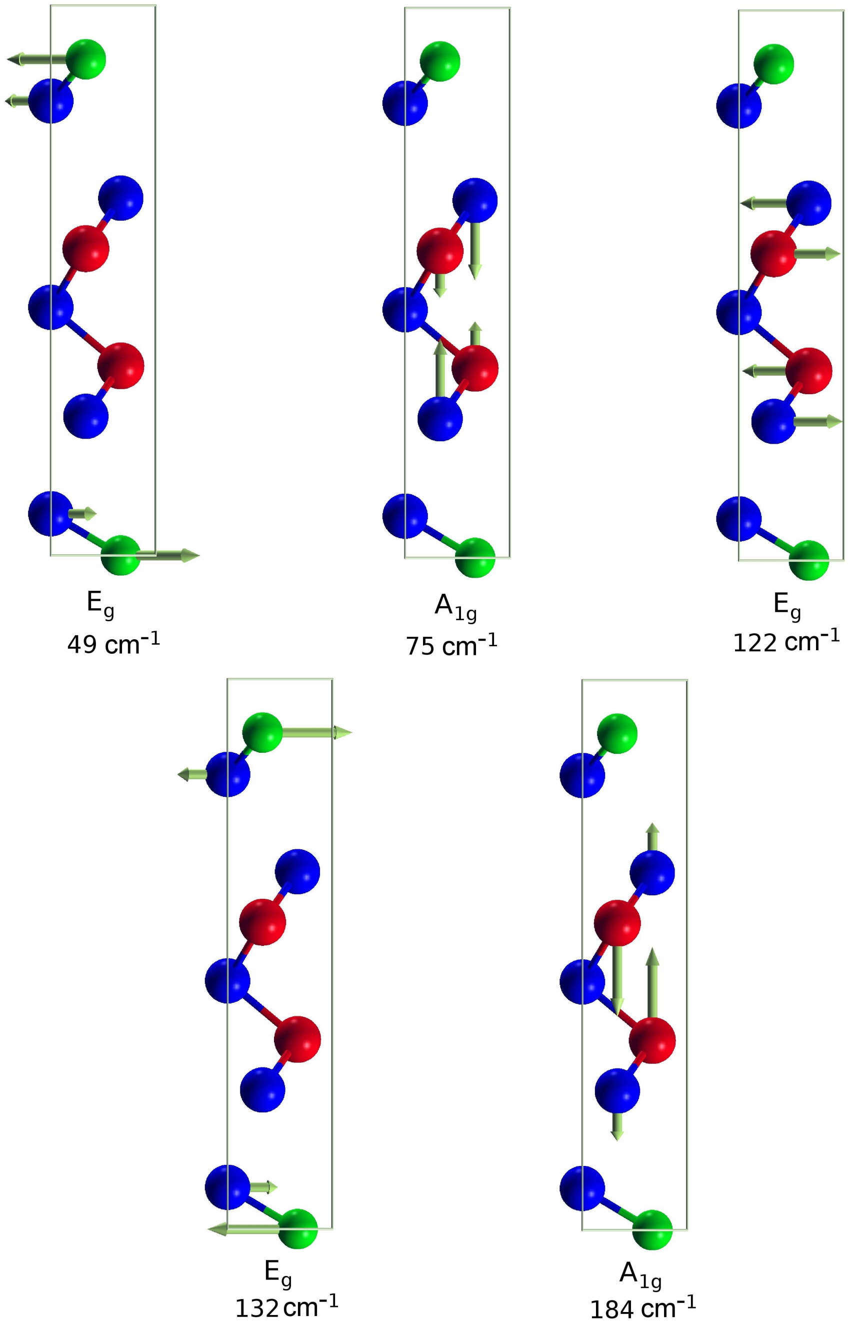

Figure 6.8: Displacement vectors of the most relevant Raman active modes of the Inverted-Petrov configuration. The frequencies are referred to the PBE+vdW calculations.

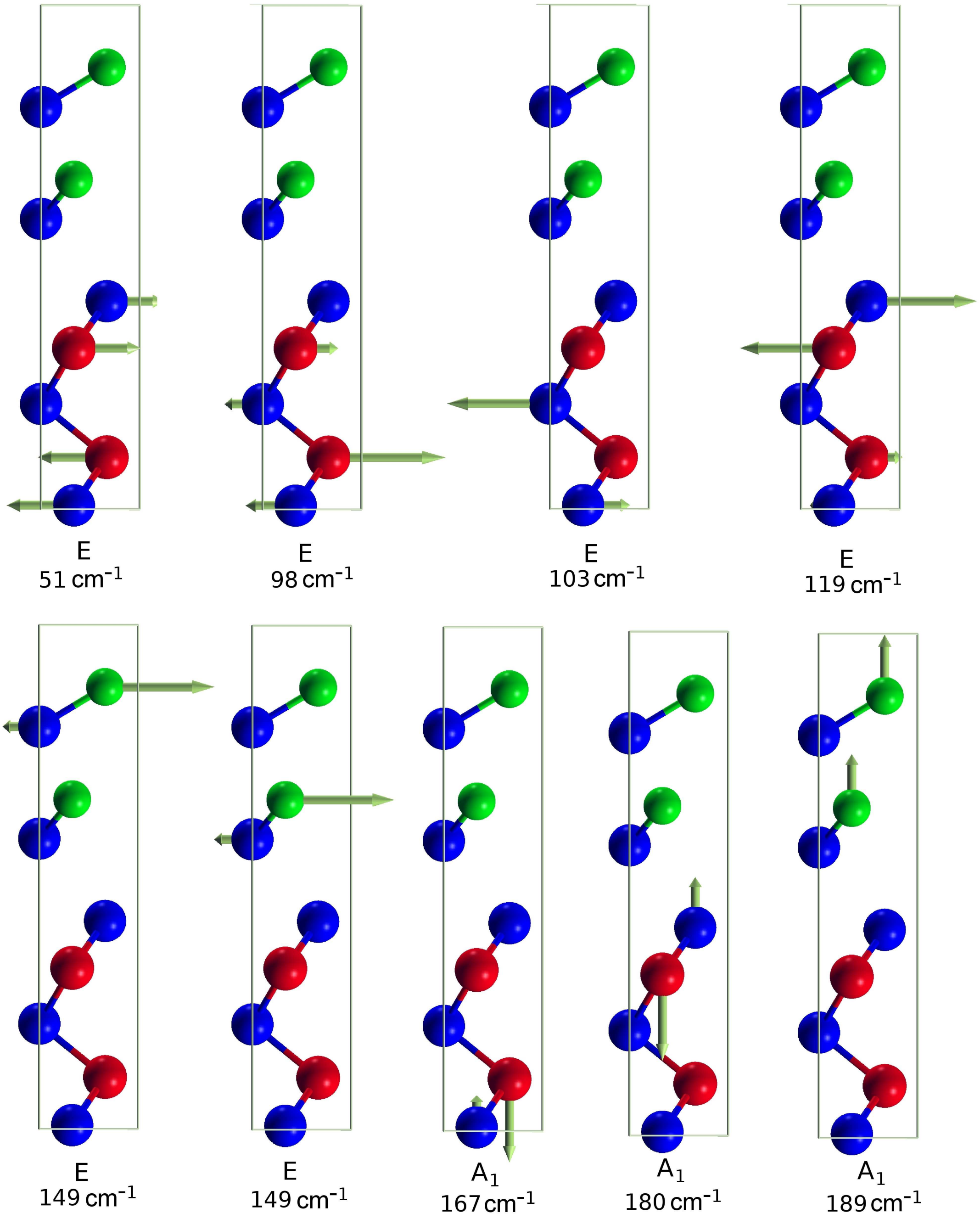

Figure 6.9: Displacement vectors of the most relevant Raman active modes of the Switched Inverted-Petrov configuration. The frequencies are referred to the PBE+vdW calculations.

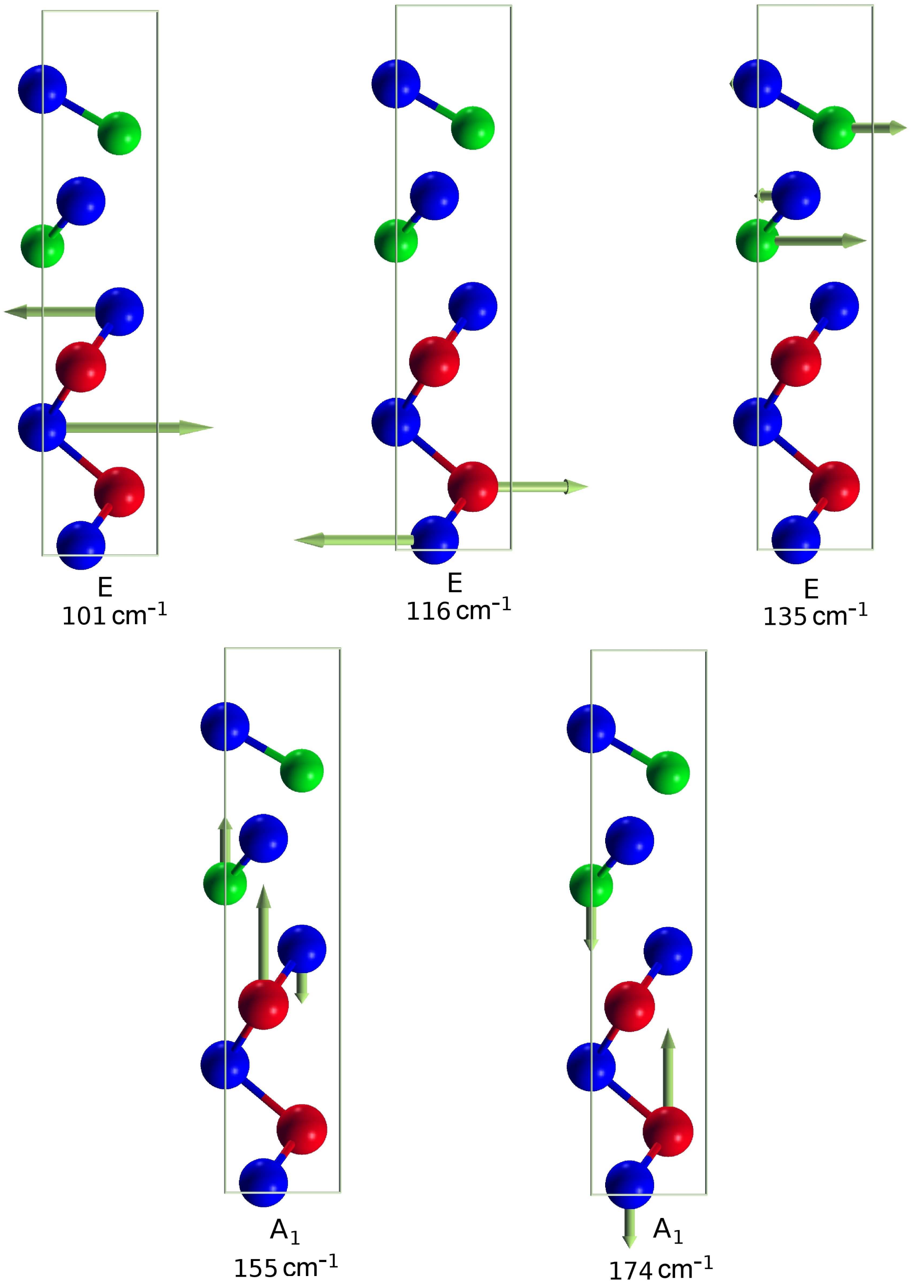

Figure 6.10: Displacement vectors of the most relevant Raman active modes of the Ferro configuration. The frequencies are referred to the PBE+vdW calculations.

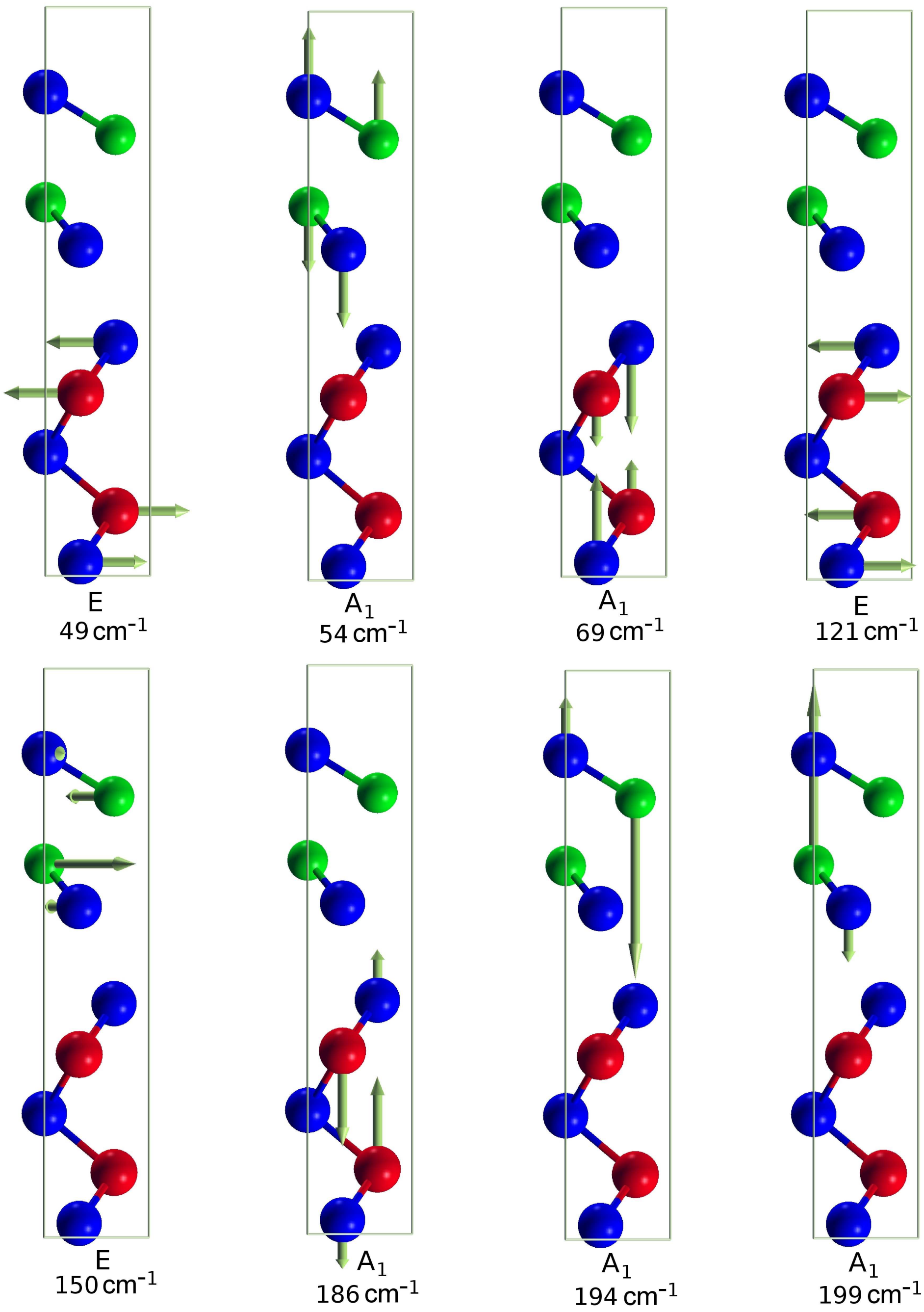

Figure 6.11: Displacement vectors of the most relevant Raman active modes of the Switched Ferro configuration. The frequencies are referred to the PBE+vdW calculations.

6.3 Conclusions

The calculation of the Raman spectra for the four $(GeTe)_2$-Sb_2Te_3 superlattices proposed for iPCM revealed that vibrational spectroscopy can be a valuable tool to experimentally identify of the structures and the monitoring the phase transition in a simpler way with respect to TEM measurements.

The reliability of out theoretical framework is demonstrated by the comparison between $Ge_1Sb_2Te_4$ theoretical and experimental spectra.

7 GeTe multilayers

Molecular Beam Epitaxy (MBE) offers a better control of the growth of GeTe-Sb_2Te_3 superlattices for the realization of iPCMs than the sputtering method used so far. The onset of the MBE growth of GeTe and GeSbTe has been studied in details by an experimental group we are collaborating with [181].

GeTe multilayers are also of interest for their ferroelectric properties. Switching of the polarization in GeTe multilayers has been reported recently.[181] Moreover the interplay between ferroelectricity and spin-orbit coupling give rise to a gigantic Rashba splitting in GeTe thin films that might have applications in spintronic devices [14].

In this section, we report the calculations of phonon modes and Raman spectra in GeTe multilayers computed by DFPT aimed explaining the evolution of Raman peaks observed during the layer-by-layer growth of GeTe on Si(111)-($\sqrt{3} \times \sqrt{3}$)R30°-Sb reported in Fig.7.1. The spectra are measured in z(y,xy)-z scattering geometry with a 633 nm laser.

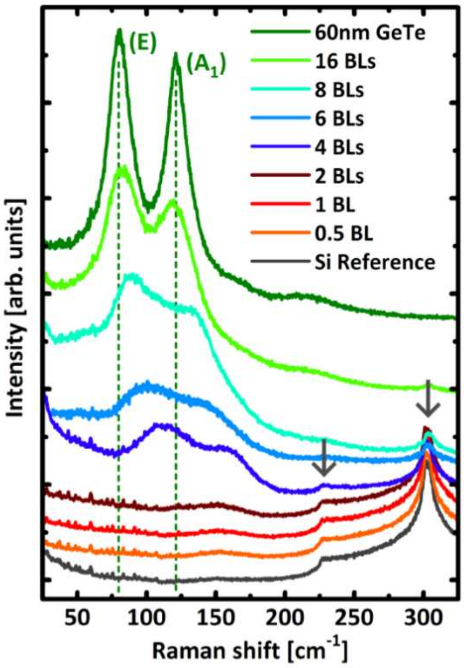

Figure 7.1: Experimental Raman spectra measured as a function of the layer thickness in GeTe multilayers grown by MBE. Arrows indicate Raman peaks of the Si substrate.

The Raman peaks for 16 GeTe bilayers (BLs) are very close to the bulk values measured for α-GeTe (see Sec.3.1.1), while for lower thickness both E and A_1 peaks are steadily shifted to higher frequencies up to 110 cm^{-1} and 155 cm^{-1} for the four bilayers (4BL) case. For 2BLs and below only the two peaks (marked by an arrow in Fig.7.1) at 225 cm^{-1} and 300 cm^{-1} corresponding respectively to the 2TA(L) and 2TA(X) modes of the silicon substrate are observed while no modes associated with GeTe are detected.

Along with the changes in the Raman spectra, a variation in the lattice parameter was measured form the streak spacing of reflection high-energy electron diffraction (RHEED) during the growth process. The distance between the $\bar{2}11$ planes sketched in Fig.7.2a is reported in Fig.7.2d as a function of the deposition time. From Fig.7.2c, in which each maximum of the oscillations correspond to the completion of a GeTe bilayer, a growth rate of 1 GeTe BL every 100s can be estimated. The reduction in the RHEED oscillations is indicative of an imperfect layer-by-layer growth in which additional layers nucleate and coalesce at the same time, before the full completion of the antecedent layers.

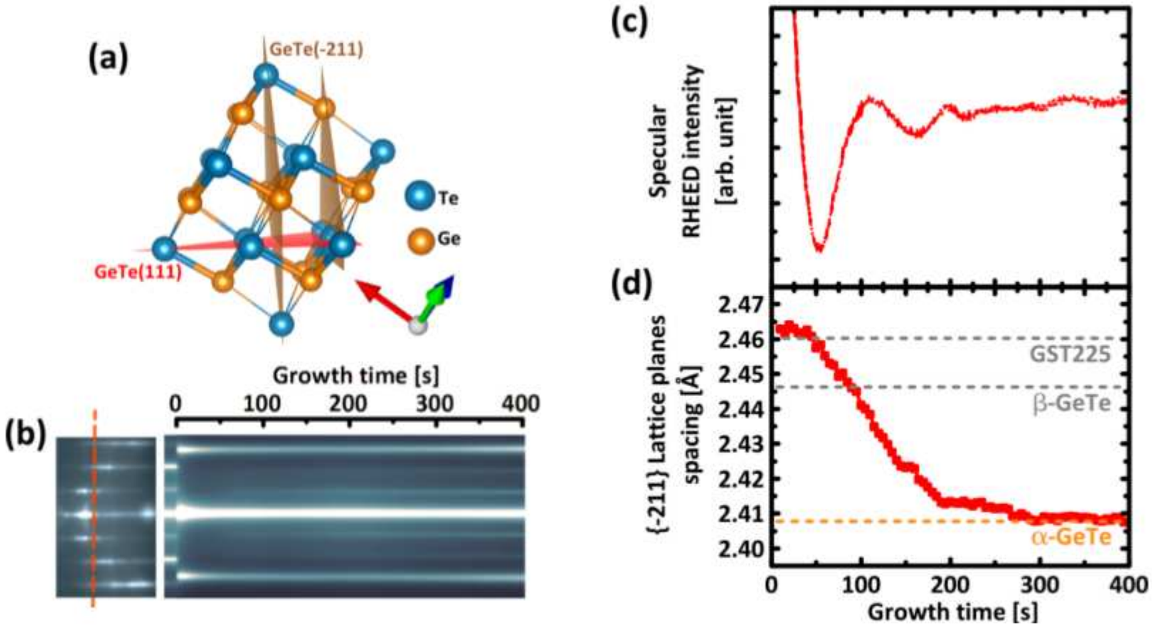

Figure 7.2: a) Schematic model of α-GeTe crystal with the $(\bar{2}11)$ planes highlighted in brown. b) RHEED intensity over time acquired along red dashed line across the $\langle\bar{2}11\rangle$ azimuth pattern. c) Integrated specular beam intensity oscillations close to growth onset demonstrating the formation of complete layers. d) $\{\bar{2}11\}$ lattice planes spacing calculated from RHEED streak spacing showing a larger in-plane spacing with respect to α-GeTe during the first 200 seconds of growth.

Immediately at the growth onset, a ($\{\bar{2}11\}$) lattice spacing of 2.46 Å was observed, larger than the value of 2.41 Å expected for α-GeTe and closer to the values of 2.446 Å expected for β-GeTe and to the 2.46 Å for the metastable cubic GST [139].

This larger lattice spacing cannot be ascribed to the matching with the lattice spacing of the substrate which has instead a smaller lattice spacing than α-GeTe. This observation together with the abrupt change in the Raman spectra for the thinnest films may indicate that the growth initiate in a different phase than the expected α-GeTe.

Because of the involvement of Sb in the surface preparation, the larger lattice spacing at growth onset could be explained by the intermixing of Sb with GeTe into a GST compound. Also the Raman spectrum of the 4BL sample, in Fig.7.1, the peaks shifted to 110 cm^{-1} and 155 cm^{-1} coincide with the Raman spectrum of metastable GST [182].

However the removal of Sb atoms from the silicon surface passivation is unlikely due to the strong covalent bonds between Sb atoms and silicon. For instance, the stability of this surface passivation can be appraised by considering that the substrate needs to be heated to 650-880 °C in order to fully desorb the monolayer of Sb.

A residual Sb contamination of the growth chamber can be ruled out because in this case because there is no reason why the contamination should be limited to the very first atomic layers.

Therefore, also for the formation of an energetically favorable GST compound, a high barrier needs to be overcome. For instance, it has been previously shown that this Sb passivation is able to retain its stability, even after annealing at 300°C in direct contact with a GST environment [183].

Furthermore, if Sb atoms are removed and silicon bonds are somehow left unpassivated, the growth of GeTe could be expected to yield in-plane twist domains, as it has been shown for GeTe grown on a partially unpassivated surface such as Si(111)-(7x7). Because no pronounced in-plane twist domains are observed when growing GeTe on the Sb passivated surface, it suggests that the surface remains widely passivated.

As the presence of Sb intermixing/contamination of GeTe is ruled out we focused on DFPT calculations of GeTe multilayers in order to understand the observed behavior. Since the real GeTe on Si(111)-($\sqrt{3} \times \sqrt{3}$)R30°-Sb system gives rise to a reconstruction too big for DFPT calculations, we mimicked the growth of GeTe multilayers on the Sb-passivated Si surface by considering a thick slab of GeTe with a numbers of layers free to move and few bottom layers frozen. We have considered both the bulk-like stacking of the frozen and free layers (AB–CA-BC-AB-) and configurations in which the free layers are shifted in the xy axis with respect to the bottom frozen layers (AB–AB-CA-BC-) in order to destroy the resonant bonding and reduce the coupling between the free layers and the frozen substrate. The effect on phonon frequency actually is marginal (cf. Tab. 7.1).

We used the PBE approximation for the exchange-correlation functional, and a 12x12x1 uniform mesh was used to sample the Brillouin Zone. The wavefunctions were expanded in plane

	a_h (Å)	E modes (cm^{-1})	A modes (cm^{-1})
Bulk reference no holes	4.21	84	152
Resonant stacking 4BL	4.21	118	163
non-resonant stacking 4BL	4.21	120	164
non-resonant stacking 2BL	4.21	140	184
non-resonant stacking 1BL	4.21	148	195
non-resonant stacking 2BL	4.26	136	178
non-resonant stacking 1BL	4.26	145	188

Table 7.1: Phonon frequency at the Γ-point of multilayers in different configurations. For the thinner multilayers we also considered the lattice parameter (in hexagonal notation) fixed to the experimental value measured during the MBE growth. Resonant and non-resonant refer due a different stacking of the free layers with respect to the substrate. The first line gives the theoretical phonon frequency in the bulk with long-range interaction included and, in parenthesis, excluded, the latter corresponding to the system with a hole concentration large enough to screen the long range interactions.

waves up to 35 Ry cutoff. The Raman spectrum has been computed as described in Sec.6.1.

For the thinner multilayers we also considered the in-plane lattice parameters fixed to the experimental value of 4.26 Å corresponding to the interplane distance measured during the MBE growth.

We also considered fully relaxed free standing multilayers with optimized in-plane lattice parameters. The in-plane lattice parameters shrink sizeably with respect to the bulk which leads to an enhancing of the difference between short and long (resonating) bonds with respect to the bulk (cf. Tab. 7.2b).

In the multilayers there are several E and A modes ideally corresponding to the folding at Γ of bulk-like phonon branches along the *c* axis of the multilayers. The mode with the largest Raman activity is actually that with with lower frequency for both the A e E modes due to upward curvature of the phonon bands from the Γ point along the *c* axis. The phonon frequency of the most intense Raman mode for the adsorbed multilayers are given in Tab. 7.1. The phonon frequencies for the multilayers should to compared with the bulk-like phonons with a finite concentration of holes that screen the long-range Coulomb interaction. The theoretical bulk Raman peak at zero temperature with a concentration of holes comparable with experiments (see Sec.3.1.1) are 84 cm^{-1} and 130 cm^{-1}. In the lack of holes, the long range Coulomb interaction shifts of the A mode seen by Raman in backscattering geometry along the *c* axis. The theoretical blueshifted frequency is 150 cm^{-1} which is not too far from the experimental value of 140 cm^{-1} obtained

Free-standing bulk lattice parameter

	d_s (Å)	d_l (Å)	E (cm^{-1})	A (cm^{-1})
1BL	2.65	–	148	198
2BL	2.82	3.31	141	188
4BL	2.82	3.31	132	175

(a)

Free-standing optimized lattice parameter

	a_h (Å)	d_s (Å)	d_l (Å)	E (cm^{-1})	A (cm^{-1})
1BL	3.93	2.75	–	166	226
2BL	4.05	2.79	3.32	155	205
4BL	4.12	2.82	3.26	140	184

(b)

Free-standing experimental lattice parameter

	a_h (Å)	d_s (Å)	d_l (Å)	E (cm^{-1})	A (cm^{-1})
1BL	4.26	2.85	–	144	191
2BL	4.26	2.83	3.32	136	181

(c)

Table 7.2: Frequency of the main Raman active A and E modes for free-standing multilayers with in-plane lattice parameters (a) fixed to the theoretical bulk value, (b) optimized to the theoretical equilibrium parameter for the free-standing slabs and (c) fixed to the value corresponding to the interplanar distance measured experimentally by RHEED for the GeTe monolayer. d_s and d_l are respectively the lengths of the short and long Ge-Te bonds to be compared with the theoretical values of 2.85 and 3.21 Å in the bulk.

by extrapolation of the low temperature data to 0 K. In this latter system the hole content is presumably very low although unknown. At room temperature we expect a redshift of both E and A modes due to temperature of about 15 cm^{-1} (see [136]).

The phonon frequencies for the free standing multilayers with lattice parameters fixed at the bulk value, at the value measured experimentally for the ultrathin layer and at the theoretical value optimized for the free standing configuration are reported respectively in Tab. 7.2a, 7.2b and 7.2c.

Overall the frequency of the supported multilayers are lower than those of the freestanding multilayers and better match the experimental spectra of the samples grown by MBE.

The DFT Raman spectrum in backscattering configuration for non-polarized light is reported in Fig.7.3 for the supported four bilayers. The displacement patterns of modes mostly contributing to the peak at 120 and 164 cm^{-1} are given in Fig. 7.4. The spectrum compares well with the experimental spectrum once the redshift due to temperature, not included in our calculations, is considered.

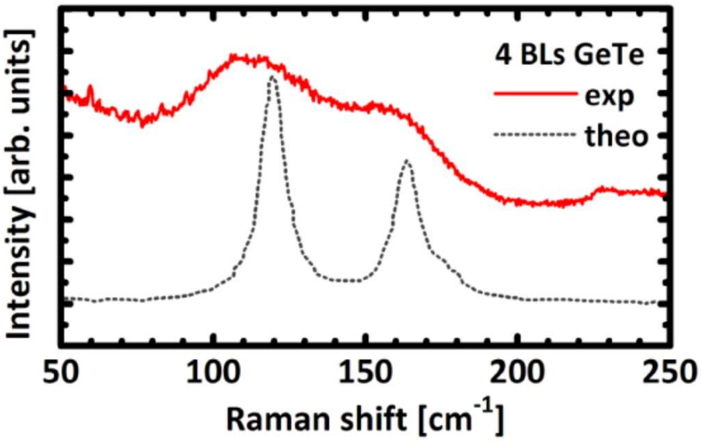

Figure 7.3: Theoretical Raman spectra of supported 4BL GeTe compared with experimental measurements.

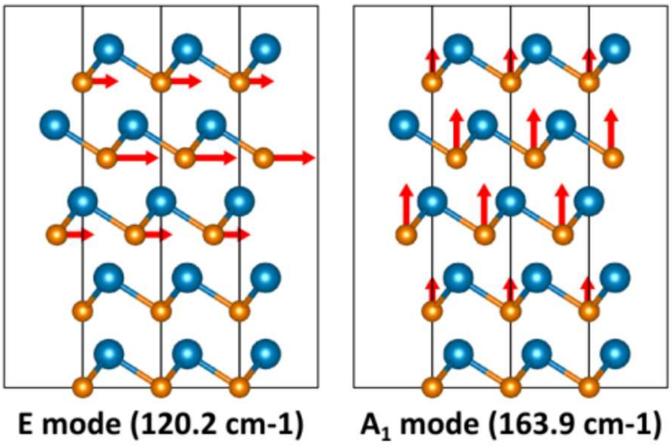

Figure 7.4: Displacement patterns for the two most active Raman modes of the 4BL supported on the bulk.

A comparison between theoretical and experimental evolution of the frequencies of the E and A modes with thickness is reported in Fig.7.5. The blue-shift of frequency for thin GeTe multilayer (form 16 to 4 BL) can be completely ascribed to small size effects.

For even thinner films (2BLs and 1BL) the calculations predict the pursuance of the blueshift trend for the Raman active modes and the maintaining of a distorted rombohedral structure for both supported and freestanding bilayers regardless of the in-plane lattice parameter.

The large difference in Raman spectra for multilayer greater or lower than 4BL, and actually the absence of any Raman signal for samples below 4BL (cf. Fig 7.5), has been interpreted as sign of an initial growth as a cubic rocksalt β-GeTe phase (See Sec.3.1) for which no first order Raman modes are expected as a consequence of the interaction with the substrate. The origin of the β-GeTe phase in 1BL and 2BL is under debate and presently under investigation.

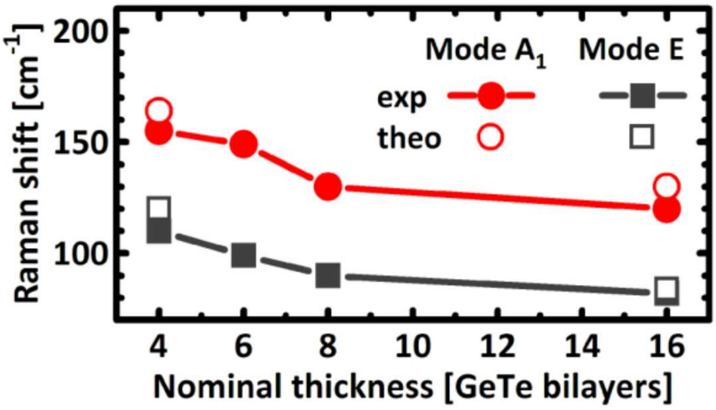

Figure 7.5: Experimental/theoretical comparison of the evolution of GeTe Raman frequency as a function of the slab thickness of the multilayers.

8 Sb_2Te_3 Nanowires

Shrinking the size of the PCM cells to the nano-scale reduces the active material of the volume to be programmed, so that shorter and less intense current pulses are required leading to a lower power consumption. One of the possible roads to size reduction is to obtain phase change materials in form of nanowires (NWs), which feature a lower melting point and lower reset currents in comparison with thin film-based conventional PCM cells. Moreover nanowires are considered one of the best candidates for new multilevel memories (See Sec.1.3.1).

In this section we report structural and total energy calculations, based on DFT, aimed at explaining the peculiar morphology of Sb_2Te_3 nanowires grown by metal-oxide chemical vapor deposition (MOCVD) by the experimental partner we collaborated with in the FP7-EU project Synapse.

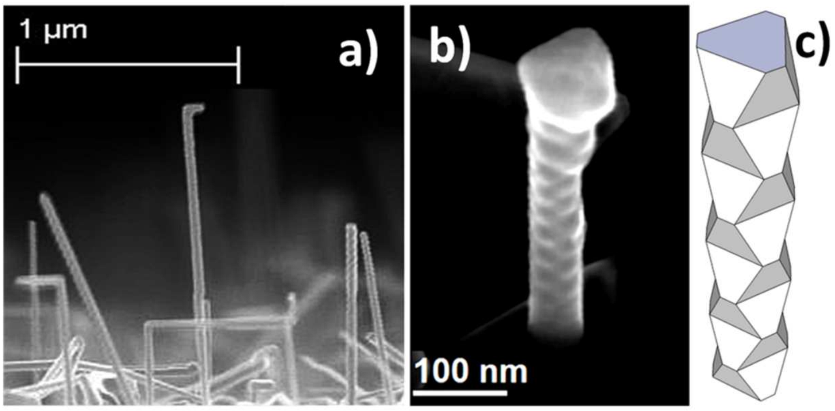

Figure 8.1: (a) SEM image of the Sb_2Te_3 NWs. (b) High magnification SEM image of a single NW showing the peculiar morphology. (c) Three-dimensional model of the nanowires.

The self-assembled NW growth was realized by exploiting the vapor-liquid-solid (VLS) mechanism assisted by Au metal-catalyst colloidal nanoparticles. A small amount of Ge (less than 3%) was introduced to control the NW growth rate and achieve the growth of NW with a diameter smaller 40 nm. The SEM micrographs showed that these small diameter nanowires, grows along the [0001] direction as happens also for larger NWs, but they have a peculiar zigzag shape due to periodic oscillation of the sidewall facet orientation, as reported in Fig. 8.1a and b and schematically represented in Fig. 8.1c.

TEM images, reported in Fig.8.2a-c for a 30 nm NW, showed a twinning period of 18 nm constant along the whole length of the nanowire. Moreover electron diffraction pattern (Fig.8.2d) revealed a symmetry which is inconsistent with the usual Sb_2Te_3 bulk crystal structure.

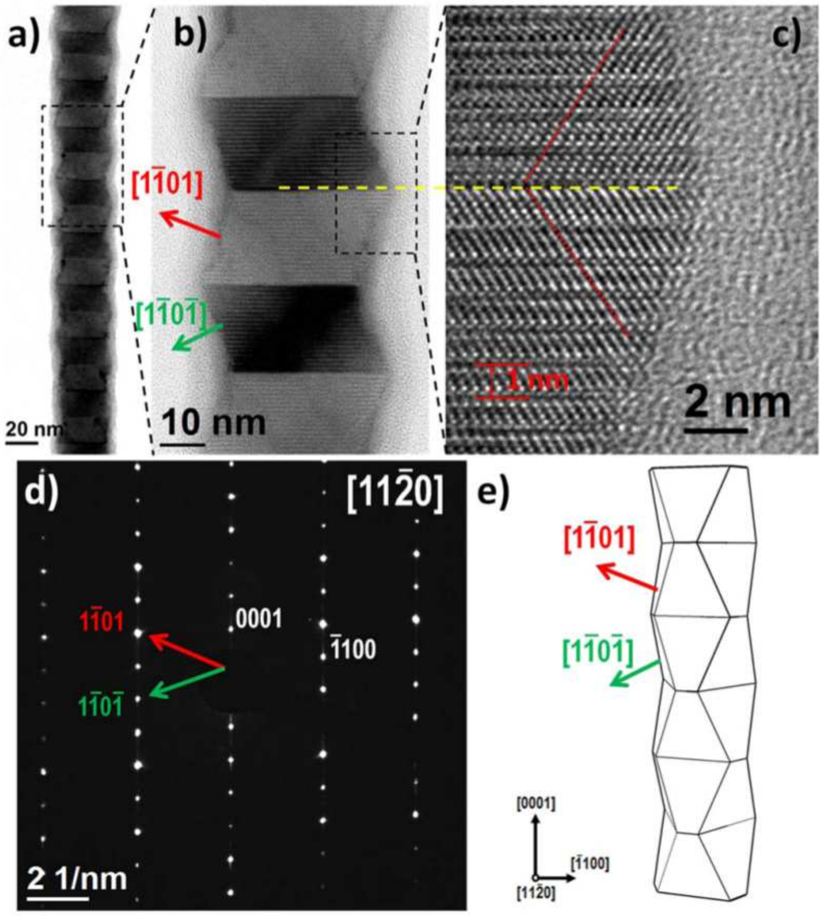

Figure 8.2: a)-c) TEM images of Sb_2Te_3, d) Electron diffraction pattern for Sb_2Te_3 nanowires, e) Model of zig-zag nanowire.

As seen in Sec.3.3.1 Sb_2Te_3 crystallizes in a rhombohedral layered structure with space group R-3m (SG 166) that can be equally described by a non-unitary hexagonal cell with lattice parameters a=4.21 Å and c= 30.45 Å containing three formula units.

The diffraction pattern observed in Fig.8.2d is compatible only with a different symmetry with a shorter periodicity along the c-axis of $c'=c/3=10.6$ Å. In particular it suggests a structure where the five-layers blocks are simply repeated along the c-axis giving rise to a primitive tetragonal lattice with space group P-3m (SG 164). The usual (SG 166) and the new suggested structure in nanowires (SG 164) are compared in Fig. 8.3 while the two structures are compared with high-resolution Z-resolved TEM images of a Sb_2Te_3 nanowire.

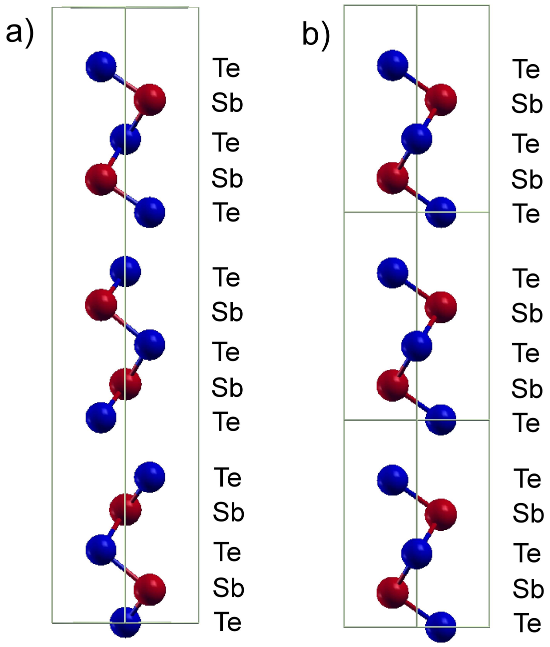

Figure 8.3: Structure of Sb_2Te_3 in the usual SG 166 phase and the newly observed SG 164.

The atomic positions inside the unit cell have been assessed by means of high resolution high-angle annular dark-field scanning TEM (STEM-HAADF) and are reported in Tab. 8.1.

In order to understand why the 164 phase appears in the nanowires but not in the bulk under any experimental conditions and the origin of the twinning in nanowires, we computed the formation energy of different surfaces of the two phases. The appearance of the 164 phase could be in fact determined by the lower formation energy of its surfaces with respect to those of the 166 phase which makes the new phase favored in nanowires with a large surface to volume ratio.

Structural parameters	Theo.	Exp.
a (Å)	4.2	4.2
c (Å)	1.043	1.06
Te1	(0,0,0)	(0,0,0)
Te2	(1/3,2/3,0.6457)	(1/3,2/3,0.6385)
Sb	(1/3,2/3,0.1896)	(1/3,2/3,0.1965)

Table 8.1: Lattice parameters of SG 164 Sb_2Te_3 and atomic positions of the atoms irreducible by symmetry measured by means of STEM-HAADF and obtained from DFT.

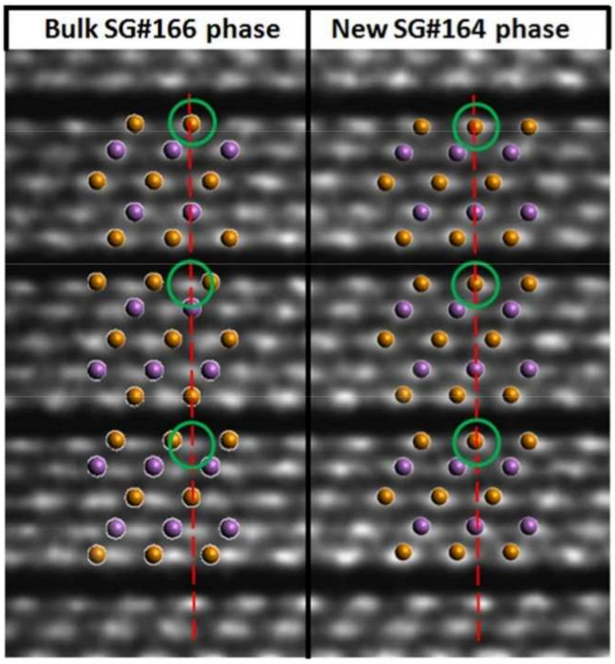

Figure 8.4: High resolution Z-contrast image of a Sb_2Te_3 NW, oriented along the [11-20] projection. The atomic model of the structure corresponding to the SG 164 and SG 166 are superimposed to the image according to the labels. To highlight the differences between the two structures. A red dashed line is drawn running parallel to the c axis and intercepting the first atomic column after each van der Waals gap, indicated by green circles.

We used PBE [81] approximation for the exchange-correlation functional with the inclusion of a semiempirical van der Waals correction according to Grimme [87]. The Kohn-Sham states were expanded on a plane wave basis up to a 35 Ry cutoff. In bulk calculations the Brillouin zone was sampled with a uniform Monkhorst-Pack mesh of 12x12x6 k-points for the hexagonal cell of the SG164-phase and of 12x12x12 k-points for the elemental rhombohedral cell of the SG166 phase. The surfaces were modeled by slabs about 30 Å thick with a vacuum 15 Å wide separating the periodic replica. The surface Brilluoin Zone was integrated with up to 6x6x1 k-point meshes.

We first computed the theoretical equilibrium cell parameters of Sb_2Te_3 in the bulk of the new SG164 phase. The structural parameters reported in Tab.8.1 are in good agreement with experimental data. Equilibrium parameters for the bulk SG166 phase are reported in Sec.3.2.1.

The internal structure of the penta-layer block is essentially the same in the two phases, the largest structural differences consisting of the stacking of the blocks which results into a different length of the weak Te-Te bond connecting the blocks (see Fig.8.3). In the SG164 phase this bond is almost 3% longer than in the SG166 phase. As expected, in the bulk the SG164 phase is higher in energy than the SG166 phase by about $\Delta\mu$=5.399 meV/atom.

To calculate the energy of the surfaces that could be exposed by a nanowire growing along the (0001) direction observed experimentally, we built slabs exposing the (11-20), (1-100), (1-102) surfaces for the SG166 phase and the (11-20),(1-100),(1-101) surfaces for the SG164 phase. The overall less costly surface is actually the (0001) face for both phases, which however can not be exposed by a wire growing along the (0001) direction.

The (11-20) and (1-100) surfaces are the lowest indexes surfaces parallel to the c-axis; the (1-101) face corresponds to the surface observed experimentally in SG164 nanowires, while the (1-102) is the surface of the SG166 phase most similar to the (1-101) of the SG164 phase. We considered different possible reconstructions of the (1-100),(1-102) and (1-101) surfaces needed to keep the stoichiometry and the surface neutrality. On the other hand the (11-20) surface is already neutral and does not need any reconstruction. The lowest energy reconstruction for each surface is reported in Figs.8.5 and 8.6.

We calculated the surface energy as the difference between the energy of the slabs and the energy of a bulk with an equivalent number of atoms divided by twice the surface area. The results are summarized in Tab.8.2.

The surface energies of the SG164 phase are lower than those of the phase SG166 for all faces.

Surface energy SG166	(11-20)	(1-100)	(1-102)
meV/Å^2	34.4	32.3	32.9
Surface energy SG164	(11-20)	(1-100)	(1-101)
meV/Å^2	34.1	31.0	27.4

Table 8.2: Surface energies for Sb_2Te_3 in the two SG166 and SG164 phases.

This is due to two concurring effects: firstly the SG164 phase is more expanded along the c direction which leads to a larger surface area for the same number of broken bonds, secondly the Te-Te bonds broken at the surface are stronger (shorter) in the SG166 phase than in the SG164 one. Therefore the NW geometry stabilize the SG164 phase because its surfaces have a lower energy than those of the SG166 phase. Moreover, experimentally the 164 phase is seen only when Sb_2Te_3 is doped with Ge for about 3 atom%. Indeed we have found that the difference in the bulk energy between the SG164 and SG166 phase is reduced to $\Delta\mu$= 4.8 meV when Sb is substituted by Ge for about 6.6 atom% (one Ge atom in a 15-atom cell). The (1-101) surface experimentally observed to be exposed by our NWs, results to be the most stable face of the SG164 phase. This plane does not contain the c axis and forms an angle of 19.6° with the NW growth direction.

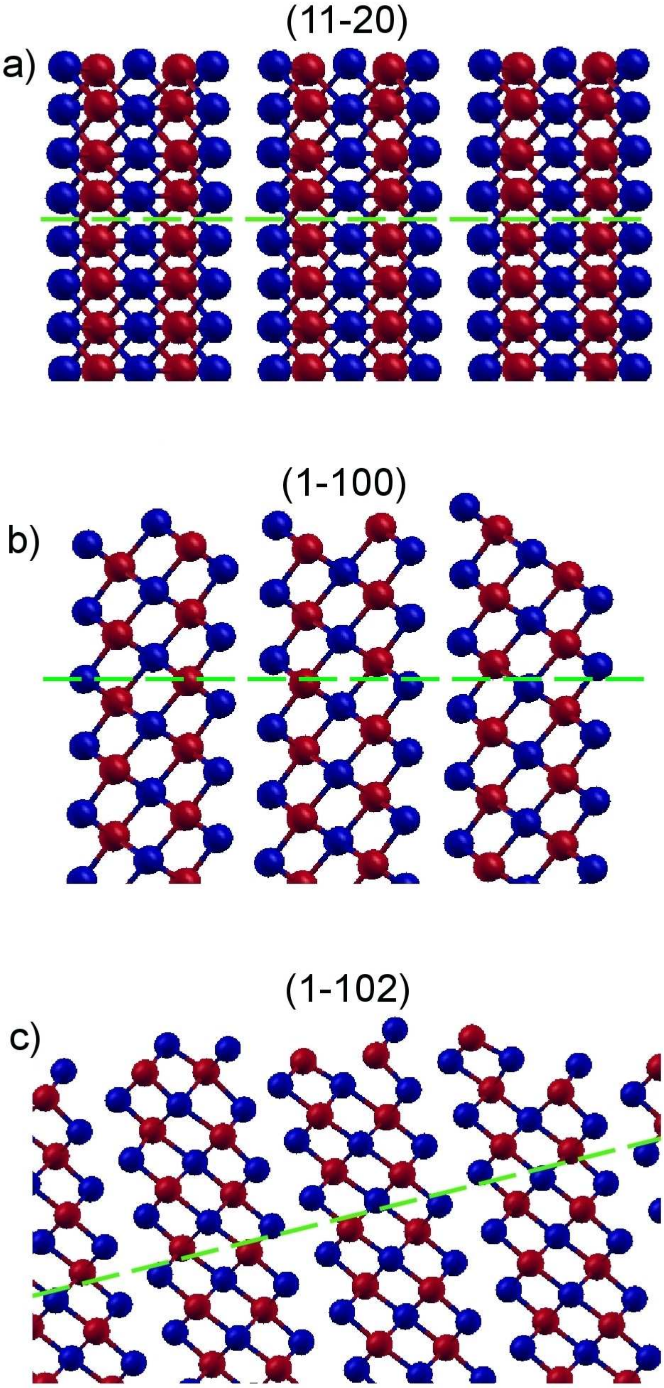

Figure 8.5: Lower energy surfaces of Sb_2Te_3 in the structure corresponding to the 166 space group.

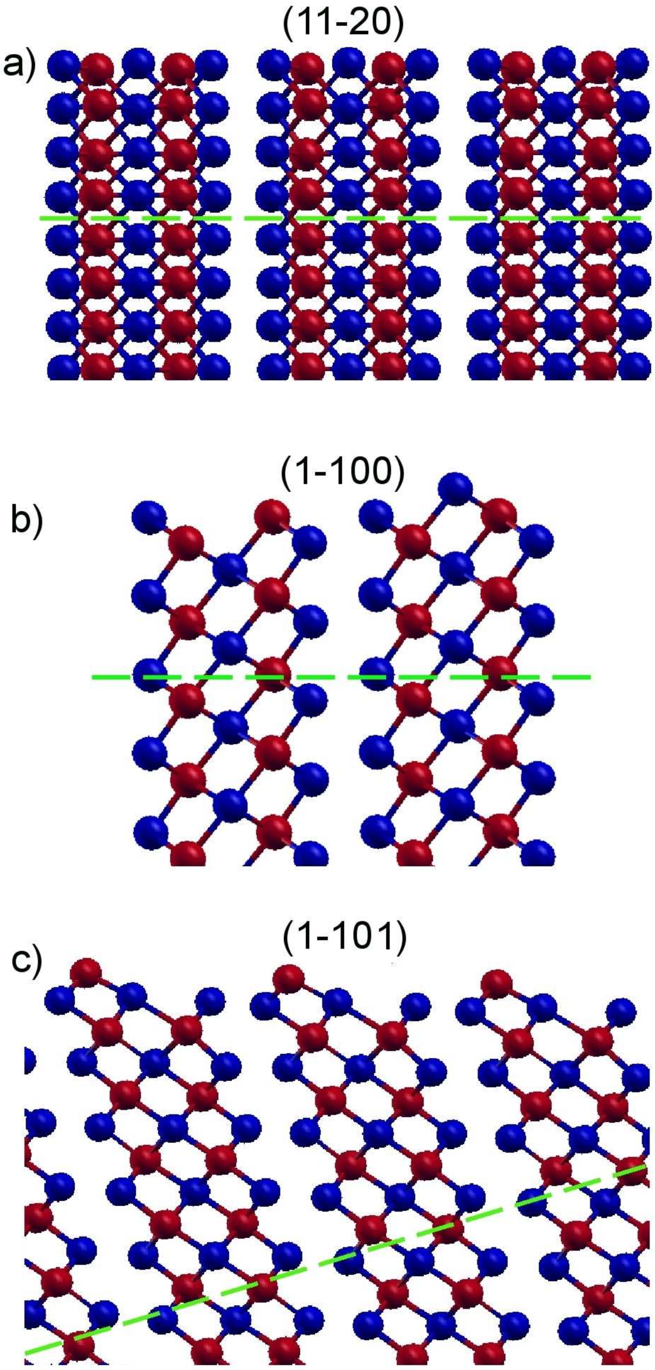

Figure 8.6: Lower energy surfaces of Sb_2Te_3 in the structure corresponding to the 164 space group.

Following the model proposed by Johansson et al.[184] the formation of the twinning can be explained as follows: a twinning forms when a NW grows trying to expose a surface (the 1-101 family in our case) that does not contain its growth direction (the [0001]); in order to maintain the growth direction, the edge of some facets increases while it decreases for the others, due to different growth rates. As a result, the hexagonal interface develops into a triangle-like shape. At a certain moment, it is energetically more favorable to create a twin plane rather than to continue growing towards a fully triangular top interface.

9 Neural Network potential for GeTe Nanowires

The study of phase change materials nanowires are one of the most recent and active fields of research for the miniaturization of the PCM technology and the realization of multilevel memories as described in Sec.1.3.1. The possibility to study phase change materials nanowires using ab-initio calculations, due to the large number of atoms involved, is limited to few properties like the surface energy considered in the previous chapter for Sb_2Te_3. The study of other crucial properties like the crystallization kinetics or thermal properties requires an alternative approach with a lower computational cost. The neural network potential previously developed in our group and described in Sec.2.6.1 proved to be very effective in the description of a wide variety of bulk properties of the prototypical phase chance material GeTe. However this potential did not include any information about the surfaces. To extend the transferability of this potential to accurately describe GeTe surfaces and thus open the possibility of the first simulations of a phase change nanowire we added 12000 new surface configurations in the fitting database. After the validation of the new potential by comparison with ab-initio simulations in small systems we applied the new potential to the study of thermal conductivity in GeTe nanowires.

9.1 Validation of the GeTe potential for nanowires

We extended the transferability of the NN potential by adding in the DFT database for the NN fitting a total of 5000 slab configurations with 128 atoms each and 7000 nanowires configurations with 128-256 atoms in the crystalline, amorphous and liquid states. An initial set of configurations have been generated from short ab-initio molecular dynamics simulations using the CP2K [185] code and the computational settings used in previous works at which we refer to for further details [12]. A first generation of the new neural network potential was built by including these first configurations and a set of unrelaxed surface configurations generated simply by cutting the bulk. Subsequently new configurations have been extracted from molecular dynamics runs executed with the most updated version of the potential and the potential was iteratively refined.

As a first step to validate the new potential we calculated the equilibrium lattice parameter for α-GeTe. The results reported in Tab.9.1 together with the equilibrium parameters of the previous version of the neural network potential, are in very good agreement with both the ab-initio results and the experimental values.

	NewNN	OldNN	DFT-PBE	Exp.
a (Å)	4.31	4.47	4.33	4.31
α	58.77°	55.07°	58.14°	57.90°
x	0.2357	0.2324	0.2358	0.2366
long,short bonds (Å)	2.85,3.21	2.81,3.31	2.85,3.21	2.84,3.17

Table 9.1: Lattice parameters of GeTe calculated with the new version of the NN potential compared with the old version of the NN potential, the ab-initio and the experimental values.

The structural properties of the bulk liquid are also well reproduced as can be inferred from Fig.9.2 where we compared the pair correlation function $g(r)$ of NN and DFT simulations performed with the CP2K code [185] with the same computational settings of Ref.[12]. The pair correlation function is defined in Eq.9.1 where η and μ indicate the atomic specie, N_η is the number of atom of the specie η, ρ_μ is the density of the atomic specie μ and r_{ij} is the distance between the atom i and j.

$$g_{\eta\mu}(r) = \frac{1}{4\pi r^2 N_\eta \rho_\mu} \sum_{i\in\eta} \sum_{j\in\mu\neq i} \delta(r - r_{ij}) \tag{9.1}$$

The pair correlation functions and the angular distribution functions for a 256-atom nanowire at 700K calculated with NN and ab-initio are reported in Fig.9.3 and 9.4 respectively. Also in this case the agreement is pretty good proving the effectiveness of the new potential in reproducing the effects of low dimensionality. A snapshot of the nanowire is shown in Fig.9.1.

As a further validation we compared the surface energy of the (2-10) surface obtained from neural network potential and ab initio calculations. The energy predicted by the NN turned out to be 8% lower than the DFT value, an error comparable to the difference in surface energy estimated with different ab-initio potentials. The choice of this surface was dictated by the fact that it is a neutral and stoichiometric surface that does not give rise to an electric dipole in slab configuration. The presence of a dipole (for example in the case of the (001) surface where one surface of the slab is terminated by Te atoms and the other by Ge atoms) represent an obstacle in the calculation of the surface energy in ab initio calculations since it introduces an additional energy term which diverges with the slab size. On the other hand it is impossible to estimate the surface energy of non stoichiometric slabs within the neural network scheme since is not possible to estimate the chemical potential of a single specie. The possible surface reconstructions suitable to eliminate the dipole is therefore considerably restricted by the constraint of keeping the stoichiometric fixed.

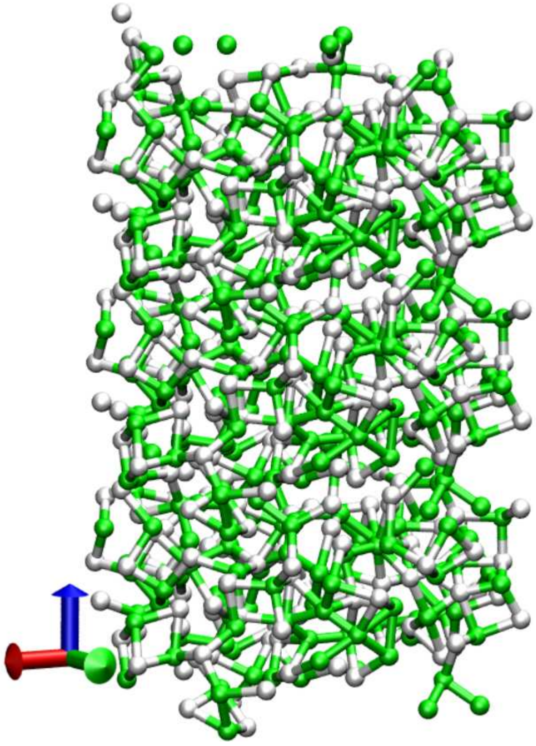

Figure 9.1: Snaposhot of the MD simulation of the 256 atoms amorphous nanowire used for the validation of the potential. The pictures represent three unit cells repeated along the direction of growth of the nanowire.

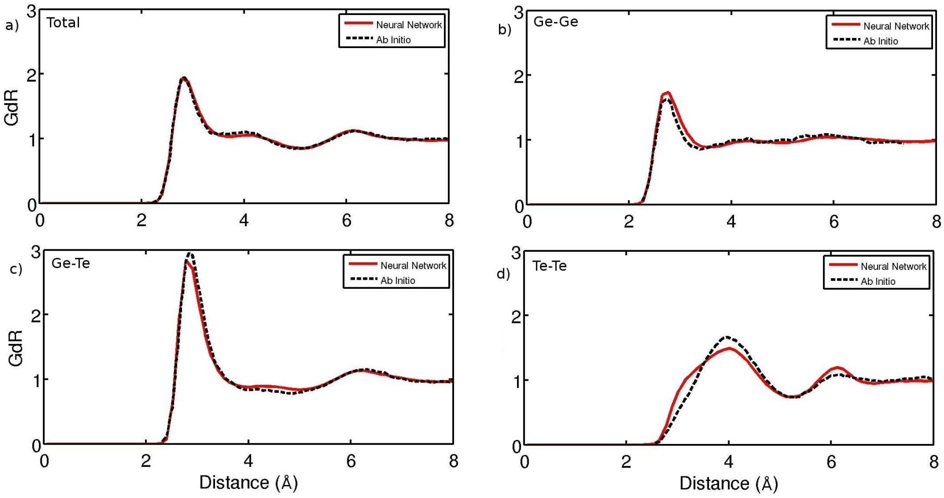

Figure 9.2: Partial pair correlation functions of liquid bulk GeTe at 1150 K calculated with the new version of the NN potential and from DFT simulations.

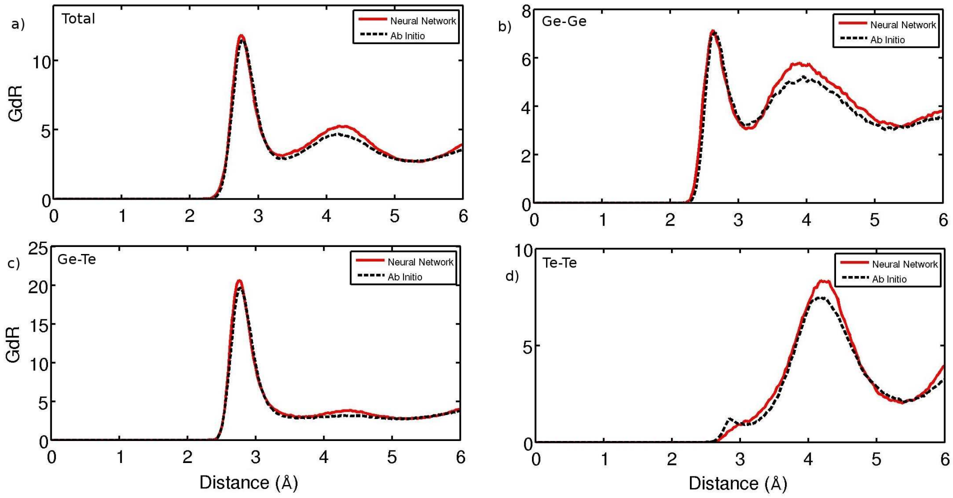

Figure 9.3: Partial pair correlation functions of amorphous nanowire of GeTe at 700 K calculated with the new version of the NN potential and from DFT simulations.

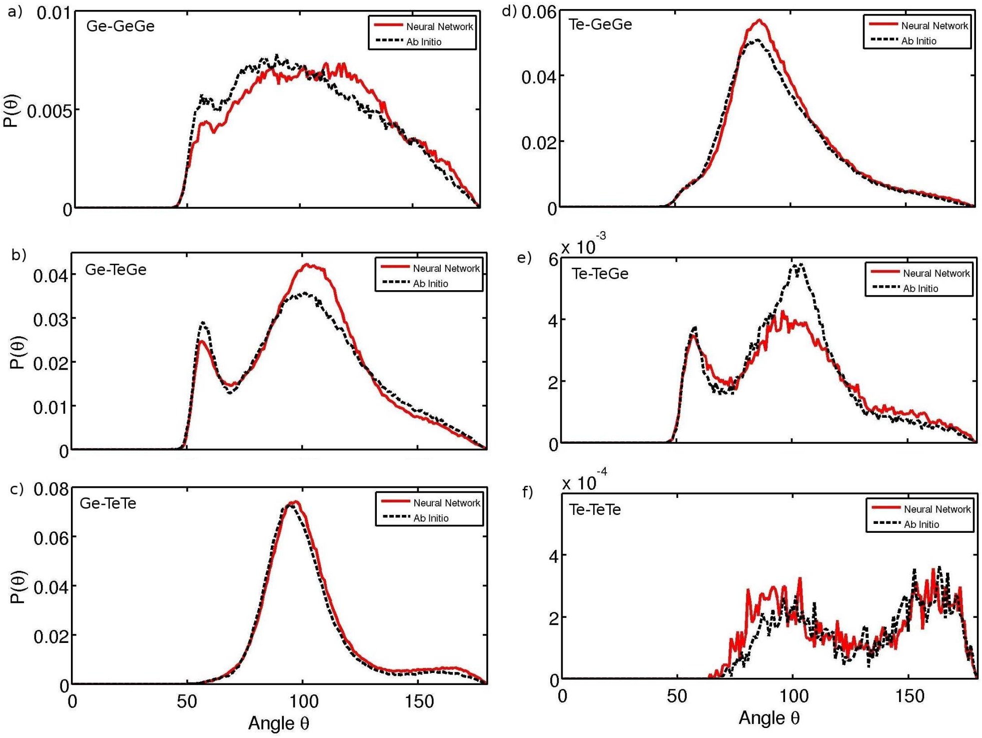

Figure 9.4: Angular distribution function of amorphous nanowire of GeTe at 700 K calculated with the new version of the NN potential and from DFT simulations.

Finally, we compared the surface relaxations of the (001) and (2-10) surfaces in the DFT and NN case. A disagreement below 4% among the two methods has been observed on the values of surface relaxations with respect to their relative bulk equilibrium positions.

In the perspective to study thermal properties in nanowires, we also checked that the new potential is still able to reproduce the thermal conductivity in both crystalline and amorphous phases. A good agreement with the previous results has been obtained in both cases. A value of κ_z=2.44 ± 0.15 W/m K inferred form the heat flux and temperature profile reported in Fig. 9.5 was obtained for a crystalline sample 25.6 nm long in close agreement with the value of κ_z=2.55 ± 0.25 W/m K obtained with the previous version of the potential. Finally the thermal conductivity computed for a 24.7 Å x 24.7 Å x 98.8 Å amorphous sample (cf. Fig. 9.6) resulted to be κ=0.24 ± 0.02 W/m K consistent with the value of κ=0.26 ± 0.02 W/m K previously obtained.

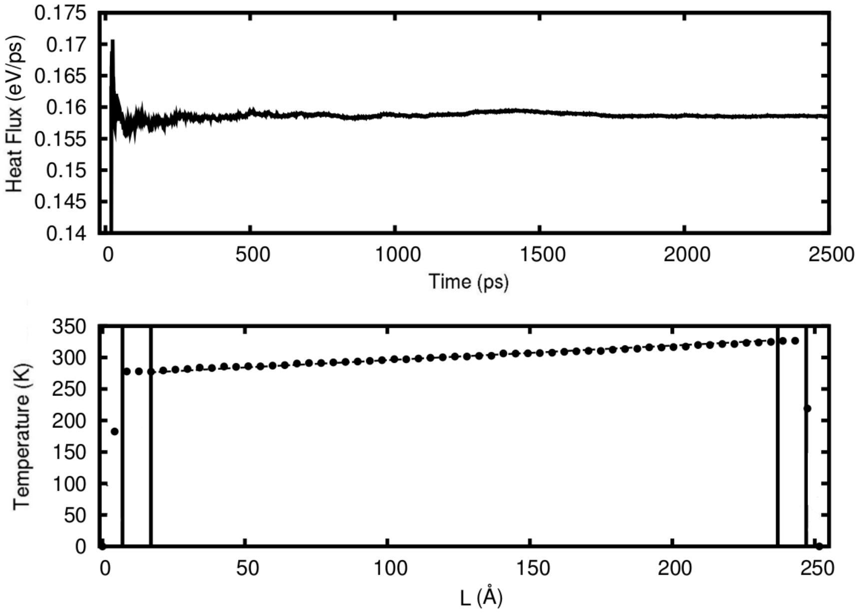

Figure 9.5: Heat flux as a function of time and converged temperature profile for a crystalline GeTe sample 25.6 nm long calculated with the new NN potential. The heat flux is directed along the c axis of GeTe.

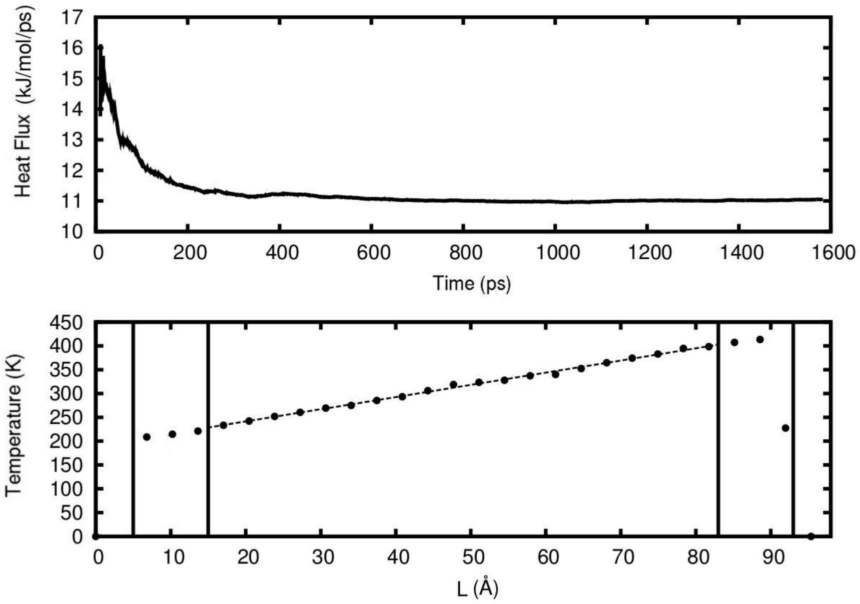

Figure 9.6: Heat flux as a function of time and converged temperature profile for an amorphous GeTe sample calculated with the new NN potential.

9.2 Thermal transport in GeTe Nanowires

In this section, we report on the calculation of thermal conductivity in GeTe nanowires carried out in order to understand the effects of a reduced dimensionality on the thermal properties. We focused on α-GeTe nanowires grown in the [220] direction (in hexagonal) notation equivalent to the [110] direction of the cubic crystal the trigonal phase of α-GeTe can be thought as originating from. The choice of the crystalline phase and growth direction are dictated by various experimental works in Refs.[186–189]. Moreover, it has been reported [186, 187] that also nanowires initially grown in the β-phase along the [110] direction turns into the more stable α-phase after one cycle of amorphization and recrystallization and it is likely that it keeps the same growth direction. The diameter of experimental GeTe nanowires is in the 40-100 nm range, too large to be directly addressed by RNEMD even using the neural network potential. However, the growth of nanowires with diameters even below 10 nm is expected and is considered an important goal for technological applications. For this reason a 6.5 nm wide nanowire has been used in these preliminary calculations. But for the growth direction, experiments do not provide information on the geometry of the exposed surfaces. A direct evaluation of the surface energy for non stochiometric slabs is not possible within the NN scheme. Therefore we used the relative melting temperatures of different surfaces as a way to assess which surface is energetically more favorable. It turned out that the tellurium-terminated (001) surfaces and the $(1\bar{1}2)$ surface in hexagonal notation (four index notation with the redundant index omitted as usually reported in literature) are the most stable. A plausible shape of the nanowire is shown in Fig.9.7 with a hexagonal geometry exposing four (001) surfaces terminated with Te atoms and two ($1\bar{1}2$) surfaces. This is the model of the nanowire employed for calculations of thermal conductivity.

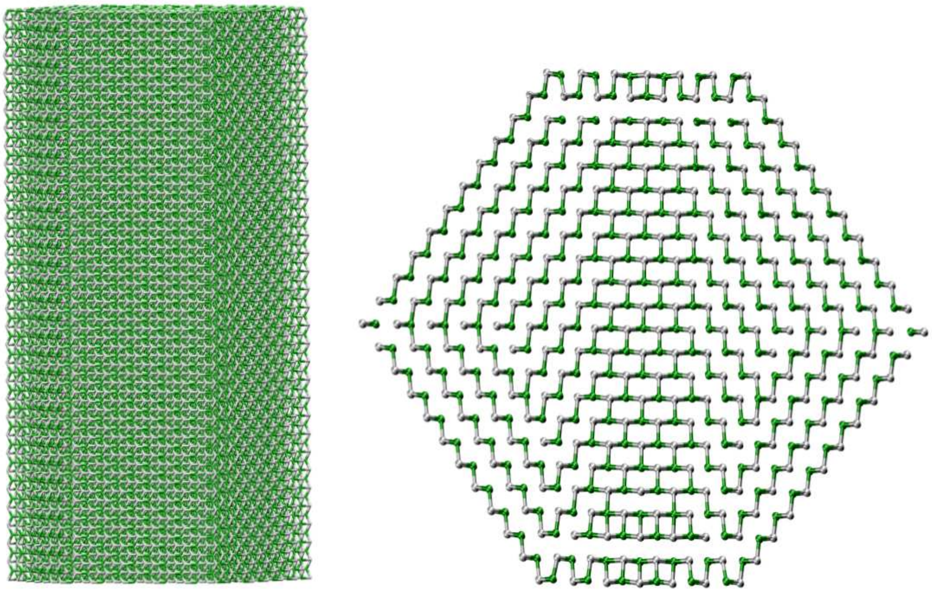

Figure 9.7: Model of the GeTe nanowire used for the calculation of thermal conductivity.

Simulations at 700 K proved the stability of the structure and showed that the lateral surfaces reconstruct forming a unitary cell of 16.53 Å along the NW growth direction, four times longer than the unitary cell obtained by truncating the bulk. The thermal conductivity has been evaluated by means of RNEMD at 300 K using a 390 Å long cell with one cold source and one hot source at the edges separated by a layer of fixed atoms 10 Å thick as in the bulk calculations (see Sec.2.5). The heat flux and temperature profile for this system are reported in Fig.9.8. The system is free of Ge vacancies. The resulting thermal conductivity is κ_{NW}=1.57±0.04 W/m K, considerably lower than the bulk value of κ=3.15±0.20 W/m K obtained from NN calculations for this crystalline direction.

Phonon scattering from the boundaries can reasonably be considered as a possible source for the reduced thermal conductivity in nanowires. To quantify the possible effect of the reduced dimensionality on thermal conductivity we looked back at the results obtained for the bulk with ab-initio techniques reported in Sec.2.3. In particular we evaluated the bulk thermal conductivity setting the upper limit of the mean free path all phonons equal to the diameter of the nanowire. This approximation represents a sensible overestimation of the effect of reduced dimensionality since limits the thermal conductivity in every direction while in the nanowire the boundaries does not limit the mean free path along the direction of growth of the wire. Anyway, we obtained a reduction of κ of of about 30% insufficient to explain alone the reduction

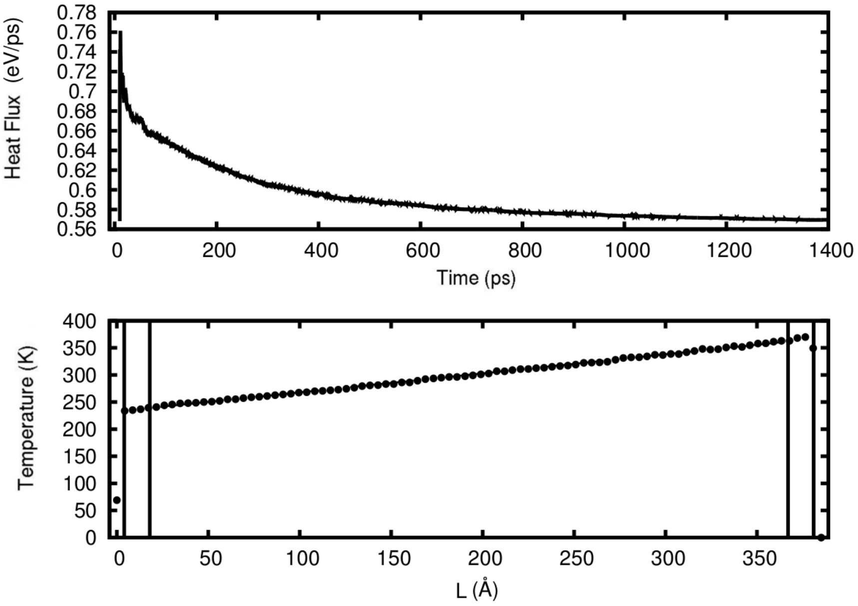

Figure 9.8: Heat flux as a function of time and converged temperature profile for a crystalline GeTe nanowire

in thermal conductivity calculated with the direct RNEMD calculation. Therefore the scattering from the NW is surely not enough to explain the reduced thermal conductivity of the NW.

To clarify the source of the reduced thermal conductivity we thus studied the effect of the reduced dimensionality on the phonon density of states and group velocities by assigning, as a first step, the values computed for the bulk to the phonon lifetimes. Due to the large unit cell of the nanowire the calculation of phonon lifetimes from the anharmonic force constants described in Sec.2.3 and used for crystalline bulk systems, is not a viable option. To this aim, we first verified for the bulk the effect of substituting the integral over the Brillouin zone with an integral over the phonon energy by writing the thermal conductivity as in Eq.9.2.

$$\kappa = \frac{1}{3}\int \hbar\omega D(\omega) v^2(\omega) \frac{\partial f_{BE}(\omega)}{\partial T} \tau(\omega) d\omega \qquad (9.2)$$

Where D is the phonon density of states per unit volume, v is the group velocity, τ the phonon lifetime and f_{BE} is the Bose-Einsten distribution function. The quantities $v^2(\omega)$ and $\tau(\omega)$ are obtained for the bulk as averages over the Brillouin zone defined by Eqs.9.3

$$v^2(\omega) = \frac{\sum_{j,\mathbf{q}} \mid \overrightarrow{v}_j(\mathbf{q}) \mid^2 \delta(\omega - \omega_j(\mathbf{q})}{\sum_{j,\mathbf{q}} \delta(\omega - \omega_j(\mathbf{q}))}$$

$$\tau(\omega) = \frac{\sum_{j,\mathbf{q}} \tau_j(\mathbf{q}) \delta(\omega - \omega_j(\mathbf{q})}{\sum_{j,\mathbf{q}} \delta(\omega - \omega_j(\mathbf{q}))}. \quad (9.3)$$

For the bulk the dynamical matrix was calculated within the NN scheme by finite difference on a 10x10x10 supercell, the phonon density of states $D(\omega)$ was determined by Fourier interpolating the dynamical matrix over 125000 **q**-points, the group velocities were calculated differentiating the phonon dispersion curves interpolated over 15625 **q**-points. The relaxation times were obtained from the anharmonic NN force constants computed by finite differences in a 1008 atom supercell and by sampling the Brillouin Zone with the Γ-point only. The above procedure yields an average thermal conductivity of κ=3.24 W/m K which is very close to the value κ=3.20 W/m K obtained in Sec.3.1.3 using RNEMD proving the effectiveness of Eq.9.2 for the bulk. As a further check we used Eqs.9.2 and 9.3 with ab-initio phonon density of states, group velocities and relaxation times obtaining a value that differs by less than 7% from the SMA solution of the Boltzmann equation carried out in Sec.3.1.2 integrating over the whole BZ.

We thus used Eq.9.2 to determine the effect on thermal conductivity of the changes in $D(\omega)$ and $v^2(\omega)$ from the bulk to the nanowire.

The phonon density of states and group velocities for the nanowire were calculated starting from harmonic force constants calculated with a finite difference method in the elementary cell of the nanowire along the growth direction 16.93 Å long and containing 2164 atoms. Phonon dispersion relations were then Fourier interpolated over a 100 **q**-point mesh in the direction of the nanowire. The resulting density of states and group velocity as a function of the phonon frequency are compared to the bulk values in Fig.9.9 and Fig.9.10 respectively.

We then computed the thermal conductivity of the nanowire either by Eq.9.4 where we used the phonon density of the nanowire but the bulk values for the group velocities and the relaxation times and by Eq. 9.5, (where also the group velocities are computed for the nanowire). We used the bulk values for the function $\tau(\omega)$.

$$\kappa_{NW1} = \frac{1}{3}\int \hbar\omega D(\omega)_{NW} v^2(\omega)_{BULK} \frac{\partial f_{BE}(\omega)}{\partial T} \tau(\omega)_{BULK} d\omega \quad (9.4)$$

$$\kappa_{NW2} = \frac{1}{3}\int \hbar\omega D(\omega)_{NW} v^2(\omega)_{NW} \frac{\partial f_{BE}(\omega)}{\partial T} \tau(\omega)_{BULK} d\omega \quad (9.5)$$

The thermal conductivities computed using Eq.9.4 and Eq.9.5 are κ_{NW1}=3.64 W/m K which is larger than the value obtained for the bulk, and κ_{NW2}=1.54 W/m K which is very close to value obtained by RNEMD. We can conclude that the changes in the phonon density of states

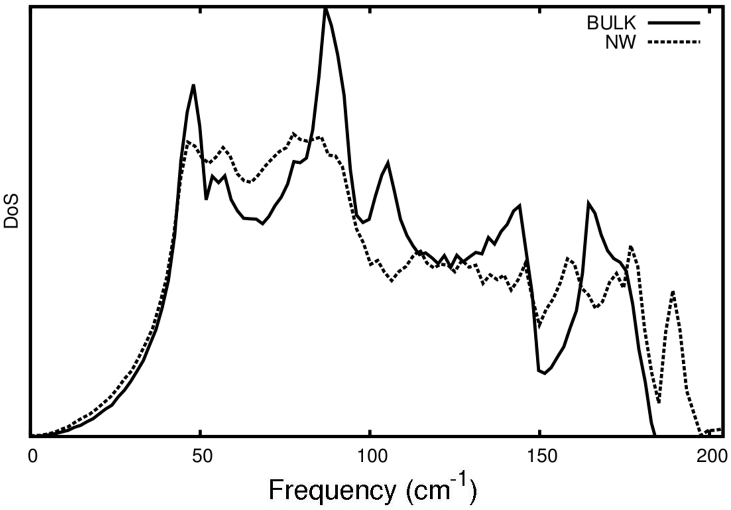

Figure 9.9: Phonon density of states of bulk α-GeTe and of the crystalline nanowire.

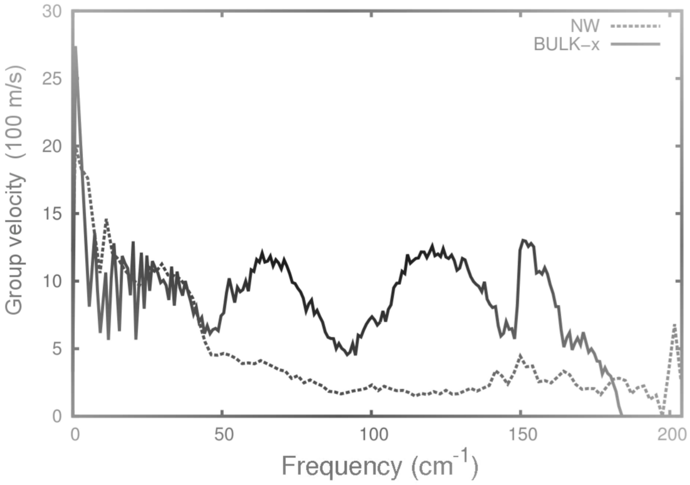

Figure 9.10: Group velocity of bulk α-GeTe and of the crystalline nanowire along the direction of growth of the nanowire.

does not play any role in the reduction of the thermal conductivity (it actually increase the thermal conductivity with respect to the bulk) while a major role is played by the reduction of the group velocity (See Fig.9.10). These results gives the first indications about the effect of nanostructuring on thermal conductivity and represents the first step towards a more systematic study of GeTe nanowires for example as a function of the diameter. These results show that in ultrathin nanowires the thermal conductivity is sizable reduced with respect to the bulk value. The electrothermal modeling of PCM made of NW thus requires parameters specific for the NW that cannot be inferred from the bulk values.

Conclusions

In the first part of this thesis we presented a study, based upon DFT calculations, of the thermal conductivity and thermal boundary resistance of some of the most common phase change materials: GST, GeTe and partially InSbTe alloys.

The calculation of the thermal conductivity in crystalline GeTe allowed us to attribute the large variability of experimental data to the important role of the scattering from vacancies whose concentration in GeTe can hardly be controlled. The comparison between ab-initio calculations based on the solution of the Boltzmann transport equation and the results for non-equilibrium molecular dynamics allowed us to check the reliability of the neural network potential in the description of anharmonic properties of GeTe, and on the other hand to validate the approximation assumed in the treatment of vacancies within the DFT approach.

The study of thermal conductivity in crystalline hexagonal GST provided a strong indication of the presence of disorder in the Ge/Sb sublattice which is still subject of debate in literature. In fact both vacancies and disorder turned out to be essential to reach a good agreement with experimental data and explain the unusual glass-like thermal conductivity of this material.

The knowledge of thermal boundary resistance plays an important role in the electrothermal modeling of the device. In particular it is important to know the different contributions to the resistance is in order to properly engineer the materials and the device architecture. Ab initio calculations of the electron-phonon interaction in self doped GeTe and GST allowed us to estimate the electron-phonon contribution to the thermal boundary resistance for these materials. This term, usually negligible in good metals, turned out to be relevant and actually even larger than the phonon-phonon contribution to the TBR due to the peculiar combination of small electron-phonon coupling and low density of states at the Fermi level but a still appreciable electronic thermal conductivity. This implies that the value of the thermal boundary resistance at an ideal interface is more dependent on the properties of the phase change material itself than on the choice of the interfacing material.

Beside the optimization of conventional PCM cells, recent progresses pushed the interest also in the direction of novel device architectures.

Among the most promising developments, interfacial phase change memories represent a great advance towards low power applications. Although their potential in reducing the programming current has been proved, their exact structure and the transition mechanism are still matter of debate. The ab initio calculation of the Raman spectra for some of the most likely structures proved that vibrational spectroscopy could be used to discriminate among different proposals and possibly also to determine the intermediates in the transition mechanism. Similarly, the Raman spectra calculated for multilayer GeTe structures helped clarifying the evolution with the thickness of the Raman peaks observed experimentally and understand the growth mechanism.

As a side activity we also analyzed the interaction between phonons and the topologically protected states appearing at the surface of the topological insulator Sb_2Te_3 and, for sake of comparison Bi_2Se_3 as well. These states have been proposed to appear also at the interface between Sb_2Te_3 and the GeTe blocks in iPCM superlattices and to be involved in the switching of the device. As opposed to some claims drawn from Helium scattering data, we do not find a strong electron-phonon coupling at the surface of Sb_2Te_3 and Bi_2Se_3.

Nanowires have also attracted a considerable interest for PCM applications because they open the possibility to improve the scaling and to overcome the size limitations intrinsic to lithographic methods. Moreover, they offer a practical way for the realization of multibit memories. The study of the surface energy of Sb_2Te_3 nanowires provided an explanation for the peculiar morphology and the unusual crystal structure observed experimentally, in nanowires but absent in the bulk. We have shown that this new phase is stabilized in nanowires as a consequence of its lower surface energy with respect to the bulk Sb_2Te_3 structure.

Finally, the neural network potential developed to describe bulk GeTe has been successfully extended to treat also surfaces and nanowires in order to study the effects of the reduced dimensionality on thermal properties, crystallization and amorphous stability. This extension allowed us to perform a preliminary study of the thermal conductivity in GeTe nanowires which revealed a sizable reduction of thermal conductivity in nanowires primarily due to reduction in group velocities due to phonon confinement.

Publications

Works related to this thesis

- D. Campi, D. Donadio, G.C. Sosso, J. Behler, M. Bernasconi,
  “Electron-phonon interaction and thermal boundary resistance at the crystal-amorphous interface of the phase change compound GeTe”, Journal of Applied Physics **117**, 15304 (2015).

- D. Campi, E. Baldi, G. Graceffa, G.C. Sosso, M. Bernasconi
  “Electron-phonon interaction and thermal boundary resistance at the interfaces of $Ge_2Sb_2Te_5$ *with metals and dielectrics”*, Journal of Physics: Condensed Matter **27**, 175009 (2015).

- E. Rotunno, M. Longo, C. Wiemer, R. Fallica, D. Campi, M. Bernasconi, A. Lupini, S. Pennycook
  “A novel Sb_2Te_3 *polymorph stable at the nanoscale”*, ACS Chemistry of Materials **27**, 4368 (2015).

- D. Campi, M. Bernasconi, G. Benedek, J.P. Toennies,
  “Surface Dynamics of Xe(111): An Ambiguous Nobility”, Journal of Physical Chemistry C **119**, 14579 (2015).

- R. Wang, D. Campi, J. Momand, B. J. Kooi, M. Bernasconi, R. Calarco
  “Peierls distortion prevented at growth onset of GeTe ultra-thin films”; submitted.

- D. Campi, M. Bernasconi
  “Raman spectra of GeTe/Sb_2Te_3 *superlattice from first principles”*; submitted.

- D. Campi, L. Paulatto, G. Fugallo, F. Mauri, M. Bernasconi
  “First principles calculation of lattice thermal conductivity in crystalline phase change materials: $Ge_2Sb_2Te_5$, Sb_2Te_3 *and GeTe”*; in preparation.

- J.-L. Battaglia, A. Kusiak, C. Gaborieau, Y. Anguy, H. T. Nguyen, C. Wiemer, M. Longo, D. Campi, M. Bernasconi, R. Fallica
  “$In_3Sb_\beta Te_\gamma$ *thin film structure and thermal conductivity up to 550 °C”*; in preparation.

Other publications in the period 2013-2015

- G. Benedek, M. Bernasconi, K.P. Bohnen, D. Campi, E.V. Chulkov, P.M. Echenique, R. Heid, I.Y. Sklyadneva, J.P Toennies
  “*Unveiling mode-selected electron-phonon interactions in metal films by helium atom scattering*” Physical Chemistry Chemical Physics **16**, 7159 (2014).

- R.D. Brown, Z.M. Hund, D. Campi, L.E. OĹeary, N.S. Lewis, M. Bernasconi, G. Benedek, S.J. Sibener
  “*The interaction of organic adsorbate vibrations with substrate lattice waves in methyl-Si(111)-(1x1)*” Journal of Chemical Physics **141**, 024702 (2014).

- Z.M. Hund, K.J. Nihill, D. Campi, K.T. Wong, N.S. Lewis, M. Bernasconi, G. Benedek, S.J. Sibener
  “*Atomic Surface Structure of CH3-Ge(111) Characterized by Helium Atom Diffraction and Density Functional Theory*” Journal of Physical Chemistry C **119**, 18458 (2015).

- Z.M. Hund, K.J. Nihill, D. Campi, K.T. Wong, N.S. Lewis, M. Bernasconi, G. Benedek, S.J. Sibener
  “*Vibrational dynamics and band structure of methyl-terminated Ge(111)*” Journal of Chemical Physics **143**, 124705 (2015).

- D. Maccariello, D. Campi, A. Al Taleb, G. Benedek, D. Farias, M. Bernasconi, R. Miranda
  “*Low-energy excitations of graphene on Ru(0001)*” Carbon **93**, 1 (2015).

- A. Molle, F. Fabbri, D. Campi, A. Lamperti, E. Rotunno, E. Cinquanta, L. Lazzarini, D. Kaplan, V. Shwaminathan, M. Bernasconi, M. Longo, G. Salviati
  “*Native Cesium Doping and temperature dependent n-type electronic transport in a MoS_2 multilayer crystal*”; submitted.

- M. Wiesner, A. Trzaskowska, B. Morz, S. Charpentier, S. Wang, Y. Song, F. Lombardi, P. Lucignano, D. Campi, M. Bernasconi, G. Benedek, F. Guinea, A. Tagliacozzo
  “*Probing Deep Interface Electron-Phonon Interaction in Bi_2Te_3/GaAs with Brillouin Scattering*”; submitted.

- D. Campi, A.P. Graham, M. Bernasconi, G. Bendek, J.P. Toennies
  “*Surface lattice dynamics of Cs*”; in preparation.

Collaborations

This work has been possible thanks to the collaboration with several experimental and theoretical groups:

- The groups of M. Longo (CNR laboratory in Agrate) and L. Lazzarini (CNR laboratory in Parma) who have grown and characterized the Sb_2Te_3 nanowires.
- The group of J.L. Battaglia (University of Bordeaux) who measured the thermal conductivity and thermal boundary resistance of phase change materials.
- The groups of V. DeRenzi (University of Modena) and A. Politano (University of Calabria) who measured surface phonons of Bi_2Se_3 and Sb_2Te_3 by HREELS.
- The group of R. Calarco (Paul Drude Institute, Berlin) who has grown and characterized GeTe multilayers.
- The group of D. Donadio (MPIP Mainz) where I spent a secondment period of one month and where I have been introduced to the use of non-equilibrium molecular dynamics.
- The group of F. Mauri (IMPMC and University Pierre et Marie Curie, Paris) where I spent two secondments periods of one and two month respectively during which I have been introduced to two theoretical methods developed by them: the variational method for the solution of the Boltzmann transport equation and the self-consistent phonon method that I have applied to the study of the $\alpha \longrightarrow \beta$ transition in GeTe, a work still in progress not reported in the present thesis.

Bibliography

[1] A. L. Lacaita, *Sol. Stat. Elec.* **50**, 24 (2006).

[2] A. L. Lacaita and D. J. Wonters, *Phys. Stat. Sol. (a)* **205**, 2281 (2008).

[3] G. Burr, B. N. Kurdi, J. C. Scott, C. H. Lam, K. Gopalakrishnan and R. S. Shenoy, *IBM J. Res. Dev.* **52**, 449 (2008).

[4] M. Suri, O. Bichler, D. Querlioz, O. Cueto, L. Perniola, V. Sousa, D. Vuillaume, C. Gamrat, B. De Salvo, *IEEE Int. Electron Dev. Mtg.* 4.4.1 (2011).

[5] D. Kuzum, R.G.D. Jeyasingh, B. Lee, H.-S.P. Wong, *Nano Lett.* **12**, 2179 (2012).

[6] A. Pirovano, A. L. Lacaita, A. Benvenuti, F. Pellizzer, S. Hudgens, and R. Bez, *IEEE International Electron Devices Meeting, 2003.*, pp. 29.6.1–29.6.4 (2003).

[7] J. P. Reifenberg, K.W. Chang, M. A. Panzer, S. Kim, J. A. Rowlette, M. Asheghi,H.-S. P. Wong, and K. E. Goodson, *IEEE Electron Device Lett.*, **31**, 56–58 (2010).

[8] U. Russo, D. Ielmini, A. Redaelli, and A. L. Lacaita, *IEEE Trans.Electron Devices* **55**, 506–514 (2008).

[9] R. Fallica, J.L. Battaglia, S. Cocco, C. Monguzzi, A. Teren, C. Wiemer, E. Varesi, R. Cecchini, A. Gotti, and M. Fanciulli, *J. Chem. Eng. Data* **54**, 1698–1701 (2009).

[10] G. Fugallo, M. Lazzeri, L. Paulatto, F. Mauri, *Phys. Rev. B* **88**, 045430 (2013).

[11] F. Muller-Plathe, J. Chem. Phys. **106**, 6082 (1997).

[12] G. C. Sosso, G. Miceli, S. Caravati, J. Behler and M. Bernasconi, *Phys. Rev. B* **85**, 174103 (2012).

[13] R. E. Simpson, P. Fons, A. V. Kolobov, T. Fukaya, M. Krbal, T. Yagi, and J. Tominaga,*Nat. Nanotechnol.* **6**, 501 (2011).

[14] D. Di Sante, P. Barone, R. Bertacco, S. Picozzi, *Adv. Mater* **25**, 2625 (2013).

[15] A. H. Edwards, H. J. Barnaby, K. A. Campbell, M. N. Kozicki, W. Liu, M. J. Marinella, *Proceeding of the IEEE* **103**, 1004–1033 (2015).

[16] Y. Jung, S.-H. Lee, A. T. Jennings and R. Agarwal, *Nano Lett. 8*, 2056 (2008).

[17] M. Wuttig and N. Yamada, *Nat. Mater.* **6**, 824–832 (2007).

[18] J. F. Dewald, A. D. Pearson, W. R. Northover and W. F. Peck, *J. Electrochem. Soc.* **109**, 243C (1962).

[19] S. R. Ovshinsky, *Phys. Rev. Lett.* **21**, 1450–3 (1968).

[20] E. T. Kim, J. Y. Lee and Y. T. Kim, *Phys. Status Solidi RRL* **3**, 103 (2009).

[21] A. Redaelli and A. Pirovano, *Nanotechnology* **22**, 254021 (2011).

[22] A. L. Lacaita and A. Redaelli, *Microelectron. Eng.* **109**, 351 (2013).

[23] http://www.intel.com/content/www/us/en/architecture-and-technology/3d-xpoint-unveiled-video.html.

[24] A. V. Kolobov, P. Fons, J. Tominaga, A. L. Ankudinov, S. N. Yannopouls and K. S. Andrikopoulos, *J. Phys.: Condens. Matter* **16**, S5103–S5108 (2004).

[25] Y. Maeda and M. Wakagi, *Jpn. J. Appl. Phys.* **30**, 101 (1991).

[26] K. Hirota, K. Nagino and G. Ohbayashi, *J. Appl. Phys.* **82**, 65 (1997).

[27] A. V. Kolobov, P. Fons, A. I. Frenkel, A. L. Ankudinov, J. Tominaga and T. Uruga, *Nat. Mater.* **3**, 703–708 (2004).

[28] K. S. Andrikopoulos, S. N. Yannopoulos, G. A. Voyiatzis, A. V. Kolobov, M. Ribes and J. Tominaga, *J. Phys.: Condens. Matter* **18**, 965–979 (2006).

[29] S. Caravati, M. Bernasconi, T. D. Kuhne, M. Krack and M. Parrinello, *Appl. Phys. Lett.* **91** 171906 (2007).

[30] R. Mazzarello, S. Caravati, S. Angioletti-Uberti, M. Bernasconi and M. Parrinello, *Phys. Rev. Lett.* **104**, 085503 (2010); **107**, 039902(E) (2011).

[31] J. Hegedüs and S. R. Elliott, *Nat. Mater.* **7**, 399 (2008).

[32] S. Kohara, K. Kato, S. Kimura, H. Tanaka, T. Usuki, K. Suzuya, H. Tanaka, Y. Moritomo, T. Matsunaga, N. Yamada, Y. Tanaka, H. Suematsu and M. Takata, *Appl. Phys. Lett.* **89**, 201910 (2006).

[33] J. Akola and R. O. Jones, *Phys. Rev. B* **76**, 235201 (2007).

[34] T. H. Lee and S. R. Elliott, *Phys. Rev. Lett.* **107**, 145702 (2011).

[35] J. Orava, A. L. Greer, B. Gholipour, D. W. Hewak and C. E. Smith, *Nat. Mater.* **11**, 279 (2012).

[36] G. C. Sosso, G. Miceli, S. Caravati, F. Giberti, J. Behler and M. Bernasconi, *J. Phys. Chem. Lett. 4*, 4241 (2013).

[37] G. C. Sosso, J. Behler and M. Bernasconi, *Phys. Status Solidi B* **249**, 1880 (2012).

[38] C. Kim, D.S. Suh, K. H. P. Kim, Y.S. Kang, T.Y. Lee, Y. Khang, and D. G. Cahill, *Appl. Phys. Lett.*, **92**, 013109 (2008).

[39] C. Xu, Z. Song, B. Liu, S. Feng, and B. Chen, *Appl. Phys. Lett.* **92**, 062103 (2008).

[40] A. M. Gibby, *Electrical Engineering*, *Stanford University*, Stanford, p. 203, (2008).

[41] F. Rao, Z. Song, L. Wu, Y. Gong, S. Feng, and B. Chen, *Solid-State Electron.* **53**, 276–278 (2009).

[42] T. D. Happ, M. Breitwisch, A. Schrott, J. B. Philipp, M. H. Lee, R. Cheek, T. Nirschl, M. Lamorey, C. H. Ho, S. H. Chen, C. F. Chen, E. Joseph, S. Zaidi, G. W. Burr, B. Yee, Y. C. Chen, S. Raoux, H. L. Lung, R. Bergmann, and C. Lam, *Symposium on VLSI Technology, Digest of Technical Papers*, pp. 120–121 (2006).

[43] F. Yan, T. J. Zhu, X. B. Zhao, and S. R. Dong, *Appl. Phys. A* **88**, 425–428 (2007).

[44] J. D. Koenig, H. Boettner, J. Tomforde, and W. Bensch, *26th International Conference on Thermoelectrics*, pp. 390–393, (2007).

[45] D. G. Cahill, *Rev. Sci.Instrum.* **61**, 802–808 (1990).

[46] J. P. Reifenberg, M. A. Panzer, S. Kim, A. M. Gibby, Y. Zhang, S. Wong, H.-S. P. Wong, E. Pop, and K. E. Goodson, *Appl. Phys. Lett.* **91**, 111904 (2007).

[47] H.K. Lyeo, D. G. Cahill, B.-S. Lee, J. R. Abelson, M.-H. Kwon, K.-B. Kim, S. G. Bishop, and B.-K. Cheong, *Appl. Phys. Lett.* **89**, 151904 (2006).

[48] J. Lee, S. Kim, R. Jeyasingh, M. Asheghi, H. S. P. Wong, and K. E. Goodson, *IEEE Electron Device Lett.* **32**, 952–954 (2011).

[49] M. Kuwahara, O. Suzuki, N. Taketoshi, Y. Yamakawa, T. Yagi, P. Fons, K. Tsutsumi, M. Suzuki, T. Fukaya, J. Tominaga, and T. Baba, *Jpn. J. Appl. Phys.* **45**, 1419–1421 (2006).

[50] W. P. Risk, C. T. Rettner, and S. Raoux, *Rev. Sci. Instrum.* **79**, 026108 (2008).

[51] R. Fallica, E. Varesi, L. Fumagalli, S. Spadoni, M. Longo, and C. Wiemer, *Phys. Status Solidi RRL* **7**, 1107–1111 (2013).

[52] C. A. Ratsifaritana and P. G. Klemens, Int. J. Thermophys. **8**, 737 (1987).

[53] C. A. Paddock and G. L. Eesley, *J. Appl. Phys.* **60**, 285–290 (1986).

[54] J. Lee, E. Bozorg-Grayeli, S. Kim, M. Asheghi, H.-S. P. Wong and K. E. Goodson, *Appl. Phys. Lett.* **102**, 191911 (2013).

[55] T. Blachowicz, M. G. Beghi, G. Guntherodt, B. Beschoten, H. Dieker, and M. Wuttig, *J. Appl.Phys.* **102**, 093519 (2007).

[56] E. T. Swartz and R. O. Pohl, *Rev. Mod. Phys.* **61**, 605–668 (1989).

[57] L. De Bellis, P. E. Phelan, and R. S. Prasher, *J. Thermophys. Heat Transfer* **14**, 144–150 (2000).

[58] W. A. Little, *Can. J. Phys.* **37**, 334–349 (1959).

[59] A. Majumdar and P. Reddy, *Appl. Phys. Lett.* **84**, 4768–4770 (2004).

[60] S. R. Ovshinsky, Q. Ye, D. A. Strand, W. Czubatyj, “Electrically erasable directly overwritable multibit single cell memory elements and arrays fabricated therefrom” *U.S. Patent Editor* (1995).

[61] S. Raoux, C. T. Rettner, J. L. Jordan-Sweet, A. J. Kellock, T. Topuria, P. M. Rice and D. C. Miller, *J. Appl. Phys.* **102**, 094305 (2007).

[62] T. Nirschl, J. B. Philipp, T. D. Happ, G. W. Burr, B. Rajendran, M.-H. Lee, A. Schrott, M. Yang, M. Breitwisch, C.-F. Chen, E. Joseph, M. Lamorey, R. Cheek, S.-H. Chen, S. Zaidi, S. Raoux, Y. C. Chen, Y. Zhu, R. Bergmann, H.-L. Lung and C. Lam, *IEEE Int. Elec. Dev. Meet.*, 461 (2007).

[63] F. Bedeschi, R. Fackenthal, C. Resta, E. M. Donze, M. Jagasivamani, E. C. Buda, F. Pellizzer, D. W. Chow, A. Cabrini, G. Calvi, R. Faravelli, A. Fantini, G. Torelli, D. Mills, R. Gastaldi and G. Casagrande, *IEEE J. Sol.-Stat. Circ.* **44**, 217 (2009).

[64] Y. F. Lai, J. Feng, B. W. Qiao, Y. F. Cai, Y. Y. Lin, T. A. Tang, B. C. Cai and B. Chen, *Appl. Phys. A, Mater. Sci. Process.* **84**, 21 (2006).

[65] F. Rao, Z. Song, M. Zhong, L. Wu, G. Feng, B. Liu, S. Feng and B. Chen, *Jpn. J. Appl. Phys.* **46**, L25 (2007).

[66] Y. Zhang, J. Feng, Y. Zhang, Z. Zhang, Y. Lin, T. Tang, B. Cai and B. Chen, *Phys. Stat. Sol., Rapid Res. Lett.* **1**, R28 (2007).

[67] B. Yu, X. Sun, S. Ju, D. B. Janes and M. Meyyappan, *IEEE Trans. Nanotech.* **7**, 496 (2008).

[68] B.L. Jackson, B. Rajendran, G.S. Corrado, M. Breitwisch, G.W. Burr, R. Cheek, K. Gopalakrishnan, S. Raoux, C.T. Rettner, A. Padilla, A.G. Schrott, R.S. Shenoy, B.N. Kurdi, C.H. Lam, D.S. Modha, *ACM J. Emerg. Technol.* **9**, 12 (2013).

[69] D. Bang, H. Awano, J. Tominaga, A. V. Kolobov, P. Fons, Y. Saito, K. Makino, T. Nakano, M. Hase, Y. Takagaki, A. Giussani, R. Calarco, and S. Murakami, *Sci. Rep.* **4**, 5727 (2014).

[70] I. I. Petrov, R. M. Imanov, Z. G. Pinsker, *Sov. Phys. Crytallogr.* **13**, 339 (1968).

[71] T. Ohyanagi et al., *Appl. Phys. Lett.* **104**, 252106 (2014).

[72] X. Yu and J. Robertson, *Sci. Reports* **5**, 12612 (2015).

[73] P. Giannozzi et al., *J. Phys.: Condens. Matter* **21**, 395502 (2009).

[74] RuNNer: A Neural Network Code for High-Dimensional Potential-Energy Surfaces, Jörg Behler, Lehrstuhl für Theoretische Chemie, Ruhr-Universität Bochum, Germany.

[75] W. Smith and T. R. Forester, *J. Mol. Graph.* **14**, 136 (1996).

[76] N.W.Ashcroft and N.D.Mermin, Thomas Learning Academic Resources Center, (1976).

[77] P.Hohenberg and W.Kohn, *Phys. Rev.* **136:B**, 864 (1964).

[78] W.Kohn and L.J.Sham, *Phys. Rev.* **140:A**, 1133 (1965).

[79] J. P. Perdew and A. Zunger, *Phys. Rev. B* **23**, 5048 (1981).

[80] J. P. Perdew and W. Yue, *Phys. Rev. B* **33**, 8800 (1986).

[81] J. P. Perdew, K. Burke and M. Ernzerhof, *Phys. Rev. Lett.* **77**, 3865 (1996).

[82] D.Vanderbilt, *Phys. Rev. B* **41**, 7892 (1990).

[83] R.Fletcher, Practical methods of optimization (2nd ed.), New York: John Wiley and Sons (1987).

[84] D.Shanno, *Math. Comput.* **24**, 647–656 (1970).

[85] L. Verlet, *Physical Review* **159**, 98 (1967).

[86] S. Grimme, *J. Comp. Chem.* **27**, 1787 (2006).

[87] S.Grimme, J.Antony, S.Ehrlich, and H.Krieg *J. Chem. Phys.* **132**, 154104 (2010).

[88] R.Car, and M.Parrinello *Phys. Rev. Lett.* **55**, 2471 (1985).

[89] P.Giannozzi. S.de Gironcoli, P.Pavone and S.Baroni *Phys. Rev. B* **43**, 7231 (1991).

[90] S.de Gironcoli *Phys. Rev. B* **51**, 6773 (1995).

[91] A.Dal Corso, A.Pasquarello and A.Baldereschi *Phys.Rev. B* **56**, 369 (1997).

[92] S.Baroni, P.Giannozzi and A.Testa *Phys. Rev. Lett.* **58**, 1861 (1987).

[93] S.Baroni, S.de Gironcoli, A.Dal Corso and P.Giannozzi *Rev. Mod. Phys.* **73**, 515 (2001).

[94] D. Campi, M. Bernasconi, G. Benedek, and J. P. Toennies, *J. Phys. Chem. C* **119**, 14579-–14584 (2015).

[95] L. Paulatto, F. Mauri, and M. Lazzeri, *Phys. Rev. B* **87**, 214303 (2013).

[96] X. Gonze and J.-P. Vigneron, Phys. Rev. B **39**, 13120 (1989).

[97] M. Omini and A. Sparavigna, *Il Nuovo Cimento D* **19**, 1537 (1997).

[98] A. Sparavigna, *Phys. Rev. B* **65**, 064305 (2002).

[99] D. A. Broido, L. Lindsay, and A. Ward, *Phys. Rev. B* **86**, 115203 (2012).

[100] P. Klemens, in *Thermal Conductivity and Lattice Vibrational Modes*, edited by F. Seitz and D. Turnbull, Solid State Physics (Academic Press, New York, 1958).

[101] R. A. H. Hamilton and J. E. Parrot, *Phys. Rev.* **178**, 1284 (1969).

[102] D. Frenkel and B. Smit, *Understanding molecular simulation*, Academic Press.

[103] M. Allen and D. Tildesley, *Computer Simulation of Liquids*, Clarendon Press – Oxford (1989).

[104] L. Verlet, *Phys. Rev.* **159**, 98 (1967).

[105] L. Verlet, *Phys. Rev.* **165**, 201 (1967).

[106] A.J.C.Ladd, B.Moran, and W. G. Hoover, *Phys. Rev. B* **34**, 5058 (1986).

[107] J. Behler and M. Parrinello, *Phys. Rev. Lett.* **98**, 146401 (2007).

[108] A. Waibel, *Neural Comp.* **1**, 39 (2008).

[109] K. Funahashi, *Neural Networks* **2**, 183 (1989).

[110] G. Cybenko, *Math. Contr. Sign. Sys.* **2**, 303 (1989).

[111] H. Gassner, M. Probst, A. Lauenstein and K. Hermansson, **J. Phys. Chem. A** *102*, 4596 (1998).

[112] J. Behler, K. Reuter and M. Scheffler, *Phys. Rev. B* **77**, 115421 (2008).

[113] S. Hobday, R. Smith and J. Belbruno, *Model. Simul. Mater. Sci. Eng.* **7**, 397 (1999).

[114] A. Bholoa, S. Kenny and R. Smith, *Nucl. Instrum. Methods Phys. Res. Sect. B* **255**, 1 (2006).

[115] G. C. Sosso, J. Colombo, E. Del Gado, J. Behler and M. Bernasconi, *J. Phys. Chem. B* **118**, 13621 (2014).

[116] G. C. Sosso, D. Donadio, S. Caravati, J. Behler, and M. Bernasconi, *Phys. Rev. B* **86**, 104301 (2012).

[117] S. Gabardi, S. Caravati, G. C. Sosso, J. Behler, and M. Bernasconi *Phys. Rev. B* **92**, 054201 (2015).

[118] J. P. Reifenberg, D. L. Kencke, and K. E. Goodson, *IEEE Elec. Dev. Lett.* **29**, 1112 (2008).

[119] E. Bozorg-Grayeli, J. P. Reifenberg, M. Asheghi, H.-S. P. Wong, and K. E. Goodson, *Annual Review of Heat Transfer* **15**, 397 (2013).

[120] K. S. Siegert, F. R. L. Lange, E. R. Sittner, H. Volker, C. Schlockermann, T. Siegrist, and M Wuttig, *Rep. Prog. Phys.* **78** 013001 (2015).

[121] L. E. Shelimova, O. G. Karpinskii, P. P. Konstantinov, M. A. Kretova, E. S. Avilov, and V. S. Zemskov, Inorg. Mat. **37**, 421 (2001).

[122] P. Nath and K. L. Chopra, *Phys. Rev. B* **10**, 3412 (1974).

[123] R. Lan, R. Endo, M. Kuwahara, Y. Kobayashi, and M. Susa, *J. Appl. Phys.* **112**, 053712 (2012).

[124] J. M. Yanez-Limon, J. Gonzalez-Hernandez, J. J. Alvarado-Gil, I. Delgadillo, and H. Vargas, *Phys. Rev. B* **52**, 16321 (1995).

[125] D. H. Damon, M. S. Lubell, and R. Mazelsky, *J. Phys. Chem. Solids* **28**, 520 (1967).

[126] M. Chen, K. A. Rubin and R. W. Barton, *Appl. Phys. Lett.* **49**, 502 (1986).

[127] K. Schubert and H. Fricke, *Z. Naturforsch* **6a**, 781 (1951).

[128] J. Goldak, C. S. Barrett, D. Innes and W. Youdelis, *J. Chem. Phys.* **44**, 3323 (1966).

[129] A. H. Edwards, A. C. Pineda, P. A. Schultz, M. G. Martin, A. P. Thompson, H. P. Hjalmarson, and C. J. Umrigar *Phys. Rev. B* **73**, 045210 (2006).

[130] A. J. Bevolo, H. R. Shanks, and D. E. Eckels, *Phys. Rev. B* **13**, 3523 (1976).

[131] R. Shaltaf et al., *Phys. Rev. B* **79**, 075204 (2009).

[132] T. Chattopadhyay, J. Boucherle, and H. Von Schnering, *J. Phys. C* **20**, 1431 (1987).

[133] P. Fons, A. V. Kolobov, M. Krbal, J. Tominaga, K. S. Andrikopoulos, S. N. Yannopoulos, G. A. Voyiatzis and T. Uruga, *Phys. Rev. B* **82**, 155209 (2010).

[134] T. Chattopadhyay, J. X. Boucherle and H. G. vonSchnering, *Journal of Physics C* **20**, 1431 (1987).

[135] H. Monkhorst, and J. D. Pack, *Phys. Rev. B* **13**, 5188 (1976).

[136] E.F. Steigmeier and G. Harbeke, *Solid State Comm.* **8**, 1275 (1970).

[137] P. B. Allen and J. L. Feldman, *Phys. Rev. B* **48**, 12581 (1993).

[138] B. J. Kooi and T. M. J. De Hosson, *J. Appl. Phys.* **92**, 3584 (2002).

[139] T. Matsunaga, N. Yamada, and Y. Kubota, *Acta Cryst. B* **60**, 685 (2004).

[140] G. C. Sosso, S. Caravati, C. Gatti, S. Assoni and M. Bernasconi, *J. Phys. : Condens. Matter* **21**, 245401 (2009).

[141] B.-S. Lee, J. R. Abelson, S. G. Bishop, D.-H. Kang and B.-k. Cheong, K.-B. Kim, *J. Appl. Phys.* **97**, 093509 (2005).

[142] A. D. Becke, *J. Chem. Phys.* **77**, 5648 (1993); J. P. Perdew and W. Wang, *Phys. Rev. B* **45**, 13244 (1992).

[143] E. Rotunno, L. Lazzarini, M. Longo, and V. Grillo, *Nanoscale* **5**, 1557 (2013).

[144] B. k. Cheong, S. Lee, J. H. Jeong, S. Park, S. Han, Z. Wu and D. H. Ahn, *physica status solidi b* **249**, 1985-1991 (2012).

[145] T. L. Anderson, and H. B. Krause, *Acta Crystallogr. B* **30**, 1307 (1974).

[146] K. Yokota and S. Katayama, *Jpn. J. Appl. Phys.* **12**, 1205 (1973).

[147] L. Men, F. Jiang and F. Gan, *Mater. Sci. Eng. B* **47**, 18 (1997).

[148] T. Morikawa, K. Kurotsuchi, M. Kinoshita, M. Matsuzaki, Y. Matsui, Y. Fujisaki, S. Hanzawa, A. Kotabe, M.Terao, H. Moriya, T. Iwasaki, M. Matsuoka, F. Nitta, M. Moniwa, T. Koga and N. Takaura, *Electron Devices Meeting, 2007. IEDM 2007. IEEE International*, 307-310 (2007).

[149] von K. Denker and A. Rabenua, *Z. Anorg. Allg. Chemie* **333**, 201 (1964).

[150] T. Schröder, T. Rosenthal, S. Grott, C. Stiewe, J. de Boor and O. Öckler, *Z. Anorg. Allg. Chemie* **639**, 2536 (2013).

[151] J.-L. Battaglia, V. Schick, C. Rossignol, A. Kusiak, I. Aubert, A. Lamperti, C. Wiemer, *Appl. Phys. Lett.* **74**, 181907 (2013).

[152] D. Roy, M. A. A. in't Zandt, R. A. M. Wolters, *IEEE Elec. Dev. Lett.* **31**, 1293-1295 (2010).

[153] G. Chen, *Phys. Rev. B* **57**, 14958-14973 (1998).

[154] M. Methfessel, A. T. Paxton, *Phys. Rev. B* **40**, 3616-3621 (1989).

[155] N. P. Breznay, H. Volker, A. Palevski, R. Mazzarello, A. Kapitulnik, M. Wuttig, *Phys. Rev. B* **86**, 205302 (2012).

[156] R.W.G. Wyckoff Second edition. Interscience Publishers, New York, Cubic close packed structure. Crystal Structures **1**, 7-83 (1963).

[157] N. Schoenberg, *Acta Chem. Scand.* **8**, 213 (1958).

[158] R. Vacher, J. Pelous, F. Plicque, A. Zarembowitch, *J. Non-Cryst. Solids* **45**, 397-410 (1981).

[159] R. O. Pohl, X. Liu, E. *Rev. Mod. Phys.* **74**, 991-1013 (2002).

[160] F. Machatschki, *Fortschritte der Mineralogie*, **20**, 45-47, (1936).

[161] J. L. Battaglia, A. Kusiak, V. Schick, A. Cappella, C. Wiemer, M. Longo, E. Varesi, *J. Appl. Phys.* **107**, 044314 (2010).

[162] S. Caravati, D. Colleoni, R. Mazzarello, T. Kuehne, M. Krack, M. Bernasconi, M. Parrinello, *J. Phys. Cond. Matt.* **23**, 265801 (2011).

[163] I. Spagnolatti, M. Bernasconi, G. Benedek, *Europhys. Lett.* **59**, 572-578 (2002).

[164] E. M. Levin, M. F. Besser and R. Hanus *J. Appl. Phys.* **114**, 083713 (2013).

[165] N. V. Kolomoets, E. Ya. Lev, and L. M. Sysoeva, *Soviet Phys. Solid State* **6**, 551 (1964).

[166] T. Matsunaga, N. Yamada, R. Kojima, S. Shamoto, M. Sato, H. Tanida, T. Uruga, S. Kohara, M. Takata, P. Zalden, G. Bruns, I. Sergueev, H. C. Wille, R. P. Hermann and M. Wuttig, *Adv. Mat.* **21**, 2232 (2011).

[167] H. Zhang , C. X. Liu, X. L. Qi, X. Dai, Z. Fang and S. C. Zhang, *Nat. Phys.* **5**, 438 (2009).

[168] X. L. Qi and S. C. Zhang *Rev. Mod. Phys.* **83**, 1057 (2011).

[169] M. Z. Hasan and C. L. Kane *Rev. Mod. Phys.* **82**, 3045 (2010).

[170] Z.-H. Pan, A. V. Fedorov, D. Gardner, Y. S. Lee, S. Chu, and T. Valla *Phys. Rev. Lett.* **108**, 187001 (2012).

[171] S. R. Park, W. S. Jung, G. R. Han, Y. K. Kim, C. Kim, D. J.Song, Y.Y. Koh, S. Kimura, K. D. Lee, N. Hur, J.Y. Kim, B. K. Cho, J. H. Kim, Y. S. Kwon, J. H. Han and C. Kim, *New J. of Phys.* **13**, 013008 (2011).

[172] R. C. Hatch, M. Bianchi, D. Guan, S. Bao, J. Mi, B. B. Iversen, L. Nilsson, L. Hornekaer and P. Hofmann, *Phys. Rev. B* **83**, 241303(R) (2011).

[173] S. Giraud and R. Egger, *Phys. Rev. B* **83**, 245322 (2011).

[174] G. Q. Huang,*Europhys. Lett.* **100**, 17001 (2012).

[175] X. Zhu, L. Santos, R. Sankar, S. Chikara, C. Howard, F. C. Chou, C. Chamon, and M. El-Batanouny, *Phys. Rev. Lett* **107**, 186102 (2011).

[176] X. Zhu, L. Santos, R. Sankar, S. Chikara, C. Howard, F. C. Chou, C. Chamon, and M. El-Batanouny, *Phys. Rev. Lett* **108**, 185501 (2012).

[177] J. Zhang et al. *Nat. Comm.* **1588**, 2 (2011).

[178] V. Chis, I. Yu. Sklyadneva, K. A. Kokh, V. A. Volodin, O. E. Tereshchenko and E. V. Chulkov, *Phys. Rev. B* **86**, 174304 (2012).

[179] J. Momand, R. Wang, J. E. Boschker, M. A. Verheijen, R. Calarco and B. J. Kooi *Nanoscale* **7**, 19136-19143 (2015).

[180] J.L. Battaglia et al. private comunication.

[181] A. V. Kolobov, D. J. Kim, A. Giussani, P. Fons, J. Tominaga, R. Calarco and A. Gruverman, *APL Mater.* **2**, 066101 (2014).

[182] P. Nemec, V. Nazabal, A. Moreac, J. Gutwirth, L. Jenes, M. Frumar, *Mater. Chem. Phys.* **136**, 935–941 (2012).

[183] C.-Y. Park, T. Abukawa, T. Kinoshita, Y. Enta, S. Kono, *Jpn. J. Appl. Phys.* **27**, 147–148 (1988).

[184] J. Johansson, L. S. Karlsson, C. P. T. Svensson, T. Martensson, B. A. Wacaser, K. Deppert, L. Samuelson and W. Seifert, *Nat. Mat.* **5**, 574–580 (2006).

[185] J. Hutter, M. Iannuzzi, F. Schiffmann and J. VandeVondele, *Wiley Interdisciplinary Reviews: Computational Molecular Science* **4**, 15–24 (2013).

[186] M. Longo, C. Wiemer, O. Salicio, M. Fanciulli, E. Rotunno; *Journal of Crystal Growth* **315**, 152 (2011).

[187] X. Sun et al., *J.Phys. Chem. C* **111**, 2421 (2007).

[188] D. Yu et al., *J. Am. Chem. Soc.* **128**, 8148 (2006).

[189] J. W. L. Yim et al., *J. Am. Chem. Soc.* **131**, 14526 (2009).